High Resolution Imaging of Quantum Gases: from Counting Fermions in Optical Tweezers to Tracking Impurities in 2D Bose Gases

Dissertation
zur Erlangung des Doktorgrades
an der Fakultät für Mathematik, Informatik und
Naturwissenschaften
Fachbereich Physik
der Universität Hamburg

vorgelegt von
Martin Schlederer

Hamburg
2024

Gutachter der Dissertation	Prof. Dr. Henning Moritz
	Prof. Dr. Ludwig Mathey
Zusammensetzung der Prüfungskommision	Prof. Dr. Günter Sigl
	Prof. Dr. Henning Moritz
	Prof. Dr. Ludwig Mathey
	Prof. Dr. Dieter Jaksch
	Jun.-Prof. Dr. Ralf Riedinger
Vorsitzender der Prüfungskommision	Prof. Dr. Günter Sigl
Datum der Disputation	05.03.2024
Vorsitzender des Fach-Promotionsausschusses Physik	Prof. Dr. Markus Drescher
Leiter des Fachbereichs Physik	Prof. Dr. Wolfgang J. Parak
Dekan der Fakultät MIN	Prof. Dr.-Ing. Norbert Ritter

Abstract

In this thesis, experimental work is presented which enabled few atom counting in a tweezer-based ^{40}K setup, the creation of 3D Bose-Einstein condensates of ^{39}K, the achievement of quantum degeneracy in bosonic 2D samples, and of local probing of polaronic physics therein. Starting from an apparatus capable of laser cooling fermionic ^{40}K, a novel dual-color magneto-optical trap capable of detecting individual atoms was implemented. This allowed reliable atom number determination with fidelities of 98% for up to five atoms and $\gtrsim 85\%$ for up to 17 atoms.

Upgrading the setup enabled us to achieve Bose-Einstein-condensation of ^{39}K, and by utilizing suitable optical potentials, to create two-dimensional samples in the regime of BKT superfluidity. In both the 2D and 3D gases polaronic physics was then studied by employing radio-frequency pulses to flip a fraction of the atoms into a strongly interacting impurity state. The polaron spectrum was measured in both cases across a Feshbach resonance, allowing us to tune the strength as well as the sign of the bath-impurity interaction. To model the spectral line shapes with good accuracy it was necessary to include excited polaronic states, in contrast to previous work.

Taking advantage of our machine's high optical resolution, spatially and temporally resolved impurity dynamics in the BKT-gas was experimentally investigated for the first time. The spatial impurity distribution observed in frequency-resolved measurements exhibits significant differences between attractive and repulsive interactions, supporting the relevance of excited polaron states. For repulsive interactions we observe an outward motion of the impurities and ultimately the expulsion of the impurities from the bath. We can accurately describe this motion when including the predicted friction term for velocities above the speed of sound.

Zusammenfassung

In dieser Arbeit wird experimentelle Forschung präsentiert, die die präzise Atomzahlbestimmung in einem auf optischen Pinzetten basierenden ^{40}K-Aufbau, die Erzeugung von 3D-Bose-Einstein-Kondensaten von ^{39}K, das Erreichen von Quantenentartung in bosonischen 2D-Systemen und die räumlich aufgelöste Untersuchung der Polaronphysik darin ermöglichte.

Ausgehend von einem experimentellen Aufbau mit lasergekühltem, fermionischem ^{40}K wurde eine neuartige zweifarbige magneto-optische Falle implementiert, die einzelne Atome nachweisen kann. Dies ermöglichte die präzise Bestimmung der Atomzahl mit einer Zuverlässigkeit von 98% für bis zu fünf Atome und $\gtrsim 85\%$ für bis zu 17 Atome.

Durch die Erweiterung des Aufbaus konnten wir die Bose-Einstein-Kondensation von ^{39}K erreichen und, durch die Verwendung geeigneter optischer Potentiale, zweidimensionale Systeme im Bereich der BKT-Superfluidität erzeugen. Mithilfe von Radiofrequenzpulsen konnte dann sowohl in 2D- als auch in 3D-Systemen ein Teil der Atome in einen anderen, stark wechselwirkenden Spinzustand transferiert werden, sodass die Untersuchung von Polaronphysik möglich wurde. Das Polaronenspektrum wurde in beiden Fällen über eine Feshbach-Resonanz gemessen, was es ermöglichte, sowohl die Stärke als auch das Vorzeichen der Wechselwirkung zwischen Bad und Verunreinigung zu kontrollieren. Um die spektralen Linienformen gut zu modellieren, war es insbesondere notwendig, angeregte polaronische Zustände zu berücksichtigen.

Durch die hohe optische Auflösung unserer Apparatur konnte die Polarondynamik im BKT-Gas erstmals räumlich und zeitlich aufgelöst experimentell untersucht werden. Die in frequenzaufgelösten Messungen beobachtete räumliche Struktur zeigt signifikante Unterschiede zwischen attraktiven und repulsiven Wechselwirkungen, was die Relevanz angeregter polaronischer Zustände unterstützt. Für abstoßende Wechselwirkungen wurde eine nach außen gerichtete Bewegung der Verunreinigungen und schließlich die Ausstoßung der Verunreinigungen aus dem Bad beobachtet. Diese Bewegung konnte akkurat modelliert werden, wenn der theoretisch hergeleitete Reibungsterm für Geschwindigkeiten über der lokalen kritischen Geschwindigkeit einbezogen wird.

Publications

The following research article has been published in the course of this thesis:

- *Single-Atom Counting in a Two-Color Magneto-Optical Trap*
  M. Schlederer, A. Mozdzen, T. Lompe, and H. Moritz,
  Physical Review A, 103(**3**), (2021).

Contents

Chapter 1

Introduction

1.1 Introduction: Polarons

Based on Landau's work on a single electron interacting with a lattice [1], Landau and Pekar in 1948 published their seminal paper [2], introducing the concept of a quasi-particle coined "polaron", which describes the combined properties of a bare electron and the reaction of the surrounding medium. This paradigmatic conceptual approach of introducing a quasi-particle with properties different from the bare particle has since found widespread adoption in condensed matter physics and beyond.

In their original work, Landau and Pekar considered the effect of a single electron on the surrounding lattice; H. Fröhlich later provided a fully quantum-mechanically description [3]. In this model, the electric charge of the single electron induces a local polarization in the medium, corresponding to a displacement from the unperturbed positions. In a simple picture, this displacement can be seen as a superposition of lattice vibrations with appropriate phase and momentum. It is this combination of optical phonons with the bare electron that forms the new quasi-particle named "polaron". This emergent particle has properties different from the bare electron: due to the local polarization, the charge of the electron is screened. Furthermore, the electron becomes inseparable from the medium's polarization, causing a "dragging" effect with any movement and leading to an effective mass $m_{eff} > m_{bare}$, resulting in reduced mobility. For example, in the limit of weak coupling and to linear order in the coupling constant α, the effective mass can be derived to be $m_{eff} = m_{bare} \cdot (1 + \alpha/6)$ [4], where α for typical materials ranges between 10^{-2} and $\sim$3 [5], resulting in effective masses deviating from the bare mass by a few percent to up to approximately 50%.

As it describes the effective low-energy physics, the same concept of an impurity "dressed" by distortions of the surrounding media, as sketched in Fig. 1.1, has since been

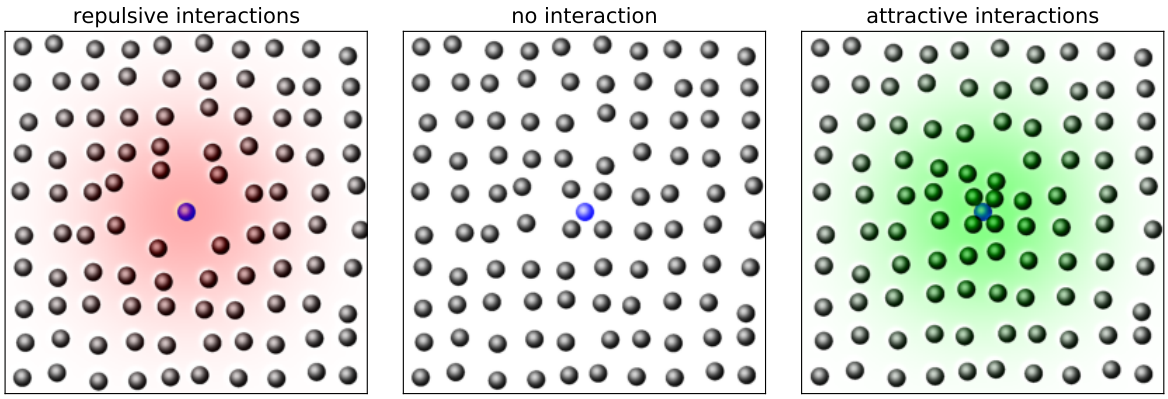

Figure 1.1: Polaron sketch. The bath (black) exhibits a typical interparticle distance. Adding an impurity particle (blue) to the setting does not affect the bath density if there is no interaction between bath and impurity (middle), but reduces the local density for repulsive bath-impurity interactions (left, red) and increases the local density for attractive interactions (right, green). In the shown schematic, the impurity interacts directly with the bath density and does not induce a polarization as in the original polaron-model.

employed in various other problems in condensed matter physics. The Kondo effect [6] is an example where the polaron concept was extended to an impurity with a fermionic bath. In this scenario, a localized and immobile magnetic impurity scatters conduction band electrons, contributing to the electric resistance. For sufficiently low temperatures, the coupling between the magnetic impurity and the fermionic bath becomes dominant and leads to a logarithmic divergence of the resistance, leading to a minimal resistance at $T > 0$, as observed in certain alloys.

Similarly, the approach has also been used in the context of colossal-magnetoresistance manganites [7–10], high-temperature superconductors [5, 11–14], and of the wide field of semiconductors [15]. Beyond condensed matter physics, the concept has, for example, been employed in the description of nuclear and quark matter [16–18]. Probably best known and triggered by the non-relativistic work by P. W. Anderson in 1963 [19], the concept has been extended to the Higgs-mechanism, where the mass of elementary field excitations like the electron originate in a dressing of the bare electron by the bosonic Higgs field, which acquires a non-zero vacuum expectation value [20–23].

A complementary conceptual approach reverses the roles played by impurity and bath: instead of focusing on the new properties of the dressed impurity, it is seen as a microscopic probe for the surrounding medium, where the dressing reveals some of the bath's properties, such as, for example, the density of states. Since the impurity is typically of the same or very similar size as the particles of the bath, it hence allows to explore the response on length scales often not accessible in other ways.

From this view point, the most crucial defining property is the statistics of the bath,

distinguishing between fermionic baths, e.g. in the Kondo-effect or in semiconductors, and bosonic baths, as in Landau and Pekar's original work where the impurity is coupled to phonons. The bath's statistics directly affects the available density of states, particularly at the low energies usually most relevant for the formation of quasi-particles. Similarly, the existence of an energy gap or the dimensionality of the system can play a crucial role.

In recent years, quantum gas experiments have emerged as an ideal platform to investigate numerous paradigmatic model systems of condensed matter physics and beyond, including the problem of an impurity interacting with a bath.

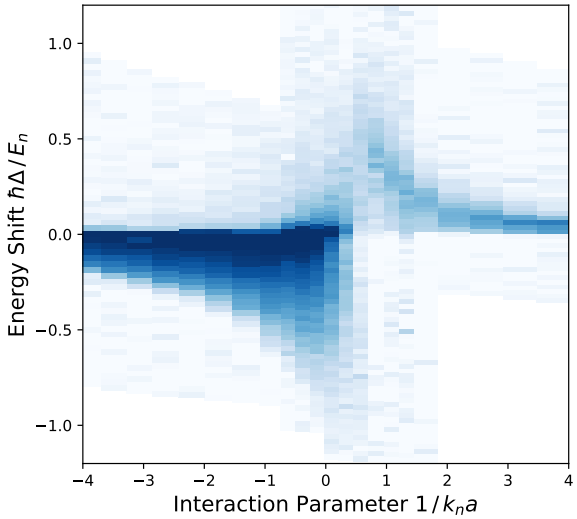

Figure 1.2: Polaron spectrum measured in a 3D BEC by injection spectroscopy. The y-axis is the observed energy shift and the x-axis is the interaction strength ranging from weakly attractive on the left to strongly attractive and strongly repulsive near the center to weakly repulsive on the right. See Sec. 4 for more details.

Quantum gas experiments offer some significant advantages over alternative implementations: in addition to the "spatial" parameters like the geometry of the trapping potential or the particle density, the most important feature available in these experiments is the possibility to control the interparticle interaction strength, both for the interaction within the bath as well as between bath and impurity. This is usually accomplished through Feshbach resonances [24], offering not only the possibility to tune tune the interaction strength but also to switch between attractive and repulsive interactions. This is directly illustrated by the spectrum shown in Fig. 1.2, where we used such a Feshbach resonance to control the interaction (corresponding to the x-axis). The negative energy shifts occur for attractive interactions, the positive energy shifts for repulsive interactions, and strongest interactions are located in the center of the plot.

Moreover, cold samples of both fermionic and bosonic species have been achieved, thus allowing to probe different particle statistics. For low enough temperatures and suitable interactions, fermions form a degenerate Fermi-gas, where all states up to the Fermi energy are occupied and higher states are empty. Bosons, on the other hand, can form a Bose-Einstein condensate and hence show a distinctively different behavior. For higher temperatures, one can of course also probe the transition from these degenerate systems to a thermal gas.

In the frame of this thesis we implemented a setup that produces such ultracold quantum gases. In particular, our machine allows us to work with either fermionic ^{40}K in small systems or with bosonic ^{39}K in larger bulk systems. In both cases, fermionic and bosonic, we can control the interaction strength and at the same time have a high degree of spatial and temporal resolution. When using bosonic ^{39}K in bulk systems, we achieved Bose-Einstein-Condensation in three dimensions and, by utilizing a repulsive optical potentials in one direction and hence creating two-dimensional systems, also created ultracold clouds well in the Berezinskii-Kosterlitz-Thouless (BKT) regime. In both of these degenerate systems we were able to measure the polaron spectra for attractive and repulsive interactions of tuneable strength. In two-dimensions, measuring the polaron spectrum in such a setting has not been reported before[1]. We analyze the observed line shapes for these spectra and develop phenomenological models that reproduce the observations very well. Especially for attractive interactions, these models suggest that excited polaronic states play a significant role in our system. Moreover, the high optical resolution allowed us to investigate spatially resolved creation of impurities in a two-dimensional BKT gas for the first time. The observed spatial structures support the relevance of excited states. Utilizing the temporal control, we were furthermore also able to observe spatially and temporally resolved impurity dynamics in this degenerate cloud. In a setting with an accelerating force on the impurities, we were able to observe motion consistent with friction for velocities above the local speed of sound.

In the remaining part of this chapter, we describe some essential aspects of our machine and of the available atomic isotopes ^{39}K and ^{40}K. Chapter 2 presents the development and implementation of a two-color MOT as a novel tool for atom number counting in quantum gas experiments like ours and furthermore discusses the further progress towards realizing paradigmatic few-fermion systems in tweezers with a special focus on implementing Anderson's orthogonality catastrophe. Turning to bosonic polaron physics for the rest of the thesis, chapter 3 starts with an overview over previous quantum gas experiments focusing on polaron physics, introduces the relevant background of physics in two-dimensional system, and finally describes the experimental preparation scheme and some more specific experimental aspects potentially interesting for readers working with similar setups.

Chapters 4 and 5 form the central parts of this thesis: Chapter 4 contains the measured spectra, line shape modeling and discussion, as well as the results extracted from these spectra. This is done for both three-dimensional systems in Sec. 4.1 and for two-

[1]During the writing phase of this thesis, a poster about a similar spectral measurement in a 2D BKT gas was presented at the BEC2023 conference by the Hadzibabic group, but no publication or pre-print has been published so far.

dimensional systems in Sec. 4.2. Chapter 5 proceeds from integrated measures used for the spectra to spatially and temporally resolved measurements of impurity dynamics in a BKT gas. Finally, a conclusion and outlook is given in chapter 6.

1.2 Machine Overview

The experiments described in the following sections have been performed on a quantum gas machine originally designed and to a large part assembled by Phillip Wieburg [25]. Here we give a brief overview over the machine and its most relevant aspects.

1.2.1 Mechanical and Optical Setup

The main technical feature of the machine are the two high-NA microscope objectives located inside the vacuum with a working distance of 2.5 mm from the atoms. With their numerical aperture of 0.75, each of them covers 16% of the solid angle and allows for a Rayleigh resolution limit of ∼620 nm at a wavelength of 767 nm. A more detailed overview of the microscopes' design, assembly, and mounting can be found in [25], section 4.4, and a cut through the machine's CAD model is shown in Fig. 1.3.

Atomic Species and Isotopes The oven inside the vacuum chamber is filled with 100 mg of potassium, with which we conduct the experiments. As an alkali element, potassium has a single electron it its outermost 4s-shell, and shows a relatively simple, hydrogen-like level structure. The relevant atomic transitions and needed laser systems will be discussed further below.

Since the natural abundance of the fermionic ^{40}K is only ∼0.01%, the sample used in this experiment has been enriched to 3% of ^{40}K, and most of the rest consists of the bosonic ^{39}K. The small natural component of bosonic ^{41}K (∼7 %) is not used in this experiment as it provides no significant advantage compared to the more abundant ^{39}K. The machine has been designed to be able to switch between the two isotopes ^{39}K and ^{40}K and therefore allows experiments both with fermionic and with bosonic particles. The atomic vapor from the heated oven is captured by a 2D MOT nearby [26], from which a push beam transfers the atoms through a differential pumping stage to the main vacuum chamber.

Main Vacuum Chamber This main chamber is a steel chamber with ∼380 mm diameter and six large CF63 vacuum windows in the horizontal plane. CF100 vacuum windows on the top and the bottom of the chamber allow for optical access along the vertical direction. Several small CF16 windows with a small angle to the horizontal plane are also present and are mostly used for imaging of various stages of the experimental cycle.

To allow for better optical access, the cooling and trapping is done at two distinct positions: the "MOT position" is aligned with the axis defined by the differential pumping

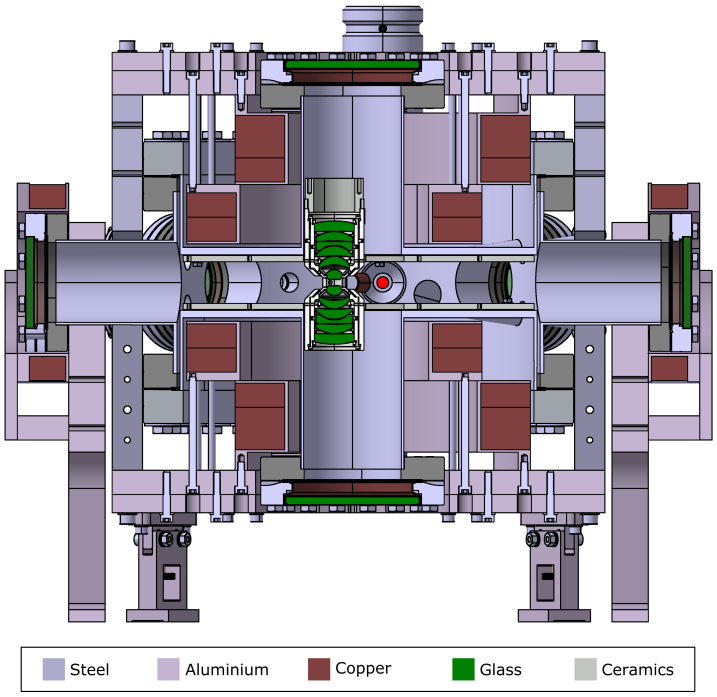

Figure 1.3: Cut through the CAD model of the main vacuum chamber. The microscopes in green are visible near the center of the chamber and define the science position. The red dot to its right is aligned with the 2D MOT axis and indicates the 3D MOT position; the distance between the MOT position and the science position is 40 mm. The cut is orientated along the transport axis, showing the quantization axis coils on the very left and right of the machine. The experiment coils, only visible by their cross section in brown, are centered around the science position, while the MOT coils are centered around the MOT position and have a larger distance to the atom plane. Adapted from [25].

section and, as the name suggests, is the position where the atoms are captured in a 3D MOT and subsequently cooled further by a gray molasses scheme. The "science position" is located 40 mm away from the MOT position and is centered between the two microscopes; the axis defined by these two positions will sometimes be referred to as "transport axis". The distance of 40 mm corresponds to ∼28 mm under an angle of 45°, allowing 1" optics to be aligned parallel to each other for both the MOT and the science position. Vertically, the MOT position can be accessed directly through the vacuum window, while the science position can only be accessed via the microscopes.

Microscopes, Imaging, and State Transfers The upper microscope is predominantly used for creating optical potentials with high spatial resolution, while the lower microscope is mainly used for optical access to image the atoms; the imaging can either be done by fluorescence imaging or absorption imaging. In the latter case, both the trapping light and the imaging light is guided through the upper microscopes such that the trapping light is focused in the atom's plane, while the imaging light is collimated.

After passing the lower microscope, these two components are separated by a dichroic mirror. The trapping light is then either dumped or reflected back, resulting in either a running wave trap or a lattice, respectively. The imaging light is, after a suitable optical setup, collected by a camera, yielding the fluorescence or absorption images as the main observable of the experiment.

The main tool to address and manipulate the atomic state is electromagnetic radiation, specifically radio-frequency radiation for transitions between the hyperfine levels within the electronic ground state, and optical and near infra-red light for almost all other applications. The relevant laser systems are discussed in Sec. 3.3.1 and Sec. 2.1.2 for ^{39}K and ^{40}K, respectively. As the vacuum chamber acts as a Faraday cage, the atoms are shielded by radio-frequency signals from outside the chamber and an in-vacuo antenna has to be used. The setup is described in a bit more detail in Sec. 3.3.1.

Magnetic System Apart from optical and radio-frequency radiation, magnetic fields are needed for manipulating the atomic behavior, e.g. for cooling in a MOT or for interaction tuning using a Feshbach resonance. These magnetic fields are created by several pairs of coils along different axis: one pair with N = 23 windings is orientated along the transport axis and is mostly used to provide a quantization axis for optical pumping and to compensate the strong North-South component of Earth's magnetic field. Another pair of coils is centered around the MOT and one pair around the science position, with N = 88 and N = 64 windings, respectively. For each of the MOT and experiment coil pairs, the current direction in one of the coils can be reversed, allowing us to switch between (quasi-)Helmholtz- and Anti-Helmholtz configuration; the experiment coil pair fulfills the Helmholtz condition (radius of the coils equals their distance), while for the MOT coil pair, this condition is not fulfilled (distance is larger than their radius), as the requirements for the homogeneity are less strict. Thus, one can switch between a homogeneous field and a gradient field at the atom position. All of these pairs consist of hollow-core, water cooled wire with an effective cross section of 10.88 mm^2 [2]; the active cooling and the current power supplies allow for currents of ∼170 A in the MOT and experiment coil pairs, corresponding to fields of up to ∼480 Gauss and ∼900 Gauss in Helmholtz configuration, respectively, and gradients of up to ∼85 G/cm and ∼110 G/cm for Anti-Helmholtz configuration. These fields allow reaching all relevant Feshbach resonances for both ^{39}K and ^{40}K. In addition to these large coils, several pairs of smaller coils orientated along different axes allow to add offset fields or gradients, e.g. for compensating earth's magnetic field or to shift the exact position of the magnetic zero. As these smaller coils use a 1 mm^2 wire

[2] Oswald Elektromotoren GmbH

and are not water-cooled, the current and therefore their magnetic field is much smaller, usually allowing for $I_{max} \approx$ 2-3 A. The field generated by these offset coils strongly depends on their winding number, but is usually on the order of one to a few Gauss when used in quasi-Helmholtz-configuration.

1.2.2 Atom Species Comparison: ^{39}K and ^{40}K

As this thesis describes experiments conducted with both ^{39}K and ^{40}K, the main similiarities and differences between them are briefly summarized here and are discussed in more detail when necessary.

Statistics and Final System Of the naturally occurring isotopes ^{39}K, ^{40}K, and ^{41}K, the first and the last are bosonic while ^{40}K is fermionic. As the abundance of ^{39}K is much higher than the abundance of ^{41}K ($\sim$93% vs $\sim$7%), we only use ^{39}K as a bosonic sample. With the fermionic ^{40}K, the systems of interest are small Fermi-Hubbard model systems and small fermionic tweezer systems, while ^{39}K is intended to be used in larger bulk systems or in a bosonic quantum gas microscope.

The reason for these different final stages is the last step of the cooling process: ^{39}K atoms cooled to very low temperatures and high phase space densities start populating the same state, thus, at least in 3D bulk systems, forming a Bose-Einstein condensate. ^{40}K atoms, on the other hand, are subject to Pauli blocking and thus their ground state in a bulk system is a Fermi gas, where all states up to the Fermi energy are occupied. The reduced available phase space near this state prevents scattering, making obtaining a cold Fermi gas at low enough temperatures is very challenging. This is especially true for ^{40}K when compared to the only other stable fermionic isoptope of an alkaline element, ^{6}Li, as the latter has a lower three-body decay rate and therefore less losses when evaporating [27]. We thus focused on smaller systems where the fermionic atoms are cooled to their motional ground state either by Raman-Sideband-Cooling (beyond the scope of this thesis, but discussed in [28]) or by enhancing the phase space density within a small subsystem by using the "dimple trick".

Preparation and Probing This difference only becomes relevant once the phase space density of the sample is on the order of unity, making the early stages of the cooling are very similar: after loading a MOT, the atoms are further cooled with a D1 gray molasses scheme, and finally optical pumping transfers the atoms to the correct state for the magnetic transport to the science positions between the microscope objectives. At the science position, the atoms are loaded into an optical dipole trap and usually cooled

evaporatively[3]. Once sufficiently cooled, the actual experiment is performed and the final state is imaged, either by absorption imaging or fluorescence imaging.

Level Structure The general level structure for ^{39}K and ^{40}K is similar and is discussed in more detail in Sec. 3.3.1 and Sec. 2.1.2, respectively. The first main difference is that ^{39}K has a lower number of magnetic substates in the electronic ground state compared to ^{40}K: ^{39}K has the two states F = 1 and F = 2 with three and five m_F-states, respectively, while ^{40}K has F = 9/2 and F = 7/2 with ten and eight m_F-states, respectively. The second large difference is that ^{40}K shows an inverted ground state structure, such that F = 9/2 is energetically below F = 7/2. While the optical transitions needed for cooling, pumping, and imaging are shifted by a few hundred MHz between the two isotopes, the machine has been designed to easily switch between those.

Interaction Tuning Both isotopes exhibit useful Feshbach resonances for at least some states. For ^{39}K, all spin combinations of the lower hyperfine state F = 1 have easily reachable Feshbach resonances, allowing for a relatively flexible tuning of the interaction between atoms in the same and in different m_F-states. One group of Feshbach resonances is located between ∼20 Gauss and ∼170 Gauss, and a second group between ∼400 Gauss and ∼600 Gauss [29–31]. Intrastate interactions are suppressed for ^{40}K due to Pauli blocking, and thus only the interstate interaction is relevant. The Feshbach resonances here are more limited, and the most relevant is the Feshbach resonance found between $|F = 9/2, m_F = -9/2\rangle$ and $|F = 7/2, m_F = -7/2\rangle$, which is located at 201 Gauss and has a width of 8 Gauss [32].

[3]Only in the attempt for small Fermi-Hubbard systems, the evaporation was replaced by Raman-Sideband-Cooling.

Chapter 2

Two-Color MOT

This chapter describes our two-color MOT scheme for few atom counting and is heavily based on the published version [33]. After a brief motivation, the implementation of this two-color MOT scheme is discussed in detail, followed by a section about the experimental realization of the Anderson Orthogonality Catastrophe in a tweezer setup and the expected signal thereof.

2.1 ^{40}K Tweezers as a Platform for Mesoscopic Fermi Systems

2.1.1 Mesoscopic Fermi Systems

Experimental setups like ours, with a high numerical aperture and therefore high optical resolution, are excellent settings for probing mesoscopic systems, i.e. the interface between single-particle or two-particle systems on the one hand, and many-particle systems on the other. This is not only due to the possibility to create and control flexible potential landscapes by employing suitable optical intensity patterns, but also due to the high degree of control over the initial conditions of the physical setup. In addition to parameters accessible in most cold-atom experiments like scattering length or average density, the high optical resolution also opens up the possibility to control the initial density locally or to set, within certain limits, the exact atom number of the initial state. This ability allows us to investigate the intermediate regime between single-particle behavior of either isolated or non-interacting particles, and many-particle effects accessible in large interacting systems as the other extreme.

An essential tool in this intermediate regime is the possibility to determine the exact

atom number[1]. In our experiment, we use a tweezer system where several atoms are confined within one tightly focused laser beam and can, for example, be used to investigate the onset of the so-called "Orthogonality Catastrophe" introduced by Philip W. Anderson in 1967 [34]. In this paper, Anderson considered a simple toy model of N non-interacting fermions confined in a spherical potential well, where determining the basis functions of this potential as well as the many-body wave function is straightforward. The introduction of a central scattering potential serves as a slight perturbation and leads to a phase shift for all wave functions near the center of the potential well. While each single particle wave function still has almost unity overlap with the unshifted case, Anderson showed that the overlap of the many-particle ground state wave functions approaches zero for $N \to \infty$, even for weak potentials. In essence, the small reduction of single particle overlap from 1 to $1-\epsilon$ leads to a total reduction to $(1-\epsilon)^N$ in a many-body wave function of N fermions, and becomes zero in the limit of $N \to \infty$. Thus, this small potential renders the ground states of these two very similar systems almost orthogonal.

This effect can be seen as an extreme case of the previously discussed problem of a bath with an impurity immersed into it, where the case of a cold fermionic bath with an immobile impurity is analyzed. The focus is then not on the properties of the impurity, but on the effects it has on the bath, and, in particular on its effects on the bath's ground state wave function as well as the overlap between the unperturbed bath and the bath with a single impurity.

Unlike in quantum gas microscopes, where the atoms spread out over a larger potential and the average occupation per site is on the order of one or below [35–38], tweezer systems do not allow for a direct in-situ fluorescence imaging, as photo-association losses would lead to a parity projection [39–41] and thus to rapid loss of fluorescence signal in the trap. To avoid these losses, we instead release the atoms from the tight optical potential and transfer them into a tight magneto-optical trap. In order to separate the weak fluorescence signal from the large background, we developed a two-color scheme, where the light responsible for trapping and cooling is different from the light used to identify the presence of an atom, allowing us to use spectral filters to increase the signal-to-noise ratio.

As this chapter deals with the fermionic ^{40}K, we start with a summary of its relevant properties, the typical system preparation scheme, and a discussion of the optical and magnetic setup needed. Readers familiar with ^{40}K may easily skip this section and proceed to the implementation and performance of the two-color MOT, presented in the following

[1]Preparing a fixed atom number is not quite as relevant, as the subset of relevant runs can always be selected in the postprocessing.

section. Finally, we discuss the technical aspects of probing Anderson's Orthogonality Catastrophe in a tweezer system in Sec. 2.3.

2.1.2 Introduction to ^{40}K

This section is intended to give a brief overview over the most relevant properties of ^{40}K. Some of those have already been mentioned in Sec. 1.2.2, but aspects only relevant for the fermionic isotope are described here.

Level Structure, Cooling, and Laser System The relevant level scheme and laser system for ^{40}K is visualized in Fig. 2.1 and has been described in more detail in [25] (Sec. 4.5). With a nuclear spin of I = 4, the $4s_{1/2}$ state has a total coupled angular momentum of either F = 9/2 or F = 7/2, where F = 9/2 has a lower energy due to the inverted hyperfine splitting in ^{40}K. Hence, the actual ground state F = 9/2 has a cycling transition, which is unusal for Alkali atoms and is also not the case for ^{39}K, as will be discussed later. Almost all transitions employed in manipulating the ^{40}K atoms are either on the D1 line, connecting the $4s_{1/2}$ state to the $4p_{1/2}$ state with a transition wavelength of 770.1 nm, or on the D2 line, connecting the $4s_{1/2}$ ground state to the $4p_{3/2}$ state with a wavelength of 767.7 nm. Initial cooling in the 2D- and 3D-MOT is done by the "Cooler Laser" operating on the D2 line, connecting $|4s_{1/2}, F = 9/2\rangle$ and $|4p_{3/2}, F = 11/2\rangle$. This laser is generated by a Toptica DLC DL Pro and amplified with a custom built tapered amplifier (TA)[2]. Since atoms can decay to the F=7/2 state, a repumping laser is needed. The frequency difference to the cooler transition is about 1.3 GHz and therefore too large to bridge with an AOM. The repumping is instead done by exciting atoms from $|4s_{1/2}, F = 7/2\rangle$ to $|4p_{3/2}, F = 9/2\rangle$ with an independent laser (Toptica DLC DL Pro, later replaced by a DFB laser diode[3]), that is also amplified by a custom built TA[4].

Imaging is usually done with the very same laser also used for the MOT cooler. In the runs presented with ^{40}K, the imaging was performed at low field, such that the presented level scheme is still valid. For higher fields, above ∼20 Gauss, the $4p_{3/2}$ state enters the Paschen-Back regime and the energy shifts due to the magnetic tuning start to become larger than the hyperfine splitting. This corresponds to a decoupling of the (total) electronic angular momentum J from the nuclear spin I, thus rendering the quantum number F meaningless.

The second stage of cooling by a Λ-enhanced molasses [42–46] is performed on the

[2]TA-0765-2000 for MOPA Setups; previously *m2k-Laser*, now *Coherent*.
[3]EYP-DFB-0767-00050-1500-TOC03-0005 by *Eagleyard*.
[4]TA-0765-2000 for MOPA Setups; previously *m2k-Laser*, now *Coherent*.

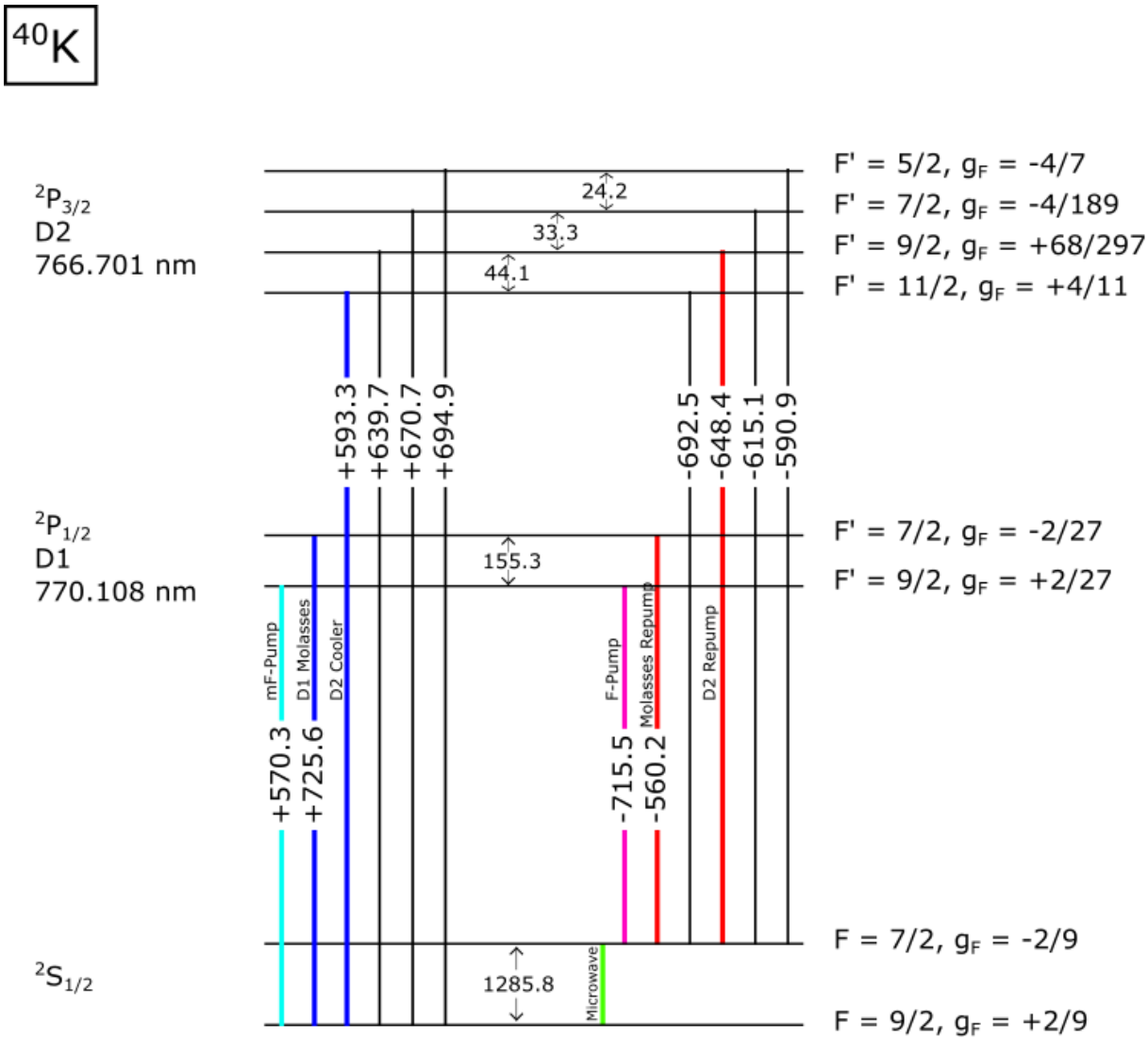

Figure 2.1: Relevant part of the level structure of ^{40}K with the electronic ground state ($4^2S_{1/2}$) and two electronically excited states ($4^2P_{1/2}$ and $4^2P_{3/2}$). The numbers in the individual connecting lines indicate the frequency shift of the respective transition at zero magnetic field with respect to the crossover with the numerical value given in MHz; the transitions used in the experiment are indicated by colored, labeled lines. The hyperfine states in both the electronic ground state as well as the $4^2P_{1/2}$ state are split by detunings too far to comfortably bridge by tuning the lasers' offsetlocks. For states within the $4^2P_{3/2}$-manifold this is possible though and no additional AOMs are needed.

D1 line. Λ-enhanced gray molasses has to be performed on a coherent combination of a $F \to F-1$ transition and a $F-1 \to F-1$ transition. Thus, we employ the $|4s_{1/2}, F = 9/2\rangle$ to $|4p_{1/2}, F = 7/2\rangle$ transition, and use an EOM to additionally modulate a sideband at a tuneable frequency around f = 1285 MHz onto the beam[5]. The modulated sideband is

[5]D1 Laser: *Toptica* DLC DL Pro; TA Chip: EYP-TPA-0780-02000-4006-CMT04-0000 by *Eagleyard*;

resonant on the $|4s_{1/2}, F = 7/2\rangle$ to $|4p_{1/2}, F = 7/2\rangle$ transition, creating the mentioned Λ-scheme. Tuning the exact modulation frequency of the EOM allows to select the point of highest final phase space density. The transition between MOT and molasses is hindered by the long decay times of the induced eddy currents when switching off the magnetic fields; we find that we effectively first form a "blue MOT" [47], similar to what has been reported in [48], and then smoothly transition into a proper molasses [28].

The same lasers are also applied at the science position between the microscope objectives, where a brief molasses phase is used to transfer the atoms from the magnetic trap into the optical trap. Collisional loading is in this case very inefficient as p-wave scattering is thermally suppressed and s-wave scattering is forbidden due to Pauli blocking. The difference in regards to the normal molasses scheme is the presence of the strong magnetic field gradient, which leads to rapid heating when applying the D1 for longer times. As the eddy current decay time of the large vacuum chamber is rather long [28], it is not possible to turn off the magnetic gradient fast enough to apply the molasses and still keep the cloud at a reasonable high phase space density, and this scheme has to be applied instead.

Optical Pumping and Magnetic Transport After the initial cooling steps of MOT and molasses, a magnetic trap transports the atoms by about 40 mm to the science position between the microscope objectives. Molasses cooling accumulates atoms in a dark state that is a linear combination of different m_F-states and therefore the atoms are distributed over the whole F = 9/2 and F = 7/2 manifolds. Turning off the EOM modulation briefly before the molasses beam transfers the atoms into the F = 9/2 state, however the atoms still need to be transferred into the correct m_F-state for magnetic trapping. Due to the inverted hyperfine structure of ^{40}K, the magnetically strongest trapped state is the $|F = 9/2, m_F = +9/2\rangle$ state, which shows the full tuning of $\Delta E = h \cdot 1.4$ MHz/G at low fields.

This transfer is done by optical pumping, which is also performed on the D1 line. The "m_F-pumper" acts on the $|4s_{1/2}, F = 9/2\rangle$ to $|4s_{1/2}, F = 9/2\rangle$ transition and is σ^+-polarized, such that atoms are pumped towards the $m_F = +9/2$ state, which is dark to the pumping beam as there is no $m_F = +11/2$ state in the relevant manifold. Depending on their initial m_F-quantum number, atoms might need several pumping cycles before accumulating in the desired state. A table of all relevant decay ratios can be found in appendix A. Atoms in the $|4p_{1/2}, F = 9/2\rangle$ state decay to the $|4s_{1/2}, F = 9/2\rangle$ in only ∼40% of the cases. Therefore a second σ^+-polarized beam on the $|4s_{1/2}, F = 7/2\rangle$ to

EOM: *Qubig* EO-K40-3L, tuning range 1.15 - 1.30 GHz

$|4p_{1/2}, F = 9/2\rangle$, usually referred to as "F-Pumper", is needed to repump the atoms back to the correct F-state. Later in the experimental cycle, the Feshbach resonance at 201 Gauss between $|9/2, -9/2\rangle$ and $|9/2, -7/2\rangle$ [32] is used to tune the interaction strength and the optical pumping has to be inverted. This is done by switching the quantization axis direction by reverting the current direction, thus switching the σ^+-polarized pumping beams into σ^--polarized beams.

Microwave Transfers Transfers within the ground state manifolds are possible at microwave frequencies around 1285 MHz for transitions between F = 9/2 and F = 7/2, and between adjacent m_F-states at theoretically arbitrarily low frequencies. Near the most relevant Feshbach resonance at 201 Gauss, the transition frequency between $|9/2, -9/2\rangle$ and $|9/2, -7/2\rangle$ is about 44 MHz. Both of these transitions can be driven by using the same in-vacuo antenna when switching the matching circuit. While a second in-vacuo antenna had been implemented specifically for the 44 MHz regime in the early stages of the experimental setup, it turned out that this device did not produce any significant RF signal detectable by a pick-up coil or the atoms (see [28] for a more detailed discussion of this topic).

Optical Potentials Most optical potentials used for ^{40}K are formed by red detuned light at $\lambda = 850$ nm, where well performing laser diodes and TA chips can be purchased commercially. These potentials are generated by an unlocked Toptica DLC DL pro as a laser source and using self-built TAs to increase the laser power[6]. Compared to typical sources at 1064 nm, the 850 nm sources are less powerful, usually only providing a few Watt of laser power, compared to several tens of Watt for 1064 nm. The advantage of 850 nm potentials is the reduced antitrapping in the excited state due to the $3d_{3/2}$ state and the $5s_{1/2}$ state, with resonance wavelengths of 1169 nm and 1244 nm, respectively, from the $4p_{1/2}$ state [49, 50]. While an atom in the ground state experiences a trapping potential, an excited atom will experience an antitrapping potential. When using 1064 nm light for the optical potentials, the amplitude of the anti-trapping is roughly four times larger than the trapping of the ground state, which leads to significant heating even during the short lifetimes in the excited states. As 850 nm is further detuned from the relevant transitions at 1169 nm and 1244 nm, the remaining antitrapping is significantly smaller and its amplitude is comparable to the trapping of the ground state.

[6]TA chips: TA-0850-3000-CM for MOPA Setups; previously *m2k-Laser*, now *Coherent*.

Interaction Tuning: Feshbach Resonances Interactions between atoms with same spin state are thermally suppressed at the relevant low temperatures as s-wave scattering is Pauli-blocked and p-wave scattering requires enough angular momentum and is therefore frozen out. The remaining relevant interactions are thus only between different spin states. For ^{40}K, a suitable Feshbach resonance is found between $|9/2, -9/2\rangle$ and $|9/2, -7/2\rangle$, located at $B_{res} \simeq 201$ Gauss with a magnetic width of $\Delta \simeq 8$ Gauss [32]. Another relevant Feshbach resonance occurs between the $|9/2, -9/2\rangle$ and the $|9/2, -5/2\rangle$ state at $B_{res} = 224$ Gauss with a width of $\Delta \simeq 10$ Gauss [51]. Plenty of other resonances have been reported [52], but most of those are not protected against spin changing collisions or only protected at higher field due to the second-order Zeeman effect.

2.2 Two-Color MOT

Collecting fluorescence light while laser cooling and trapping the atoms in a magneto-optical trap (MOT) has proven to be a reliable and well established method to measure atom numbers with single particle resolution [53–65] and is especially suited for experiments studying few atoms confined in optical tweezers, where in situ imaging would lead to photo-association losses. As the number of photons emitted by a single atom is quite limited, these experiments require considerable effort to maximize the signal-to-noise ratio of the fluorescence signal. Common techniques for achieving this include the use of large magnetic field gradients to compress the MOT and thereby spatially concentrate the fluorescence signal, using optics with high numerical aperture to maximize the number of collected photons, as well as employing highly sensitive and low noise cameras. At the same time, detrimental stray light collection is suppressed as far as possible by employing laser cooling beams with small diameters, avoiding the presence of unwanted scattering surfaces close to atoms, and spatial filtering of the fluorescence signal.

Using these techniques, single atom atom resolution for atom numbers in excess of 300 has been achieved [61, 63]. However, the stringent limits on the amount of stray light present in the system render this method unsuitable for many experimental setups that were not specifically designed for this purpose. Suppressing stray light detection is particularly challenging in experimental setups that feature in-vacuum components such as electrodes, high-resolution optics or atom chips, as spatial filtering of stray light that originates close to the atoms is inefficient.

In the following sections, a technique that addresses this issue by using two different transitions is described. In brief, we cool and trap fermionic ^{40}K atoms using light on the D2 transition but collect fluorescence on the D1 transition. The D2 MOT light propagates along all three spatial directions and hence generates a large amount of stray light which can be filtered out before the camera with dichroic mirrors. Meanwhile, D1 fluorescence photons are generated by a D1 pumping beam whose size and beam path have been chosen specifically to avoid scattering surfaces and thereby minimize the amount of stray light that is generated. This scheme allows us to perform single atom counting of up to 17 atoms with an average classification fidelity of 95 % in an experimental setup featuring a high-resolution microscope objective placed inside the vacuum chamber very close to the atoms.

In the following, first the experimental setup is described in Sec. 2.2.1, followed by a discussion of the image post-processing and atom number determination in Sec. 2.2.2. The classification fidelity and the limiting factors are discussed in Sec. 2.2.3, and finally

Sec. 2.2.4 will present a simple model in order to better understand the sensitivities of the setup.

2.2.1 Technical Setup

The central element of our setup to study ultracold few-body systems is a pair of microscope objectives with high numerical aperture[7] placed inside the vacuum chamber, see Fig. 2.2(a). These objectives are ideally suited to generate arbitrary potentials and image single atoms with high spatial resolution. However, at the same time, they represent a significant challenge for performing atom counting with a MOT.

The first constraint placed by the objectives is that they cover such a large fraction of the solid angle that the vertical MOT beams have to pass through the objectives. This precludes using the objectives to detect the fluorescence created by the MOT light, as the fluorescence signal will be completely drowned out by the MOT beams. At the same time the geometry of the vacuum chamber, which has to accommodate the in-vacuum components, severely limits the optical access for fluorescence light collection along other directions. Combined with the large background of MOT light scattered by the objectives this makes it exceedingly difficult to measure the fluorescence on the MOT transition with a signal to noise ratio sufficient for single atom resolution.

Fortunately, both of these issues can be addressed by using our two-color approach. By adding a retroreflected D1 pumping beam that propagates orthogonal to the objective axis, we create fluorescence light on the D1 transition while causing very little D1 stray light to enter the objective. As the wavelengths of the D1 and D2 transition differ by $\sim$3nm, this allows us to collect the D1 fluorescence photons with one of the in-vacuo objectives while filtering out the D2 MOT light with two dichroic longpass filters[8] with very steep edges transmitting in total more than 90 % of the D1 light at 770.1 nm but less than 10^{-8} of the D2 light at 766.7 nm [66, 67].

In the following, the D2 MOT and the D1 excitation scheme are described in more detail. The D2 MOT is formed by three beam pairs addressing the cycling transition between the F = 9/2 and F' = 11/2 hyperfine states. The horizontal D2 MOT beams have $1/e^2$ beam waists of 1.5 mm and are retroreflected, while the vertical beams are independent of each other and have waists of only 340 μm and 480 μm, as the short focal length of the microscope strongly constrains the maximal achievable beam size. The

[7] Special Optics Type 54-31-20, N.A. = 0.75, working distance = 2.5 mm, effective focal length f = 20 mm, achromatic for 770 nm, 870 nm and 590 nm.

[8] Alluxa LC-HBP770.7/3, nominal center wavelength 770.7 nm, FWHM: 3 nm, transmission >95 % at 770.1 nm, blocking >OD4 at 766.7 nm.

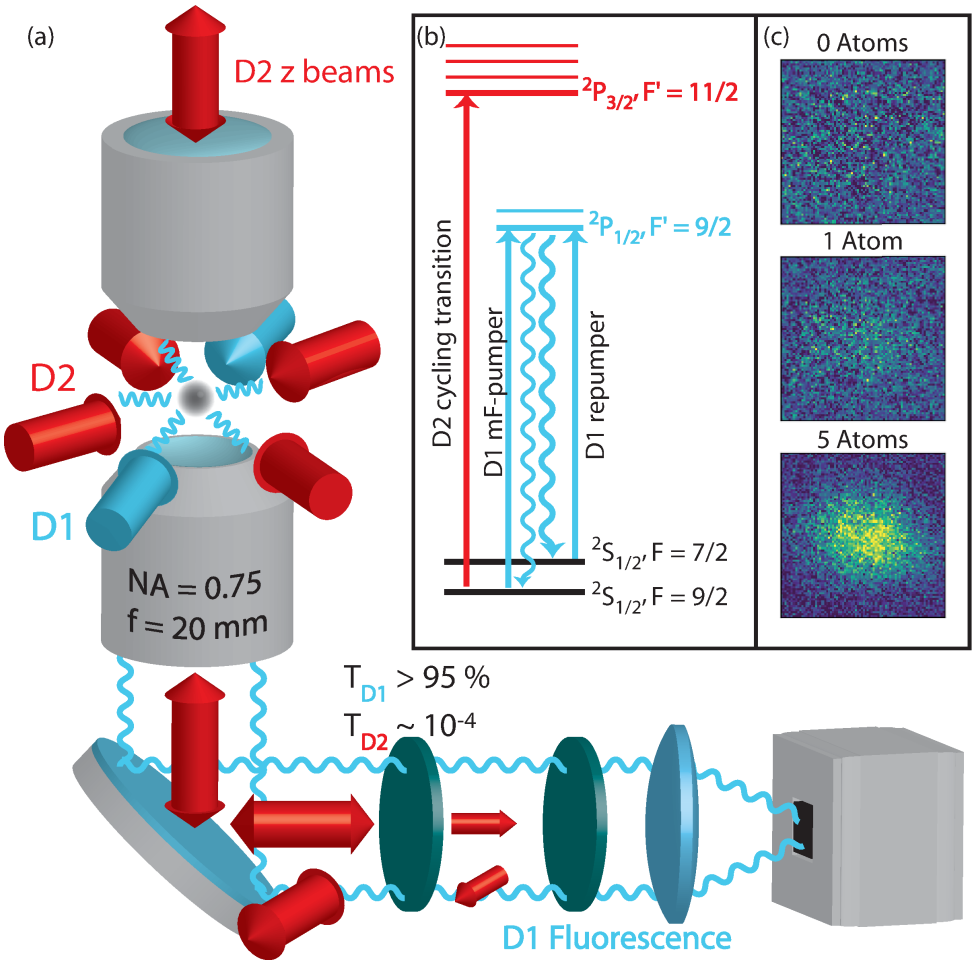

Figure 2.2: **a)** Sketch of the experimental setup. The detection MOT is formed by three pairs of D2 trapping beams (dark red), while a pair of D1 beams (light blue) generates D1 fluorescence for detection. The D1 fluorescence light is collected by an in-vacuum microscope objective (NA = 0.75, f=20 mm), separated from the D2 trapping beams using dielectric filters, and finally imaged on an sCMOS camera. **b)** Simplified level scheme showing the atomic transitions utilized in the detection MOT: The D2 line is used for cooling and trapping the atoms, while the D1 repumper addresses atoms that decay into the F = 7/2 state. The D1 mF-pumper excites atoms from the ground state to the $^2P_{1/2}$ manifold and thereby enhances the D1 fluorescence. **c)** Typical fluorescence images containing 0, 1, and 5 atoms.

magnetic quadrupole field for the MOT is provided by a set of magnetic field coils in an anti-Helmholtz configuration. To decrease the influence of background light on the atom counting we use a strong quadrupole field with a gradient of $dB/dz = 132$ G/cm in the vertical axis to make the MOT as small as possible and thereby concentrate the fluorescence signal in the smallest possible area. For our setup we find an optimum at a combined saturation parameter for the D2 light of 12 and 31 for the horizontal and vertical beams, respectively, and a detuning $\Delta\omega_{D2}$ of $-1.2\,\Gamma$, where $\Gamma/2\pi = 6$ MHz is the natural linewidth of the excited state. The detuning of the D2 MOT beams is a

compromise between minimizing the MOT size, which is minimal for small detunings, and a stable scattering rate that is not too sensitive to detuning changes, which is the case at larger detunings. We note that our D2 MOT differs from a standard MOT in one aspect: There are no D2 beams that repump atoms that have decayed into the F = 7/2 hyperfine ground state and thereby became dark to the cycling transition. Instead, this repumping is performed by one of the D1 excitation beams.

The D1 beams propagate in the horizontal plane along an axis having a 45° angle to the D2 beams and have waists of 1.2 mm. The first beam addresses the F = 7/2 ↔ F' = 9/2 transition. This repumper brings atoms that have decayed into the F = 7/2 hyperfine state back to the F = 9/2 ground state. It operates with a saturation parameter of 14 and a detuning $\Delta\omega_{D1}$ of +0.6 Γ.

However, using only this repumper does not produce enough D1 fluorescence for imaging as the F = 7/2 hyperfine state is populated only slowly while cooling on the D2 cycling transition. This is due to the fact that decay from the excited state F' = 11/2 of the D2 MOT cycling transition to the F = 7/2 state is forbidden and one has to rely on off-resonant excitations to the F' = 9/2 state in the D2 manifold, which is 8.5 Γ detuned from the D2 laser frequency. Hence, we use a second D1 beam to drive the F = 9/2 ↔ F' = 9/2 transition. This so-called mF-pumper addresses the prevalent F = 9/2 ground state atoms and excites them to the F' = 9/2 manifold. From there, the atoms decay into the F = 9/2 in about 30% and the F = 7/2 manifold in about 70% of the cases. If the atom is pumped into the F = 7/2 manifold, the subsequent repumping results in an average of three more photons being emitted on the D1 line before the atom is pumped back to the F = 9/2 manifold. By varying the strength of this mF-pumper we can therefore control the amount of D1 fluorescence emitted by the atoms. For our imaging the mF-pumper transition is driven resonantly with a saturation parameter of 7. The resulting significant amount of light pressure on the atoms is cancelled by retroreflecting the beam.

The D1 fluorescence light emitted by the atoms is collected by one of the microscope objectives and imaged onto an sCMOS camera, examples of typical fluorescence images obtained with the setup are shown in Fig. 2.2(c). The total collection efficiency of the imaging system is estimated to be 12.7±1.6 %, with the dominant effect being the relative solid angle covered by the microscope (17 %). Together with the quantum efficiency of 38 % [9], this leads to 4.8±0.6 % of the photons actually being detected. On average, the camera detects $2.3 \cdot 10^4$ photoelectrons per atom for an exposure time of 1 s, corresponding to a scattering rate of 470 kHz on the D1 transition. The imaging time of 1 s is needed to obtain a large enough signal-to-noise ratio to distinguish 17 atoms. For smaller atom

[9] Andor Zyla 5.5.

numbers, shorter imaging times would be sufficient. Adding a retroreflected D1 beam pair along the second horizontal axis did not result in a significant improvement in the signal-to-noise ratio. While the fluorescence increased by about 20%, adding the additional beams also increased the amount of background light, resulting in a similar signal-to-noise ratio.

The number of background photons due to scattered light is ∼175/pixel, which for typical regions of interest of 120 x 120 pixels corresponding to 150 μm x 150 μm amounts to about $2.5 \cdot 10^6$ photons. This background level is dominated by stray light from the D1 beams, the background originating from the D2 beam directly incident onto the objective accounts for less than 10 % of the background light. To achieve this low background it is essential to not only perform the obvious filtering of D2 light with filters in front of the camera, but also to suppress the broad pedestal of incoherent light emitted by the semiconductor lasers and amplifiers generating the D2 beams. This is achieved by placing two ultra-narrow 780 nm bandpass filters[10] angle-tuned to 766.7 nm in the beam path between the tapered amplifier and the fibers.

2.2.2 Image Post-Processing and Atom Number Extraction

To characterize our imaging scheme and establish a protocol for determining the atom number from the fluorescence signal we generate a large number of sample images of MOTs containing a small number of atoms. We achieve this by releasing atoms from a far detuned optical trap and then recapturing them with the MOT. This leads to a random number of atoms in the imaging MOT, where the mean value can be controlled via the atom number in the optical trap and the time delay between releasing the atoms and switching on the MOT. While the two-color scheme described in Sec. 2.2.1 yields fluorescence signals of single atoms that are significantly above the background noise (see Fig. 2.2(c)), some steps of image post-processing are required to extract reliable particle numbers from this data. The following detailed description can be summarized into three main points: In the first step, the background of scattered light is subtracted from the fluorescence images and the raw fluorescence signal is determined by summing up the camera counts within a defined region around the current center of the MOT. Slow drifts in the fluorescence per atom and the zero atom offset are then determined and corrected by time-resolved fitting of these two parameters, thus providing a normalized fluorescence signal. A histogram of the normalized fluorescence signals, see Fig. 2.3(b), shows clearly discernable peaks corresponding to different atom numbers. To assign atom numbers to

[10] Laseroptics Garbsen L-08729 IF780nm/6, FWHM ≈ 0.3 nm, transmission ≈ 90%

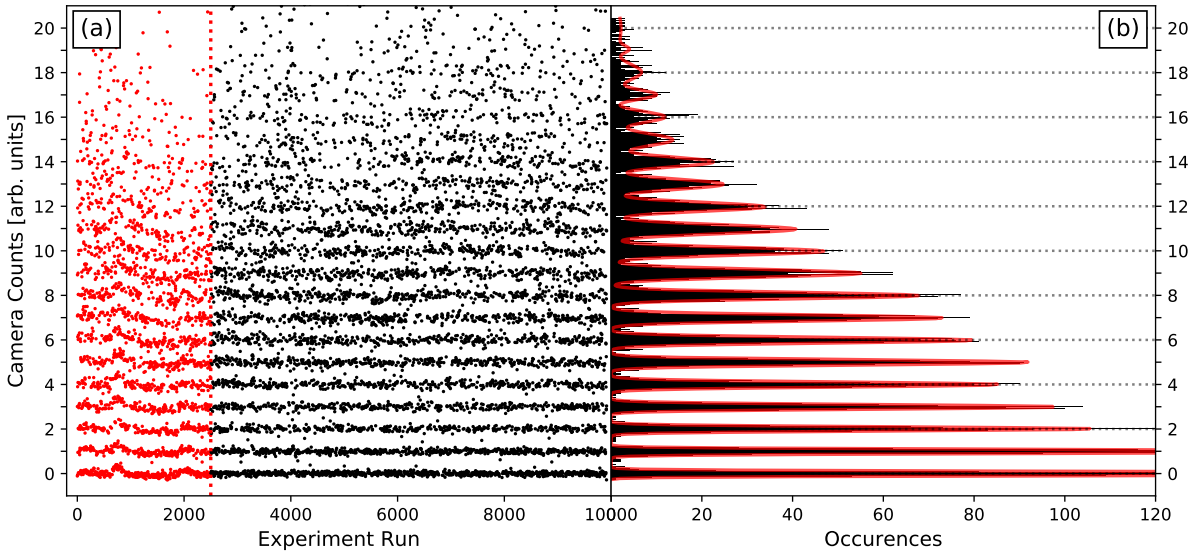

Figure 2.3: **a)** Timeline of the fluorescence level over ∼10.000 experiment runs, where each dot shows the result of a single experiment run. The red dots to the left of the vertical dotted line show the raw fluorescence levels without correcting for time-dependent changes in offset and scattering rate, the black dots are corrected for these effects. **b)** Histogram of the corrected fluorescence levels. The red line shows a fit to the data, consisting of a sum of 20 Gaussians with independent centers x_N, widths σ_N, and amplitudes. We can reliably determine the atom number for systems with up to about 17 atoms. Above this number, both the limited statistics of the data set and the width of the distributions prevent a reliable classification.

individual images, we first quantify the positions and widths of the peaks by fitting a sum of Gaussians to the histogram. We then define classification intervals around each peak based on their widths and assign atom numbers to all fluorescence measurements that fall within these intervals.

We now go through each step of the analysis in more detail, starting with the subtraction of the background signal. To achieve this we make use of a principal component analysis, as this approach reduces noise compared to subtracting a reference image taken shortly after each atom image. To this end, a set of reference images without atoms yet otherwise the same experimental conditions is taken and the main components are determined using singular value decomposition. For the data shown in Fig. 2.3, 100 reference images were taken at random times during the ∼10.000 runs and used for the singular value decomposition. The components with the ten highest singular values were then projected out of the actual data images [68] by subtracting these basis vectors, weighted with the scalar product between them and the atom image. Using more reference images or projecting out more components does not result in a significant improvement in the signal-to-noise ratio, as the components are not necessarily orthogonal to the fluorescence

signal.

Next, the current MOT position on each of these background-free images is determined by fitting a gaussian to an averaged image obtained from the current and the ten preceding and following images. This allows us to compensate for slow drifts of the MOT position over time and use a tight region of interest of only 150 μm x 150 μm for summing up camera counts. The resulting camera counts recorded by the experiment are shown as a function of time in Fig. 2.3(a) (red dots). While discrete steps in the fluorescence for different atom numbers can be clearly made out by eye, there are slow drifts in the signal levels over time and simple thresholds are not sufficient to reliably distinguish between different atom numbers with high fidelity. To provide the time-resolved values of the zero atom offset and of the fluorescence per atom, we determine the current average count levels for 0, 1, 2, and 3 atoms from the 20 realizations closest in time containing these atom numbers, respectively, and fit a linear relation to these levels. The camera counts are then corrected for these drifts, resulting in the black data points shown in Fig. 2.3(a).

Fig. 2.3(b) shows a histogram of these corrected fluorescence levels, which we then fit with a sum of gaussians with centers x_N and standard deviations σ_N. We classify events within $x_N \pm 2\sigma_N$ to have N atoms present; events outside these limits are discarded. For the data shown in Fig. 2.3, about 6% of the events are rejected. Tighter classification intervals lead to higher identification fidelity, but to a larger fraction of events being rejected. We find that the mean fluorescence level x_N grows linearly with the atom number N, as shown in Fig. 2.4(a), indicating no sign of density-dependent effects.

2.2.3 Resolution Limit and Classification Fidelity

After establishing our post-processing procedure we now analyze the data to determine the fidelity of our atom number determination and find the limiting factors of the detection scheme. For our evaluation we assume that the peaks in the histogram are clearly distinguishable and we can assign reliable atom numbers as long as the separation of the peaks is larger than 4σ. Hence the maximal atom number we can resolve is limited by the observed growth of the peak width σ_N with the atom number N, see Fig. 2.4(b).

The peak width is determined by three noise sources, which can be assumed to be independent and therefore are added up quadratically [63]: These are a constant background noise stemming from the shot noise of the background light (including D1 and D2 light) and the read-out noise of the camera, the shot noise of the fluorescence photons collected by the camera, which scales with the square root of the atom number, and shot-to-shot fluctuations in the average fluorescence rate per atom, which scale linearly with the atom

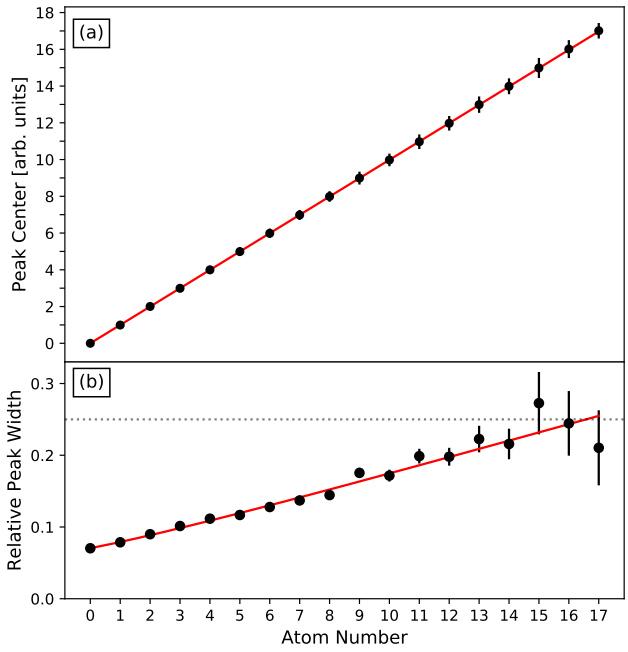

Figure 2.4: Mean value x_N (**a**) and width σ_N (**b**) of the fluorescence signal as a function of atom number, as determined from the fit to the histogram shown in Fig. 2.3(b). The mean fluorescence increases linearly with atom number (red solid line), indicating that density dependent effects are negligible. The error bars represent the $\pm 2\sigma_N$ confidence intervals. The widths σ_N of the peaks in the histogram are normalized to the average fluorescence per atom and shown in panel (b). We assume the peak widths to be a quadratic sum of a constant background noise, photon shot noise scaling with $\sqrt{N}$ and a linear noise contribution due to short-term variations in the intensity and detuning of the imaging light. Fitting the data with this model (red curve) shows that the noise is dominated by the linear term. The dotted line shows the point where the $\pm 2\sigma_N$ classification regions of two neighboring peaks start to overlap, which roughly indicates the point where we can no longer reliably assign an atom number to an event.

number.

When analyzing the data we find that for atom numbers < 20 the shot noise of the fluorescence photons contributes $\sigma_{ph}^2 \lesssim 0.01^2$ to the variance and the atom-number independent background noise is about $\sigma_{bg}^2 \approx 0.07^2$. These noise sources therefore only play a small role in in limiting our atom number determination.

Instead, the dominant effect is a linear growth of the peak width σ_N with the atom number N, see Fig. 2.4(b), which strongly suggests that our atom number determination is limited by fluctuations in the atom fluorescence. While long-term drifts are removed by the rescaling method described in Sec. 2.2.2, shot-to-shot fluctuations or drifts on timescales shorter than a few tens of shots are not significantly suppressed with this method. We note that one-color schemes [53, 56, 57, 60, 61, 63, 64] are less sensitive to frequency or power fluctuations due to the high saturation of the single cooling transition. In contrast, in our two color scheme the F = 9/2 ground state is addressed by two transitions, i.e. the

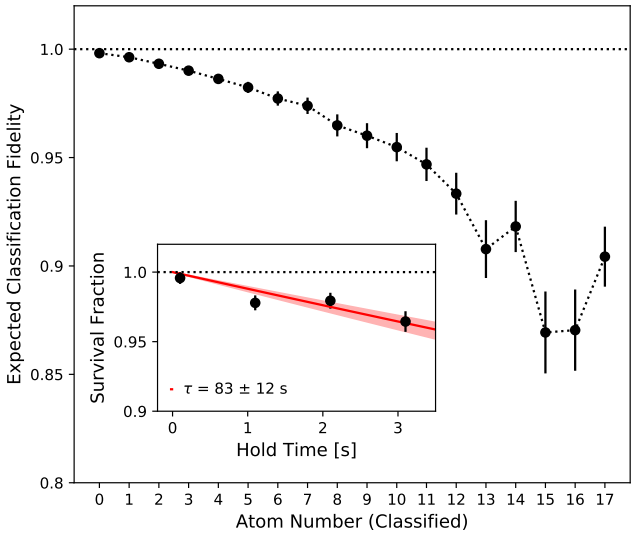

Figure 2.5: Simulated classification fidelities for systems with different atom numbers using the noise characteristics determined from in Fig. 2.3(b) and an independent measurement of the MOT lifetime (see inset; assuming an exponential decay of the atom number). The classification fidelity is limited by the ratio of imaging time to life time: loss events during the imaging time reduce the number of collected fluorescence photons and thus can cause the fluorescence signal to fall into the classification bin of a lower atom number.

D2 cooler and the D1 mF-pumper, which thus compete with each other. Hence, relative power fluctuations directly translate into fluctuations of the fluorescence per atom and lead to a faster growth of σ_N than in one-color schemes. A simple toy model investigating the dependencies on external parameters such as power fluctuations is described below in Sec. 2.2.4.

For the data set shown in Fig. 2.4 the threshold value $\sigma_N = 0.25$ where the $\pm 2\sigma$ intervals of neighboring histogram peaks start to overlap is reached for $N \approx 17$. Beyond this threshold, we define the boundary between N and $N+1$ atoms as $(x_N + 2\sigma_N + x_{N+1} - 2\sigma_{N+1})/2$, and our ability to separate the fluorescence signals belonging to different atom numbers substantially decreases. We therefore consider $\sigma_N < 0.25$ to roughly indicate the threshold for fluorescence measurements with single atom number resolution. We note that this condition is significantly more conservative than the requirement $\sigma_N < 1$ used by other authors [61, 63, 64]. Extrapolating our observed peak width growth indicates that we reach $\sigma_N = 1$ for $N \approx 80$.

In addition to the noise sources discussed above, which broaden the fluorescence peaks and therefore limit our ability to reliably distinguish between different atom numbers for larger values of N, there is another effect that can limit the fidelity of our atom number determination: loss of atoms from the MOT during the imaging period. As the lifetime of atoms in our imaging MOT is on the order of 80 s, much longer than the imaging time of 1 s,

loss events are very rare when measuring small atom numbers, but become more relevant for measuring larger systems. Also, depending on the number of atoms in the system and at which time during the measurement it occurs, not every loss event necessarily leads to an incorrect determination of the atom number. To obtain a quantitative estimate of the influence of the various noise sources on our classification fidelity we therefore perform a phenomenological Monte-Carlo simulation of our system using the following model for the counts c_i observed in run i:

$$c_i = \alpha_i + \beta_i \cdot \sum_{n=1}^{N} \gamma_{i,n} \cdot \min\left(1, \frac{\tau_{i,n}}{t_{Im}}\right), \tag{2.1}$$

where α_i, β_i, and $\gamma_{i,n}$ are gaussian distributed random numbers with mean 0, 1, and 1, respectively. The standard deviations σ_α, σ_β, and σ_γ of these three random numbers are a priori free parameters that model the noise sources of the fluorescence signal described above, where σ_α corresponds to the atom-number independent noise, σ_β to the global and hence correlated fluctuations in fluorescence per atom, and σ_γ to the fluorescence shot noise from each uncorrelated atom. The values of these parameters are fitted to best reproduce the observed peak widths in the fluorescence count histogram[11]. The possibility of atom loss is taken into account by comparing the imaging time t_{Im} to a time $\tau_{i,n}$ after which atom n is lost from the MOT in run i that is drawn from an exponential distribution using the experimental lifetime of (83 ± 12) s, and taking the shorter of the two times to calculate the fluorescence of each atom. The counts from the simulation are processed and classified based on the experimentally determined intervals as described in Sec. 2.2.2. The classification fidelity is estimated by comparing the initial atom number with the classification result for each simulated run. The lifetime has been measured by loading 0, 1, or 2 atoms into the MOT and comparing the fluorescence level of two measurements with some variable time delay between them, see inset of Fig. 2.5. In the ∼4000 runs used for this, not a single event of loading an atom from the background gas has been observed, thus limiting the background loading rate to be below $3 \cdot 10^{-4} s^{-1}$ at 68 % CL, thus not affecting the classification fidelity.

Fig. 2.5 shows the resulting classification fidelities, which are close to 100 % for low atom numbers, decrease to ∼95 % for 10 atoms and to ∼87 % for the highest atom numbers we can reliably distinguish. When working with at most 10 (17) atoms, the average fidelity is ∼98 % (∼95 %). The vast majority of the incorrectly classified events stem from atom loss, especially having one more atom initially than classified: when working with at most 10 (17) atoms, this is the case for $>$ 99 % ($>$ 95 %) of the incorrectly identified atom

[11] $\sigma_\alpha = \sigma_{bg} = 0.07 \pm 0.01$, $\sigma_\beta = 0.034 \pm 0.012$, $\sigma_\gamma = \sigma_{ph} = 0.012 \pm 0.005$

numbers.

One interesting insight that can be gained from the simulation is that while the classification fidelity strongly depends on the MOT lifetime, this is not directly visible in the peak widths: a limited lifetime leads to a broad background in simulated histograms emulating the one shown in Fig. 2.3(b). The peaks are still quite narrow and clearly identifiable, but loss of atoms during imaging can move the fluorescence count into the classification region of a lower atom number. This can in principle be improved by increasing the lifetime of our MOT as the fraction of incorrectly identified events scales linearly with the inverse lifetime, but in our case the MOT lifetime is already close to the vacuum limited lifetime of the system. It seems more realistic to reduce the width of the fluorescence peaks by improving the power and frequency stability. This would increase the classification fidelity as smaller peak widths decrease the probability of misclassifying events involving atom loss. Alternatively, such an improved stability would allow to reduce the imaging time while keeping the classification fidelity the same.

2.2.4 Fluorescence Stability Modeling

As shown in the prior section, the classification fidelity is mostly limited by the fluorescence stability. It is therefore instructive to consider a simple toy model of the two-color MOT. We do this by approximating the problem as a three level system consisting of a single ground state and two excited levels corresponding to the ${}^2P_{1/2}$ and the ${}^2P_{3/2}$ levels, and model the dynamics with optical Bloch equations, where the ground state is coupled to both excited states.

In a one-color MOT working at a high saturation parameter s and small detuning, the scattering rate scales as $1-1/s$ and power noise only weakly influences the scattering rate. In our two-color MOT, each transition is individually saturated and the atom will scatter photons close to the maximum rate of $\Gamma/2 \simeq 18$ MHz. However, the two transitions can compete with each other. For the special case of zero detuning for both transitions, solving the Bloch equations of the three level system analytically is straightforward. The scattering ratio obtained is

$$\frac{\rho_{11}}{\rho_{22}} = \frac{\Omega_1^2}{\Omega_2^2} \cdot \frac{\Gamma^2 + \Omega_1^2}{\Gamma^2 + \Omega_2^2} \propto \frac{s_1}{s_2} \frac{\Gamma^2 + k s_1}{\Gamma^2 + k s_2} \xrightarrow{\Omega_2^2 \gg \Gamma} \frac{s_1(\Gamma + k s_1)}{k s_2^2}, \tag{2.2}$$

where k is some constant. ρ_{11} and ρ_{22} are the population fractions in the ${}^2P_{1/2}$ and the ${}^2P_{3/2}$ states, respectively; the ratio ρ_{11}/ρ_{22} is therefore the ratio of scatterings on the D1 line and the D2 line. Since the square of Rabi frequencies Ω_i is proportional to the power

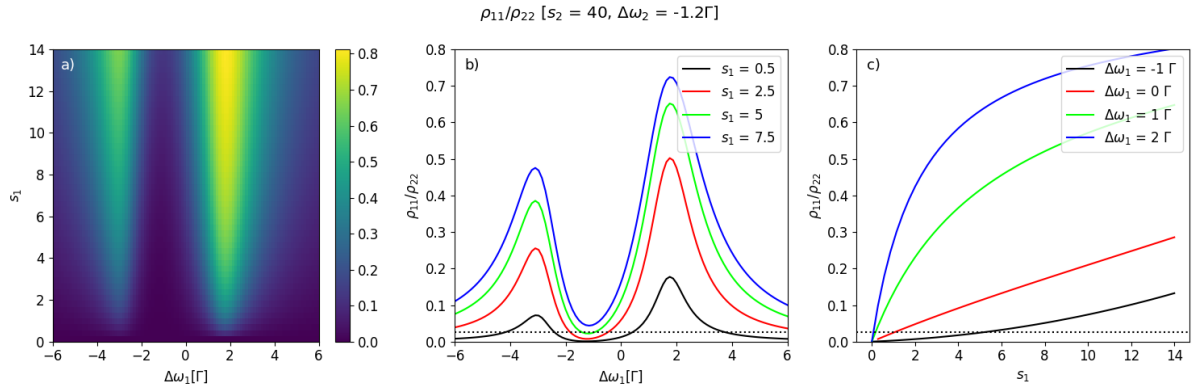

Figure 2.6: Numerical results for the relative scattering rate on the D1 transition, based on the optical Bloch equations described in the main text. The D2 light parameters are set to a saturation parameter of $s_2 = 40$ and a detuning of $\Delta\omega_2 = -1.2\,\Gamma$. **a)** Relative fluorescence on the D1 transition for a range of detunings and powers. **b)** Line cuts for a few fixed saturation parameters s_1. **c)** Line cuts for a few fixed detunings $\Delta\omega_1$. The dotted horizontal line in b) and c) indicate the approximate scattering ratio we observe in our MOT. The high intensity and nonzero detuning of the D2 light leads to an asymmetric splitting of the D1 fluorescence. The line cuts in b) and c) indicate that it is more stable to work around a detuning of $\sim -1\,\Gamma$, where the variation of the fluorescence rate with the saturation parameter is rather small.

and thus to the saturation parameters s_i, the above expression is linear in each saturation parameter for low intensities, and quadratic at high intensities. This already indicates that the two-color scheme is inherently more sensitive to power fluctuations compared to the one-color scheme.

Typically, s_2 is large as trapping within a small region needs a large restoring force via the D2 beams and hence a large saturation parameter s_2. For fixed and large s_2, the above expression suggests that it is more stable to use a low saturation parameter s_1, but there is a lower limit set by the background noise level and the available imaging time.

In the more general case of non-zero detuning, the dynamics has to be analyzed numerically. The time evolution of the density matrix is given by

$$\partial_t \rho = \frac{1}{i\hbar}\,[H, \rho] + \mathcal{L}, \tag{2.3}$$

where ρ is the density matrix, H is the Hamiltonian, and $\mathcal{L}$ is the Lindblad operator, which implements the decay of excited population and coherence. The Hamiltonian depends on the individual Rabi frequencies Ω_1 and Ω_2 coupling the ground state to the excited levels via the D1 and the D2 line, respectively, as well as on the individual detunings $\Delta\omega_1$ and $\Delta\omega_2$. Since the model is a rough approximation, we neglect the difference in decay rates for the two excited levels and furthermore assume that the coherence dephasing rate $\gamma_\perp$ is dominated by the atomic decay, i.e. $\gamma_\perp = \Gamma/2$.

Numerical results derived from the optical Bloch equations for parameters comparable to the ones used in the experiment are shown in Fig. 2.6. The strong intensity of the D2 light used for trapping the atoms within a small region leads to a splitting of the D1 line, and the nonzero detuning of the D2 light furthermore creates an asymmetry within this splitting. Subplots (b) and (c) in Fig. 2.6 suggest that working with a small effective detuning (i.e. roughly centered between the now two D1 lines) leads to a smaller dependence of the scattering ratio on the saturation parameter s_1, and thus to a more stable fluorescence level. Based on these simulations, the observed fluctuations in the atomic fluorescence within each imaging run could be explained by frequency noise on the order of 60 kHz ($\sim 0.01\,\Gamma$), by power fluctuations of $\sim 1.4\%$ in the D1 power, or by D2 power fluctuations of $\sim 0.1\%$. For the D2 system, the absolute requirement on the power stability is similar as for the D1 system, leading to a correspondingly tighter requirement on the relative stability.

2.3 Anderson's Orthogonality Catastrophe in a Two-Color Tweezer Setup

Anderson's Orthogonality Catastrophe as the limit of the polaronic problem with a cold fermionic bath and an infinitely heavy impurity has already been briefly introduced above, and will be discussed in a bit more depth here. For simplicity, one considers N non-interacting fermions in a three-dimensional potential well of infinite depth. The single particle solutions to the this system, ϕ_n, are spherical waves multiplied with spherical harmonics, where the index n summarizes the relevant quantum numbers. Adding a small, immobile and weak potential at the center of the potential will introduce a phase shift near the center of each wave function, such that a new solutions ψ_n are almost identical to ϕ_n, but with some phase shift near the origin. The single particle wave function overlap $A_{nn'} \equiv \langle \phi_n | \psi_{n'} \rangle$ will then, for small potential depths, be close to unity for $n = n'$ and close to zero for $n \neq n'$.

The many-body wave function can then be constructed by using the Slater determinant and the overlap Z of two many-body ground state wave functions (one without, and one with the small scattering potential) can be written as

$$Z = \det|A_{nn'}|, \text{ with } E_n, E_{n'} < E_F, \tag{2.4}$$

where E_F is the Fermi energy. The quantity Z is usually referred to as *quasi-particle residue*, and Anderson derived the expression of

$$Z \leq N^{-\sum[(2l+1)/3\pi^2]\sin^2\delta_l}, \tag{2.5}$$

where δ_l indicates the central phase shift for angular momentum l and the sum extends over all angular momenta. The quasi-particle residue thus exhibits a power-law decrease with increasing atom number and approaches zero for large systems even when the scattering potential is very weak, showing that the ground states of the two systems are almost orthogonal. This behavior is referred to as the "Orthogonality Catastrophe".

This "catastrophe" for example appears in pump probe schemes with solid-state systems: upon exciting an electron from the valence band to the conduction band, the spatial distribution of the remaining electrons is initially unaffected. However, in the new system (i.e. with the valence hole and conduction electron) this spatial distribution does not correspond to the ground state, but has large contributions of excitations near the Fermi surface. The subsequent reordering and screening of the valence hole, as well as the

asymmetric line shape observed in a following probe pulse can be understood as a consequence of Anderson's Orthogonality Catastrophe [69]. The situation is very similar in X-ray absorption spectra, where the Orthogonality Catastrophe leads to a typical power law behavior [70].

The Anderson Orthogonality Catastrophe has been investigated theoretically [71, 72] and experimentally [73, 74] in the context of cold quantum gases; in our context, the latter work, performed in the group of Selim Jochim is most relevant. In their experiment, a one-dimensional tweezer was filled with atoms of two different spin states: one state served as scattering center, while the other modeled the filling of the Fermi sea. By accurately measuring the Rabi frequency of a radio-frequency transfer to a third spin state, they were able to extract the quasi-particle residue and the scaling with increasing atom number. However, the required accuracy was challenging. Since the interaction strength in one-dimensional systems *decreases* with the number of atoms present in the trap, the phase shift for each individual level was not constant but also changed when altering the atom number, hence strongly reducing the effect of the Orthogonality Catastrophe.

2.3.1 Implementation in a Two-Color Tweezer Setup

In our case, we propose an alternate approach to investigate the orthogonality catastrophe by creating the scattering potential not by a different atomic spin state, but by a small optical potential. Here, two relevant atomic states are involved: the atoms are initially prepared in the $|F = 9/2, m_F = -9/2\rangle \equiv |\downarrow\rangle$ ("spin down") state and can be transferred to the $|F = 9/2, m_F = -7/2\rangle \equiv |\uparrow\rangle$ ("spin up") state by using a radio-frequency pulse with appropriate frequency and power. After preparation, a tightly focused laser beam creates an additional optical potential. Wavelength and polarization are chosen such that the down state is not affected, while the up state experiences an additional potential. The eigenfunctions of the up-state atoms are slightly different from the wave functions of the down-atoms due to this additional potential, akin to the scenario described in Anderson's seminal paper. Coupling the two states via radio-frequency will lead to the typical Rabi oscillations, but with a reduced Rabi rate due to the mismatch in the spatial overlap. This reduced Rabi frequency serves as a measure for the orthogonality of the states. By varying the strength of the optical potential, the strength of the wave function mismatch can be changed. Additionally, by varying the atom number one can probe the scaling with the atom number, which constitutes the "catastrophe" in Anderson's model.

Spin-dependent Potentials

To create a difference in the potentials experienced by the spin down and spin up atoms, we need to use carefully chosen laser parameters. We decided to employ a scheme very similar to the one demonstrated in [75], where a tightly focused laser beam allowed spin flips of individually selected atoms in a quantum gas microscope. The essential trick is that the small potential leads to a differential light shift of the two relevant spin states. By tuning the radio-frequency to this shifted value, only the atoms experiencing the small potential are on resonance and can be flipped.

One possibility would be to use σ^--polarized light tuned between the D1 and the D2 line. In this case, the down atoms in the $|F = 9/2, m_F = -9/2\rangle$ state cannot couple to the $^2P_{1/2}$-manifold, as there is no final state allowed by dipole selection rules. There are only F=9/2 and F=7/2 hyperfine states and therefore there are also no $m_F = -11/2$ states that the light can couple the initial state to. The $^2P_{3/2}$-manifold on the other hand, has the hyperfine states F=5/2, F=7/2, F=9/2, and F=11/2, and therefore a possible final state to couple to. This is plotted in Fig. 2.7(a), by the black line: the polarizability for the $m_F = -9/2$ state does not show any divergence at 770.11 nm, i.e. at the D1 line, as the atoms are dark for this transition. The spin up atoms ($m_F = -7/2$) on the other hand, show a diverging polarizability when the light field's frequency is tuned close to the atomic resonance (illustrated by the red line, divergences at 766.70 nm and 770.11 nm). Since the potential depth depends linearly on the polarizability, it is for now sufficient to only consider the latter. With this choice of parameters, a net-zero potential can only be created for the spin up atoms, not the spin down atoms, but this just conceptually reverses the role of the two.

The major problem with using σ^--polarized light is the exact wavelength of zero energy shift: For light fields tuned between the D1 and the D2 line, the light is red detuned with respect to the D2 line, while it is blue detuned with respect to the D1 line, and there will be both attractive and repulsive contributions to the total trapping potential. These two contributions are exactly balanced for the spin up atoms when using σ^--polarized light at a wavelength of (769.86 $\pm$ 0.01) nm, about 0.25 nm from the D1 line, corresponding to a detuning of $\sim$127 GHz. This very small detuning leads to large scattering rates, even for the small powers needed in this context. For realistic parameters as discussed below, using this wavelength would lead to scattering rates on the order of 50 Hz, which would be very challenging to work with.

For π-polarized light, the potentials experienced by the spin states are exactly the same and are not helpful in this context. However, σ^+-polarized light, just as for σ^--polarization, has a spin-dependent effect. While neither of the two states is completely

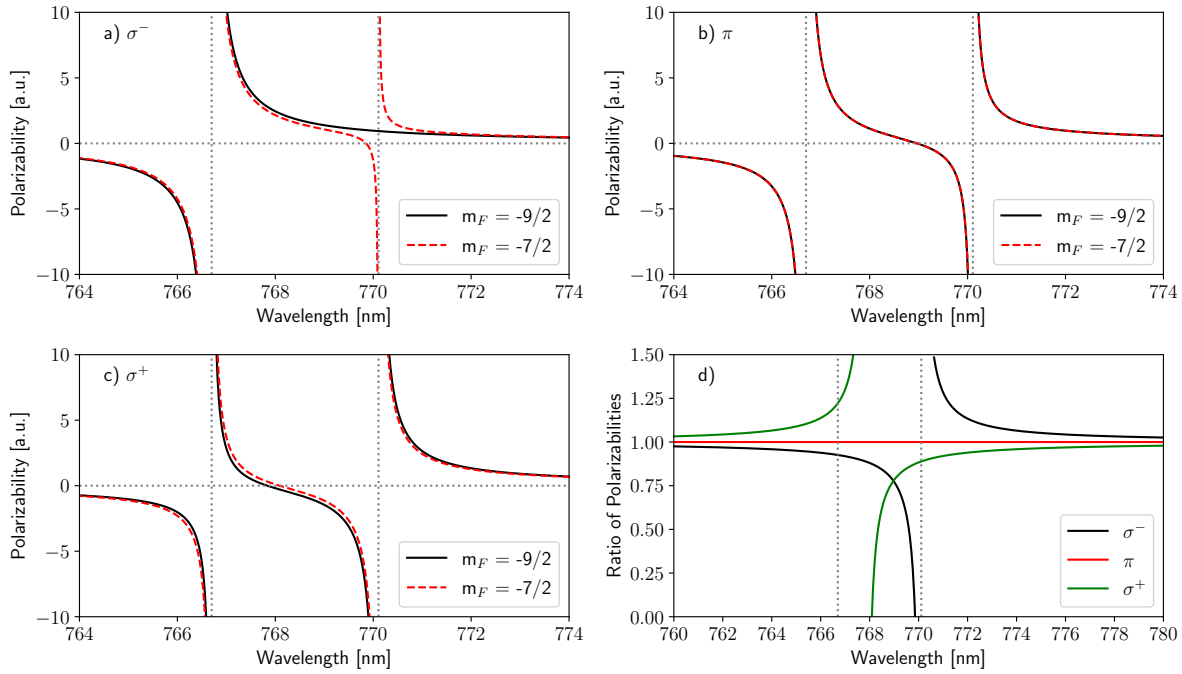

Figure 2.7: Polarizabilities of the relevant spin states for different light field polarizations near the D1 (770.11 nm) and D2 (766.70 nm) lines. **a-c**: The solid black line indicates the polarizability of the spin down atoms, the dashed red line the polarizability of the spin up atoms. **a)** For σ^--polarized light, the spin down atoms cannot couple to any state in the $^2P_{1/2}$ manifold, and hence their polarizability does not show a resonance at the D1 line. The spin up atoms have a zero-shift wavelength at ∼769.86 nm, i.e. the trapping and anti-trapping contributions from the D1 and D2 line, respectively, cancel exactly. **b)** For π-polarized light, both spin states experience the same potential. **c)** For σ^+-polarized light, the two relevant states experience almost the same potential, but their zero-shift wavelengths are shifted by a small amount with respect to each other. **d)** Ratio of the polarizabilities $\alpha(\uparrow)/\alpha(\downarrow)$ for the different polarizations. The zero crossings correspond to $\alpha(\downarrow) = 0$.

dark with respect to one of the relevant transitions, their coupling is still different and they both experience a differential light shift. They also both possess wavelengths of zero energy shift: (767.84 ± 0.01) nm for the spin down atoms and (768.08 ± 0.01) nm for the spin up atoms. Thus, they are roughly centered between the D1 and the D2 line, leading to a lower scattering rate compared to the case of σ^--polarization.

The third option would be to use a further detuned beam. When the detuning is on the order of the D1/D2 separation, the two states still experience a different trapping potential. As indicated in Fig. 2.7(d), the differential light shift quickly reduces with larger detuning though, leading to higher power needed to achieve the necessary difference in wave functions. A more detailed calculation can, for example, be found in [76].

Difference in Wave Functions

In order to estimate the effect of the second potential, it is instructive to take a look at the eigenfunctions of the total potential. For simplicity, this is here done only for the axial and radial dimension separately. The following, realistic parameters for our experimental setup are considered throughout this section: the "main tweezer" is created by π-polarized light at 850 nm, has an e^{-2} waist of 1.5 µm and a power of 1.0 mW. The Rayleigh length is then 8.3 µm. For the "phase shift tweezer", 1.5 µW of σ^+-polarized light at 767.84 nm focused to a waist of 0.7 µm, giving a Rayleigh length of 2.0 µm, is assumed. At this wavelength, the spin down atoms do not experience any additional potential. As outlined below, these parameters are on the upper end of the parameters needed to produce an observable signal. The intensity of the phase shift tweezer leads to a scattering rate on the order of 20 Hz.

Assuming a Gaussian profile along the radial direction with e^{-2}-waists of w_M and w_P and maximal depths U_M and U_P for the main tweezer and the phase shift potential, respectively, and expanding the radial potential to quadratic order, one has

$$|U(r)| = 2\frac{r^2 U_M}{w_M^2} \cdot \left[1 + \frac{U_P}{U_M} \cdot \left(\frac{w_M}{w_P}\right)^2\right] \equiv \frac{1}{2} m\omega_r^2 (1+\alpha) r^2, \tag{2.6}$$

i.e. the radial trapping frequency ω_r is corrected by a factor of $\sqrt{1+\alpha}$, where $\alpha = (U_P/U_M) \cdot (w_M/w_P)^2$. For the typical parameters used in our case, $\alpha \sim 0.1 - 0.2$.

For a diffraction limited Gaussian beam, the axial profile is given by $U(z) = U_0/[1 + (z/z_R)^2]$, where $z_R = \pi \cdot w_0^2/\lambda$ is the Rayleigh length. Expanding the profiles of both the main tweezer and the phase shift potential to quadratic order in z and adding them, one obtains

$$U(z) = \frac{z^2 U_M \lambda_M^2}{\pi^2 w_M^4} \cdot \left[1 + \left(\frac{U_P}{U_M}\right)\left(\frac{\lambda_P}{\lambda_M}\right)^2 \left(\frac{w_M}{w_P}\right)^4\right] \equiv \frac{1}{2} m\omega_a^2 (1+\beta) z^2. \tag{2.7}$$

Similarly to the radial profile, the trapping frequency is corrected by a factor $\sqrt{1+\beta}$, where $\beta = (U_P/U_M)(\lambda_P/\lambda_M)^2(w_M/w_P)^4$. The above expression assumes $z\lambda/(\pi w_0^2) \ll 1$ for each tweezer individually. For the phase shift tweezer, a 10% error is reached at ~ 2 µm distance from the focal position, and for the main tweezer at ~ 8 µm. The correction term $1+\beta$ describes the effective change in the trapping frequency near the center; for our typical parameters, one has $\beta \sim 0.4 - 0.8$. Since $\beta/\alpha = (\lambda_P/\lambda_M)^2 \cdot (w_M/w_P)^2 \simeq 3.8$, the axial component of the wave function is expected show a stronger effect in the reduction on the overlap than the radial one. As the dominant contribution is from the waist ratio

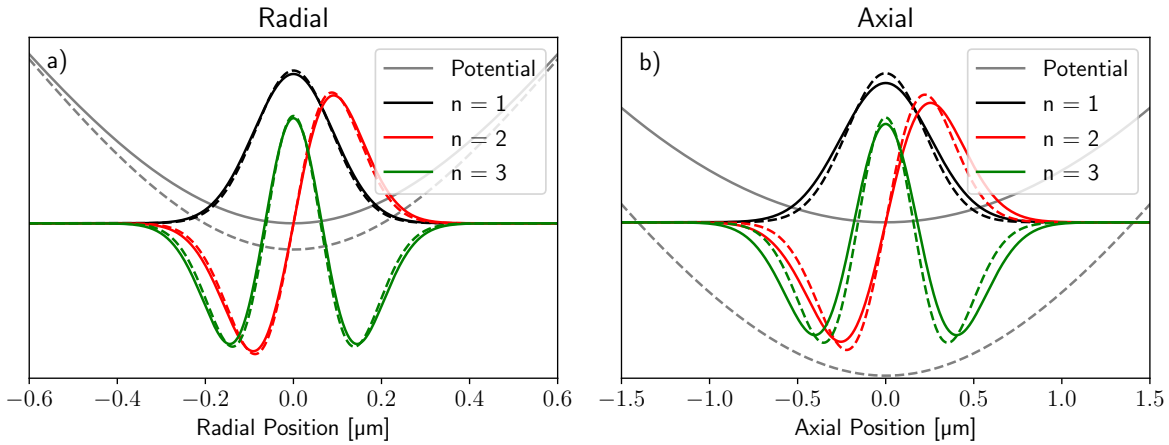

Figure 2.8: Potential and lowest wave function along the radial **(a)** and axial **(b)** direction for the two relevant spin states. The gray lines indicate the potential, while the black, red, and green lines show the lowest three vibrational levels. The solid lines correspond to the unperturbed potential, i.e. for the spin down atoms, and the dashed lines correspond to the perturbed potential, i.e. for the spin up atoms. As expected from the estimates in the main text, the difference in wave functions is more pronounced for the axial component than for the radial one.

w_M/w_P, it is crucial to use tweezers with different focus sizes to create a detectable signal.

Figure 2.8(a) and (b) show the three lowest levels along the radial and axial direction, in a one-dimensional approximation for the parameters stated above, respectively. The gray, black, red, and green lines indicate the potential, the ground state wave function, the first excited wave function, and the second excited wave function, respectively. For each color, the solid line shows the case of spin down atoms, and the dashed line corresponds to spin up atoms.

For higher levels, the wave function overlap between the unperturbed and perturbed states slowly decreases with increasing vibrational quantum number, as shown in Fig. 2.9. As expected, the decrease in overlap is much faster along the axial direction.

Observable: Quasi-Particle Residue

As described in the beginning of the section, the many-particle wave function overlap between the original and the perturbed ground state can be calculated as

$$Z = \det|\langle\psi_{n'}|\phi_n\rangle|; \text{ with } E_n, E_{n'} < E_F. \tag{2.8}$$

For the system Anderson considered, $Z \propto N^{-f(\delta)}$ is obtained, where $f(\delta)$ is a function of the phase shift δ introduced by the scattering potential. Figure 2.10 shows the many-body wave function overlap for the parameters stated above for different particle numbers and

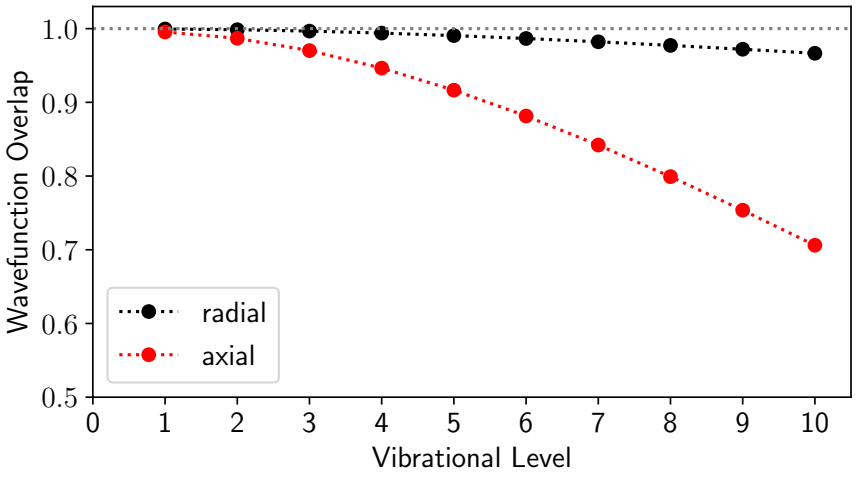

Figure 2.9: Reduction of single particle wave function overlap between the spin down and spin up state atoms. The plot shows the overlaps $|\langle\phi_n|\psi_n\rangle|$, where ϕ_n is the wave function for the potential as experienced by spin up atoms, and ψ_n is the wave function for the potential as experienced by the spin down atoms. The radial contribution (black) reduces much slower than the axial contribution (red).

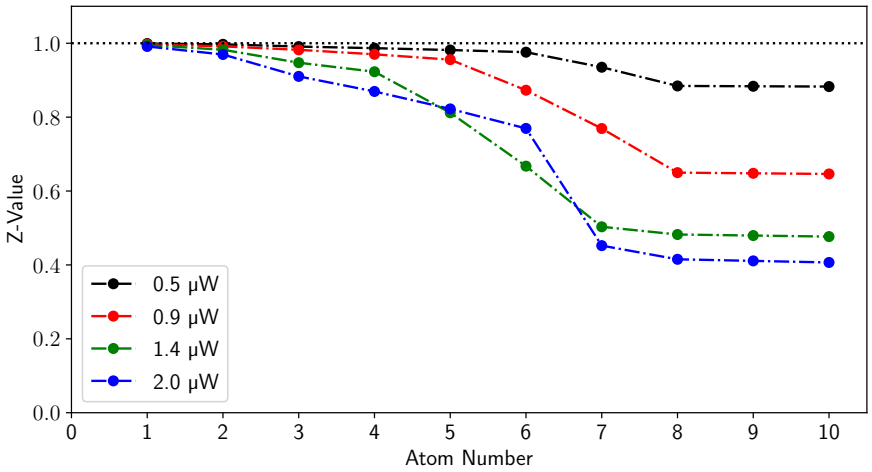

Figure 2.10: Many-body wave function overlap for different powers of the phase shift potential and different atom numbers. The overlap decreases with larger power in the phase shift potential, corresponding to a larger phase shift due to the scattering potential in Anderson's model. The dependency on the atom number is modulated by the aspect ratio of the axial and radial trapping frequencies: in this case, the trapping frequency aspect ratio is ∼1:7, and the overlap for eight, nine, or ten atoms is very similar: in this regime, higher radial levels are getting occupied. For the radial levels, the difference between unperturbed and perturbed levels is rather small, and the overall overlap barely changes.

different powers of the phase shift tweezer. The overlap can be probed rather directly by employing a radio-frequency pulse for the transfer between the two relevant spin states: the overlap matrix element and therefore the Rabi-rate for transfers between an initial state $|i\rangle$ and a final state $|f\rangle$ is determined by

$$\Omega_{Rabi} \propto \langle f|\hat{H}_{RF}|i\rangle = \langle f_{internal}|\hat{H}_{RF}|i_{internal}\rangle\langle f_{spatial}|i_{spatial}\rangle \propto Z, \tag{2.9}$$

where the momentum kick by the radio-frequency photons has been neglected, such that $\hat{H}_{RF}$ does not affect the spatial wave functions. In most cases, the spatial overlap of the initial and final state is close to one, but the spin dependent potentials considered here form an exception. Measuring the Rabi frequency of a resonant transfer between the spin up and spin down states allows the extraction of the spatial overlap of the many-body wave functions. By varying the power of the phase shift potential and the atom number, this scheme allows to observe the build-up of Anderson's Orthogonality Catastrophe.

However, it should be noted that in this case the system is not a rotationally symmetric three-dimensional system as Anderson used. With the parameters used here, the aspect ratio of axial and radial trapping frequency is $\sim 1:7$, and the simple power law of eq. 2.5 is expected to be modified.

Low Entropy System Preparation

Before even applying the phase shift potential and the radio-frequency coupling, it is essential to prepare a system with the lowest few energy levels occupied. The exact number of atoms in the potential can be accounted for in the data processing after counting the atom number of that run and hence is not too critical to control. To do this, we need to start with a cold Fermi gas in an optical dipole trap; the tweezer can then be filled with high fidelity by employing the dimple trick. The dimple trick consists of adding a small but deep potential to a large reservoir. The mean occupation number of a state i in the reservoir with temperature T and chemical potential μ is given by the Fermi-Dirac distribution

$$n_i = \left[\exp\left(\frac{E_i - \mu}{k_B T}\right) + 1\right]^{-1}, \tag{2.10}$$

where E_i is the energy of the state and the trap minimum has been defined as $E = 0$. When adding a small trap, e.g. a tweezer, with depth $|V_T| \gg k_B T$, localized states with $|E| \gg k_B T$ are created. For typical parameters like $|V_T| \approx 10 k_B T$ and $\mu \lesssim 0.5 k_B T$, the occupation probability of the deep lying tweezer states quickly exceeds 99%. One implicit assumption in this consideration is that the temperature and the chemical potential are not

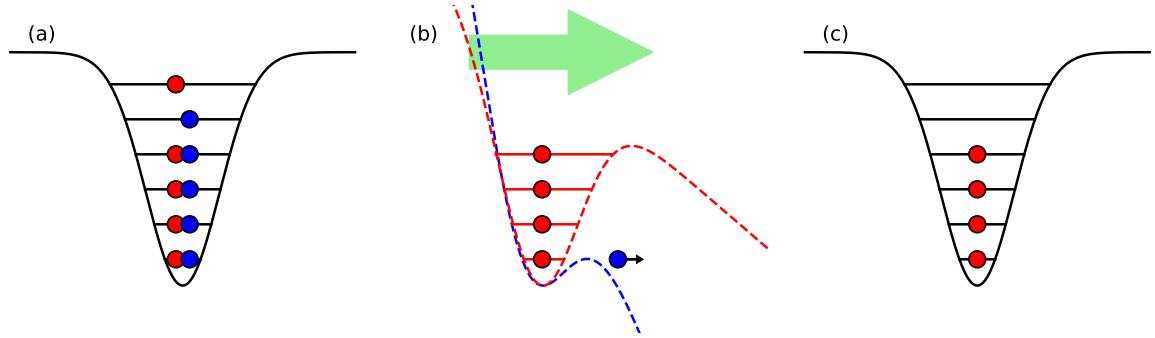

Figure 2.11: Magnetic spilling of the optical tweezer. **a)** The tweezer is filled with two spin states, where the higher lying states have a lower occupation probability. **b)** Applying a magnetic gradient (green arrow), the total potential is tilted and previously bound states become unbound. Depending on the magnetic gradient, the spin state's magnetic moment, and the optical power, it is possible to remove one spin state completely while still trapping another spin state. **c)** After spilling, the tweezer contains a deterministic number of atoms.

affected by the small potential, i.e. that the number of bound states therein is relatively small compared to the number of atoms in the trap. This condition, together with an adiabatic turn on of the trap to avoid heating, is not critical as it is easily fulfilled for the realistic experimental parameters. The more crucial assumption is that the Fermi-Dirac distribution still accurately describes the occupation probability in the tweezer, i.e. that atoms are able to thermalize into this new potential - Pauli blocking causes the scattering to freeze out for low enough temperatures, so the thermalization time might become too long. In this case, it might be necessary to introduce a second spin species, such that scattering and thermalization can occur between the different spin states.

After loading the tweezer, the reservoir potential is turned off and only the tweezer remains. To prepare a deterministic atom number, the unnecessary atoms can be removed with magnetic spilling as it has been demonstrated in [60] and is depicted in Fig. 2.11. Here, a magnetic gradient is added to the (ramped down) optical potential of the tweezer tilts the potential, such that the higher lying states are not bound anymore or quickly tunnel through the remaining barrier. As the potential introduced by the magnetic gradient B' is given by $V(x) = \mu_j B' x$ and hence depends on the magnetic moment μ_j, the remaining potential height is different for different spin states. One can therefore use this scheme to completely remove one spin component while preparing a selected number of atoms for the other spin state.

Spin Dependent Detection

The main observable of this experimental approach is the Rabi frequency of the transfer between the atoms in the spin down state and the atoms in the spin up state. In order to measure this frequency, one needs a spin dependent detection scheme. As our counting scheme employs lasers addressing both hyperfine states, we have to remove one spin component before detection.

To achieve this objective, a resonant blowout pulse can be used. In this scheme, the atoms quickly scatter many photons from one direction. When this happens in free space or faster than the trapping period of the confining potential, the momenta of the absorbed photons add up linearly, $p_{atom} \simeq N\hbar k$, yielding a kinetic energy of $E_{kin} \simeq N^2\hbar^2k^2/(2m)$. In the opposite regime, i.e. beams from different directions or with the scattering rate lower than the trapping frequency, the atoms perform a random walk in momentum space, where the typical momentum after scattering N photons scales as $\sqrt{N}\hbar k$ and the kinetic energy becomes $E_{kin} \simeq N\hbar^2k^2/(2m)$. In both cases the momentum kick imparted by emitted photon has been neglected, which will always lead to an additional random walk in momentum space. After absorbing enough photons, the addressed atoms have a large momentum and quickly escape the region of interest, while atoms dark to the blowout beam are still present.

In our experiment, the atoms are first released from the tweezer and, once the density is low enough to avoid photo-association losses and hyperfine changing collisions, a microwave-frequency pulse is applied to transfer the spin up atoms from the $|F = 9/2, m_F = -7/2\rangle$ to the $|F = 7/2, m_F = -7/2\rangle$ state. After hiding this spin state in the F = 7/2 hyperfine state, the $|F = 9/2, m_F = -9/2\rangle \rightarrow |F' = 11/2, m_F = -11/2\rangle$ cycling transition can be driven by a σ^--polarized laser beam of corresponding frequency. Due to the dipole selection rules, the atoms can only decay back to their initial state, where they absorb again. After scattering at saturation intensity for ∼2 µs and absorbing ∼40 photons from the blowout beam, the atom's momentum corresponds to a speed of ∼500 µm/ms, compared to ∼20 µm/ms for atoms only released from the tweezer. After a brief subsequent time of flight, the atoms addressed by the blowout pulse will have left the trapping region for our imaging scheme and consequently do not contribute to the extracted atom number.

2.3.2 Conclusion and Current State of the Project

To summarize this section, a two-color MOT scheme for counting small numbers of atoms as well as an experimental roadmap to investigate Anderson's Orthogonality Catastrophe

in a tweezer system has been presented. With the two-color MOT scheme, we are able to reliably perform atom number measurements with single particle resolution for systems of up to about 17 atoms with classification fidelities of $\sim 98\%$ when working with up to five atoms, and fidelities of $> 85\%$ when working with up to 17 atoms. The number of atoms we can distinguish is determined by the stability of the fluorescence rate on the probing transition and hence by the technical performance of the frequency locks and power stabilizations used, which can be improved if a need to count larger atom numbers arises. The two-color scheme significantly reduces the influence of light scattered from the MOT beams and thereby enables such single-atom resolved measurements in systems that have not been purpose-built for this application and, for example, contain in-vacuum components.

In summary, we established a pathway to study the fermionic immobile impurity limit in a small system with variable atom number and scattering phase shift. As an essential tool for doing this, we developed and characterized a two-color MOT scheme for atom number counting; the production of cold Fermi gases as well as the implementation of magnetic spilling has been started [77], but has not been discussed in more detail here. The next steps are the setup and characterization of the spin dependent potentials, before the Orthogonality Catastrophe can be studied in our experiment.

In the following chapters we focus on a complementary, but very different approach to study polarons. Instead of a small fermionic system, a two-dimensional bosonic bulk system is prepared and investigated.

Chapter 3

Polarons in a Degenerate Two-Dimensional Bose-Gas

For the remainder of this thesis, we focus on the other species available in our experiment: the bosonic ^{39}K and bulk systems thereof. Chapter 3 presents the necessary background, while chapter 4 and 5 discuss the measured polaron spectra and spatially resolved impurity dynamics, respectively.

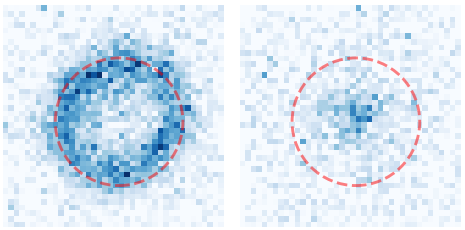

Figure 3.1: Impurity distribution measured for repulsive interactions in our setup for small detuning (left) and large detuning (right), with the radius of the condensate indicated by the red circle. Impurities are predominantly created at positions where the mean field shift $\propto gn(r)$ equals the applied RF detuning. For low detuning, this condition is fulfilled near the edge of the condensate at low density, and for high detuning near the center at the highest density.

In order to be able to investigate polaronic physics, and especially polaronic physics in bosonic two-dimensional systems, we adapted the machine setup for this goal. This included switching isotopes, adapting the laser system to the changed transitions, implementing several new steps in the system preparation, related technical improvements on the machine, and finally accomplishing the evaporation of ^{39}K to high enough phase space densities to observe Bose-Einstein condensation. Once we reached the degenerate regime, we proceeded to implement RF transfers to an impurity state and built suitable optical setups to transform the degenerate gas into an effectively two-dimensional geometry and to image both the bath and the impurities therein. A typical image of the spatial impurity distribution for two different RF detunings at some repulsive interaction strength are shown in Fig. 3.1 and will be discussed further below.

However, before focusing on our measured polaron spectra in chapter 4 and the observed impurity dynamics in chapter 5, we use this chapter to present some theoretical

and experimental background. We first briefly summarize previous work in the field of polaronic physics in quantum gas experiments for fermionic and bosonic systems, both in three and in two dimensions, and with a focus on the used experimental techniques. We then introduce the most relevant theoretical and experimental aspects of two-dimensional systems in Sec. 3.2 and finally discuss details of the experimental setup and of the system preparation in Sec. 3.3. Readers familiar with two-dimensional quantum systems can easily skip these sections and proceed to the next chapter discussing the obtained polaron spectra.

3.1 Previous Work on Polarons in Quantum Gas Experiments

Polarons, or more generally speaking impurities immersed in a bath, have in recent years been studied in ultracold quantum gases for both fermionic and bosonic environments.

3D Fermionic Baths Parallel to extensive theoretical work [78–82], the three-dimensional Fermi polaron has been studied in several experimental works: In [83], a cold fermionic cloud of ^{6}Li at $T \sim 0.14T_F$ has been prepared, where the majority of atoms were in hyperfine state $|1\rangle$, while a small fraction was in state $|3\rangle$. A Feshbach resonance allowed to control the strength of the attractive interaction between these two spin components. By transferring atoms via an RF pulse from either $|1\rangle$ or $|3\rangle$ to a separate, only weakly interacting state $|2\rangle$, the authors measured the polaron energy and could observe the transition from polaronic to molecular binding. In the same year as the Zwierlein group, Nascimbène et al. [84] investigated the behavior of a ^{6}Li cloud after compression, where the degree of spin polarization in the sample was adjustable. For high imbalance, they observed a decoupling of the excited oscillation frequencies in the two components, consistent with an increased effective mass for the minority component due to the polaronic interactions with their environment. Both attractive and repulsive interactions have been examined in [85] for a cloud of ^{6}Li atoms with ^{40}K atoms as impurities. Initially superimposing the degenerate Lithium cloud with the dilute cloud of ^{40}K atoms is done at negligible interactions. The polaron energy could then directly be measured by observing the detuning needed for the radio-frequency to flip the ^{40}K atoms into a different, strongly interacting hyperfine state, while the line width allowed to extract the state's lifetime. The decay in amplitude for Rabi-oscillation between the weakly and the strongly interacting states furthermore gave access to the quasi-particle residue.

2D Fermionic Baths Two-dimensional fermionic systems were studied theoretically around the same time [86–89]. Momentum-resolved photoemission spectroscopy was used to study this problem experimentally [90]: using two hyperfine spin states of ^{40}K and a Feshbach resonance between the two, the polaronic state is first prepared adiabatically for either attractive or repulsive interactions. After transferring the impurity atom to a third, non-interacting hyperfine state and a subsequent free expansion, the spatial distribution of this third state gives direct access to the momentum distribution of the original impurity state. The Fermi polaron's spectral function, its effective mass, as well as its lifetime (for repulsive interactions) can be extracted from this.

3D Bosonic Baths Early experimental work on impurities in a bosonic system focused on implementations without the ability to tune the interaction strength. In [91], the authors prepared Cesium atoms as impurities in a cold Rubidium cloud and determined the three-body loss rate in this setting, while the Oberthaler group [92] measured the decoherence of (fermionic) ^{6}Li impurities immersed in a sodium BEC, and [93] investigated a system with a magnon formed in a ferromagnetic spinor BEC and measured its dispersion relation, the energy gap, and effective mass.

In 2016, three-dimensional systems with bosonic baths and useful interstate Feshbach resonances started to be used to investigate the Bose polaron. This allowed to measure the polaron's energy, line width, and lifetime for both attractive and repulsive interactions [94, 95]. Subsequently, the observed line shapes have also been analyzed in more detail [96]. A few years later, Yan et al. [97] were able to even measure the spatially resolved response and investigated the temperature dependence of the polaron energy. Some more details of their work is presented in the context of our measured 3D polaron spectra in Sec. 4.1.

In a series of papers, the Aarhus group then focused on the formation dynamics of polarons [98–100]. By using a Ramsey-type scheme of creating a bath-impurity superposition with subsequent free evolution and final transfer back to the initial state, they were able to track the quasi-particle formation. This allows the probing of the transition between two-body dynamics relevant for short times (and thus high energies) as well as weak interactions, and the many-body dynamics relevant for strong interactions and long times by identifying their unique signatures in the time-dependence of the coherence amplitude decay.

In parallel, a significant amount of theoretical work on different aspects of the 3D Bose polaron has been performed [101–118].

2D Bosonic Baths In contrast to the extensive work performed for three-dimensional bosonic systems, the two-dimensional case has not been experimentally realized so far. The first theoretical study on polarons in a two-dimensional study focused on its energy, its effective mass, and the signature in Bragg scattering by utilizing a variational approach to determine the ground state of the polaron for different temperatures [119]. Renormalization group studies followed a few years later, with partially different predictions, especially regarding the transition into the self-trapping regime [120]. While [121] later also focused on the weak coupling regime, the authors of [122] and [123] used quantum Monte Carlo techniques to study the strong coupling regime, calculating the polaron energy, the effective mass, and the quasi-particle residue. A comparison of these results with a simpler mean-field study was subsequently published in [124], and the case of a dipolar gas was studied in [125].

Physically, the two-dimensional bosonic system is interesting for two main reasons: the role of quantum fluctuations combined with quasi-long range order, and the similarity to layered solid state materials.

Quantum fluctuations become more relevant in lower dimensions, while two-dimensional bosonic systems still exhibit quasi-long range order, i.e. order over a length scale well above the system size. The two-dimensional bosonic ground state is therefore quite similar to the three-dimensional Bose-Einstein condensate and, for example, also shows superfluid behavior.

Superconducting cuprates are layered materials, leading to the idea that they can be modeled as a stack of two-dimensional systems that are weakly coupled to each other. In a bosonic degenerate cloud, the linear Bogoliubov dispersion relation matches the linear phonon dispersion relation, making the two-dimensional degenerate Bose gases a promising candidate to simulate existing solid state systems.

3.2 Introduction to Two-Dimensional Quantum Gases

Before proceeding to our experimental implementation of a degenerate bosonic cloud in Sec. 3.3, we discuss some relevant theoretical and practical aspects of two-dimensional quantum systems.

Dimensionality is Important

Changing the dimensionality of a system affects one of its most fundamental qualities, and it is therefore not surprising that it can drastically affect the observed behavior of the system of interest. Examples for this can be found in different fields of physics: in General Relativity, for example, only a spacetime with at least three spatial dimensions allows for gravitational waves, while in the case of two spatial dimensions, the gravitational field is completely determined by the density distribution, and hence no (in vacuum propagating) gravitational waves can exist [126]. Two spatial dimensions also can lead to new, more flexible statistics for particles to follow. These so called "anyons" possess neither an integer nor a half-integer spin. For the exchange of two particles, the total wave function hence does not pick up a phase of 2π or π, for bosons and fermions respectively, but instead some other value, depending on the exact system considered [127, 128]. Less abstract is the problem of a single particle within an attractive potential. While a one-dimensional or two-dimensional system exhibits a bound state for arbitrarily weak potential strengths, three-dimensional systems do not have a bound state if the attractive potential is too shallow [129, 130].

A typical quantity strongly influenced by the dimensionality of the system and relevant for condensed matter systems is the density of states $D(E)$. In a three-dimensional system without potential, the number of states available for a maximum momentum p_{max} is simply $N_{3d}(p_{max}) \propto p_{max}^3/\hbar^3$. Expressing this over the available energy $E = p_{max}^2/(2m)$, one has $N_{3d}(E) \propto E^{3/2}$, and the density of states becomes $D_{3d}(E) \equiv \partial_E N_{3d}(E) \propto E^{1/2}$. The same reasoning in two dimensions gives $N_{2d}(p_{max}) \propto p_{max}^2/\hbar^2$ with $D_{2d}(E) =$ constant, while in one dimension one has $N_{1d}(p_{max}) \propto |p_{max}|/\hbar$ with $D_{1d}(E) \propto E^{-1/2}$. This different behavior in the density of states lead to Bose-Einstein condensation in three dimensions, while both two and one dimension do no exhibit this feature [131].

More generally, in two or less dimensions, the Mermin-Wagner theorem prohibits true long-range order in systems with continuous Hamiltonian symmetry and sufficiently short-ranged interactions at T > 0 [132–135], as they appear in quantum gas experiments.

This general behavior can be considered a consequence of the increased importance of fluctuations in lower dimensions or, conversely, the stronger suppression of fluctuations

in higher dimensions. An intuitive picture for this is a chain or lattice of spins $\mathbf{S}_i$ with interaction energies $E \propto -J_{ij} \sum_{i,j} \mathbf{S}_i \cdot \mathbf{S}_j$, where $J_{ij} = 0$ if spins i and j are not next to each other and $|J|$ is the coupling strength. In this model spin orientation misalignment between nearest neighbors are energetically costly. Assuming a one-dimensional system and two of those spins to have fixed orientation, there is only one possible path between these two spins, such that it is straightforward to introduce a slowly varying spin orientation matching these boundary conditions. However, the higher the dimension is, the more paths between the two fixed spins are possible, all of which prefer to have an only slowly varying spin orientation. Higher dimensions are therefore more prone to showing frustration, increasing the energy required for this specific spin orientation pattern. This suppression of available states at low temperature leads to a reduced relevance of fluctuations in higher dimensions. Stated alternatively, fluctuations in lower dimensions are less costly and hence have a larger effect even for low temperatures.

The Mermin-Wagner theorem can be circumvented by breaking the first condition and introducing a confining potential that breaks the translational symmetry of the Hamiltonian, therefore changing the density of states of the system. In this case, true condensation is also be possible in two dimensions at T > 0 [136].

Berezinskii-Kosterlitz-Thouless Transition

However, even without relying on the confining potential, these systems can still exhibit "quasi-long-range" order, where the decay length of correlations is very large. This is the case in two-dimensional systems with repulsive interactions cooled below the critical temperature of the Berezinskii-Kosterlitz-Thouless (BKT) transition, which marks the freeze-out of free vortices [137, 138]. Above the critical temperature, vortices are unbound and destroy long-range phase coherence. At T_{BKT}, it becomes favorable to form vortex-antivortex pairs which, on distances much larger than their separation, do not have a net effect on the phase correlation. The remaining decay of phase coherence is due to the remaining phononic excitations, which only lead to a much slower decay of correlations. The correlation function $g_1(r)$ in an uniform gas with repulsive interactions, for example, shows a decay of $g_1(r) \propto r^{1/\rho}$ at low enough temperatures, where $\rho = n_s \lambda_{th}^2$ is the phase space density, n_s is the superfluid density and $\lambda_{th} = h/\sqrt{2\pi m k_B T}$ is the thermal wavelength. As the BKT transition happens around $\rho \simeq 4$ [136], the exponent $1/\rho$ is small and the decay of correlations is very slow, and often leading to no noticeable reduction over the extent of the atomic sample. Experimental demonstrations of this behavior have been reported, for example, in [139] and more recently in a spatially resolved manner in [140]. Under such conditions, the quasi-long-range order is effectively the same as a true

long-range order. This general description remains true even for harmonic confinement, where actual condensation is also possible due to the change in the density of states. For realistic parameters, T_{BKT} is well above the condensation temperature T_{BEC}, such that the BKT-phase is the more relevant one. The BKT-transition is smooth and does not exhibit a clear transition in the density profile or the momentum distribution, as in the case for Bose-Einstein condensation, where clear bimodal distributions indicate the crossing of the critical temperature. The transition can in fact be considered a phase transition of "infinite-order", as neither the free energy nor any of its derivatives show discontinuities. Instead, the discontinuity appears in the topology of the wave function's phase, making this transition the prime example of topological phase transitions, even leading to its discoverers being awarded the Nobel Prize in Physics in 2016 [141].

One experimentally very important consequence of the BKT transition is the emergence of a critical velocity, signaling superfluid behavior. In a superfluid, excitation modes have a non-zero minimal speed – in contrast to, for example, free particles, where $E = p^2/(2m)$ and the speed becomes arbitrarily small for low enough momentum. In a superfluid the excitation spectrum is linear in the momentum $\hbar k$ for small momenta, and gradually transforms into a quadratic spectrum for larger values of $\hbar k$. The linear behavior for small k corresponds to a momentum-independent velocity c of the mode, which takes the form

$$c = \sqrt{gn/m}, \tag{3.1}$$

where g is a coupling constant introduced below, n is the density, and m is the particle mass. No phonons can be created for disturbances moving through the cloud with a velocity smaller than this speed, therefore making c to be the critical velocity. The linear behavior of the dispersion relation for low momenta is similar to the behavior of sound waves in classical mechanics and (obviously closely related) of phonons in solid state physics, resulting in the adaption of the term "phonon" for low-momentum excitations in quantum gases and to the term "speed of sound" for c.

Practical 2D: Experimental Aspects

Effectively 2D Obviously, our world has three spatial dimensions, leading to the question whether any real world systems can be considered two-dimensional. The abstraction as a two-dimensional system usually becomes relevant when a system is "kinetically 2D", i.e. when movement along one spatial dimension is restricted in such a way, that motion along this axis is not possible at the available energies. An intuitive example of this are large scale eddies in Earth's atmosphere, that occur during hurricanes. With several

hundred to a thousand kilometers, the diameter is much larger than their vertical extent, which is set by the height of the troposphere and is ∼15 km, resulting in an aspect ratio on the order of ∼30-100. This two-dimensional confinement leads to an inverse cascade, where energy is transported from smaller eddies to larger ones, exactly the opposite of what happens in three dimensions [142].

In quantum mechanical systems as ours, "kinetically 2D" refers to situations where a tight confinement along one axis, say z, is applied. The wave function can then be decomposed into a product $\Psi(x, y, z) = \Phi(x, y) \cdot \chi(z)$, where $\chi(z)$ is the ground state wave function along z. Assuming a harmonic potential along the z-direction with trapping frequency $\omega_z = 2\pi\nu_z$, this condition implies that the harmonic oscillator length along z must be much smaller than both the healing length and the thermal wavelength, and that the level spacing $\hbar\omega_z$ must be much smaller than the temperature and the chemical potential [136]. In very cold fermionic systems, the latter condition also implies that the Fermi energy must be much smaller than the vertical level spacing $\hbar\omega_z$. In such a setting, the system does not have enough energy to create excitations along z, and the vertical profile is only determined by the confining potential. The only remaining degrees of freedom are therefore within the x-y-plane.

Probing 2D Systems: Density Profile In order to analyze and interpret the observed spatial structures, the density profile of the undisturbed bath needs to be known. For two-dimensional Bose gases, the ground state at low temperature is described by the Berezinskii-Kosterlitz-Thouless (BKT) theory [137, 138].

Unlike the BEC-condensation, the BKT-transition does not show an abrupt change in the density- or momentum profile. Instead, the population in the ground state gradually increases while the occupation of excited states decreases. For very low temperatures, the density profile in an interacting system approaches the Thomas-Fermi profile derived by the assumption of negligible kinetic energy [143, 144]. In this limit, the time-independent Gross-Pitaevskii equation [145, 146] becomes a simple algebraic equation:

$$E\Psi = \left[-\frac{\hbar^2}{2m}\nabla^2 + V_{ext}(\mathbf{r}) + g|\Psi|^2\right]\Psi \rightarrow E\Psi = \left[V(\mathbf{r}) + g|\Psi|^2\right]\Psi. \tag{3.2}$$

Assuming harmonic confinement and with the density $n(\mathbf{r}) \equiv |\Psi(\mathbf{r})|^2$, one obtains

$$n(\mathbf{r}) = n_0\left[1 - \left(|\mathbf{r}|/R_{TF}\right)^2\right] \tag{3.3}$$

for $|\mathbf{r}| < R_{TF}$ and zero otherwise. The central density then is $n_0 = \mu/g$, where the

total energy E has been equated with the chemical potential μ, and the Thomas-Fermi radius is $R_{TF} = \sqrt{2\mu/(m\omega^2)}$. As we are here concerned with two-dimensional geometries, the above expression is only valid within the horizontal plane, while the vertical density profile is determined by the trapping potential's ground state wave function, i.e. usually a gaussian for the typical harmonic confinement. For a radially symmetric two-dimensional system, eliminating the chemical potential and instead introducing explicit dependencies on the particle number N and the coupling parameter g leads

$$R_{TF} = \left[\frac{4Ng}{\pi m(2\pi\nu_{rad})^2}\right]^{1/4}. \tag{3.4}$$

Thus, the Thomas-Fermi radius only shows a weak dependence on particle number, coupling parameter, and trapping frequency – similarly to the 3D case where $R_{TF} \propto (gN/\nu^2)^{1/5}$. Since this profile density is simply a parabola and describes the observed density very well, we will sometimes employ this density profile when doing analytic calculations below. Note that the Thomas-Fermi approximation of negligible kinetic energy fails near the edge of the cloud where the density is low and the interaction term is small.

The experiments described below are usually performed at temperatures around 50 nK with phase space densities $\rho \gg 10$, and are therefore well above the critical phase space density $\rho_c = 4$. The temperature is also well below the temperature needed for sizable excitations along the tightly confined axis, $\hbar\omega_z/k_B \simeq 300$ nK for $\omega_z = 2\pi \cdot 6.5$ kHz, justifying the treatment as a two-dimensional system.

Probing 2D Systems: Imaging 2D systems are relatively convenient to image, since the spatial distribution can, provided that the resolution is sufficient, be imaged directly, if the imaging axis coincides with the axis of strong confinement, only one layer of the system is prepared (i.e. not a stack of 2D systems), and saturation is of no concern. The integration along the line of sight then only changes the signal's amplitude, but otherwise does not distort the actual density distribution. In contrast, the signal is integrated along different densities in 3D systems, making the signal extraction more involved [147, 148].

Similarly, the momentum distribution is, as in many quantum gas experiments, also comparably easy to obtain. Assuming ballistic expansion, a long enough free expansion converts initial momentum to positions after the time-of-flight $\mathbf{r}_0 \rightarrow \mathbf{r}_0 + \mathbf{p} \cdot t_{TOF}/m$, and makes the momentum distribution readily available, provided that the initial position becomes negligible, i.e. $\mathbf{p} \cdot t_{TOF}/m \gg \mathbf{r}_0$. For strongly interacting systems, the assumption of ballistic expansion can be problematic, and collisions during the expansion lead to a redistribution of momentum, hence preventing the extraction of the initial momentum

distribution. The strong confinement along one axis in 2D systems serves as an advantage in such cases: it leads to a large momentum uncertainty $\Delta p_z \simeq \hbar/\Delta z$, and therefore to a fast expansion along the strongly confined axis. The density then drops drastically over a timescale of $\sim 1/\nu_z$, reducing the chance of collisions and helping to map the original momentum distribution to a spatial distribution.

Scattering in Quasi-2D The confinement along the vertical direction also affects the scattering properties, and therefore the interactions between particles.

Since we consider cold particles, all but the s-wave channel are frozen out due to their higher required higher angular momentum and hence higher required energy. In three-dimensional systems, a plane wave scattered by a small potential at $\mathbf{r} = 0$ leads to an asymptotic wave function for $|\mathbf{r}| \to \infty$, which is usually parametrized as

$$\psi_{\mathbf{k}}(\mathbf{r}) \sim e^{i\mathbf{k}\cdot\mathbf{r}} + f(\theta, \phi, k)\frac{e^{i\mathbf{k}\cdot\mathbf{r}}}{|\mathbf{r}|}, \tag{3.5}$$

where the first part is the incident wave, the second part is the scattered wave, and $f(\theta, \phi, k)$ is the scattering amplitude. Per definition, for s-wave scattering $f(\theta, \phi, k)$ does not have an angular dependence and it can be expressed as [149]

$$f(k) = \frac{1/k}{-\frac{1}{ka} + \frac{r_0 k}{2} - i}. \tag{3.6}$$

The square of the scattering amplitude $|f(\theta, \phi)|^2$ is the differential cross-section, and hence the total cross-section can be obtained by angular integration $\sigma_{total} = \int d\Omega |f(\theta, \phi, k)|^2$. In the limit of small relative momentum k, i.e. $ka \to 0$, the scattering amplitude approaches a finite value and the total scattering cross-section becomes $\sigma_{total} = 4\pi a^2$. For identical particles in two different initial states, the symmetrization of the wave function leads to an additional factor of 2, i.e. $\sigma_{total} = 8\pi a^2$ [150]. The coupling constant g_{3D}, appearing, for example, in the Gross-Pitaevskii equation, is then $g_{3D} = 4\pi\hbar^2 a/m$.

In a truly two-dimensional system, the wave function after scattering with relative momentum $\hbar\mathbf{k}$ becomes [151]

$$\psi_{\mathbf{k}}(\mathbf{r}) \sim e^{i\mathbf{k}\cdot\mathbf{r}} - \sqrt{\frac{i}{8\pi}} f(k) \frac{e^{i\mathbf{k}\cdot\mathbf{r}}}{\sqrt{\mathbf{k}\cdot\mathbf{r}}}, \tag{3.7}$$

where the scattering amplitude $f(k)$ for two identical bosons is

$$f(k) \approx \frac{4\pi}{-\ln(k^2 a_{2D}^2) + i\pi}. \tag{3.8}$$

a_{2D} denotes the 2D scattering length, and $k = |\mathbf{k}|$. Note that the scattering amplitude does not converge to a finite, nonzero value for $k \to 0$, in contrast to 3D where $f_{3d}(k \to 0) = -a$.

The more realistic case of a system strongly confined in one direction has been discussed in [152, 153] under the assumption that the vertical extent of the cloud l_z is still much larger than the 3D scattering length a_{3D}. As a boundary condition, the scattered wave function along z has to asymptotically match the profile determined by the confining potential, which gives

$$f(k) \approx \frac{4\pi}{\sqrt{2\pi} l_z / a_{3D} - \ln(B k^2 l_z^2) + i\pi}, \tag{3.9}$$

for the (quasi-) 2D scattering amplitude, where $B \approx 3.47$ is a numerical constant. Note that the term "quasi-2D" is sometimes used to distinguish between "true" 2D as in Eq. 3.8 and "tightly confined 3D, thus effectively 2D" as in Eq. 3.9, while the same expression sometimes refers to the regime of $k_B T \lesssim \hbar\omega_z$, where remaining vertical excitations are relevant. Here, we only use the term "quasi-2D" in the former sense. Comparing Eqs. 3.8 and 3.9, one obtains

$$a_{2D} = l_z \sqrt{B} \exp\left(-\sqrt{\frac{\pi}{2}} \frac{l_z}{a_{3D}}\right). \tag{3.10}$$

The coupling parameter in 2D g_{2D} becomes

$$g_{2D} = -\frac{4\pi\hbar^2}{m \ln(k^2 a_{2D}^2 / 4\pi)} \simeq \frac{\sqrt{8\pi}\hbar^2 a_{3D}}{m l_z} \equiv \frac{\hbar^2}{m}\tilde{g}, \tag{3.11}$$

where the approximation assumes $a_{3D} \ll l_z$ [123]. It is furthermore convenient to introduce the dimensionless coupling parameter $\tilde{g}$:

$$\tilde{g} \equiv \frac{m}{\hbar^2} g \simeq \sqrt{8\pi} \frac{a_{3D}}{l_z}, \tag{3.12}$$

which is depicted in Fig. 3.2. The coupling constant g directly appears in the interaction energy, scaling as $E_{int} \propto gN^2/V$, where N is the number of particles and V is the available volume. For a flat potential, kinetic energy and interaction energy are equal around $\tilde{g} = 2\pi$. Without Feshbach resonances, most quantum gas experiments can only operate in regimes of $\tilde{g} \sim 10^{-2} - 10^{-1}$, while liquid helium has $\tilde{g} \sim 1$ [136, 154].

Note that the 2D scattering length, as defined in Eq. 3.9, is always positive, while a_{3D} can also be negative, indicating attractive interactions. The difference is that a_{2D} does not have the same significance as a_{3D} – comparing Eqs. 3.6 and 3.9 indicates that the interaction parameter $1/ka_{3D}$ in 3D is replaced by $\ln(ka_{2D})$ in 2D.

The latter can be both positive or negative, indicating attractive or repulsive interactions, respectively. Using the above conventions and definitions, the interaction signs are switched such that attractive interactions are indicated by negative $1/ka_{3D}$ and by positive $\ln(ka_{2D})$. Repulsive interactions correspondingly have positive $1/ka_{3D}$ and by negative $\ln(ka_{2D})$. In both cases, the regimes around $1/ka_{3D} \approx 0$ and $\ln(ka_{2D}) \approx 0$ indicate the strongest interactions.

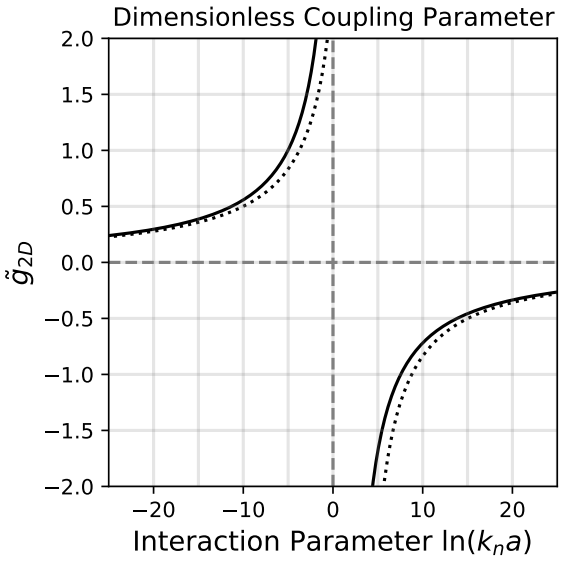

Figure 3.2: Relation between the interaction parameter $\ln(k_n a)$ and $\tilde{g}_{2D}$. The solid line uses the defining expression of Eq. 3.11 and the dotted line shows the approximate expression, where parameters typical for our experimental setup have been used.

Since the interaction parameter explicitly involves the momentum k, one needs to choose a reference momentum for stating any explicit value. For fermionic systems, this naturally is the Fermi-wavevector k_F as scattering for much smaller momenta is Pauli blocked and much higher momenta are not populated. For bosonic systems, one usually simply follows this definition and uses the wavevector of a fermionic system with flat potential of the same density, i.e. $k_n^{3D} = (6\pi^2 n)^{1/3}$ and $k_n^{2D} = \sqrt{4\pi n}$. This momentum also defines a natural energy scale given by $E_n = \hbar^2 k_n^2/2m$, resulting in $E_n^{3D} = \hbar^2(6\pi^2 n)^{2/3}/2m$ and $E_n^{2D} = 2\pi\hbar^2 n/m$.

Integrated signals obtained in the experiments described below additionally involve the integration over different densities due to the harmonic confinement. In these cases, we will always refer to the peak density and therefore the highest k_n within the sample. Due to the square root and the logarithmic dependence, the exact value of the peak density only has a weak influence on the interaction parameter.

3.3 Experimental Setup and Preparation

Before proceeding to more specific discussions, Sec. 3.3.1 describes the relevant basic properties of ^{39}K in the context of cold quantum gases, where we put a special focus on differences to ^{40}K as the other isotope available in our machine, and on properties especially relevant with our experimental boundary conditions. Readers familiar with ^{39}K can easily skip this section. Sec. 3.3.2 then summarizes the experimental procedure implemented during this work to obtain an ultracold bosonic gas in either three or two dimensions, resulting in a Bose-Einstein-condensate or a BKT-gas, respectively.

Finally, Sec. 3.3.3 and Sec. 3.3.4 dicuss the technical details of implementing high field imaging and the magnetic field calibration, respectively.

3.3.1 Introduction to ^{39}K

^{39}K Levelscheme and Relevant Transitions There are two main differences between the level scheme of ^{39}K, shown in Fig. 3.3, and the level scheme of ^{40}K, shown in Fig. 2.1 in Sec. 2.1.2. The first one is the different nuclear spin of I = 3/2 for ^{39}K and I = 4 for ^{40}K, and correspondingly the different number of m_F-substates within the electronic ground state. The second difference is the normal and the inverted ground state structure for ^{39}K and ^{40}K, respectively.

The hyperfine splitting depends on the nuclear spin I, $\Delta E_{HFS} \sim A \cdot I + B \cdot I^2$ [157], and therefore the hyperfine splitting of ^{39}K is significantly smaller than for ^{40}K. The ground state splitting of ∼461.7 MHz still makes it more convenient to use two independent lasers for the cooler and repumper transition addressing the F=2 and F=1 ground state, respectively. In contrast, for the excited state manifolds of $4p_{1/2}$ and $4p_{3/2}$ the energy differences at zero field are only $E/h = 55.5$ MHz and $E/h = 33.8$ MHz, respectively, and thus can easily be tuned by an offsetlock. Therefore, it is possible to, for example, use the same laser to address either the $|4s_{1/2}, F = 2\rangle \leftrightarrow |4p_{1/2}, F = 1\rangle$ or the $|4s_{1/2}, F = 2\rangle \leftrightarrow |4p_{1/2}, F = 2\rangle$ transition; the switching time is limited by the performance of the offsetlock which, in our machine, usually takes a few ten milliseconds. While the frequency difference of 55.5 MHz $\simeq 9.25\,\Gamma$ between F=1 and F=2 on the D1-line is large enough to clearly separate the lines, the separations on the D2-line are 3.3 MHz, 9.4 MHz, and 21.4 MHz, corresponding to $\simeq 0.5\,\Gamma$ between F=0 and F=1, to $\simeq 1.5\,\Gamma$ between F=1 and F=2, and to $\simeq 3.5\,\Gamma$ between F=2 and F=3. The MOT transition to F=3 is thus reasonably well separated from the other states, but offresonant excitations will always be much more relevant for ^{39}K than they are for ^{40}K, and the F=0 and F=1 states can barely be resolved.

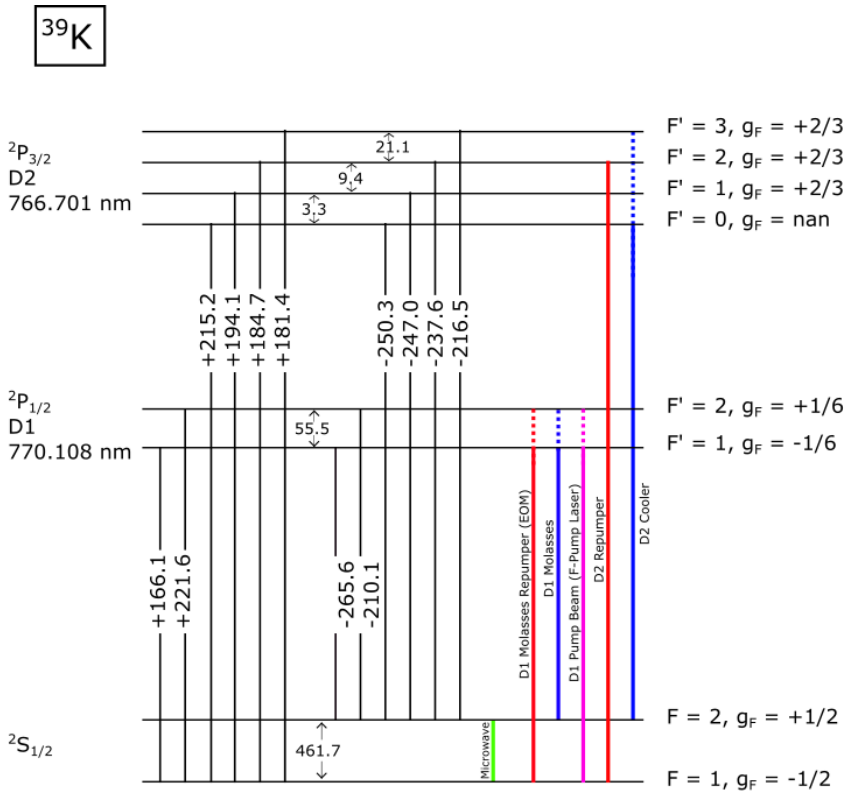

Figure 3.3: Relevant part of the level structure of ^{39}K, showing the electronic ground state ($4^2S_{1/2}$) and two electronically excited states ($4^2P_{1/2}$ and $4^2P_{3/2}$). The numbers in the individual connecting lines indicate the frequency shift of the respective transition at zero magnetic field with respect to the crossover with the numerical value in MHz; the transitions used in the experiment are indicated by colored, labeled lines. Compared to ^{40}K, the energy differences between different hyperfine levels within each manifold are much smaller, hence allowing to address different final F'-states by just tuning the laser's offsetlock appropriately, as is indicated by the dotted lines. The D2 repumper is an exception, as it serves as a reference laser and hence only has a small tuning range. Frequency values taken from [155] and [156].

MOT and Molasses Cooling The MOT transitions are very similar to what has been described in Sec. 2.1.2, only that the cooler laser now addresses the $|4s_{1/2}, F = 2\rangle \rightarrow |4p_{3/2}, F = 3\rangle$ transition, and the repumper the $|4s_{1/2}, F = 1\rangle \rightarrow |4p_{3/2}, F = 2\rangle$ transition. To realize this in the experiment, one AOM in the spectroscopy arm of the D2 setup has to be switched off, the respective mirror has to be realigned to compensate for the new deflection angle, and new locking flanks in the offset locks of the repumper and the cooler have to be selected, such that switching between a ^{40}K-MOT and a ^{39}K-MOT can be done in less than a minute by an experienced user[1].

The Λ-enhanced gray molasses is conceptually unchanged: the principal beam now addresses the $|4s_{1/2}, F = 2\rangle \rightarrow |4p_{1/2}, F = 1\rangle$ transition (i.e. still a $F \rightarrow F-1$ transition),

[1]Within 42 seconds, limited by the walking time around the optical table.

and the EOM-modulated repumper the $|4s_{1/2}, F = 1\rangle \rightarrow |4p_{1/2}, F = 1\rangle$ transition. As the EOM frequency of ∼462 MHz is significantly different from the ∼1285 MHz for ^{40}K, a second EOM with an accordingly tuned resonance in the beam path of the laser is used, such that the applied modulation can be controlled by switching the RF power onto the respective EOM.

Unlike in ^{40}K, ^{39}K does not allow for the convenient blue MOT scheme during the transition time while the magnetic field is decaying. Instead, we employ a hybrid-MOT scheme similar to what has been used in [158]; the background and implementation of this scheme will be discussed in more detail in [28].

Imaging is usually done either at low field ($B \lesssim 5$ G) or high field ($B \approx 500$ G), corresponding to the Zeeman regime and the Paschen-Back regime, respectively. At low field, the MOT cooler transition $|F = 2, m_F = 2\rangle \rightarrow |F = 3, m_F = 3\rangle$ on the D2 line is most convenient as it is a cycling transition. At high fields, choosing an imaging transition is less obvious as one is deep in the Paschen-Back regime and the $|F, m_F\rangle$-basis ceases to be meaningful. The selection of a reasonably working imaging transition and the connected challenges are discussed in Sec. 3.3.3.

Magnetic Substructure The magnetically strongest trapped ground state for ^{39}K is the $|F = 2, m_F = +2\rangle$-state in which we transfer the atoms into before the magnetic transport. Unlike in ^{40}K, we partially pump on the D1 line and partially on the D2 line - the "F-pump" role is fulfilled by a laser on the D1 transition from $|4s_{1/2}, F = 1\rangle$ to $|4p_{1/2}, F = 2\rangle$, and the "m_F-pump" role by a laser on the D2 transition from $|4s_{1/2}, F = 2\rangle$ to $|4p_{3/2}, F = 2\rangle$. The pumping is split between D1 and D2 due to technical reasons: with 55 MHz level splitting in the $4p_{1/2}$ manifold, the equivalent to the ^{40}K m_F-pumper would need a 25 MHz AOM, which was not available; in our case, employing the pre-existing D2 beam was more convenient. A table of all relevant decay ratios for both ^{39}K and ^{40}K can be found in appendix A. Once pumped to the correct spin state, the atoms can be loaded into a magnetic trap and, for example, be transported.

Additionally to the incoherent (i.e. entropy removing) optical pumping, radio-frequency transitions can be used to transition between states within the electronic ground state. For transitions between F = 1 and F = 2 at low field, these transitions are around 460 MHz and can in our machine be driven with an in-vacuo single loop antenna. At high fields, the energy difference between the lowest few m_F states only weakly depends on the magnetic field and is between 80 and 120 MHz; the same antenna with a different matching circuit is used to drive these transitions (discussed in [28]). The details of the spin preparation are discussed in Sec. 3.3.2.

Optical Potentials In general, the discussion about optical potentials from Sec. 2.1.2 also applies to ^{39}K as the relevant lasers are far detuned and thus not sensitive to the level structure. However, the creation of two-dimensional degenerate Bose gases involves no transfers to the excited states during the preparation and hence the anti-trapping of the excited states are less relevant. We therefore also employ potentials formed by $\lambda = 1064$ nm light, provided by a MOPA 25NE Mephisto (from *Innolight*, now *Coherent*), and an ALS 1064/532 dual output fiber laser from *Azurlight Systems*. The latter also provides blue-detuned light at $\lambda = 532$ nm used for repulsive potentials.

Interaction Tuning: Feshbach Resonances Since ^{39}K is a bosonic species, s-wave scattering between same state atoms is possible and relevant. Additionally, interstate scattering, just as for the fermionic ^{40}K, is also possible. For the lower lying hyperfine state with F = 1, one thus has six different scattering channels that can all exhibit Feshbach resonances. For the fields achievable in typical quantum gas machines, there are two relevant regions of Feshbach resonances for ^{39}K [29–31]: the "intermediate field" region between ∼20 Gauss and ∼170 Gauss, and the "high field" region between ∼400 Gauss and ∼600 Gauss.

When selecting suitable resonances, several boundary conditions are relevant: First, the higher field region is more convenient to use as imaging is easier there: as discussed in more detail in Sec. 3.3.3, the imaging transitions become more closed at higher field and hence the need for a repumping beam decreases. Brief imaging of dense atomic samples can thus be done with only one laser, reducing the overhead needed for locking and frequency shifting as well as for finding the correct detunings. Furthermore, the required frequencies at these higher fields are easier to achieve with the existing laser transitions needed for the D2 MOT and commercially available AOMs.

Another boundary conditions limits the useful interstate Feshbach resonances: due to the second order Zeeman shift, the scattering $|F = 1, m_F = +1\rangle + |F = 1, m_F = -1\rangle \rightarrow 2 \cdot |F = 1, m_F = 0\rangle$ is energetically allowed at any temperature and field and, at the relevant fields, releases energy on the order of $h \cdot 20$ MHz, which is well above the typical trap depth used. Spin mixtures of $m_F = \pm 1$ thus rapidly populate the $m_F = 0$ state, leaving $|1, -1\rangle + |1, 0\rangle$ and $|1, 0\rangle + |1, -1\rangle$ as usable interstate combinations.

A further limit on the interstate resonances stems from the typical initial conditions of the experiments at hand. Usually, the sample is cooled by evaporative cooling down to the formation of a Bose-Einstein condensate, which is only reasonably stable for repulsive interactions[2]. It is therefore convenient to have an intrastate Feshbach resonance for

[2]To be more precise, it is also stable for weak attractive interactions, as long as the (effectively

enhancing the scattering rate during the cooling, and an interstate resonance on the repulsive side of the intrastate resonance to provide both a stable "bath" system and a tuneable interaction at the same time. Furthermore, all involved Feshbach resonances should have large enough widths to reduce the effect of magnetic field noise.

Useful combinations fulfilling these requirements are the intrastate Feshbach resonance of the $|1,-1\rangle$ state at 561 Gauss in combination with the $|1,-1\rangle+|1,0\rangle$ Feshbach resonance at 526 Gauss, as well as the $|1,0\rangle$ resonance at 472 Gauss together with the $|1,0\rangle+|1,+1\rangle$ interstate resonance at 445 Gauss. If no interstate resonance is required, the $|1,+1\rangle$ intrastate resonance at 402 Gauss is most convenient, as it only requires one spin transfer from the magnetically trapped $|2,+2\rangle$ state.

3.3.2 System Preparation

Initial Preparation and Transport Every experiment cycle starts with the cooling and trapping of atoms in a MOT, followed by a magnetic transport to the science position between the microscopes, and the transfer of the transported atoms from the magnetic trap to an optical dipole trap. The transfer from the magnetic trap to the optical trap is done by collisional loading, where atoms scatter into a deep potential. The efficiency of this scheme depends strongly on the density at the overlapping region, and it is therefore beneficial to start with a high density in the magnetic trap.

Simply loading the magnetic trap from a MOT is in this case not sufficient, and additional steps are needed in order to increase the density. As the first step, Λ-enhanced gray molasses [42–46] cools the atoms to $\sim$ 10-20 µK, leading to a denser cloud in the magnetic trap. In our setup, this step is limited by the eddy currents within the large vacuum chamber and the aluminum breadboards nearby – eddy currents within these structures have decay times of a few milliseconds, and hence limit the switching times of the magnetic field configurations. As the molasses follows immediately after the MOT and the final temperature reached in the molasses strongly depends on the remaining magnetic field [47, 158], the few milliseconds of eddy current decay time lead to a significant expansion of the cloud. The molasses only provides a cooling force, but has not restoring force, and hence cannot compensate for the lost density. We reduce this effect by using a "hybrid MOT" scheme to first cool the atoms and increase the density with the magnetic field still present, similar as it has been described in [158]: after increasing the gradient by $\sim$50%, the D2 cooler is turned off and replaced by the D1 molasses beams, while the D2 repumper is still present. This scheme leads to lower temperatures while still maintaining

repulsive) kinetic energy term dominates over the attractive interaction term.

a restoring force [28, 158], and is followed by a rapid switch off of the D2 repumper and the gradient field; due to the lower temperature, the following expansion until molasses is fully operational is reduced, and we reach a phase space density of $\sim 3 \cdot 10^{-5}$, compared to a phase space density of $\sim 4 \cdot 10^{-9}$ at the end of the MOT.

The next additional step is optical pumping to the spin state experiencing the strongest gradient. Since the energy shift $\Delta E \propto m_F \cdot g_F \cdot B'$ depends on the magnetic gradient $B' = \nabla \vec{B}$, the Landé-factor g_F, and the magnetic quantum number m_F, a large m_F is beneficial to obtain a large potential gradient and therefore a high density. The atoms are therefore pumped to the $|F = 2, m_F = +2\rangle$-state as $g_F > 0$ for F=2. Collisions in this polarized gas are spin-protected, and therefore no hyperfine-changing collisions are possible, resulting in a reduced loss rate.

Once pumped to the correct spin state, the magnetic trap is rapidly switched on. The initial switch-on is done only to a finite field in order to match the density distribution of the free cloud; afterwards the trap stiffness is increased adiabatically by ramping the magnetic field gradient from ∼22 G/cm to ∼85 G/cm. The transport of ∼40 mm at constant gradient is performed by reducing the current through the MOT coils while increasing the current in the coils centered around the science position; additional offset coils allow the exact positioning in all spatial dimensions.

The transfer from the magnetic trap to the deep optical dipole trap is enhanced by collisional loading, similar to what has been described in [159]. As a deep trap is favorable, we use a $P = 17$ W beam at $\lambda = 1064$ nm, focused down to waists of 14.5 and 17 µm, corresponding to a Rayleigh length of 620 µm and 850 µm, respectively, and a maximum potential depth of ~ 6 mK.

Degeneracy Since we work with the $|1, -1\rangle$-intrastate and the $|1, -1\rangle + |1, 0\rangle$-interstate Feshbach resonances, the atoms have to be transferred from the $|2, +2\rangle$ state to the $|1, -1\rangle$ state. This is done by three RF π-pulses: from $|2, +2\rangle$ to $|1, +1\rangle$, and then via the "Λ-transfer" over $|2, 0\rangle$: $|1, +1\rangle \rightarrow |2, 0\rangle \rightarrow |1, -1\rangle$, as is shown in Fig. 3.4(a) and (b).

The reason for this Λ-transfer is that we observed poor performance when using a more standard Landau-Zener transfer from $|1, +1\rangle$ to $|1, 0\rangle$ and further to $|1, -1\rangle$. While the first sweep to $|1, 0\rangle$ works well, the second one only transfers a small fraction to the desired $|1, -1\rangle$ state. We attribute this to thermally allowed scattering events from $|1, 0\rangle + |1, 0\rangle \rightarrow |1, -1\rangle + |1, +1\rangle$ and $|1, -1\rangle + |1, +1\rangle \rightarrow 2 \cdot |1, 0\rangle$ scatterings with a small remaining $|1, +1\rangle$ population, introducing rapid decoherence and hence preventing an efficient Landau-Zener transfer.

To avoid this, we use two π-pulses: after the initial pulse transferring the atoms from

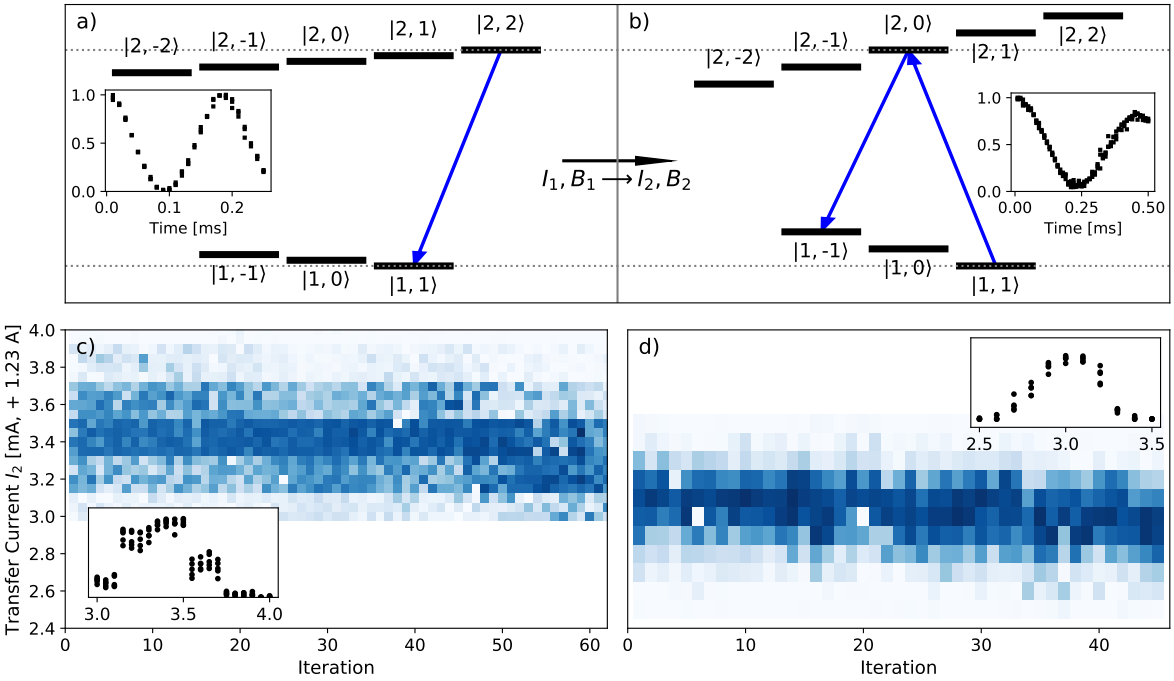

Figure 3.4: Illustration of the "Λ-scheme" used for the spin preparation. **a)** The first RF pulse transfers the atoms from the magnetically trapped $|2,2\rangle$ state to the $|1,1\rangle$ state. The inset shows the $|2,2\rangle$-population for different transfer pulse times. **b)** The magnetic field is then increased such that the same radio-frequency is now resonant for the $|1,1\rangle \rightarrow |2,0\rangle$ transition. Directly after this pulse, the atoms are transferred to $|1,-1\rangle$, i.e. the desired final state, thus closing the second leg of the Λ-scheme. The advantage of this approach is that the spin changing collisions for $m_F = 0$ are avoided by reducing the time staying in such a state. The inset shows the $|2,0\rangle$-population for different $|2,0\rangle \leftrightarrow |1,-1\rangle$ transfer pulse times. As both $|2,2\rangle$ and $|1,1\rangle$ are spin-protected, their lifetime is long and allows us to ramp the magnetic field appropriately. **c)** Spectrum obtained for the second transfer current I_2 (y-axis) over several hours (x-axis). The obtained signal is color coded and the adjustment needs to be precise to ∼0.1 mA. As a 16-bit analog channel is used to control the current through the coils, the 10 V output range is quantized in 10 V / $2^{16} \simeq 0.15$ mV steps, clearly visible in the spectrum. This problem was solved by adding a voltage divider between analog output and power supply, therefore effectively halving the quantization steps, as can be seen in **d)**. Since the exact resonance position drifts over the course of several hours, we have a script running that measures a reduced version of the spectrum every few hours, extracts the center position of the resonance, and readjusts the current settings. The shown y-range of 1.6 mA corresponds to ∼8 mG field shift, and therefore to ∼6 kHz detuning shift of the relevant transitions.

$|2,+2\rangle$ to $|1,+1\rangle$ ($\Omega_{Rabi} \simeq 2\pi \cdot 5.3$ kHz), we use one pulse to transfer the atoms to $|2,0\rangle$ and immediately after to the $|1,-1\rangle$, each with $\Omega_{Rabi} \simeq 2\pi \cdot 2.2$ kHz. While this leads to some atom losses due to hyperfine-changing collisions, it still performs better than a pulsed transfer over the $|1,0\rangle$, which we attribute to the higher Rabi-frequency due to the larger difference in m_J.

The spin transfer only works well when both the magnetic field and radio-frequency match each other. As it was slightly more convenient in our machine, we chose to adjust the current instead of the radio-frequency. Fig. 3.4(c) shows a timeline of measurements

over ∼12 hours with the signal observed after the second π-pulse. One can clearly observe plateaus due to the quantization of the 16 bit digital-to-analog output[3] with a resolution of 10 V/2^{16} ≃ 153 µV. As the power supply[4] only accepts control voltages of 0-5 V, the analog output was reduced by a voltage divider, effectively doubling the current resolution. This resulted in the data shown in Fig. 3.4(d), where the resolution is fine enough to track the position. The required current stability of $\sim 10^{-4}$ is close to typical performances of commercially readily available power supplies. Choosing a suitable model (i.e. reasonable low maximum current, and hence a smaller absolute variation) together with synchronizing the experimental cycle with the electricity grid's 50 Hz cycle was sufficient to obtain the required short-term stability. To compensate for the slow drift visible in Fig. 3.4(c), (d) and between the two, we take a spectrum for both fields B_1 and B_2 of the transfers every couple hours, and the center position is extracted. These extracted centers are then used in the actual subsequent experiment runs until they are updated again.

The main origin of these drifts has not been investigated in too much detail, but we suspect the drift of the Earth's magnetic field to be the main contribution: the typical drift in the absolute value of the magnetic field within a day and at a fixed position is on the order of few $\cdot 10^{-8}$ T = few $\cdot 10^{-1}$ mG [160], so somewhat less than the typical drifts of ∼0.5-1 mG we sometimes observed within a day. A similar or slightly larger contribution originates in the variation of the magnetic field angle, which is on the order of 0.1° within a day and at fixed position [161, 162]. Due to the vector addition of offset field and Earth's magnetic field, the total field will therefore also vary even if the magnitude was constant. For a typical vertical quantization field $B_{coil} \approx 5$ G and with the inclination angle θ of 68° 38' in Hamburg, Germany (measured to the horizontal plane) [163], the total field roughly is

$$B_T \simeq \sqrt{B_{coil}^2 + B_{earth}^2 + 2B_{coil}B_{earth}\sin(\theta)} \simeq B_{coil}\left[1 + \sin(\theta)\frac{B_{earth}}{B_{coil}}\right], \tag{3.13}$$

where $B_{earth} \simeq 0.5$ G. The variation introduced by a varying angle is then $\Delta B_T \simeq B_{earth}\cos(68)\Delta\theta \simeq 0.3$ mG. While a definitive proof should show the correlation with externally measured changes in total field strength and inclination angle, we conclude that the typical variations in Earth magnetic field are large enough to account for a significant fraction of the observed variation.

Once transferred to the required spin state, the magnetic field is rapidly ramped up to fields near the Feshbach resonance at 561 G, where the evaporation is performed.

[3] National Instruments: PXIe 6738, 32 channels, 16 bit resolution, ±10 V output range.
[4] Statron 3240.2, U_{out} = 0-16 V, I_{out} = 0-6.4 A

The evaporation happens in two different optical traps - while the initial evaporation is performed in the deep YAG trap, we continuously ramp up a pair of perpendicular $\lambda = 850$ nm beams, both located within the imaging plane of the microscopes, and with waists of 30 µm and 32 µm, respectively. The cold atoms accumulate in the intersecting region of the YAG and the two 850 beams; once the YAG evaporation has progressed far enough, it is switched off and the evaporation is continued in the 850 trap only. The intersection of these two beams causes a tighter confinement and therefore a higher scattering rate, leading to more efficient evaporation compared to the single YAG trap with the axial confinement determined by its Rayleigh length of ∼600-800 µm. Finally, we obtain a BEC with ∼5000 atoms in a harmonic potential with trapping frequencies of 220, 230, and 320 Hz and a temperature of $T \lesssim 0.2T_c$.

3D to 2D The degenerate cloud is a three-dimensional system and still has to be transformed into an effectively two-dimensional system. This can be achieved by freezing out one spatial degree of freedom, i.e. by adding a tight confinement along one axis, such that the system does not have enough energy to be in any state but the ground state for this axis. Specifically, the temperature and the chemical potential have to be much smaller than the trapping frequency of the tight axis; for fermionic systems, the Fermi energy would also become relevant.

We create this effectively two-dimensional system by using a repulsive optical lattice along the vertical direction, effectively restricting any motion to the x-y plane. This repulsive lattice is formed by two laser beams with $\lambda = 532$ nm and $P \simeq 290$ mW per beam, interfering at an angle of $2 \cdot 5°$. With horizontal waists of 267 µm and 268 µm, and vertical waists of 21.0 µm and 21.5 µm, the resulting optical potential has a lattice constant of 3.05 µm and a trapping frequency of $\omega = 2\pi \cdot 6.5$ kHz

The transfer between the three-dimensional and the two-dimensional setup is achieved by using a "squeeze beam". This is a red detuned, highly elliptical laser beam which squeezes the condensate into a pancake-like form and allows to load it into a single layer of the vertical lattice. By using a piezo-controlled mirror in its setup, it furthermore allows to adjust the vertical position of the condensate, such that the transfer to the green lattice causes as little heating as possible. With a horizontal waist of 372 µm and a vertical waist of 11.8 µm, its aspect ratio is ∼1:30, and therefore provides a strong vertical, but only minimal radial confinement. For the transfer, the squeeze power is ramped up to its full power of 480 mW within 100 ms, while the 850 power is reduced to ∼2% of its maximal value, resulting in a trapping frequency ratio of $\nu_z/\nu_r \simeq 7 - 10$. The 100 ms are much longer than the timescale set by the radial trapping frequency with $1/\nu_r \approx 7 - 10$ ms. As

the vertical confinement is dominated by the squeeze beam at this stage, the condensate's vertical position is also determined by the squeeze position, allowing to position the cloud at the correct position with respect to the green lattice.

After reshaping the atomic cloud into this elliptical shape, the squeeze power is ramped down again within 100 ms, and the green lattice power is increased at the same pace. After these two transfers, the vertical confinement is provided by the green lattice, the harmonic radial confinement is provided by the 850 beams, and the squeeze is turned off again.

Imaging Imaging is usually performed along the vertical axis through the microscopes, as this provides the largest numerical aperture and allows us to extract spatially resolved information. The relevant fields and imaging beam properties are discussed in Sec. 3.3.3; here we briefly describe the optical system. The in-vacuo microscope has a high NA of 0.75, which allows for a high spatial resolution of $\delta x \simeq 620$ nm at $\lambda = 767$ nm. In order to take advantage of this resolution by matching it to the camera's pixel size, we employ two telescopes with individual magnifications of M = 50 and M = 0.3, providing a combined magnification of M = 15. The first of these telescopes consists of the microscope with f = 20 mm and a 2" lens with f = 1000 mm, where the large focal length was chosen to allow for a larger working distance and better optical access [25]. The second telescope consists of two achromatic lenses with f = 500 mm and f = 150 mm, respectively; the latter is mounted on a z-stage[5], which allows fine adjustment of the image plane onto the camera chip. The camera used is an Andor Zyla 5.5 with a sCMOS chip and a pixel size of 6.5 µm [164]. With the magnification of M = 15, the effective pixel size in the imaging plane is therefore 433 nm. The choice of imaging transition is discussed further below.

Radio-Frequency Transfers As already mentioned above, radio-frequency transfers are essential for the system preparation. The transfers involved in the Λ-transfer are at frequencies $f \simeq 459$ MHz and $f \simeq 465$ MHz, i.e. near the hyperfine splitting of the F=1 and F=2 ground states. For this transfer, high Rabi rates are essential to reduce the observed atom losses when populating the $|F = 2, m_F = 0\rangle$-state. The second transfer range is around 119.5±0.1 MHz and is used to flip atoms from the bath state to the impurity state. For this transfer, the optimal Rabi rate is less clear - a fast transfer can allow for the investigation of early dynamics, like the polaron formation dynamics similar to what has been achieved in 3D systems in [98] or initial acceleration within the effective potential. On the other hand, short pulse times reduce the spectral resolution due to Fourier broadening; furthermore, the contribution of excited polaron states might

[5]Thorlabs, SM1Z - z-Axis Translation Mount

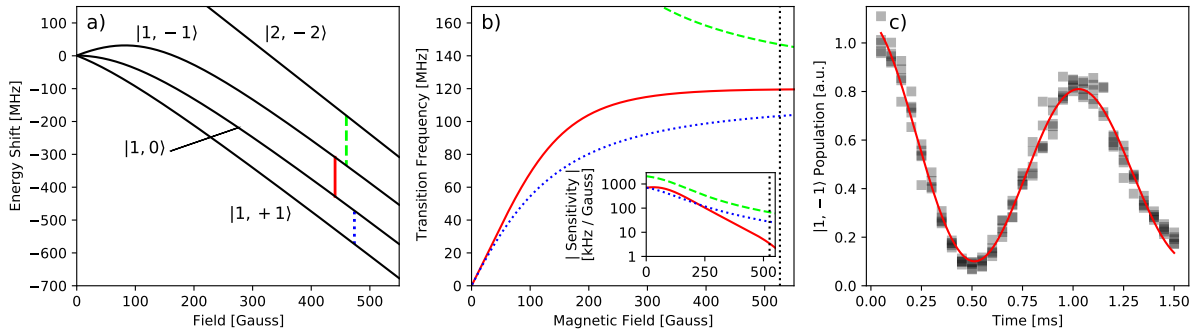

Figure 3.5: Radio-frequency spin transfer to create impurities. **a)** Relevant part of the level scheme, showing the F = 1 states and the F = 2, m_F = -2 state, i.e. states containing large contributions of m_J = -1/2. **b)** Transition frequencies of the $|1,+1\rangle \leftrightarrow |1,0\rangle$ transition (dotted blue line), the $|1,0\rangle \leftrightarrow |1,-1\rangle$ transition (solid red line), and the $|1,-1\rangle \leftrightarrow |2,-2\rangle$ transition (dashed green line). The red line corresponds to the bath-impurity transition. The inset shows the variation of the transition frequencies with the magnetic field, indicating that the required magnetic field stability is on the order of $\lesssim$0.1 Gauss for the bath-impurity transition, and ∼0.01 Gauss for the other two transitions, corresponding to relative stabilities of $\Delta B/B \simeq 10^{-4}$ and $\simeq 10^{-5}$, respectively. **c)** Experimental data showing the $|1,-1\rangle \leftrightarrow |1,0\rangle$ Rabi transfer in a cold cloud sightly above the condensation threshold, resulting in a Rabi frequency of $\Omega_R/(2\pi) = (0.935 \pm 0.007)$ kHz. The visible damping is most likely caused by scattering due to the scattering length of $a \simeq 125a_0$ at the given field.

be more relevant as the transfer becomes less adiabatic.

From a technical side, the achievable Rabi rates in our setup are limited by the large steel vacuum chamber. The frequencies of ∼120 MHz and ∼460 MHz correspond to wavelengths of ∼2.5 m and ∼0.6 m, respectively, and are much larger than the vacuum windows with ∼0.15 m diameter. The chamber hence acts as a Faraday cage, significantly reducing the obtainable effect at the location of the cold atoms. Therefore, a single-loop coil inside the vacuum chamber, about 4 cm from the atoms, is being used as an RF antenna. The coil is orientated such that the created magnetic field is perpendicular to the quantization axis; since the spin flip interaction term is $\propto \vec{\mu} \times \vec{B}$ [165], this leads to the maximal effect when starting in the m_F = -1 state. The technical challenge in this context is mostly the resonance matching: as the connection line and the feed-through lead to additional effective coils, one can have resonances in different parts of the setup. Therefore, we cannot only rely on reflection minima as a measure to determine and optimize the matching circuit. The alternative way of measuring the emitted power with a pick-up coil and determining the resonance positions from this is also barely possible due to the shielding by the vacuum chamber (i.e. the Faraday cage formed by it). One therefore has to rely on the somewhat tedious approach of verifying the resonances with the atoms themselves.

While using the same antenna and amplifier, two high-power switches[6] were used to switch between different matching circuits; one for the transfers at ∼460 MHz, and one centered at 119 MHz.

Details about the procedure to obtain the final Rabi frequencies are documented in [28]; eventually, we achieved $\Omega_R \simeq 2\pi \cdot 5.3$ kHz for the $|2,2\rangle \rightarrow |1,1\rangle$-transfer, and $\Omega \simeq 2\pi \cdot 2.2$ kHz for the $|1,1\rangle \rightarrow |2,0\rangle$- and $|2,0\rangle \rightarrow |1,-1\rangle$-transfers, while the $|1,-1\rangle \rightarrow |1,0\rangle$-transfer at high field showed $\Omega_R \simeq 2\pi \cdot 1$ kHz, as is shown in Fig. 3.5. This enables a frequency resolution of ∼1 kHz, and allows for pulse times on the order of $\lesssim 1$ ms, which is sufficient for our purposes.

3.3.3 High Field Imaging

All of the information we extract from the prepared system is obtained from absorption imaging. Therefore, selecting a suitable imaging transition is essential, and in order to do so, one first needs to decide on convenient Feshbach resonances and hence a magnetic field region to work in.

Feshbach Resonance Selection As mentioned in 3.3.1, ^{39}K atoms exhibit plenty of different intrastate and interstate Feshbach resonances, but not all of those are equally convenient to use for our purposes. The general dependence of the scattering length a on the magnetic field B near an isolated Feshbach resonance can be stated as

$$a(B) = a_{BG}\left(1 - \frac{\Delta}{B - B_{res}}\right), \tag{3.14}$$

where a_{BG} is the background scattering length, i.e. the scattering length reached far from resonance, Δ is the width of the resonance, and B_{res} is the position of the resonance [24]. It is straightforward to show that the scattering length has a zero crossing at $B_{zero} = B_{res} + \Delta$, i.e. $a(B_{zero}) = 0$ and the scattering length changes its sign when crossing this field, thus switching between repulsive and attractive interactions. For our scheme, one intrastate Feshbach resonance is needed for the evaporation to degeneracy, and one interstate Feshbach resonance is needed to control the interaction between the bath and the impurity atoms.

For the evaporation, one needs to be on the repulsive side of the respective Feshbach resonance, and has to be able to control the scattering length to reasonable precision. It is convenient to use a rather broad Feshbach resonance, as any noise on the magnetic

[6] Teledyne Relays: Coaxial Switches SP6T 28V SMA, CCR 38S16O

field only leads to a small variation in the scattering length and therefore allows a more stable evaporation process. In addition, broad Feshbach resonances lead to lower three-body losses compared to narrow resonances [27]. Typical convenient Feshbach resonance widths Δ are on the order of a few ten Gauss.

The same stability argument applies to the interstate Feshbach resonance, which should also be reasonably wide. Furthermore, the resonance's location must be located on the repulsive side of the intrastate resonance, and should allow for enough tuning range while keeping the intrastate scattering length within a reasonable range. Specifically, the zero crossing of the intrastate resonance has to be avoided, as the degenerate cloud becomes unstable for large enough attractive interactions. Additionally, approaching the intrastate resonance must be avoided as an increasing scattering rate will inevitably lead to more three-body losses.

Two combinations were considered in more detail: at intermediate fields of ∼100 Gauss, one has a suitable intrastate resonance for $|1,-1\rangle$ atoms located at $B_{res} \simeq 162$ G with $\Delta \simeq -61$ G, and an interstate resonance for the $|1,-1\rangle + |1,0\rangle$ combination at $B_{res} \simeq 114$ G with $\Delta \simeq -19$ G. Additionally, there is another intrastate $|1,-1\rangle$ Feshbach resonance located at $B_{res} \simeq 33.6$ G with $\Delta \simeq 79.5$ G. This resonance has, unlike most other resonance for ^{39}K, a positive Δ, and hence attractive interactions at fields below, and repulsive interactions at fields above the resonance. The combination of these two intrastate resonances leads to the absence of the usual zero crossing, and to repulsive interactions for the whole range between the two resonances at $B \simeq 33.6$ G and $B \simeq 162$ G. Alternatively, there is a suitable combination at high fields of ∼500 Gauss: a $|1,-1\rangle$ intrastate resonance with $B_{res} \simeq 561$ G and $\Delta \simeq -55$ G and a $|1,-1\rangle + |1,0\rangle$ interstate resonance with $B_{res} \simeq 526$ G and $\Delta \simeq 28$ G.

While both of these combinations fulfill the requirements stated above, and the avoidance of the zero crossing at the lower field combination is convenient, it is more advantageous to choose the high field combination as it is further within the Paschen-Back regime. This has two main effects: the first being a lower sensitivity of the $|1,-1\rangle \leftrightarrow |1,0\rangle$ radio-frequency transition to magnetic field noise, as the energies of both states in this regime tune very similarly with the magnetic field. The second advantage is that the imaging is more convenient at higher fields compared to the fields around 100 G, where the transition between the Zeeman- and the Paschen-Back regime occurs. In this intermediate regime, one does not have a closed transition for imaging, and therefore one would need a second laser to repump atoms from dark states. However, unlike at low fields ($\lesssim 10$ G), where the existing MOT cooler and repumper laser are readily available to be tuned to the transition, the absolute frequencies at this intermediate regime are detuned far enough to

require a more dedicated setup.

Imaging Transition Selection In the high fields of ∼500 G the possible transitions between the electronic ground state and the excited states have split up and have significantly different transition frequencies, i.e. their differences are usually well outside the available offsetlock tuning ranges. Just scanning over all possible transitions and selecting the best performing one is therefore not possible. Instead, a suitable imaging transitions and the respective frequency shifts have to be determined beforehand and will here be discussed in more detail.

At low fields, the nuclear spin I and the total angular momentum of the electrons J couple to form the total angular momentum $F = |I \pm J|$. The magnetic quantum number m_F can then take all values of $m_F = -F... + F$ in integer steps. At higher fields, this Zeeman regime breaks down and the Paschen-Back regime is entered, which is illustrated in Fig. 3.6 top left: instead of the electronic angular momentum and the nuclear spin pairing up to a total angular momentum, which then interacts with the external field, the two components align independently with the external magnetic field as the interaction terms $\mathbf{I} \cdot \mathbf{B}$ and $\mathbf{J} \cdot \mathbf{B}$ dominate over the $\mathbf{I} \cdot \mathbf{J}$-term. In this regime, F and m_F cease to be good quantum numbers, and instead m_I and m_J become relevant. While we usually ignore this and refer to the states by the F and m_F quantum number they are continuously connected to, it has relevant consequences for the possible imaging transitions as changes in m_I become suppressed at high fields.

Following the framework in [157], we numerically determine the compositions of the relevant states in the $|m_I, m_J\rangle$ basis for the fields of interest and from this determine the allowed transitions and the needed frequency shifts with respect to the zero-field values. For $B \approx 520$ G, one obtains

$$|F = 1, m_F = -1\rangle \simeq \sqrt{0.975}|-1/2, -1/2\rangle + e^{i\theta_1}\sqrt{0.025}|-3/2, +1/2\rangle, \tag{3.15}$$

which is also illustrated for variable field in Fig. 3.6 bottom left, and

$$|F = 1, m_F = 0\rangle \simeq \sqrt{0.977}|+1/2, -1/2\rangle + e^{i\theta_2}\sqrt{0.023}|-1/2, +1/2\rangle \tag{3.16}$$

where $\theta_{1,2}$ are phases which are not relevant here and the right hand side states are expressed in the $|m_I, m_J\rangle$ basis. Dipole selection rules at high fields state that transitions are only allowed for $\Delta m_I = 0$ and $\Delta m_J = 0, \pm 1$. In the existing setup, one additionally has the constraint that the imaging axis through the microscope is parallel to the magnetic field direction. Thus, it is not possible to have any (sizable) π-polarization component

in the imaging beam; the imaging beam will always be σ^+-polarized, σ^--polarized, or a linear combination of these two. The only relevant transitions are then with $\Delta m_I = 0$ and $\Delta m_J = \pm 1$.

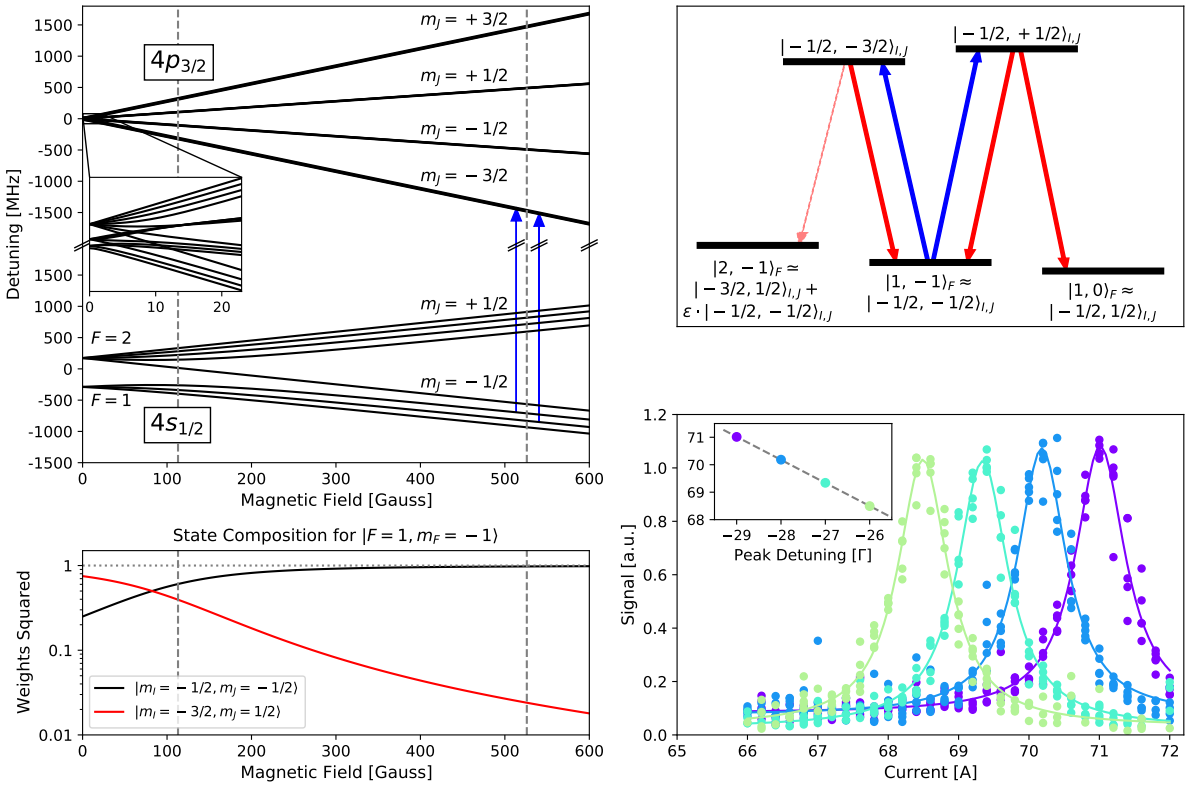

Figure 3.6: Illustrations of different aspects of the high field imaging. **Top left:** level structure of the $4s_{1/2}$ ground state and the $4p_{3/2}$ excited state for different magnetic fields. For $4s_{1/2}$, the transition from the Zeeman regime to the Paschen-Back regime occurs at ∼100 G, while for $4p_{3/2}$ the transition already happens at ∼5 G. The two vertical dashed lines indicate the relevant interstate Feshbach resonances discussed in the main text. The left one is located in the transition region between Zeeman-regime and Paschen-Back regime for the ground state, while the right one is deep in the high-field regime. For both resonances, the excited state is deep in the Paschen-Back regime. The two blue vertical arrows indicate the imaging transitions for the bath state and the impurity state, as discussed in the main text. **Bottom left:** State composition of the bath state. At low fields, the state has significant contributions from both the $|m_I = -1/2, m_J = -1/2\rangle$ state and the $|m_I = -3/2, m_J = +1/2\rangle$ state with weights of $\sim \sqrt{0.3}$ and $\sim \sqrt{0.7}$, respectively. At high fields, the state continuously approaches a pure $|m_I = -1/2, m_J = -1/2\rangle$. At the higher relevant Feshbach resonance, the remaining contribution from $|m_I = -3/2, m_J = +1/2\rangle$ is $\sim 2 - 3\%$. **Top right:** Decay channels for different final states for the bath imaging. Allowed final states with significant overlap are the $|-1/2, -3/2\rangle$ state and the $|-1/2, +1/2\rangle$ state. The latter decays to two different states in the ground state, each with similar probability. The $|-1/2, -3/2\rangle$, on the other hand, only has ∼1% chance to decay to a different state than the atoms started from, and the imaging transition is almost closed. **Bottom right:** Calibration data. As the curves of the states' energies are almost linear, the detuning needed for the imaging is almost perfectly linear in the current. This allows to calibrate the detuning needed for an applied current, and thus an automatic tuning to the correct imaging detuning.

As the dominant component of the $|F = 1, m_F = -1\rangle$ state is the $|m_I = -1/2, m_J = -1/2\rangle$, the two most relevant final states in the $4p_{3/2}$-manifold are the third-lowest state, consisting mostly of $|m_I = -1/2, m_J = -3/2\rangle$, and the tenth-lowest state, predominantly consisting of $|m_I = -1/2, m_J = +1/2\rangle$. Both final states have additional admixtures with weights of $\approx \sqrt{10^{-4}}$; the latter one, for example, from $|m_I = +1/2, m_J = -1/2\rangle$.

From the two possible final states, the suitable one can be selected by considering the final states these can decay to: the first state has $m_J = -3/2$, while the second state has $m_J = +1/2$. As the decay can have $\Delta m_J = 0, \pm 1$, the final state may have $m_J = -5/2, -3/2, -1/2$ in the first case, and $m_J = -1/2, +1/2, +3/2$ in the second case. As the electronic ground state has $J = 1/2$, there are no states available with $m_J = -5/2$ or $m_J = \pm 3/2$, and thus the third lowest state can only decay to a state containing $|m_I = -1/2, m_J = -1/2\rangle$, while the tenth-lowest state can decay to states containing either $|m_I = -1/2, m_J = -1/2\rangle$ or $|m_I = -1/2, m_J = +1/2\rangle$. The latter case has two relevant decay channels, and is therefore not well-suited for imaging, while the former has an almost-closed imaging transition. It is then preferable to apply σ^--polarized light and transfer the atoms from $|F = 1, m_F = -1\rangle \approx |m_I = -1/2, m_J = -1/2\rangle$ to the state mostly consisting of $|m_I = -1/2, m_J = -3/2\rangle$.

A similar discussion applies for the $|F = 1, m_F = 0\rangle$-state, which will be used as the impurity state. A suitable final state for imaging is the second lowest state in the $4p_{3/2}$-manifold, mostly consisting of $|m_I = +1/2, m_J = -3/2\rangle$. The imaging of both states thus requires the same imaging light polarization.

Loss Channels When applying the above scheme, three different loss channels are present. The first one originates in off-resonant excitations to other states: due to the large energy differences between different states this is usually energetically suppressed and, at the fields discussed here, usually leads to a loss probability of $< 0.1\%$. The second loss channel is decay from the minor component of the final state: as the final state has admixtures with other m_I-values, the final state after the subsequent decay does not necessarily have the same m_I as the initial state. A rough estimate for the strength of this effect is the square of admixture weight in the excited state, and is usually around 10^{-4}. Finally, the third and strongest loss channel is the decay back to the initial m_I, m_J-combination, but within a different $|F, m_F\rangle$-state as is indicated by the thin decay line in Fig. 3.6, top left: for simplicity, let us assume the atoms start in the $|F = 1, m_F = -1\rangle$-state with the m_I, m_J combination stated above, get excited, and then decay back to the $|m_I = -1/2, m_J = -1/2\rangle$-state. The $|F = 1, m_F = -1\rangle$-state has a small admixture of $|m_I = -3/2, m_J = +1/2\rangle$; similarly, other states can have a small admixture of the

$|m_I = -1/2, m_J = -1/2\rangle$-state the atoms decay to. In this case, the state connected to $|F = 2, m_F = -2\rangle$ has about $\sqrt{0.025}$ weight of this component, and while an exact calculation requires a more careful treatment, the weights already indicate that this non-closed part of the transition is on the order of a few percent. Using this imaging transition should hence create sufficient signal even without an additional repumping beam. For the extraction of atom numbers, however, the loss probability and therefore increasing transparency during the imaging process has to be taken into account.

Frequency Detunings The next parameter to determine is the frequency detuning needed for the imaging transitions. In the Paschen-Back regime, the energy of an individual state mostly depends on m_J, and one roughly has $\Delta E \propto m_J \cdot B$. As the final state of the imaging has a larger $|m_J|$, the tuning of the upper state is stronger than the tuning of the ground state: while the energy of the lower state increases with increasing magnetic field, the final state's energy decreases even faster. The energy difference between the two relevant states therefore reduces with increasing field. For the bath imaging, i.e. imaging of the state connected to the $|F = 1, m_F = -1\rangle$ state, and a field of $B \simeq 520$ G, this energy difference corresponds to a frequency detuning of $\Delta f = \Delta E/h \approx -960$ MHz with respect to the zero field transition from the $|4s_{1/2}, F = 1\rangle$ to the $4p_{3/2}$-manifold, i.e. the "repumper" transition. Similarly, the impurity imaging, i.e. imaging of the state connected to $|F = 1, m_F = 0\rangle$, requires a detuning of ≈ -850 MHz, and thus one has ≈ 110 MHz $\simeq 18.3\,\Gamma$ relative difference for the two imaging transitions.

Although the relevant states are connected to states usually addressed by the "repumper" laser, the large negative detuning required makes it more convenient to use the "cooler" laser for the imaging, as it is red detuned by $\Delta E_{HFS} \simeq -461.7$ MHz from the repump transition, which reduces the needed additional detuning by about 50%. Taking into account the fact that the "cooler" laser is not running directly at resonance, but is redshifted to the resonance by an AOM, the bath imaging requires an additional detuning of ∼-410 MHz, and the impurity imaging ∼-300 MHz. As each of those frequency shifts can easily be covered by a single path AOM, we set up two independent imaging paths with one AOM and mechanical shutter each, and then combine both beams by a non-polarizing beam splitter cube before coupling them into an optical fiber guiding it to the experimental setup. For both paths we use an AOM with the a resonance frequency of 350 MHz and a bandwidth of 50 MHz[7]; while both 300 and 410 MHz are already more than the bandwidth from the center frequency, the power requirements for the imaging are very low, and the low efficiency is of no concern. Compared to a single AOM setup,

[7] Gooch&Housego, 3350-125

this two-path setup allows a more flexible application of the individual imagings, for example for imaging of both components with minimal time delay. Furthermore, the large difference between the two AOM frequencies avoids having to drive the offsetlock to large detunings, which can sometimes lead to instabilities.

Intermediate Fields For completeness, we also briefly discuss the case of the intermediate field region around 100 G and outline the main challenges. For simplicity, we only discuss the bath imaging; similar conclusions apply for the impurity imaging. At 114 G, the initial state is

$$|F=1, m_F=-1\rangle \simeq \sqrt{0.61}|-1/2,-1/2\rangle + e^{i\theta_1}\sqrt{0.39}|-3/2,+1/2\rangle. \tag{3.17}$$

At this field, the states in the $4p_{3/2}$-manifold are typically pure except some $\sim \sqrt{0.5}\%$ admixture, leading to about two orders of magnitude more losses than at the high field discussed above. Compared to the high field composition, the initial state has a much higher admixture of some 20-30 %, compared to ∼2 % for $B \approx 500$ G. When applying σ^+-light and tuning the laser frequency to the correct value, one can transfer atoms to a the final state mostly consisting of $|-3/2,+3/2\rangle$. Due to the selection rules and the available values of m_J in the ground state, this state can only decay to the $|-3/2,+1/2\rangle$ state. Significant contributions of this are present in the initial state connected to the $|F=1, m_F=-1\rangle$, and in the state connected to the $|F=2, m_F=-2\rangle$:

$$|F=2, m_F=-2\rangle \simeq \sqrt{0.39}|-1/2,-1/2\rangle + e^{i\theta_1}\sqrt{0.61}|-3/2,+1/2\rangle. \tag{3.18}$$

Note that this state has the same components as the one above, just with the weights switched. About half of the decays will end in this state, preventing a single beam imaging as it is possible at high fields. Instead, one would need a second imaging beam, detuned by ∼50 MHz. For imaging both the bath and the impurity state in a flexible manner, a total of four beam would then be necessary. While possible, the intermediate field regime therefore adds more complexity and makes imaging close to the high field Feshbach resonances simpler to implement.

3.3.4 Field Calibration

In order to extract the unshifted transition frequencies, we have to calibrate the magnetic field near the relevant $|1,-1\rangle+|1,0\rangle$ interstate Feshbach resonance at 526 Gauss, which we do by spectroscopic measurements. To reduce interaction effects, we here work with a

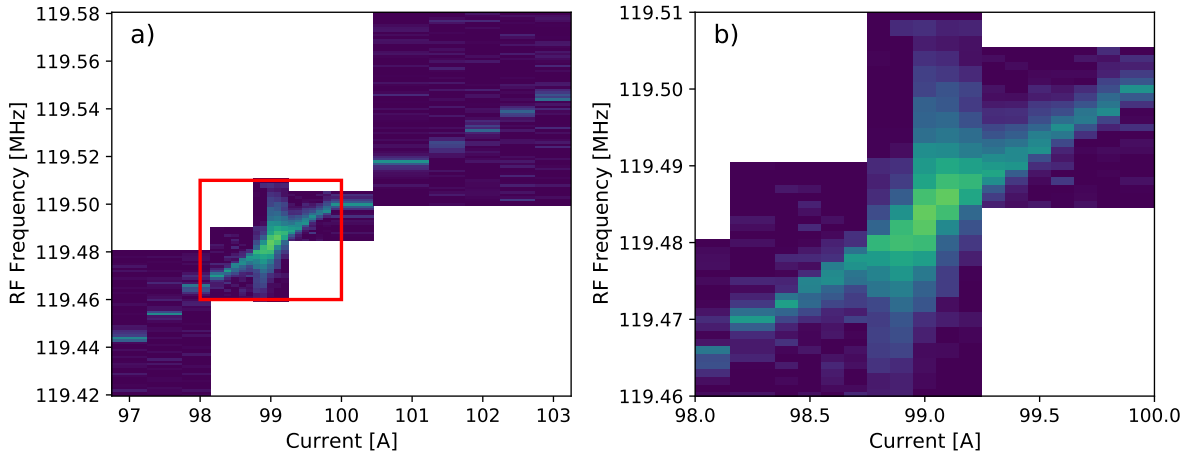

Figure 3.7: **a)** Loss signal over a range of coil currents. **b)** Close-up of the central region. The Feshbach resonance between the $|1,-1\rangle$ bath state and the $|1,0\rangle$ impurity state is clearly visible around 99.0 A by the broadening of the loss signal. The asymmetry in the loss signal is due to the mean field shift becoming relevant at large scattering lengths, and thus introducing shifts in opposite directions for repulsive and attractive interactions.

thermal gas slightly above the condensation threshold.

With a radio-frequency pulse, we transfer atoms from the $|1,-1\rangle$ state to the $|1,0\rangle$ state, let the cloud settle for 10 ms, switch off the trap and then measure the remaining population in the $|1,-1\rangle$ state after 1.8 ms of time-of-flight. The radio-frequency pulse is switched on at full power for 3 ms, leading to a Fourier broadening of $\sim$300 Hz. Since we expect the Feshbach resonance to be located at 526.21 Gauss, i.e. $\sim$99.0 A, we measure the transition frequency at different currents between 97.0 A and 103.0 A, corresponding to $\sim$515 Gauss and $\sim$547 Gauss, respectively. These limits avoid the zero crossing of the bath-state scattering length (located at 506.2 Gauss $\simeq$ 95.5 A) and the Feshbach resonance of the bath state, located at 561.4 Gauss $\simeq$ 105.6 A.

Fig. 3.7 shows the atom loss signal of these reference runs. The Feshbach resonance is clearly visible by the broadening of the loss signal. We attribute the broadening to a combination of two effects, one leading to symmetric broadening and one leading to an asymmetric broadening. The symmetric contribution is collisional broadening, where the increased collision rate due to the larger scattering length leads to faster decoherence of the transfer pulse, and the asymmetric contribution is due to the remaining mean field shift in the trap. As we observe the total signal from the trap, we integrate over different densities and different magnitudes of the mean field shift. While the magnitude varies, the sign of the mean field shift is, for a fixed field, always the same, and leads to an asymmetric broadening. With the present level scheme as sketched in Fig. 3.8(a), this asymmetric broadening shifts the transition to lower frequencies for repulsive interactions

(currents below the interstate Feshbach resonance at $\simeq$ 99.0 A), and shifts the transition frequencies to higher values for attractive interactions at currents above $\simeq$ 99.0 A. From the spectrum at each current, we extract the position of maximum transfer by fitting a Gaussian line shape to the extracted remaining population.

To extract the relationship between current and actual field at the position of the atoms, we fit the measured transition frequencies with the theoretical expectation, where the tuning of the field with the current is the only free parameter. The ground state manifold of ^{39}K has its transition between the Zeeman regime and the Paschen-Back regime at magnetic fields of $\sim$50-100 G, such that F and m_F are not a good basis anymore when operating at $\sim$500 G. For convenience, we nevertheless still label our states with the F and m_F quantum numbers of the state that continuously connects to the state of interest.

The theoretical model follows Eq. 32 in [166] with the values for experimentally determined parameters like A_{hfs} taken from [157]. The hyperfine Hamiltonian can be expressed as

$$H_{hfs} = A_{hfs}\mathbf{I}\cdot\mathbf{J} + B_{hfs}\frac{3(\mathbf{I}\cdot\mathbf{J})^2 + \frac{3}{2}\mathbf{I}\cdot\mathbf{J} - \mathbf{I}^2\cdot\mathbf{J}^2}{2I(2I-1)J(2J-1)} + \frac{\mu_B}{\hbar}(g_J m_J + g_I m_I)B, \tag{3.19}$$

where $\mathbf{I}$ and $\mathbf{J}$ denote the nuclear spin and the electronic angular momentum (including in general both spin and orbital angular momentum), respectively, and m_I and m_J are their respective magnetic quantum numbers. For ^{39}K, one has $|\mathbf{I}| = 3/2$. A_{hfs} and B_{hfs} are parameters that have to be determined experimentally, g_J and g_I are the electronic and nuclear g-factors, and B is the magnitude of the external magnetic field. The first term describes the interaction between the magnetic field created by the electron and the nuclear spin's magnetic moment, the second term incorporates the electric quadrupole interaction between nucleus and electron, and the third term is the interaction of the electronic and nuclear spin with the external magnetic field. As we are here only concerned with the ground state manifold, we have $|\mathbf{J}| = 1/2$, and the quadrupole interaction term vanishes. We implement this calculation employing the matrix element expressions provided originally in [167]. Note that Eq. 3.19 has the correct expression (2J-1) in the denominator of the quadropule term, where the factor of 2 was missing in [166]. Furthermore, the diagonal matrix element stated in Eq. 50 in [166] incorrectly states a factor of 3/2 in front of the m_I^2 term, where the correct factor is 3.

The resulting Hamiltonian is then numerically diagonalized, and the transition frequency between the relevant states at a given field can be extracted. In order to reduce the effect of the remaining mean field shift, we exclude the measurements closest to the

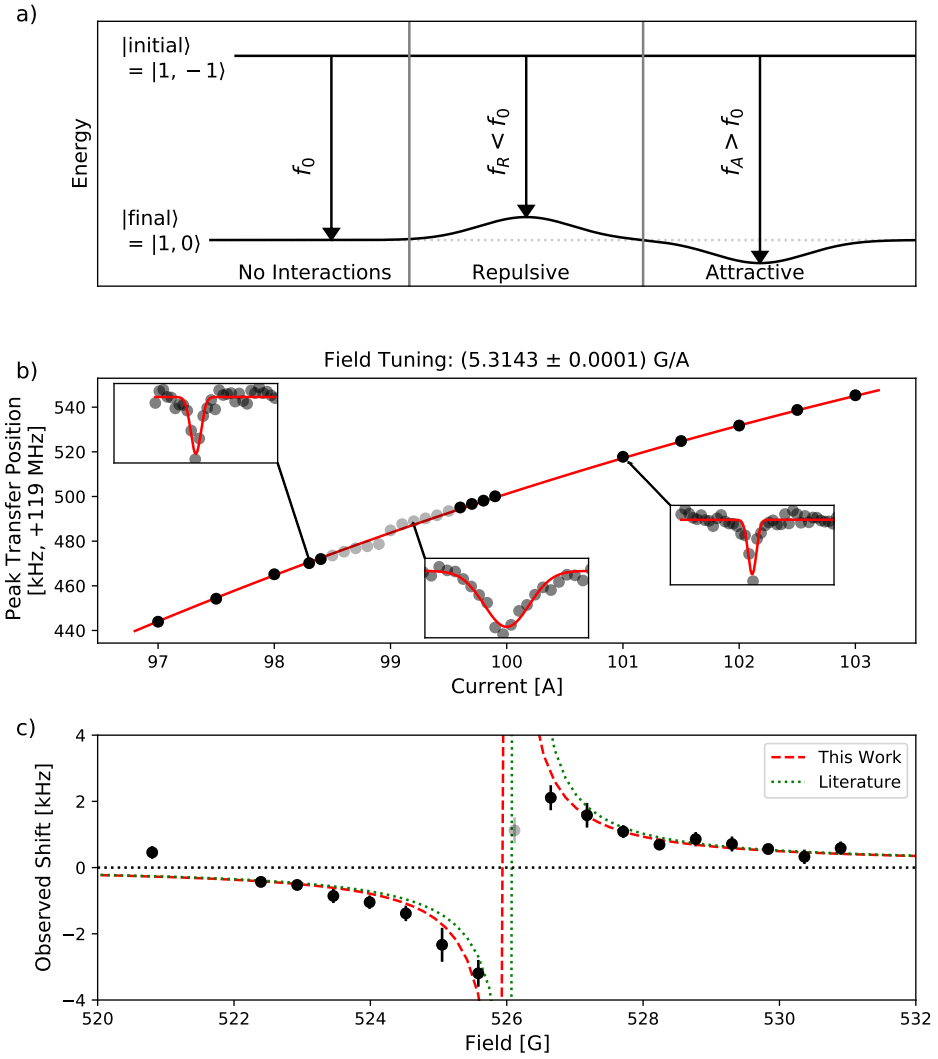

Figure 3.8: **a)** Sketch of the relevant part of the level structure. The initial state $|1, -1\rangle$ has a higher energy than the final impurity state $|1, 0\rangle$. For repulsive interactions, the energy of the impurity state is raised and the transition frequency decreases. For attractive interactions, the transition frequency correspondingly decreases. **b)** Extracted center positions (black data points) and resulting fit with the model described in Eq. 3.19. The insets show three spectra for different interstate scattering lengths: moderately repulsive ($a_{inter} \simeq 185\, a_0$) at 98.3 A, strongly attractive ($a_{inter} \simeq -1400\, a_0$) at 99.2 A, and moderately attractive ($a_{inter} \simeq -120\, a_0$) at 101 A. At the same time, the intrastate scattering length changes between $\simeq 12 a_0$ at 98.3 A and $\simeq 36\, a_0$ at 101 A. Only the dark data points have been used for the fit, and the gray ones have been excluded to avoid biases in the extracted field tuning due to the mean field interaction shifts near the resonance. These shifts are very clearly visible in the (zoomed in) residuum plot **c)** near the Feshbach resonance position, where the x-axis has been rescaled from currents to fields. As most of the residual originates from the cloud's mean field shift, it can be used to determine the Feshbach resonance position. The two lines show fitted mean field shifts. The dotted green line uses the literature value from [31] for the Feshbach resonance parameters and only has the amplitude as a free parameter. The dashed red line additionally adds the Feshbach position as a free parameter. The difference is about (0.19 ± 0.06) G and therefore significantly more than the uncertainty of 0.05 G stated by [31].

Feshbach resonance, and then fit the measured transition frequencies by the model in Eq. 3.19. The only free parameter here is the proportionality constant between set current and actual field, i.e. $B = \gamma_{Coil} \cdot I$, resulting in a field tuning of the coils of $\gamma_{Coil} = (5.3143 \pm 0.0001)$ G/A. Allowing the current-field relationship to include a constant offset field, i.e. $B = \gamma_{Coil} \cdot I + B_0$, changes the value of γ_{Coil}, as we only probed rather high currents around 100 A. The predicted field at each current does not change significantly though, as a small positive offset field is compensated by a slightly smaller value of γ_{Coil}, such that the effect cancels out over the region of interest. Fig. 3.8(b) and (c) show the used center frequencies (black markers), the resulting fit (red line) as well as the residual.

The excluded data points near the Feshbach resonance in Fig. 3.8(b) and (c) show a clear shift near the resonance and thus allows us to verify the Feshbach resonance position. As we are interested in the position of the Feshbach resonance, we treat both the overall amplitude (hence including the density) and the position as free parameters. For the resonance width and background scattering length we assume the literature values given in [31]. Fig. 3.8(c) shows the extracted shift both for the literature value of the Feshbach resonance position, and the result of the variable position, where the optimal position has been found to be shifted to slightly lower fields. The difference is about (0.19 ± 0.06) G, and thus significantly more than the uncertainty of 0.05 G stated by [31]. Introducing a more sophisticated model for the individual spectra, where we include both the collisional broadening and the asymmetric mean field shift, does not resolve this tension. As the reason for the discrepancy is not known and the difference is rather small, we will use the literature values from [31] for converting fields to scattering lengths.

Chapter 4

Excitation Spectra in 3D and 2D

4.1 3D Polaron Spectra

Before proceeding to a two-dimensional system, we spectroscopically investigate a three-dimensional system. This has previously done and we reproduce spectra in agreement with [94] and in general agreement with [95]. Before presenting our spectra, we briefly summarize the relevant previous work.

In 2016, the authors of [94] prepared a ^{87}Rb BEC with weakly interacting ^{40}K impurities. An RF pulse was then used to flip the ^{40}K atoms into a hyperfine state which exhibits a Feshbach resonance with the surrounding BEC. The strength and sign of the ^{40}K-^{87}Rb interaction could therefore be controlled, allowing to extract the energy, spectral width, and lifetime for both attractive and repulsive interactions. Around the same time, a BEC formed by ^{39}K atoms was used in Aarhus to measure the spectrum and line width across a Feshbach resonance between two different m_F-states [95], also leading to a later, more in-depth analysis of their observed line shapes [96].

A slightly different approach was chosen a few years later by Yan et al. [97]. Similar to [94], they immersed a dilute cloud of ^{40}K into a BEC, in their case formed by ^{23}Na. In contrast to *injection* spectroscopy done in the earlier works, they used *ejection* spectroscopy by first adiabatically creating a strongly interacting polaron and then transferring the impurities into a weakly interacting state. Furthermore, their high optical resolution allowed them to resolve the density profile of the BEC, and hence also enabled them to image the spatially dependent response for different detunings. By varying the bath's temperature, they investigated its influence on polaron's energy and lifetime. Most notably, they found that for strong enough attractive interactions, the polaron's energy decreases with temperature again, i.e. that the strongest bound polaron occurs at finite temperatures of $T \approx 0.4T_c$, while the lifetime continuously grows below T_c.

As ejection and injection spectroscopy are sensitive to different aspects - for example, states with short lifetime cannot be investigated in ejection spectroscopy due to the adiabatic preparation - and we perform injection spectroscopy, the work performed in Boulder [94] and Aarhus [95] are most directly comparable to what is presented in the section below. As mentioned above, our results are in good agreement with [94] and, apart from some differences discussed below, in general agreement with [95].

We here first summarize the experimental parameters and procedure, then discuss the measured spectra, followed by a more detailed analysis of the observed line shapes, which we can describe very well when employing custom models that include excited polaron states. Finally, we conclude with the extracted peak energies and a comparison with the previous work.

4.1.1 Experimental Procedure

The experimental sequence for obtaining the polaron spectrum in our ^{39}K BEC is very simple: As described in Sec. 3.3.2, we prepare a condensed cloud of ∼5000 atoms in the $|1,-1\rangle$ hyperfine state at a temperature of $T \lesssim 0.2T_c$. From here on, we will usually refer to the $|1,-1\rangle$ state as the bath state, and to the $|1,0\rangle$ state to the impurity state. The interaction parameter $1/k_n a$ implicitly depends on the density as $k_n^{3D} = (6\pi^2 n)^{1/3}$; we will always refer to the peak density and therefore to the peak interaction parameter[1].

The condensate is trapped in an optical dipole trap formed by two 850 nm beams with trapping frequencies of 220 Hz radially and 310 Hz vertically. Over the range of interest, the interaction within the bath is weakly repulsive: the scattering length ranges from ∼10 a_0 at 98 A to ∼24 a_0 at 100 A. With these parameters, the peak density of the cloud is between $2 \cdot 10^{14}$ cm^{-3} and $3 \cdot 10^{14}$ cm^{-3}, and the corresponding mean field shift in the center of the bath is between 500 and 700 Hz. After ramping the field to a suitable value, we apply a radio-frequency pulse at or near the transition frequency between the $|1,-1\rangle$ bath state and the $|1,0\rangle$ impurity state. Unless mentioned otherwise, the RF pulse is driven at full power for 2 ms, corresponding to a ∼4π-pulse in a non-interacting system. Due to the large interaction between bath and impurity atoms, the Rabi oscillation here rapidly decoheres and no oscillation can be observed. After the pulse, the system is left to thermalize for 10 ms, and subsequently released from the optical trap. After 2 ms of time of flight, the cloud is imaged with absorption imaging as described in Sec. 3.3.2. The imaging is done at the field of the RF transfer, and the imaging laser therefore has to be ramped to the correct detuning at the same time. The resulting density profiles

[1] Note that [95] used the average density with, assuming a Thomas-Fermi profile, $n_{av} = 0.4 \cdot n_0$, leading to a ∼25% smaller k_n and hence a ∼36% larger value of the interaction parameter.

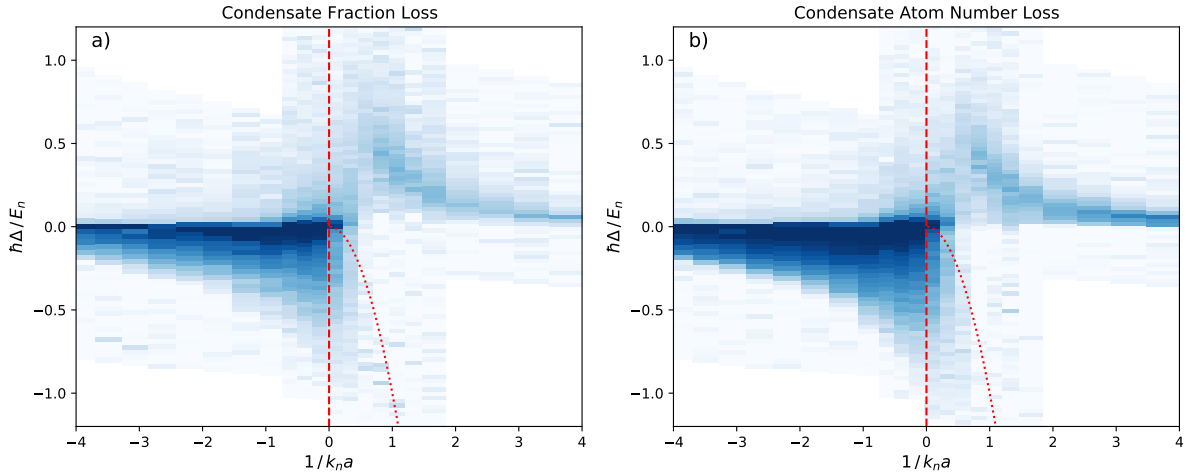

Figure 4.1: Polaron spectrum of the 3D system. **a)** Condensate fraction loss. **b)** Condensate atom number loss. Both measures show similar spectra, but differ in the exact line shapes discussed later: for attractive interactions (negative values of $1/k_n a$), the signal is continuously increasing with the maximum observed signal at zero detuning, i.e. at the unshifted frequency value. Repulsive interactions, on the other hand, show a clearly distinct branch, where the maximum loss occurs at increasingly positive detuning for increasing interacting strength and a vanishing signal at the unshifted frequency. The position of the Feshbach resonance is marked by the vertical red dashed line, and the molecular branch is indicated by the red dotted line starting in the center of the plot.

are fitted with a bimodal distribution, from which the BEC atom number, the gaussian background, and the condensate fraction are extracted. The main observables discussed here will be the BEC atom number and the condensate fraction.

4.1.2 3D Polaron Spectrum

The obtained loss spectra are shown in Fig. 4.1, where (a) shows the loss in condensate fraction, while (b) shows the loss of condensate atom number. The y-axis is the detuning shift of the final state, i.e. the difference between the unperturbed transition frequency at the respective field and the probed transition frequency, and has been rescaled by the natural energy scale $E_n = \hbar^2 k_n^2/(2m)$ with $k_n = (6\pi^2 n)^{1/3}$ as introduced above. The sign of this difference has been flipped as the initial state is energetically higher lying than the final state that the atom is flipped into. In the plot the presented shift is negative for attractive interactions and positive for repulsive interactions. Over the relevant range, E_n/h ranges between ∼60 kHz at $1/k_n a = -4$ over ∼75 kHz at $1/k_n a = 0$ to ∼80 kHz at $1/k_n a = 4$.

Both the condensate fraction loss and the condensate atom number loss show very asymmetric spectra: on the attractive side, the signal is strongest close to zero detuning and becomes weaker towards more negative detuning. For positive detuning, there is only

very little loss visible, especially for interaction parameters of $1/k_n a < -2$. For repulsive interactions, on the other hand, we observe an upwards bending branch with decreasing weights towards both lower and higher detuning. The branch both broadens and becomes weaker when approaching the Feshbach resonance from the repulsive side. Near the Feshbach resonance, the branch is vanishing as expected: for very strong interactions, the quasi-particle residue should decrease, leading to a lower transfer rate and hence a weaker signal. We attribute the in general stronger signal on the attractive side to dynamics happening after the creation of the impurities: while repulsive interactions should lead to an expulsion of impurities, and hence a limited time of interaction, attractive interaction should cause impurities to accumulate at the center of the condensate. Following this interpretation, it is to be expected that attractive interactions lead to a stronger reduction of the condensate fraction. The dotted line in Fig. 4.1 indicates the molecular bound state energy, which is responsible for the Feshbach resonance. As its energetically below the repulsive branch, the repulsive polaron can relax into the molecular state, and in consequence to loss from the system.

Fig. 4.2 shows the influence of varying RF power and pulse length, where (a) shows the spectra at full RF power, (b) shows the spectra at 30% of the maximal amplitude, i.e. 10% of the full power, and (c)-(e) show the line shapes for selected interaction parameters and different settings. We observe a small dependence on the power of the radio-frequency pulse for attractive interactions, where the onset of signal shifts to more negative detuning for higher RF power. However, increasing the pulse time at full RF power even further leads to no further shift, suggesting a saturation of the effect. In case of the attractive interaction, we are mostly interested in the onset of the signal as we interpret this as the signal originating from the densest region. For these regions, the long pulses are not problematic as the signal stays small and the back reaction on the system can therefore be assumed to not be relevant.

4.1.3 Line Shape Modeling

Fig. 4.4 shows a selected few individual line shapes for the condensate atom loss. In order to extract meaningful parameters, we try to derive a model explaining the observed line shapes, starting with the repulsive side.

Repulsive Interactions For repulsive interactions, the authors of [96] suggest a loss model, where the impurity atoms are expelled from the central trapping region due to the repulsive interaction with the condensate. During expulsion, the impurity atoms can

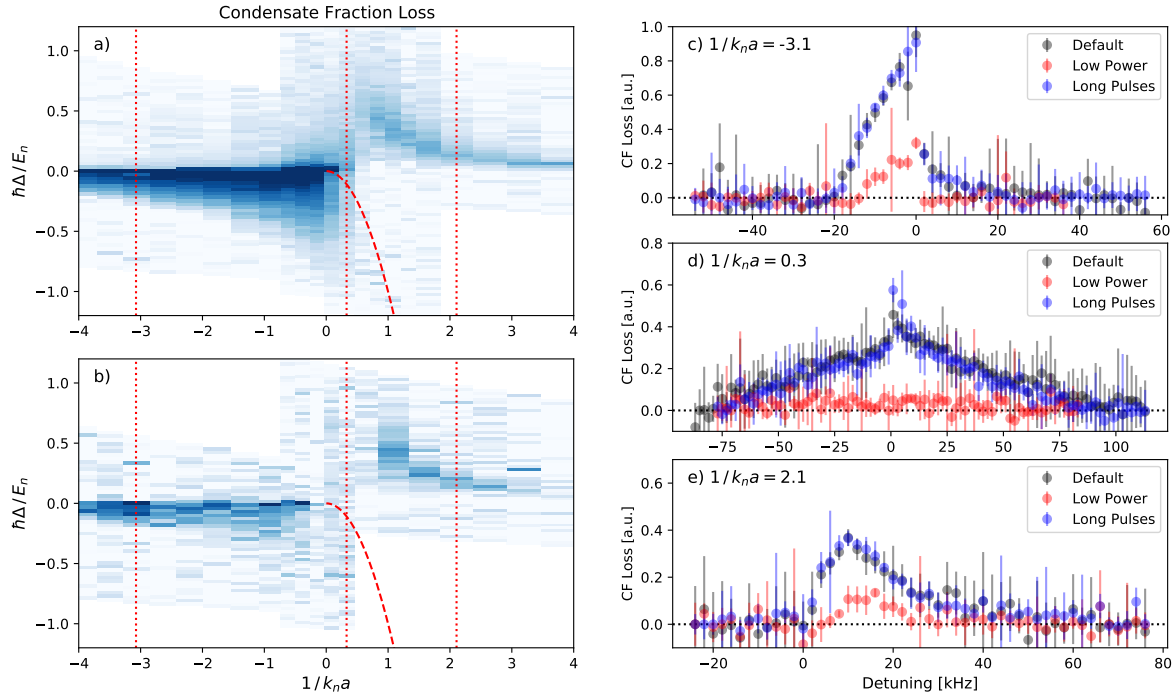

Figure 4.2: High Power / Low Power Comparison Plots. **a)** and **b)**: High and low power spectrum for the condensate fraction, respectively. The dotted vertical lines indicate the positions of the line cuts shown on the right. **c)** Line shapes for attractive interactions for high power, low power, and longer pulses at high power. **d)** Same as c), but on resonance. **e)** Same as c), but for repulsive interactions. Compared to lower RF powers, the high power data for attractive interactions shows a consistent shift to more negative detunings, while the line shape is preserved. For repulsive interactions, no significant shift is observed. In the case of longer pulses, we used 3 ms radio-frequency pulses instead of 2 ms. No difference in the spectra are observed in this case, suggesting a saturation of the signal.

undergo three-body collisions with two condensate atoms, leading to a larger loss signal from dense regions.

Starting with no collisions, and assuming an energy shift that is proportional to the local density (as one has on the mean field level), the signal strength $S(f)$ in a 3-dimensional system is obtained by integrating over the resonant region in the condensate:

$$S(f)df \propto \int_{r_1}^{r_2} r^2 n(r) dr \propto \int_{n_{res}}^{n_{res}+\Delta n} \sqrt{1-n} \cdot n dn, \tag{4.1}$$

where it has been used that the Thomas-Fermi profile as depicted in Fig. 4.3(a) with $n(r) = n_0(1 - r^2/R^2)$ leads to $r^2(n) = R[1 - n/n_0]$ and $\partial r/\partial n \propto 1/\sqrt{1 - n/n_0}$. Thus, one obtains $S(f) \propto n \cdot \sqrt{1-n}$. To reproduce the measured signal, this line shape additionally has to convoluted with the frequency broadening due to the finite pulse width. This leads to a small broadening and smoothing out, but keeps the main features intact: there is no signal for detunings below zero, as the shift is repulsive for any density, and the signal

has a sharp drop towards the maximum frequency as the relevant volume quickly reduces. Including the enhanced losses from three-body collisions also does not significantly alter these features. The dominant effect is only additional loss at high densities, leading to an enhanced signal at high detunings. This is due to a combination of the higher scattering probability resulting directly from the higher density, and the slower acceleration of impurity regions in the flatter density distribution, and therefore larger propagation time.

Fig. 4.4(a) shows one typical repulsive spectrum taken at an interaction parameter of $1/k_n a = 2.6$, together with expectations of this model, where different values for the three-body recombination rate have been used in order to illustrate its effect. It is obvious that this model performs poorly on our data: it does not at all reproduce the exponential decay of signal for larger detuning.

We instead consider two other heuristic models: the first one considers the condensate fraction loss signal and is a purely phenomenological model. It mostly serves to extract parameters from the line shape. In this case, we describe the line shape by a linear increase starting at zero detuning up to some maximum detuning, and an exponential decay of the signal strength for even higher detuning. Apart from amplitude and offset of the signal, the only free parameters are the detuning of maximum signal and the frequency decay scale entering the exponential decay.

The second model follows a physical motivation: in this case, flipping atoms into the impurity state is not only possible at one fixed detuning for each density, but also at higher detunings. We interpret this as flipping into an excited polaron state, while the lowest possible detuning (at a fixed density) corresponds to the creation of the polaronic ground state. We expect the overlap, and hence the transition probability, to decrease for higher excited states and model the decreasing overlap heuristically with an exponential decay. The total signal is then obtained by integrating over all densities:

$$S(f)df \propto \int_0^{n_0} n \cdot \sqrt{1-n} \cdot \theta(\delta_{local}) \cdot \exp(-\delta_{local}/f_{decay}) dn, \tag{4.2}$$

where $\delta_{local} \equiv f - f_{max} \cdot n/n_0$ is the local detuning with respect to the maximum shift at the respective density and n_0 is the peak density in the center of the condensate. With this expression, we implicitly assume that the local energy shift and the maximum energy shift are given by the mean field shifts $g \cdot n(r)$ and $g \cdot n_0$, respectively This expected signal is then convoluted with the frequency response due to the finite pulse length.

This model is similar to a simplified version of the attractive-regime model by [96]. They consider three contributions relevant at different detunings: at resonance, the response is a delta-peak broadened by the finite pulse width. To higher frequencies, this

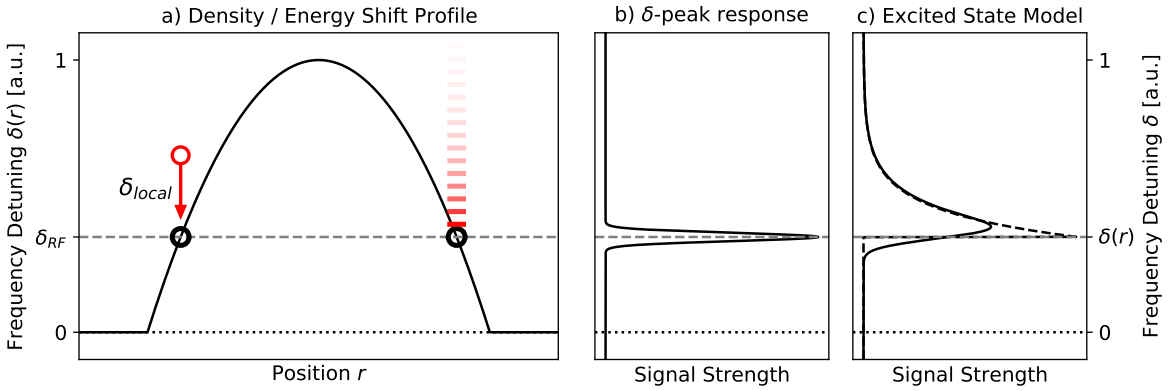

Figure 4.3: Sketch of the line shape model used for repulsive interactions as described in Eq. 4.2. **a)** Profile of the energy shift when assuming that the local energy shift is proportional to the density, i.e. $\delta(r) \propto n(r)$. When only considering resonant transfers, applying an RF pulse with detuning δ_{RF} can flip atoms into the impurity state only at the positions marked with the black circles. However, in our model we also include the possibility to create "excited polarons" at a position r even when $\delta_{RF} > \delta(r)$ as indicated by the red circle. For any positive local detuning $\delta_{local} \equiv \delta_{RF} - \delta(r)$ we assume excited states to exist, although the probability of transfer decreases exponentially, as illustrated by the red lines on the right side of the potential hill. **b)** Signal strength obtained at a fixed position or, equivalently, density when assuming a δ-peak response with pulse-width broadening. **c)** Signal strength obtained at the same position when assuming the excitation model described in Eq. 4.2. The black dashed line shows the expression inside the integral and the solid line the same after a frequency convolution modeling the finite pulse width. For the shown position/density, detunings below $\delta(r)$ do not produce a signal. For frequencies above $\delta(r)$ the signal strength decreases exponentially, where the decay scale is a free parameter.

is followed by an exponential decay of signal, which eventually transitions into a power law with exponent -5/2 in order to capture the expected contact profile. The relative integrated weight of the exponential and the power-law part then contains information about the quasi-particle residue. In our case, fitting this model reproduces the simpler model described above, where the relative weight of the resonant peak becomes negligible and the transition to the power-law behavior is located at high detunings, where the noise becomes dominant, and we are therefore not sensitive to the exact transition frequency.

Fig. 4.4(b) and (c) show a typical repulsive line shape with these two models fitted to the data. In contrast to the repulsive-regime model used by [96], these two models capture the features of the observed line shapes in the loss of condensate fraction very well and allow us to extract the peak frequency f_{max} and the decay scale f_{decay}. For the loss of condensate atom number, these two models do not capture the flattening of the curve near the peak very well.

Attractive Interactions For attractive interactions, the line shapes are very different: we observe the strongest response close to zero detuning, and decreasing signal towards

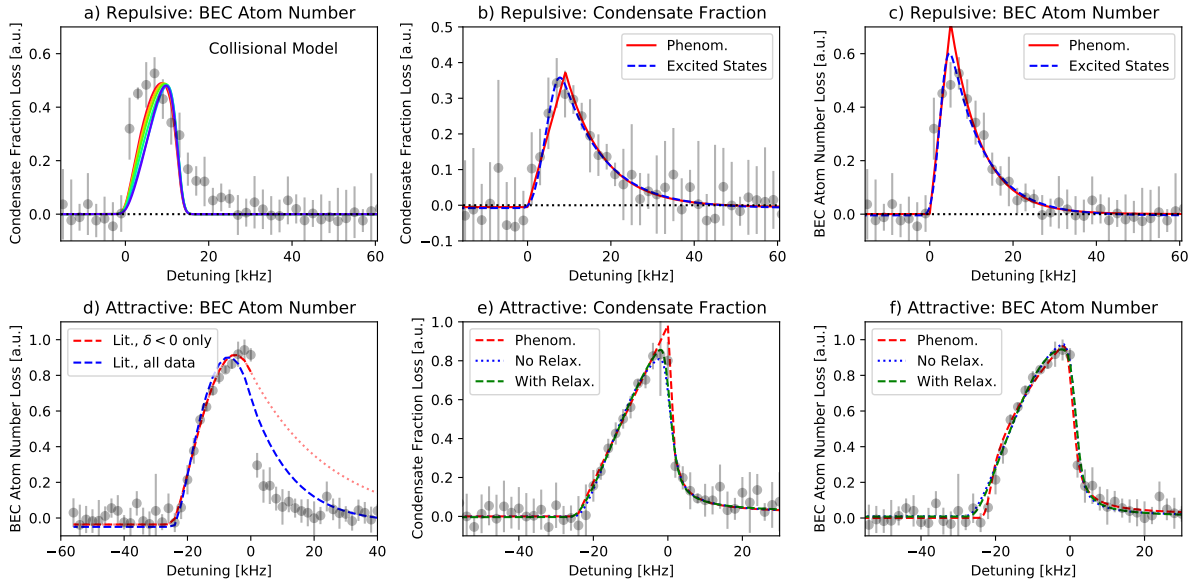

Figure 4.4: Line shape models for repulsive and attractive interactions in the top and bottom row, respectively. **a) - c)** Repulsive interactions at $1/ka = +2.6$. Independent of the exact value of the three-body recombination rate, the loss model described in [96] describes the data very poorly, while both the phenomenological and the physically motivated model work very well for the condensate fraction loss (center) and reasonably well for the BEC atom number loss (right). In the latter case, the models fail to properly describe the saturation of the signal near the peak. **d) - f)** Attractive interactions at $1/ka = -2.6$. **d)** The model used by [96] reproduces the signal for negative detunings, but predicts a much stronger response for positive detunings. The phenomenological model as well as the excited states model discussed in the main text succeed much better at describing the observed signal for both the loss in condensate fraction **e)** and the loss of BEC atom number **f)**. Including the relaxation term slightly improves the agreement with the observed condensate fraction loss.

further negative detuning until the signal stops rather rapidly. Towards positive detuning, we observe a rapid suppression of response. The above mentioned attractive line shape model by [96] is used in Fig. 4.4(d) to describe the observed spectrum for an attractive interaction at $1/k_n a = -2.6$. The signal at negative detunings can be reproduced quite well, but in contradiction to what we observe, the model predicts a too large response at positive detunings.

The striking feature observed for the attractive branch is the very rapid decrease of signal for larger negative detunings. We interpret the point of vanishing signal as stemming from the region with highest density, and thus being the most interesting parameter. In order to simply extract this parameter, we therefore again resort to a purely phenomenological model: for the condensate fraction, we model this with no loss below some lower cutoff frequency, and then a linearly increasing signal up to zero detuning. For the condensate atom number, we use a quadratic profile instead of the linear increase. For positive detunings, the data in both cases is well described by a power law. Apart

from amplitude and offset, the free parameters are then the maximum amplitude and the power law index.

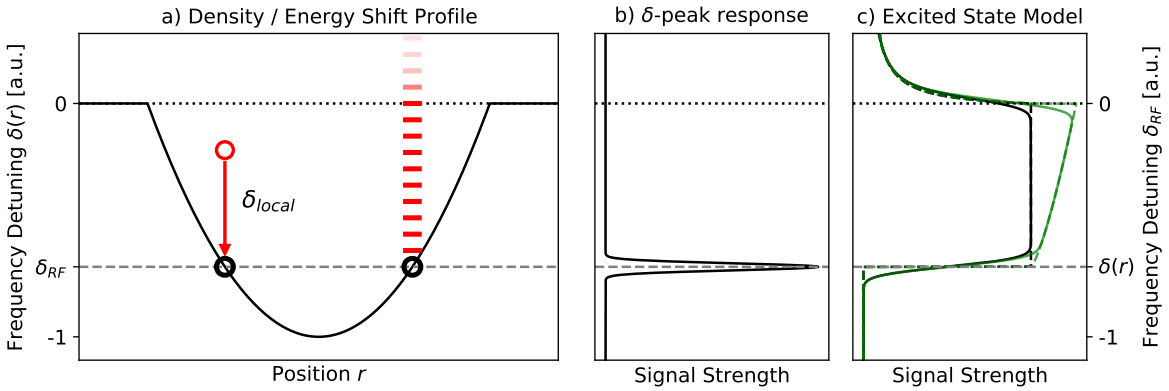

Figure 4.5: Sketch of the line shape model used for attractive interactions as described in Eq. 4.3. **a)** Energy shift profile when assuming $\delta(r) \propto n(r)$. As in the repulsive case in Fig. 4.3 resonant transfers with δ_{RF} can only flip atoms at the positions marked with the black circles. For the attractive line shapes we again also allow for excited states to be created when $\delta_{RF} > \delta(r)$ as indicated by the red circle and the red lines. Within our model, the transfer weights are constant for states bound within the attractive condensate and quickly decrease for unbound states. **b)** Signal strength obtained at a fixed position or, equivalently, density when assuming a δ-peak response with pulse-width broadening. **c)** Signal strength obtained at the same position when assuming the excitation model described in Eq. 4.3. The black dashed line shows the expression inside the integral and the solid line the same after a frequency convolution modeling the finite pulse width. For the shown position/density, detunings below δ_{RF} do not produce a signal. Between $f = \delta_{RF}$ and $f = 0$, the created signal is constant. For $f > 0$ the signal amplitude decreases with a power-law behavior. The green lines correspond to the same settings but with the parameter for delayed energy deposition c set to 0.25 instead of 0, i.e. allowing for the relaxation of excited polarons.

A second, more physically motivated model, is sketched in Fig. 4.5 and compared to actual data in Fig. 4.4(e) and (f). It assumes the possibly to create excited states at any energy δ_{local} above the local maximum shift $\delta(r)$, similar to the repulsive case, but distinguished between "bound polarons" and "free polarons". Considering a fixed density, "bound polarons" can in this model be created for detunings δ_{RF} between the maximum shift $\delta(r)$ and the unshifted transition frequency, i.e. for $\delta(r) \leq \delta_{RF} \leq 0$. These states are still trapped within the effective potential formed by the bath state. "Free polarons" are relevant for for $\delta_{RF} > 0$ and correspond to states that are no longer trapped within the effective potential. Including the volume effect, the integrated signal thus becomes

$$S(f)df \propto \int_0^{n_0} n \cdot \sqrt{1-n} \cdot [g_{bound}(n,f) + g_{free}(n,f)]\, dn, \tag{4.3}$$

where $g_{bound}(n,f)$ models the contribution originating from "bound polarons" and $g_{free}(n,f)$ models the contribution from "free polarons".

For g_{bound}, we assume a homogeneous profile

$$g_{bound}(n, f) = \theta(\delta_{local})\theta(-f), \tag{4.4}$$

where θ is the Heaviside step function and $\delta_{local} \equiv f - f_{max} \cdot n/n_0$ is the local detuning with respect to the maximum shift at the respective density and n_0 is the peak density in the center of the condensate. This corresponds to the repulsive line shape model in Eq. 4.2 in the limit of $f_{decay} \to \infty$. When using a finite decay scale instead, this free parameter becomes very large, effectively just reproducing the homogeneous profile. We therefore removed this parameter from the model.

For g_{free} we assume a power law decay which we parametrize as

$$g_{free} = \theta(f) \cdot \left[\frac{f + \sigma}{\sigma}\right]^{\alpha}, \tag{4.5}$$

where σ is the frequency broadening due to the finite pulse width and the power law index α is a free parameter, that should be negative to produce a decreasing signal strength. Our physical motivation for the different functional forms of the two regimes is the assumption that for $f > 0$ the created state is not bound by the attractive condensate and the wave function extends over the size of the optical trap. Compared to a state trapped within the condensate, we therefore expect the spatial overlap to be reduced by a factor of at least $(\sigma_{Trap}/R_{TF})^3 \gtrsim 10^2$, and attribute the rapid loss of transfer probability to the reduced wave function overlap with the final state.

The physically motivated model describes the data very well, indicating that we indeed have a large population in excited states. Note that the functional form of g_{free} differs from the one used for the repulsive case, where we assumed an exponential reduction of transition probability for excited states. Changing this, i.e. assuming exponential suppression for the attractive case or power-law decay for repulsive interaction, describes the observed data significantly worse. We speculate that the reason for this is due to the different dynamics in both cases: while the created impurity state is unbound in both cases, the interaction between impurity and condensate leads to an increased spatial overlap for attractive interaction, and an expulsion for the repulsive interaction. The transition probabilities for these two cases are therefore expected to be different, which might lead to the two different functional forms needed to model the data well.

We also considered an additional contribution from excited bound states relaxing and therefore leading to additional heating. This is included by an additional contribution in

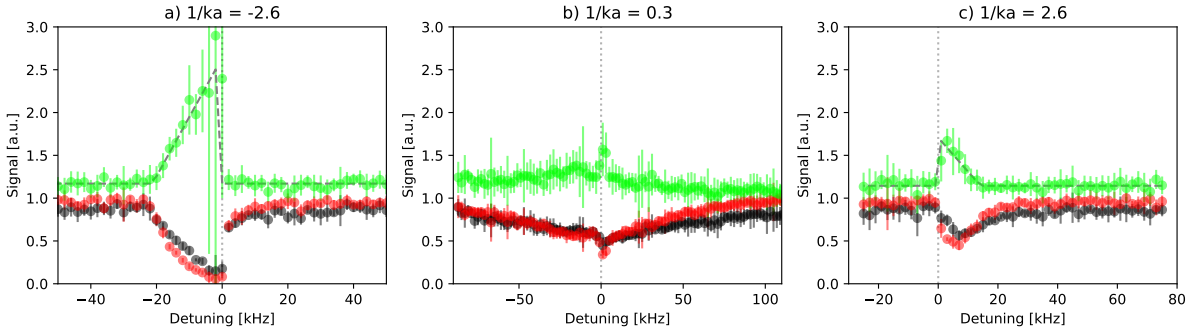

Figure 4.6: **a) - c)** Signal ratio between BEC atom number loss and condensate fraction at $1/ka = -2.6$, $1/ka = 0.3$, and $1/ka = 2.6$, respectively. Except for the region closest to the Feshbach resonance, the ratio between the BEC atom number loss and the condensate fraction loss is a simple linear function. Extracting the cutoff frequencies from this measure results in approximately the same maximum frequencies for attractive interactions, but consistently somewhat higher values for repulsive interactions. Near the resonance, the ratio is more complicated and does not allow to extract the cutoff frequency in this manner.

g_{bound} by

$$g_{bound}(n, f) = \theta(-f) \cdot \theta(\delta_{local}) \cdot \left[1 + c \cdot \delta_{local}^{3/4}\right], \tag{4.6}$$

where c is a free parameter and the exponent $3/4$ arises due to the atom number dependence of the condensate with $N_c \propto 1 - (T/T_c)^3$ and the internal energy scaling of $E \propto T^4$. The effect of this contribution is illustrated by the red curves in Fig. 4.5(c). Including the relaxation term only slightly improves the fit for the loss in condensate fraction, but seems to be of rather limited importance. As one would expect, this relaxation model simply reproduces the model without relaxation (i.e. $c \approx 0$) when fitting the loss in condensate atom number.

We also considered density fluctuations as the mechanism for the broadening the signal away from a single peak at fixed density, but found that this does not reproduce the data well. Density fluctuations lead to a distribution of higher and lower densities around the mean density at the respective trap position and hence to smaller and larger detuning shifts. Apart from unreasonably high temperatures needed to explain the observed broadening, the main problem is that the distribution of the density fluctuations is continuous, which leads to a smoothing out of the response onset for the attractive interactions. This is in stark contrast to the rapid onset of signal that we observe in the spectra and is shown for example in Fig. 4.4(d). Density fluctuations therefore do not seem to be the reason for the strong presence of signal at relatively high detuning.

4.1.4 Peak Shift Extraction by Signal Ratio

One, if not the main parameter to extract from the polaron spectrum is the energy of the polaron. On a mean field level one expects to be proportional to the local density, $E \propto g \cdot n$. For attractive interactions, the largest observed shift can therefore be interpreted as the lowest possible state at the highest density, i.e. in the center of the trap. For repulsive interactions, the extraction is more convoluted: possible excited states produce signal at higher detuning while lower density regions produce signal at lower detunings. Two methods to extract the peak shifts, i.e. the shifts corresponding to the highest density, have been described above in the discussion of the line shapes.

However, the line shapes shown in Fig. 4.4(e) and (f) motivate an additional approach to extract the peak frequency: while the signal in the condensate fraction loss is almost linear at negative detunings, the BEC atom number loss signal is roughly quadratic. When taking the (suitably rescaled) signal from these two measures and dividing it by each other, one obtains a signal as shown in Fig. 4.6 for three different interaction strengths. The ratio increasing for some detunings indicates a stronger relative signal in the loss of condensate atom number compared to the relative loss of condensate fraction, i.e. we observe a strong loss in condensate atom number while the condensate fraction is reduced less. A possible explanation could be three-body losses, where three atoms leave the condensate but do not contribute to the thermal background as they are completely lost from the trap. For attractive interactions, the ratio is very well described by a linear function between some cutoff value and zero detuning. Outside of this range, i.e. below the cutoff detuning and above zero detuning, the ratio is some constant value. The extracted cutoff detuning agrees with the value obtained from the fitting models described above. While the same with reversed signs applies for repulsive interactions, the extracted cutoff frequency are consistently higher than the ones obtained from the fitting models described above, and are hence located within the exponentially decaying tail of the signal.

4.1.5 Peak Energy Shifts

Fig. 4.7(a) shows the extracted parameters of $f_{max} = E_{max}/h$. The maximum shift frequency extracted is consistent with the mean field expectations only for the weaker repulsive interactions, while the observed shift is larger than expected for strong repulsive interaction, and significantly stronger for all tested attractive interactions. The reason for this difference is not understood yet. However, Guenther et al. theoretically predicted increasing energy shifts for increasing temperature, i.e. a stronger bound state which might be connected to our observation [111]. Fig. 4.7(b) shows the extracted exponent

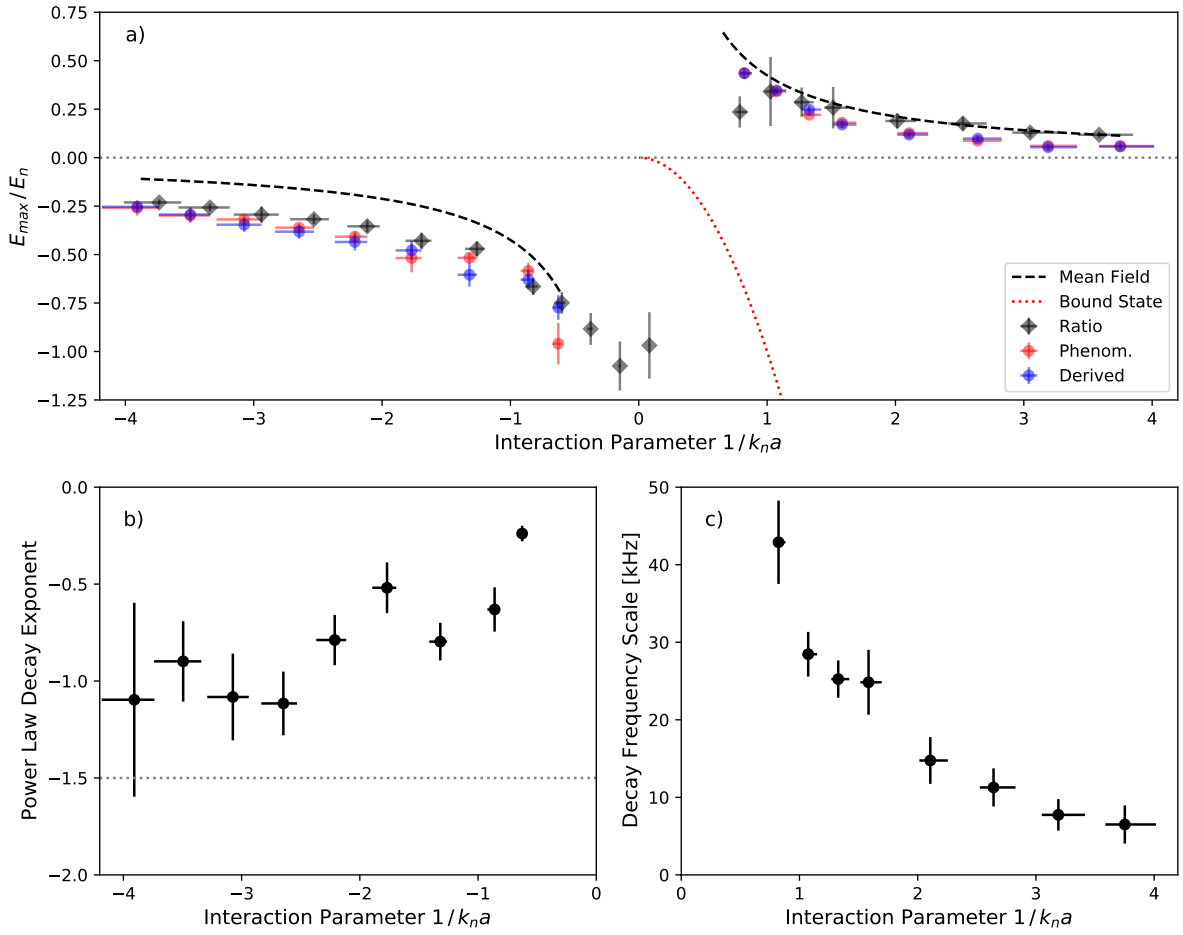

Figure 4.7: **a)** Extracted maximum shifts. The observed maximum frequency shifts agree with the mean field expectations only for rather weak repulsive interactions, but are much larger for all tested attractive interactions. **b)** Power law exponents for the attractive side. For weak interactions, it is around -1 and increases when approaching the unitary regime. The expected value from the contact is -3/2 and is indicated by the dotted line. **c)** Decay scale for the repulsive side. It is roughly inversely proportional to the interaction parameter.

of the power law decay for positive detuning at attractive interaction. For interaction parameters below -5, it stays constantly at an exponent of -1, while it increases for stronger interaction strengths to ~ -0.5. This is hence not following the expectation from the contact, which predicts a power law index between -3/2 and -5/2 [168]. However, the contact scaling is expected to be valid only for very high detunings of several 100 kHz in our case, and our experimental data is far outside the range of applicability.

The exponential frequency decay scale obtained from the repulsive interactions is shown in subplot (c). It is roughly inversely proportional to the interaction parameter. Attributing the exponential decay to an effectively shorter pulse time due to collisions of the created impurities with the background condensate would predict this frequency scale

to increase quadratically with interstate scattering length a_{inter}. While we obtain the same scaling as observed for weaker repulsive interactions of $1/k_n a \gtrsim 3$, the amplitude is lower than expected from the scattering rate. For stronger repulsive interactions the observed frequency decay scale does not follow the scaling expected from the scattering rate, indicating that the increase in decay scale is not a consequence of effectively broadened pulses.

In summary, the magnitude of the observed shift is consistent with the mean field expectation only for weakly repulsive interactions, but is much larger for attractive interactions. The observed line shapes can be reproduced when including excited states both for attractive and repulsive interactions. The excited state contribution is especially relevant for attractive interactions, where a large amount of homogeneous excitations across the condensate are necessary in order to reproduce the observed spectra.

Compared to the previous work done by [94] and [95], the spectra observed in our system agree very well with the spectra documented in [94] for both attractive and repulsive interactions. In contrast, [95] observed slightly different peak energies: in their work, the energy shift magnitude was very similar for both attractive and repulsive interactions, while we and [94] observe a larger shift for attractive interactions at same $|1/k_n a|$. Our observed line shapes for attractive interactions furthermore show a much more pronounced linear behavior than what has been reported in [95] (although the linear behavior, while not discussed, can be recognized in their data, e.g. in Fig. 2(c)-(e)). The reason for this discrepancy is not known, although we suspect that their relatively short RF pulse times might lead to a rather low frequency resolution and weak signal at large detunings for attractive interactions, thus shifting the signal to lower detuning values.

In the next section we will proceed to similar measurements, but in a two-dimensional Bose gas with tuneable interaction strength, where we again record the spectroscopic signal and discuss the observed line shapes.

4.2 2D Polaron Spectra

4.2.1 System Preparation

Obtaining the 2D polaron spectrum used essentially the same procedure as the 3D case. After preparing the two-dimensional sample from the BEC by transferring the cloud into a optical lattice with very strong confinement along the vertical direction, we have about 3000 atoms at $T \lesssim 0.1 T_{BKT}$. Again, the $|1,-1\rangle$ state will be refered to as the bath state and the $|1,0\rangle$ state as the impurity state. While the BKT cloud is not a condensate, we will occasionally still informally refer to it as a condensate as its characteristics are often very similar to a BEC.

The cold cloud is vertically confined by a repulsive optical lattice with a trapping frequency of $\nu_z = 2\pi \cdot 6.5$ kHz and radially by an attractive optical potential with trapping frequency $\nu_{radial} = 110$ Hz. Together with the relatively weak repulsive bath-bath interaction, this gives peak area densities of 70-100 μm^{-2} for the probed range of magnetic fields. The peak mean field shift due to the bath-bath interaction is ∼500 Hz.

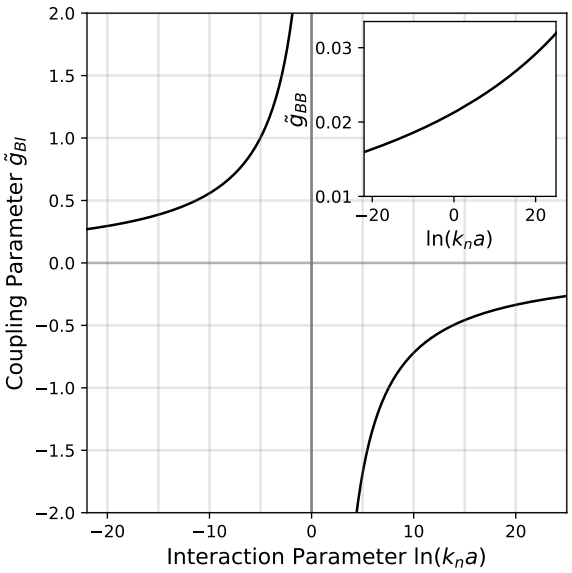

Figure 4.8: Relation between the interaction parameter $\ln(k_n a)$ and the dimensionless coupling parameters $\tilde{g}_{BI}$ and $\tilde{g}_{BB}$ for bath-impurity interactions and bath-bath interactions, respectively, over the relevant range near the bath-impurity Feshbach resonance. While $\tilde{g}_{BI}$ shows large variations, $\tilde{g}_{BB}$ is almost constant and very small.

For the interaction parameter $\ln(k_n a)$ we always, as previously in the 3D case, will employ the peak density to define the typical momentum k_n by the relation $k_n = \sqrt{4\pi n}$ introduced in Sec. 3.2. The stated detunings are often rescaled by the natural energy scale $E_n = \hbar^2 k_n^2/(2m)$. Over the relevant range, E_n/h ranges between ∼210 kHz at $\ln(k_n a) = -21$ over ∼190 kHz at $\ln(k_n a) = 0$ to ∼160 kHz at $\ln(k_n a) = 20$.

Unless stated otherwise, the RF pulses flipping atoms into the impurity state lasted for 3 ms, followed by 10 ms of thermalization and 1.8 ms of time-of-flight before imaging the system. Imaging is again done as described in Sec. 3.3.2.

4.2.2 2D Polaron Spectrum

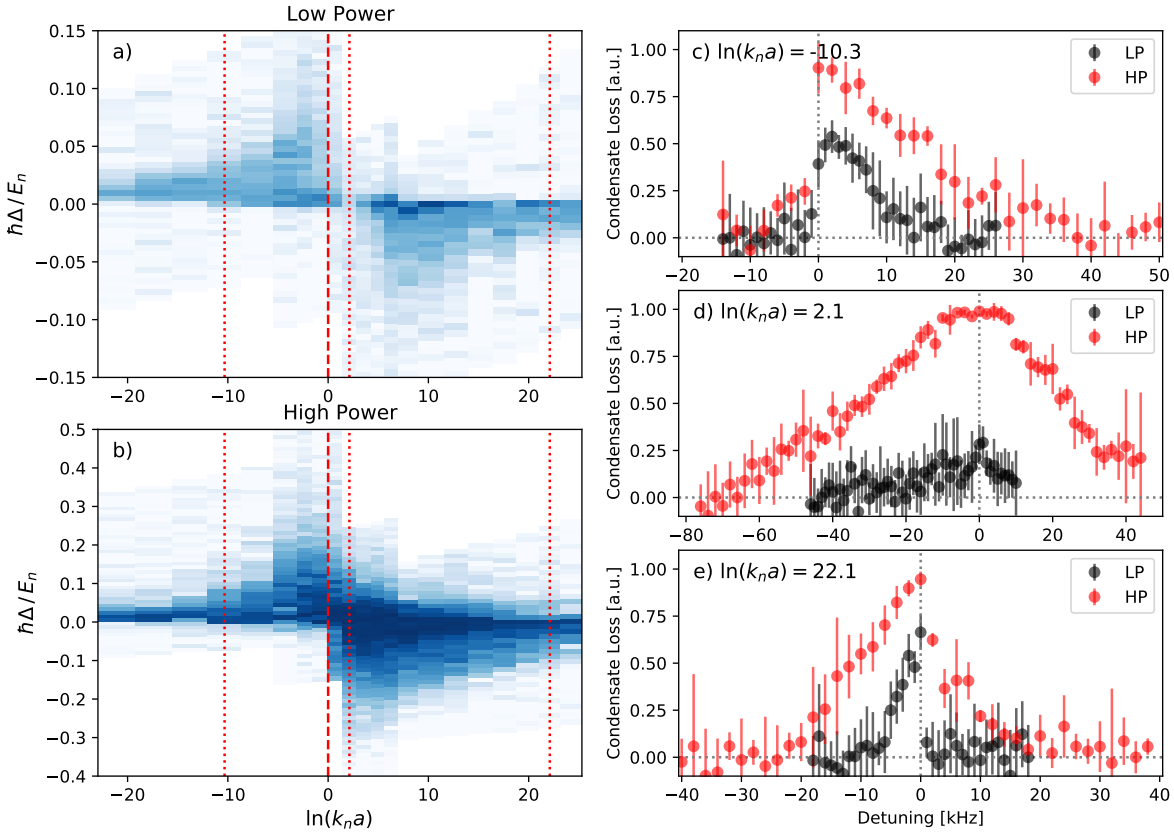

Figure 4.9: **a, b)** Low RF power and high RF power spectra, respectively. Note the different scaling for the y-axis for the two spectra. **c, d, e)** Linecuts through the spectra at repulsive interaction, near resonance, and at attractive interaction, respectively. All data shows the loss of atoms in the condensate. Low power and high power RF pulses lead to very different maximum detunings, where loss can still be observed. This is in stark contrast to the three-dimensional case, where the signal saturated at some maximum detuning. The attractive interaction in general shows larger shifts, but otherwise shows a response rather similar to the repulsive interaction. In three dimensions, the repulsive interaction exhibited to a well-separated branch, which is not present in this system.

The recorded spectra for a two-dimensional system are shown in Fig. 4.9. Note that due to the definition of the interaction parameter as $\ln(k_n a)$, the repulsive side is located on the left and the attractive side is located on the right of the spectrum. Fig. 4.9(a) shows the spectra when using 30% amplitude in the radio-frequency, i.e. $\sim 10\%$ power, and Fig. 4.9(b) shows the spectrum when using full power. Several striking features can be observed, especially in contrast to the spectra obtained in three dimensions: unlike in the three-dimensional results, there is no well separated repulsive branch visible. Instead, both the attractive and repulsive side show signals continuously between zero detuning and some maximum detuning where the signal vanishes. Furthermore, the attractive and the repulsive interaction show roughly the same signal strength, while the attractive

interaction leads to a much stronger signal for the three-dimensional system.

The main difference we observe is the position of the maximum detuning though: unlike in the three-dimensional case, where the radio-frequency pulse power and duration had little effect on the exact line shape once one entered a saturated regime, we observe a massive dependence in the two-dimensional case. For an interaction parameter of $\ln(k_n a) = -10.3$ as shown in Fig. 4.9(c), for example, we observe a signal over about twice as large of a frequency range for high power compared to the low power data. The behavior is similar for attractive interactions as shown in Fig. 4.9(e). Similar to the three-dimensional case, we again observe little to no signal near the resonance for low power. We suspect that this is due to a Quantum-Zeno-like effect, where the large scattering rate effectively prohibits the radio-frequency to actually drive transitions into the impurity state and leads to a reduced amount of losses.

4.2.3 Line Shape Modeling

Analogously to the line shapes observed in the three-dimensional system, we here discuss different models in order to understand the observed line shapes and extract the relevant parameters. Fig. 4.11(a) and (d) show the agreement with the repulsive and attractive interaction model from [96], where the volume weighting has been adapted to the two-dimensional density profile, replacing the volume and density factor of $n\sqrt{1-n}dn$ to ndn. Just as in the 3D-case, the model clearly disagrees with the observed data for the repulsive interaction, and also does not fit well for attractive interactions. Again, we suspect that the effect of unbound excited states is not properly accounted for, leading to the large disagreement especially for positive detunings.

Instead, we resort to custom models. The first one is again a purely phenomenological model, consisting of a peak amplitude at zero detuning. For attractive interactions, the signal decreases linearly towards negative detuning and follows a power law with variable power law index for positive detunings. For repulsive interactions, we use the same model with switched signs, i.e. a linear decrease of signal for positive detuning and quickly decaying signal for negative detuning.

For the second model, we distinguish between repulsive and attractive interactions.

Repulsive Interactions For the former, we adapt the model from Eq. 4.2 to a two-dimensional system, sketched in Fig. 4.10(b):

$$S(f)df \propto \int_0^{n_0} n \cdot \theta(\delta_{local}) \cdot \exp(-\delta_{local}/f_{decay})dn, \tag{4.7}$$

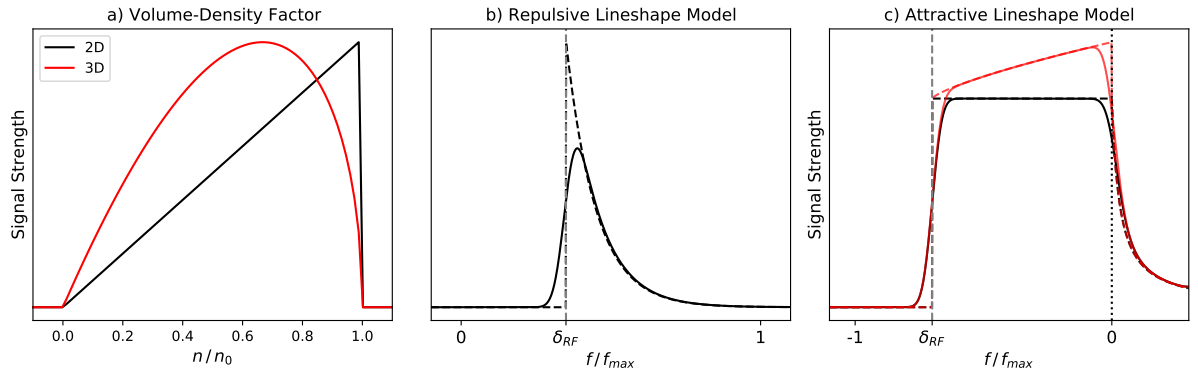

Figure 4.10: Line shape contributions. **a)** Volume-density contribution for 2D (black) and 3D (red) as described in the main text. In both cases, the largest signal is expected at the largest detuning, while we observe the largest signal at zero detuning. **b)** Repulsive line shape model with exponentially suppressed excited state contribution, i.e. the same as shown and described in more detail in Fig. 4.3(c). **c)** Attractive line shape model with homogeneous excitation weight for $\delta_{RF} \leq f \leq 0$ and power-law decay of the signal for $f > 0$. The red line includes delayed energy deposited as motivated by possible excited state relaxation. This is the same as shown and described in more detail in Fig. 4.5(c).

where again $\delta_{local} \equiv f - f_{max} \cdot n/n_0$ is the local detuning with respect to the maximum shift at the respective density and n_0 is the peak density in the center of the cloud. The only difference to Eq. 4.2 is the volume weighting of n instead of $n \cdot \sqrt{1-n}$. This tends to shift the signal more to larger absolute detunings, i.e. puts more relative weight to the strongest shift, which can also be recognized in Fig. 4.10(a).

Attractive Interactions For attractive interactions, we similarly again assume homogeneous excitations across the condensate and employ the same model as defined for three-dimensional systems in 4.3 and also sketched in Fig. 4.10(c), only that it has been adapted to the different density profile in two dimensions:

$$S(f)df \propto \int_0^{n_0} n \cdot [g_{bound}(n,f) + g_{free}(n,f)]\, dn, \tag{4.8}$$

where the difference to 4.3 is the factor of n instead of $n \cdot \sqrt{1-n}$. The "bound states" contribution is again being modeled as

$$g_{bound}(n,f) = \theta(\delta_{local})\theta(-f) \tag{4.9}$$

and the "free states" contribution as

$$g_{free}(n,f) = \theta(f) \cdot \left[\frac{f+\sigma}{\sigma}\right]^{\alpha}, \tag{4.10}$$

where δ_{local} has been defined above, σ is the frequency broadening due to the finite pulse width, and the power law index α is again a free parameter and should fulfill $\alpha < 0$. Fig. 4.11(e) and (f) show the agreement of this model with both the condensate fraction and the condensate atom number for attractive interactions.

Including a relaxation term as described in the 3D-case in Eq. 4.6 turned out to not significantly improve the agreement between the data and the model and is hence omitted here.

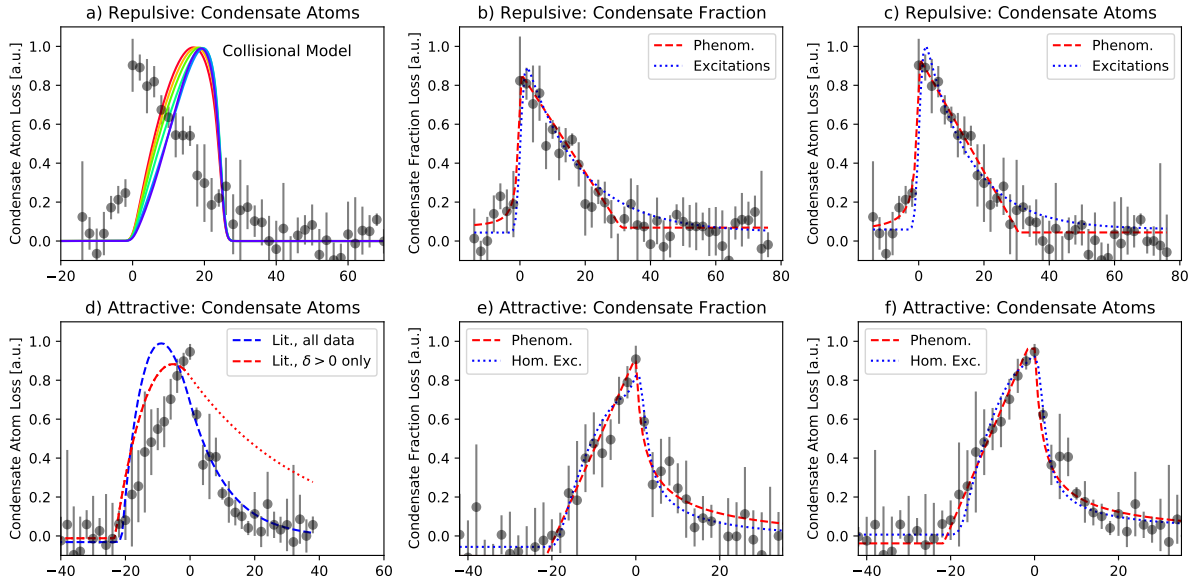

Figure 4.11: Line shape models for repulsive and attractive interactions (top and middle row, respectively), similar to the three-dimensional case shown in Fig. 4.4. For repulsive interactions **a)-c)** at $\ln(k_n a) = -10.3$, the collisional model from [96] again performs poorly, while the phenomenological model and the excited states model described in the main text fit the data reasonably well. The interpretation of the physically motivated model for repulsive interactions is unclear though, as the fit converges to a setting with vanishing peak shift and reproduces the signal only via the excited states. The attractive model of [96], shown in **d)**, again fails to convince, while the phenomenological model and the homogeneous excitations model work for both the condensate fraction **e)** and the condensate atom number **f)**, here shown for $\ln(k_n a) = 22.1$.

Model Performance The performance of these models is shown in Fig. 4.11 (b), (c) for a repulsive interaction parameter of $\ln(k_n a) = -10$ and in Fig. 4.11 (e), (f) for attractive interactions at $\ln(k_n a) = 22$. The phenomenological and the motivated models succeed in describing the data well. In contrast to the three-dimensional case, the condensate fraction and the condensate atom number show very similar line shapes and therefore also provide similar results in the fits. For the attractive interaction, the onset of the loss does not show the large difference between condensate fraction and condensate atom number as observed in the three-dimensional case and, while the volume weighting of

$\propto n$ instead of $n \cdot \sqrt{1-n}$ should lead to more weight at the maximum shift, we observe a smoother onset of signal in the two-dimensional system. In the repulsive regime, the motivated model Eq. 4.7 is completely dominated by the exponential decay for positive energies, and does therefore not predict a nonzero peak detuning. The interpretation of this observation is not clear. For all interactions, the main obstacle for the interpretation of the two-dimensional data is the lack of saturation in the signal, and the hence very different results for low and high RF power.

Peak Shift Extraction by Signal Ratio The ratio of condensate fraction and condensate atom number showed a perfectly linear relationship in the three-dimensional system. The onset of this linear relation allowed for an alternative way to extract an estimate of the peak energy. In two dimensions this ratio is shown in Fig. 4.12 and is only linear for weak interactions. It is better described by a power law with an index of ~ -1 for stronger interactions, i.e. $\sim 1 + 1/f$. For the sake of concreteness, we still fit a linear relation to the power law and extract the detuning where the signal vanishes in the constant offset.

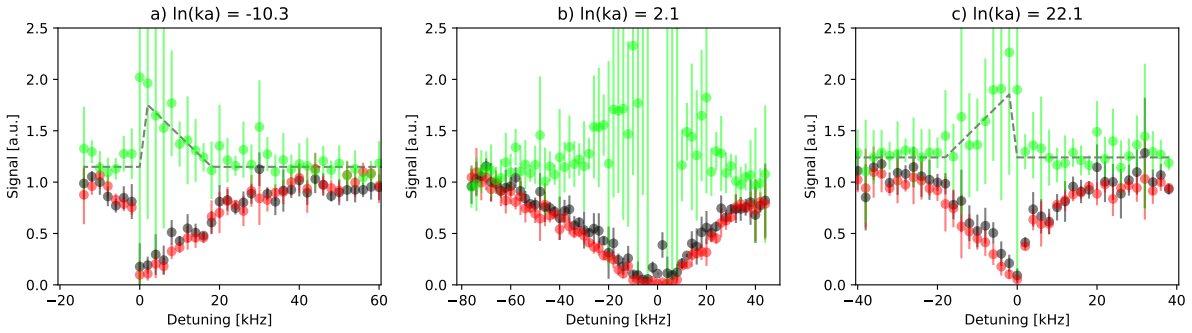

Figure 4.12: Signal ratio (green) between condensate fraction (black) and condensate atoms (red) signal. **a)** Repulsive interactions at $\ln(k_n a) = -10.3$. **b)** Resonant interactions at $\ln(k_n a) = 2.1$. **c)** Attractive interactions at $\ln(k_n a) = 22.1$. For weak interactions, the relation is close to being linear, while it tends to a power-law like behavior with exponent of ~ -1 for stronger interactions.

4.2.4 Peak Energy Shifts

The resulting peak shifts extracted with the different models are shown in Fig. 4.13.

Subplot (a) presents the average of the different methods for both low and high RF power (in blue and red, respectively) and shows the expression derived by the authors of [123][2] Our data agrees well with the predictions for low RF power and for weaker

[2]Note that Eq. 5 in [123] has a typo, where the correct factor of 2 has been replaced by 4. The correct version is obvious when following the derivation in appendix A and furthermore agrees with the plots of the paper.

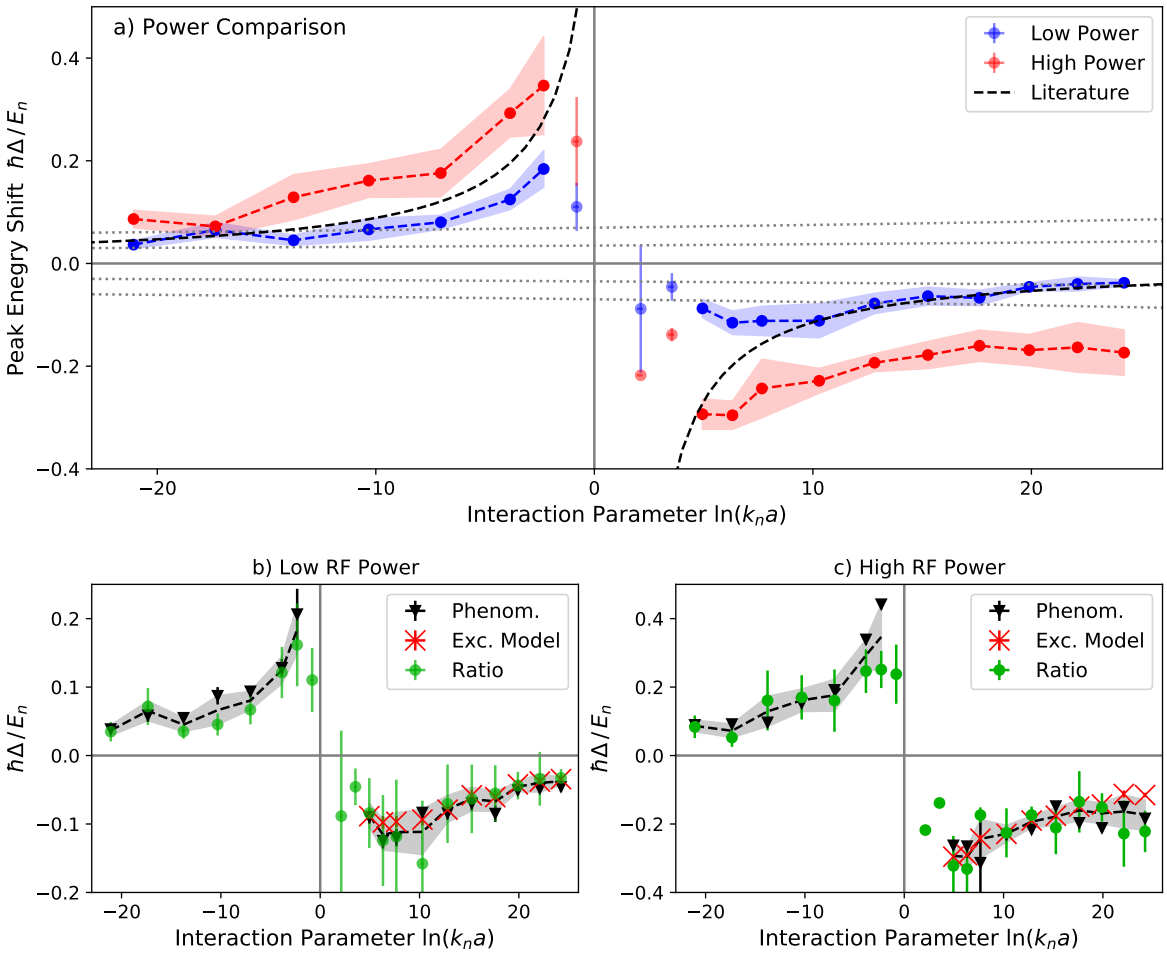

Figure 4.13: **a)** Extracted maximum energy shift for different interaction parameters $\ln(k_n a)$. Repulsive interactions are located on the left half with $\ln(k_n a) < 0$, attractive interactions on the right with $\ln(k_n a) > 0$. For both the low RF power (blue) and the high RF power (red), we here show the averaged results and indicate the uncertainty by the shaded area (see also (b) and (c)). The plot additionally presents the prediction derived in [123] with the dashed black line, which agrees very well with the low RF power data and weaker interactions, but clearly deviate near the resonance and for high RF power. The almost horizontal dotted gray lines correspond to the energy shift of excitations in the vertical confinement (here shown -$2\nu_z$, -ν_z, ν_z, and $2\nu_z$). For virtually all interactions probed, the observed shift is on the level of the vertical level splitting or even well above it. This indicates that the polaronic state is three-dimensional, while the bath is still two-dimensional.
b) and **c)**: Comparison of the results for the individual peak shift extraction methods for low and high power, respectively. The black data (triangles) is obtained by the phenomenological model described in the beginning of Sec. 4.2.3, the red data (crosses) is obtained from the excited state models defined in Eqs. 4.7 and 4.8, and the green data is obtained from the signal ratio as described in the main text. For both low and high RF power, the three methods result in similar values and we therefore use the average in subplot (a), here indicated by the dashed line, with the uncertainty depicted by the shaded area. For strong interactions, the fits become unreliable, especially for the phenomenological and the physically motivated model and we only show the values extracted by the signal ratio approach. Note that we excluded the results of the physically motivated model on the repulsive side, since the interpretation of the frequency scales is unclear as is described in the main text.

interactions, while it is in clear disagreement for strong interactions ($|\ln(k_n a)| \gtrsim 5$) and for all of the high power data.

Fig. 4.13 (b) and (c) present the peak energy shifts extracted with the different methods described above for low and high RF power, respectively. Since the obtained results are consistent for both power settings, we use the average to compare our data with the predictions in (a). Note that the motivated model data has been excluded on the repulsive side due to the unclear interpretation.

While the interpretation is currently not clear and deserves further investigation, we speculate that this might be connected to observations made in theoretical studies by Guenther et al. [111] for three-dimensional Bose polarons: when only considering the impurity-phonon interactions, they only find a single polaron state for $T < T_c$; if they furthermore include terms corresponding to scattering of atoms into and out of the condensate, two polaronic branches appear, which coincide in energy for zero temperature as all phonons are frozen out for $T = 0$. For increasing temperature, the two branches split up: the upper one increases in energy, corresponding to a weaker bound polaron, and vanishes at T_c. The lower one actually *decreases* in energy with increasing temperature due to the enhanced interaction with thermally excited phonons, reaches its lowest energy at T_c and still exists above T_c. While the authors in [111] consider a three-dimensional condensate, they state that the relevant dynamics is due to the bath's gapless excitation spectrum also present in 2D. The observed shift to lower energies when using higher RF powers might therefore reflect the heating and subsequent stronger coupling of the polaron: when applying an RF pulse with high detuning, only a few impurities are flipped off-resonantly and subsequently heat the system. Once the system has a higher temperature, the polaron's new energy is closer to the RF detuning being applied, and a runaway process is started until the RF pulse ends or its detuning becomes too large again. For higher RF power, more impurities are created, speeding up the whole process and shifting the signal to higher detunings.

Additionally or alternatively, the quasi-particle residue might be relevant: as it approaches zero for strong interactions [123], the creation of a ground state polaron should become harder for increasing interaction strength. Instead, excited polaronic states might be created, showing a lower energy shift for attractive interactions. Higher RF powers could compensate for the lower quasi-particle residue and still create the ground state polaron (or a state closer to it) and therefore shift the observed signal to higher detunings. For repulsive interactions, the same reasoning suggests a *lower* extracted detuning for higher RF power though, in contrast to what we have observed. The interpretation of the power dependence is not clear yet, and the question deserves further investigation in

order to test the hypotheses stated above.

For reference, we also indicate the size of a vertical excitation in Fig. 4.13(a) with the almost horizontal, dotted gray lines. The slight slope is due to the density-dependence of the normalization factor E_n. As the bath-bath scattering length changes with the magnetic field, the bath density also changes. For all interactions, the observed shift is comparable or even well above the vertical level splitting. For a non-interacting system, one would expect the additional vertical level to not be relevant: while a transfer of atoms to a higher vibrational level might be energetically allowed, the RF photon does not carry enough momentum to make the spatial matrix overlap element non-zero. For the weak interaction within the bath, this reasoning still holds as the vertical Thomas-Fermi radius is smaller than the harmonic oscillator length. However, for the large bath-impurity interactions, the final state of the combined system will introduce small-scale correlations and therefore admixtures from higher vibrational states. Within this limit, the polaronic state can then probably be considered three-dimensional, while the surrounding bath environment still is two-dimensional with the respective excitation spectrum. Creating a purely two-dimensional polaronic state would in our system require vertical level splittings on the order of ∼60 kHz, which is out of reach for our experimental setup.

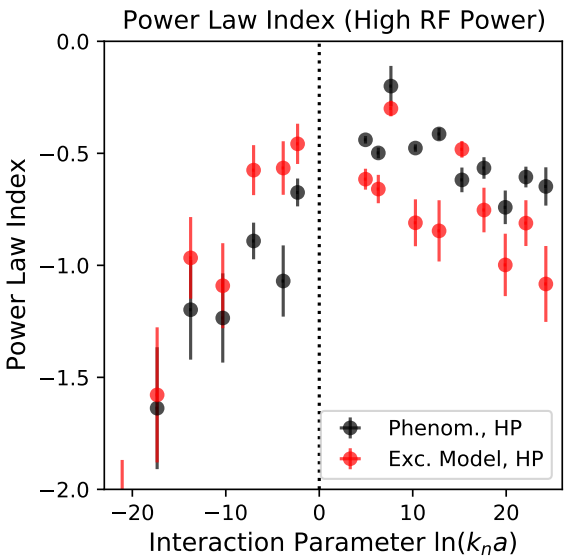

Figure 4.14: Extracted power law exponent for the signal decay for negative detunings for repulsive interactions and for positive detunings for attractive interactions. Only the extracted power law index for high RF power is presented, as the low RF power did not show visible decays and did hence not allow to extract a power law exponent. For attractive interactions ($\ln(k_n a) > 0$), the power law tends from ~ -1 at weak interactions to ~ -0.5 closer to the resonance, similar to what was observed in the 3D case. Repulsive interactions do not show a saturation for weaker interactions.

Fig. 4.14 shows the power law exponents for the signal decay for negative detunings at repulsive interactions and for positive detunings at attractive interactions. Only data obtained with high RF power is included here, as low RF power shows a very rapid drop off in the signal for the respective detunings and therefore does not allow to extract a power law exponent. The exponent usually ranges between ~ -1 at weaker interactions and -0.5 near the resonance, where the repulsive side shows a stronger dependence, but

also weaker signal, leading to larger uncertainties. It shows the same behavior as in the three-dimensional system, suggesting that the reason for this behavior lies within the short-range physics not strongly affected by the vertical confinement.

Summary

To summarize this chapter, we measured the polaron spectrum in a three-dimensional BEC as well as in a degenerate two-dimensional Bose gas.

In the three-dimensional case, we observe energy shifts in agreement with previously published results. Furthermore, we can reproduce the observed line shapes very well when introducing models that include significant contributions from excited states.

For two-dimensional degenerate Bose gases, where no such spectrum has been published so far, we extract peak shifts in agreement with theoretical predictions for low RF power and weak interactions. However, in contrast to the 3D case, we observe a strong dependence of the peak energy shift on the used RF power. Furthermore, the two-dimensional system does not show the well-separated repulsive branch present in the three-dimensional system. Instead, the spectrum shows similar behavior for attractive and repulsive interaction. By adapting our three-dimensional line shape models to two dimensions, we achieve good agreement with our observations, again supporting the relevance of transfers to excited states in our system.

The role of these excited states and the dependence on the RF power deserves further investigation. We suspect that these two observations are linked, and measuring the population in higher excited vertical states after the injection pulse might shed new light on the nature of these excited states, their creation, and on how they affect the bath system.

Chapter 5

Spatially Resolved Impurity and Bath Dynamics

The spectra presented in chapter 4 employ parameters characterizing the system as a whole, most notably the atom number loss and the reduction in condensate fraction. While this already provides valuable information, our setup allows us to go beyond the measurement of global observables and permits the spatially resolved observation of impurities within a 2D Bose gas for the first time. We can therefore observe the positions the impurities are created at and follow their subsequent dynamics.

The creation of impurities is expected to be possible when the applied RF detuning equals the local bath-impurity mean field shift. Since the atoms are trapped by a harmonic trap, the density varies and the resonance condition can only fulfilled at certain positions. By scanning the frequency, one should therefore be able to selectively create impurities at different positions, as shown in Fig. 5.1. However, our observations reported here support the ev-

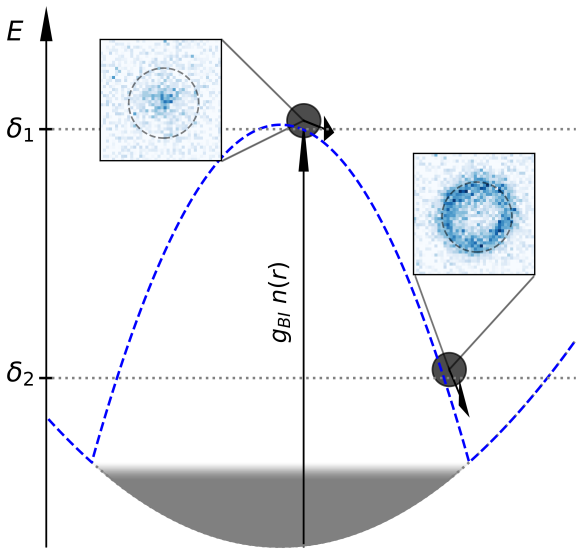

Figure 5.1: Sketch of the impurity creation for repulsive bath-impurity interactions. Impurity creation in the BKT cloud (gray) with density profile $n(r)$ trapped by an optical potential (thin gray line) is only expected to happen when the local mean field shift $g_{BI}n(r)$ (blue dashed line) equals the RF detuning δ. For a high detuning δ_1, this condition is fulfilled near the center of the BKT cloud, and for a low detuning δ_2 it is fulfilled near the edge. Insets illustrate the measured impurity densities. Upon creation, the repulsive interaction leads to an expulsion of the impurities.

idence for excited states discussed in the previous chapter 4. These excited states lead to impurities being created at positions not expected when only considering the mean field shift.

The impurity behavior after creation should differ significantly between repulsive interactions and attractive interactions: for the former, the impurities should be expelled from the bath upon creation, while attractive interactions should lead to a motion towards the center. As reported in Secs. 5.3 and 5.4 we were able to observe this expected expulsion from the bath and can model the motion within the condensate when including the two-dimensional friction term for speeds above the local speed of sound, which counteracts the expected acceleration. A potential disagreement with simulations performed by V. Singh and predicting much slower motion is currently being discussed and might be connected to a lower effective mass than expected or to self-trapping not observed in our experiments.

For attractive interactions, our measurements did not match expectations. Instead of the ring-like structures at low detunings as in the repulsive case, we observed nearly uniform excitation patterns. We interpret this as excited states being created at positions where the detuning is higher than the local mean field shift. These excited states are located closer to the center of the cloud, therefore "filling up" the hole of the expected ring-shaped impurity distribution. Furthermore, we observe a rapid loss of impurities, prohibiting us from reliably observing the expected inwards motion. We attribute these losses to three-body recombinations that become more severe for attractive interactions and therefore locally enhanced densities.

In summary, we achieved the spatially resolved observation of impurity creation and of the subsequent dynamics in a two-dimensional Bose gas with tuneable interactions for the first time.

The spatially resolved impurity creation is introduced in Sec. 5.1, followed by a discussion of the correlated bath-impurity dynamics in Sec. 5.2. Secs. 5.3 and 5.4 then focus on repulsive interactions and the expulsion of impurities from the bath. In Sec. 5.3, we test the possibility to extract the effective mass, and in Sec. 5.4 we focus on the initial dynamics within the condensate. Sec. 5.5 finally briefly discusses the dynamics observed for attractive interactions, which is dominated by rapid loss.

5.1 Potential Mapping

Before going into more detail for specific experimental settings, we briefly discuss some generic effects in tomographic measurements as illustrated in Fig. 5.2, where spatially and

frequency-resolved information becomes available. The top row (a) shows the impurity densities obtained after a short RF pulse of 300 µs and for repulsive interstate interactions, where the applied detuning with respect to the unshifted resonance frequency increases to the right. Near zero detuning, only atoms near the edge of the condensate can be flipped as the density-dependent energy shift is small, while for increasing detuning, atoms closer to the center of the bath become resonant as the repulsive interaction shift compensates for the detuning. With increasing detuning the region of maximum response therefore moves closer to the center until finally even the maximal shift is not sufficient anymore and no more atoms can be flipped. Similarly, Fig. 5.2(b) shows the densities for attractive interactions, now with the detuning *decreasing* from zero to the right. With increasing distance from the unshifted transition frequency, the impurities are more concentrated in the center. However, unlike in the repulsive case, no rings can be observed for any detuning.

The same data is shown as radially averaged data in Fig. 5.2(b), where the vertical axis corresponds to the detuning, and the spatial axis has been transformed into a bath-density axis by assuming a Thomas-Fermi profile. The observed density is color-coded. The remaining plots (c)-(h) show similar data for different interaction strengths, where the middle row corresponds to repulsive interactions and the bottom row to attractive interactions, and the interaction strength increases from the left to the right. The shown repulsive interaction parameters correspond to $\tilde{g}_{BI} \simeq 0.25$, $\simeq 0.28$, and $\simeq 0.55$, and the attractive ones correspond to $\tilde{g}_{BI} \simeq -0.21$, $\simeq -0.25$, and $\simeq -0.39$. Consistent with the spectra discussed in Sec. 4.2, stronger interactions lead to signal created at higher detunings.

Two potentially connected effects are clearly visible. The first effect is the clear difference in the spatial structure for repulsive and attractive interactions when applying radio-frequency of near zero detuning. For repulsive interactions, exemplarily shown for $\delta = 1$ kHz in the inset in Fig. 5.2(d), the impurities are created in a ring-structure at the edge of the condensate, where the density and thus the interaction shift is small. Attractive interactions, in contrast, show an almost flat impurity density even when being close to the unshifted resonance frequency. A typical image is shown in the inset of Fig. 5.2(g) for δ = -1 kHz, and the clear contrast to the repulsive case is evident. The same effect is present for all interactions as long as the maximum interaction shift is larger than the Fourier broadening of the RF-pulse, as is also visible in the radially averaged densities. The second effect is visible in Fig. 5.2(c) and (e), where a reappearance of signal strength can be observed for high detunings and central areas of the bath. We attribute this effect to vertically excited impurity states; additionally to the interaction shift, energy is

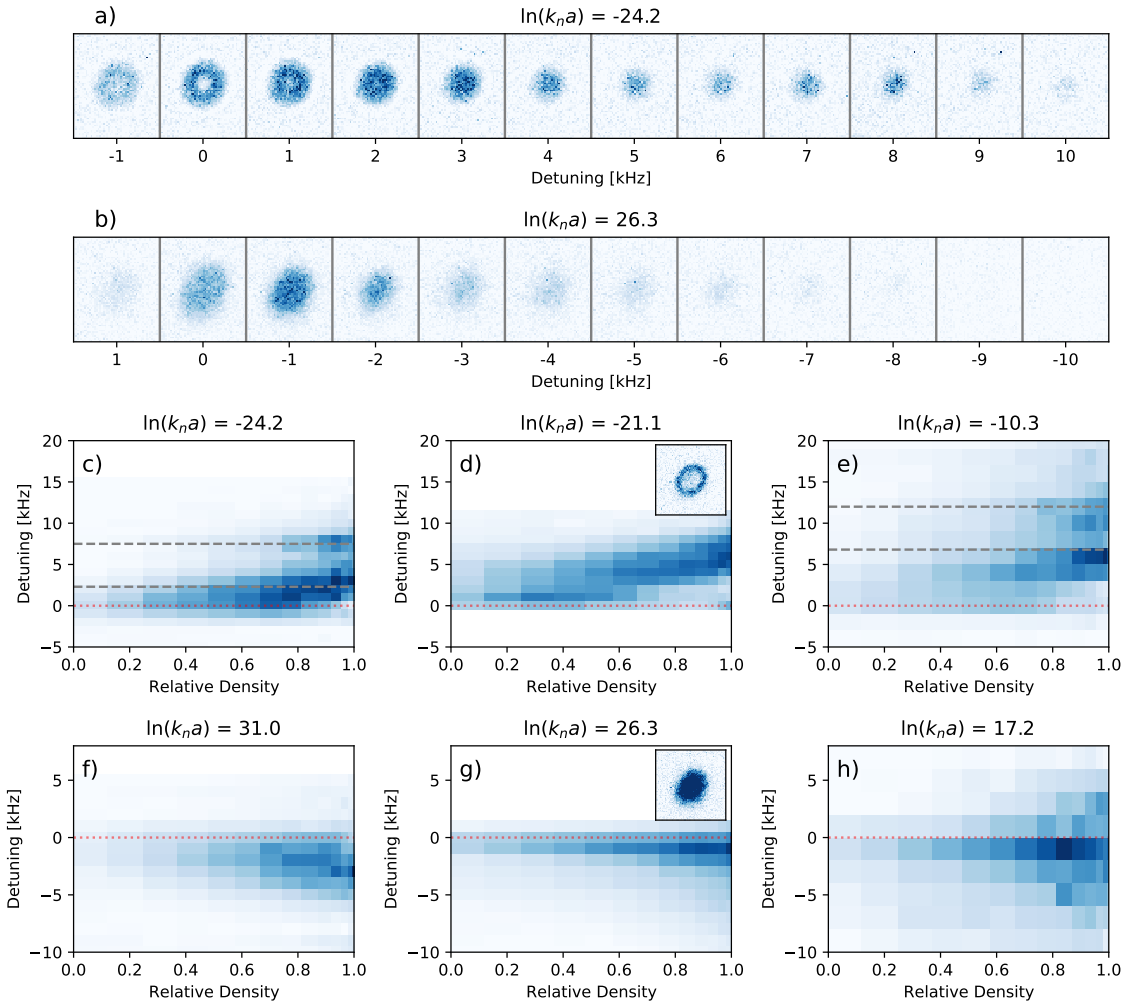

Figure 5.2: Frequency- and spatially resolved impurity imaging for different interaction strengths. **a)** and **b)** Impurity density distribution for different detunings at a repulsive interaction parameter of $\ln(k_n a)$ = -24.2 ($\tilde{g}_{BI} \simeq 0.25$) and at an attractive interaction parameter of $\ln(k_n a) = 26.3$ ($\tilde{g}_{BI} \simeq -0.25$), respectively. For repulsive interactions, higher detuning leads to impurity creation closer to the center of the cloud. Similarly, attractive interactions show the same behavior for more negative detuning. However, the ring structure near zero detuning can only be observed for repulsive interactions and not for attractive interactions. **c) - h)** Radially averaged frequency-resolved impurity densities for different repulsive (**c)-e)**) and attractive (**f)-h)**) interactions, where the interaction strength increases from left to right. The relative density displayed on the x-axis is calculated by assuming a Thomas-Fermi profile. For the repulsive interactions, a detuning near zero leads to impurities created at low density. With increasing detuning, the peak response moves closer to the center of the cloud. **c)** and **e)** also clearly show a revival of signal for high enough detunings, which we interpret as excited states. The dashed gray lines in **c)** and **e)** have a distance of 5.2 kHz, corresponding to the frequency difference one would expect for vertically excited states. The insets in **d)** and **g)** show typical impurity densities obtained near zero detuning, where repulsive interactions exhibit a ring-like structure, while attractive interactions lead to an almost flat profile. While the ring can immediately be understood as the edge of the condensate, where the density and thus the local interaction shift is small, the interpretation of the flat profile in **g)** is less clear and is discussed in the main text.

transferred into a vertical excitation.

With a trapping frequency of $\nu_z \simeq 6.5$ kHz, and a density overlap of 80% (calculated assuming a harmonic confinement) between the vertical ground state and the first excited state, we expect an energy shift of ∼5.2 kHz. This difference is marked by the two horizontal dashed lines in Fig. 5.2(c) and (e), showing that this expectation agrees very well with the data obtained for $\ln(k_n a) = -10.3$, but a slightly smaller difference is observed for $\ln(k_n a) = -24.2$. The reason for this difference is not clear, but could be connected to the implicit assumption that the interaction shift scales linearly with the density overlap.

The question arises if vertically excited states can explain the flat density profile for the attractive interactions. For attractive effective potentials and $\delta = 0$ kHz, a vertically excited state would be located further within the condensate, roughly where the mean field shift equals 80% of $\hbar\omega_z$, i.e. $\delta_{res} \simeq 5.2$ kHz. Together with the frequency broadening due to the final pulse time, the imaging resolution, and potentially some dynamics between creation and observation of the impurities, this might lead to the observed almost flat profile. However, this idea is somewhat contradicted by the positive detuning data: for positive detunings of, e.g., $\delta \approx \nu_z/2$ one would expect that vertically excited but radially not confined states can be created. The local detuning would be smallest near the edge of the condensate, and thus the impurity imaging should show a ring-like structure again. Instead, we observe the strongest population near the center when applying positive detuning (Fig. 5.2(h)).

One possible explanation might be that the probability for a $\delta n_z \neq 0$ transition increases with higher density. An increasing probabilty for $\delta n_z \neq 0$ transitions with density would, for example, be expected when the interacting final state shows a significant distortion of its vertical profile. The distorted vertical profile corresponds to contributions from different levels of the vertically confining potential. A "vertically excited polaron" living, for example, mostly on $n_z = 1$ could therefore also have significant contributions from the $n_z = 0$ level and the overlap to the bath $n_z = 0$ would be rather large. For the higher densities near the center, the distortion should be come larger, leading to more overlap and hence more signal. Alternatively, the flat profile might have a completely different origin and not be connected to the vertically, but rather to radially excited states, where the local density distribution around the impurity atom is not in its ground state. In this case, it would be surprising that we do not observe similar effects in the repulsive case. At the time of writing, we are not able to confidently distinguish between these or other scenarios, and the question deserves further investigation.

5.2 Time-Resolved Dynamics and Bath-Impurity Correlation

In the tomographic measurement shown in Fig. 5.2, the short RF pulse time was immediately followed by imaging the impurity density in order to extract the initial distribution as well as possible. Our setup also allows us to vary the time delay between creation and observation and gives access to temporally resolved dynamics. This is exemplarily shown in Figs. 5.4 and 5.5, where the dynamical evolution over a few milliseconds is shown for repulsive and attractive interactions and near zero detuning, respectively. Both figures show the real-space density of both bath and impurity in a false-color image in the top row (see Fig. 5.3 for a color scale) and the bath depletion (i.e. change in bath density compared to reference runs without RF pulse) in the middle row.

The false-color images were obtained by imaging the impurity and the bath density in independent measurements with different imagings enabled, but with otherwise the same settings. With higher time resolution, the bottom row shows the radially integrated density depletion of the bath (left) and the impurity density (right) in the bottom row.

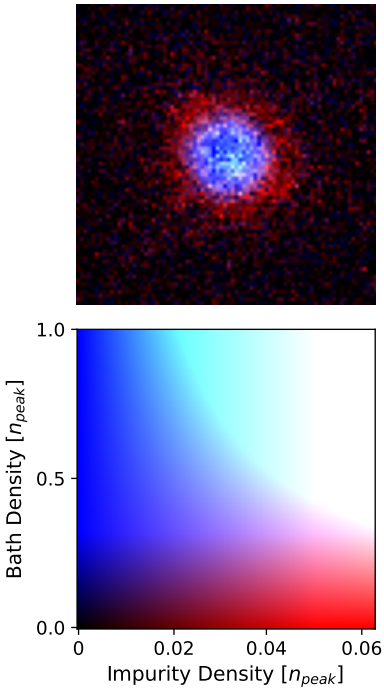

Figure 5.3: Colormap for the false-color images showing both the bath density (blue) and the impurity density (red). **Top**: False-color image of a cloud with repulsive interactions. **Bottom**: Color map showing what densities the colors correspond to.

Attractive and repulsive interactions lead to drastically different dynamics. Repulsive interactions lead to an expulsion of the impurity fraction from the condensate, which is clearly visible in the two-color images in the top row of Fig. 5.4. The initial strong overlap reduces within ∼2 ms to almost zero, and then increases again after the impurities have reached their turning point in the optical trap and return to the center. At the same time, a density-depletion wave propagates through the bath, reaching the center after ∼2 ms, and then propagating outwards again. Furthermore, a weak bath component increase can be consistently observed just outside the bath radius (best visible around 8 µm in the bottom left of Fig. 5.4, or weakly as a brighter ring in the middle row of the same figure). We attribute this to a cold, but thermal component created by removing a fraction

of the initial condensate via the RF-pulse and its subsequent dynamics.

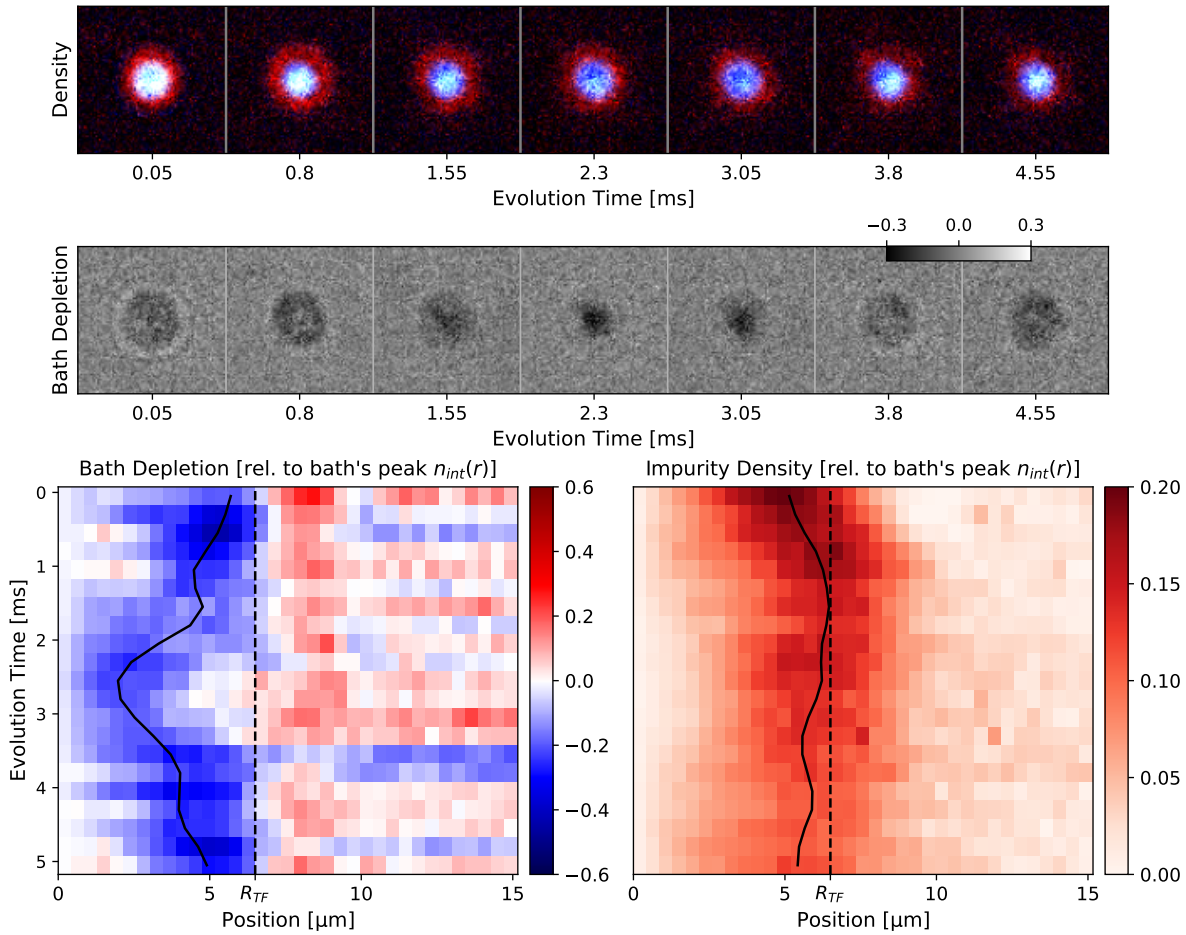

Figure 5.4: Correlated bath and impurity densities for repulsive interactions at $\ln(k_n a) = -10.3$ ($\tilde{g}_{BI} \simeq 0.55$). **Top row**: false-color image of superimposed bath (blue) and impurity (red) densities for different evolution times after an RF-pulse with near zero detuning. Overlapping densities are shown as white. Even without the qualitative analysis, this image already shows some aspects of the general behavior, like the expulsion of impurities in the first ∼2 ms and their return around 4 ms. **Middle row**: bath depletion, i.e. density difference with respect to reference runs with disabled RF pulse. Reduced densities are shown by a darker shade, increased density by a brighter shade of gray, ranging from -30% to +30% of the peak density. The impurity creation induced an oscillatory motion, similar to a breathing mode. **Bottom row**: radially integrated bath density depletion (left, reduced density in blue, increased density in red) and impurity density (right), where the x-axis indicates the radial position and the y-axis is the evolution time (running from top to bottom). The vertical dashed lines indicate the Thomas-Fermi radius in equilibrium and the solid lines indicate the maxima of depletion and impurity density in the left and right plot, respectively. The data is normalized to the peak integrated line density of $\sim 10^3$ μm^{-1}, reached at $R_{TF}/\sqrt{3}$. At low detunings, the created impurity fraction is expelled from the condensate and starts oscillating in the effective potential formed by the repulsive condensate and the optical potential: the maximum extent is reached around 2.5 - 3 ms, and they return closer to the trap center at ∼5 ms; at the same time, the bath exhibits an oscillation with about twice the frequency of the impurity component.

In the case of an attractive interaction, on the other hand, we observe a rapid loss of

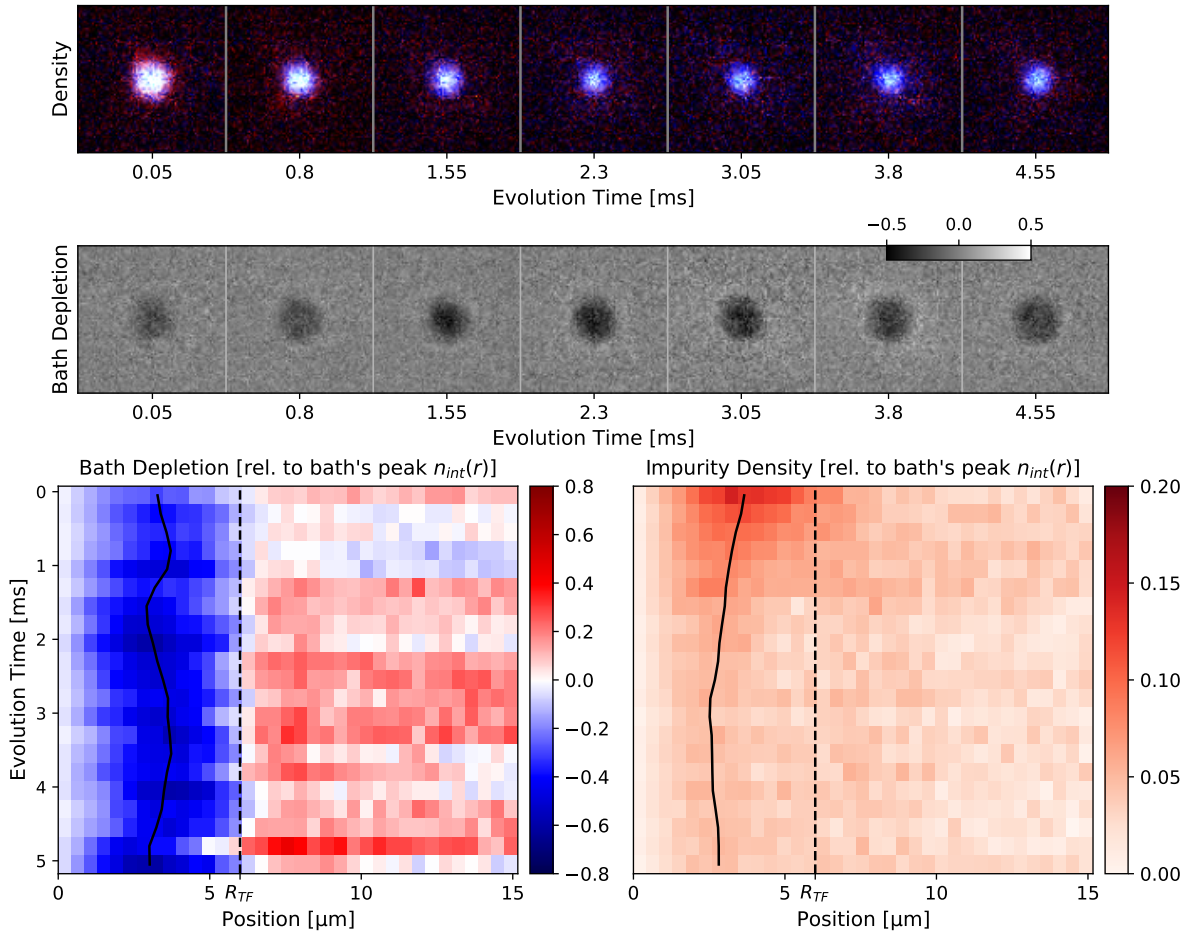

Figure 5.5: Correlated bath and impurity densities for attractive interactions at $\ln(k_n a) = 15.3$ ($\tilde{g}_{BI} \simeq$ -0.49). **Top row**: false-color image of superimposed bath (blue) and impurity (red) densities for different evolution times after an RF-pulse with near zero detuning. Overlapping densities are shown as white. The impurity component shows a rapid loss, especially in the outer regions. We attribute this to an inward motion due to the attractive bath-impurity interaction and subsequent losses in the dense center of the trap. **Middle row**: bath depletion, i.e. density difference with respect to reference runs with disabled RF pulse. Reduced densities are shown by a darker shade, increased density by a brighter shade of gray, ranging from -50% to +50% of the peak density. Compared to the repulsive interaction, very little dynamics is visible: after an initial loss, the depletion profile is rather constant. **Bottom row**: radially integrated bath density depletion (left, reduced density in blue, increased density in red) and impurity density (right), where the x-axis indicates the radial position and the y-axis is the evolution time (running from top to bottom). The vertical dashed lines indicate the Thomas-Fermi radius in equilibrium and the solid lines indicate the maxima of depletion and impurity density in the left and right plot, respectively. The data is normalized to the peak integrated line density of $\sim 10^3$ µm^{-1}, reached at $R_{TF}/\sqrt{3}$. As already visible in the top row, the attractive interactions lead to an inward motion of the impurities at initial times. However, the rapid losses with a time scale of $\lesssim$1 ms prohibit the observation of the expected oscillatory behavior within the bath. We attribute the rapid losses to three-body recombinations in the dense cloud.

impurity signal with a millisecond timescale; at the same time, the central bath density

reduces and the density of a thermal bath component increases, indicating three body losses and subsequent heating. This is consistent with the strong signal observed for attractive interactions in the spectra discussed before.

5.3 Repulsive In-Trap Oscillations

As shown in the two previous sections, the upgraded setup allows us to extract more information than just the integrated parameters observed in time-of-flight before and discussed in chapter 4. In this section we report on the attempt to utilize the high spatial resolution to extract another fundamental parameter of the impurity system: the effective mass, which is expected to differ from the bare mass and to increase with the interaction strength. For repulsive interactions, this increased mass should lead to a signature in the impurity momentum distribution after the expulsion from the condensate. More specifically, we compare the energy provided by the RF pulse with the kinetic and potential energy of the impurities after expulsion - the effective mass should lead to a difference between these energies.

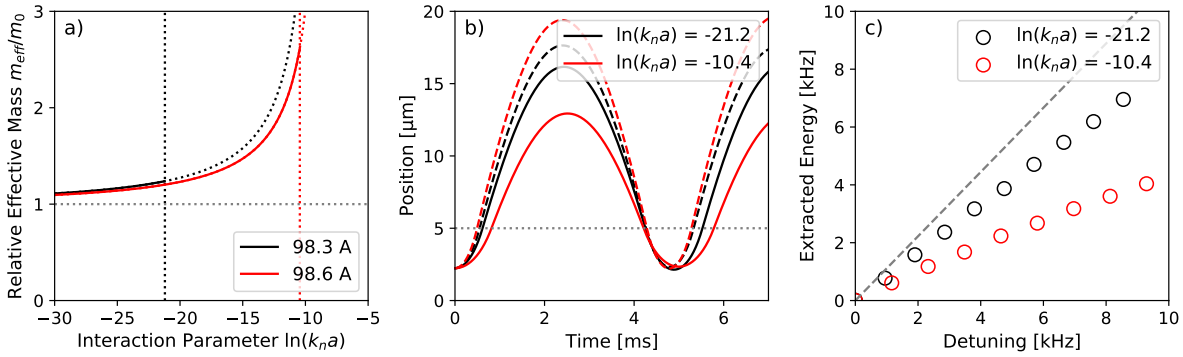

Figure 5.6: Effective mass and its possible signatures. **a)** The effective mass as calculated on mean field level in [123] for two different currents and thus two different peak interaction strengths. As the interaction parameter $\ln(k_n a)$ depends on the density, the effective mass varies within the condensate. The solid parts of the lines correspond to the densities and hence interaction parameters achievable in our experiment while the dotted parts can not be reached. **b)** Trajectory of a classical particle in the combined potential of repulsive bath and attractive optical trap when neglecting the effective mass (dashed lines) and when including the effective mass (solid lines) for two different peak interaction strengths (black/red), i.e. interaction strength at the highest density of the cloud. **c)** Extracted energy by extracting the peak potential energy of the classical trajectories, where the difference to the energy provided by the RF-pulse (dashed line) contains information about the effective mass.

Effective Mass As the bath density around an interacting impurity changes, a propagating impurity will also lead to a density redistribution within the bath, thus influencing the dispersion relation of the propagating polaron state. To lowest order, the effective mass can be expressed as

$$m_{eff} = m_0 \left[1 - \frac{\ln(4\pi) - \ln(k_n a_{BB})}{2[\ln(4\pi) - \ln(k_n a_{BI})]^2} \right]^{-1}, \tag{5.1}$$

and becomes larger inside the condensate where the density, and therefore $k_n \propto \sqrt{n}$, increases [123]. For parameters typical for our experimental setup, the relative effective mass m_{eff}/m_0 calculated by Eq. 5.1 is shown in Fig. 5.6(a) and might reach values up to ∼2.5 times the bare mass m_0. The two different currents correspond to different interstate scattering lengths and to different peak interaction parameters; since the bath-bath scattering length also varies slightly, the two curves do not collapse exactly.

Within a classical model, the force acting on an impurity atom within the repulsive bath is determined by the experimentally determined maximum energy shift and the size of the cloud. Assuming that the energy shift is proportional to density, one has $F(r) = [U_{max}/R_{TF}^2] \cdot r$, i.e. no dependence on the effective mass. The acceleration $a = F/m_{eff}$ then depends on the location within the condensate as the force increases towards the edge of the condensate while the mass decreases. Compared to the case of $m_{eff} = m_0$, the acceleration starts at a lower value near the center of the trap, but reaches the same value near the edge, and the impurity therefore exhibits a lower final speed. For a classical particle, this is visualized in Fig. 5.6(b), where the dashed lines correspond to $m_{eff} = m_0$, and the solid lines include the effective mass as predicted by the expression above. The lower final speed upon leaving the condensate corresponds to a lower kinetic energy than classically expected and it is this kinetic energy that we will here focus on. Note that the effective mass also slows down the dynamics within the condensate, thus increasing the effective oscillation period.

Impurity Energy Extraction The approach to extract the impurity's energy is essentially a T/4- or momentum measurement [169–172]: in a classical model, the impurity atoms climb the potential hill formed by the attractive optical potential until reaching their turning point, where all their kinetic energy is converted into potential energy and they subsequently roll down into the optical trap again. Quantum mechanically, the evolution within a harmonic potential corresponds to a rotation in phase space, where an evolution for a quarter of the trapping period equals a rotation by 90°, and thus maps the initial momentum distribution into a spatial distribution and vice versa. In our case, there are two main differences to the usual T/4-measurement. Since the goal is to extract the total energy, the needed rotation in phase space is not necessarily 90°: as the relevant "initial" point is the exit of the impurity from the condensate, the impurity's energy consists of both kinetic and potential energy already, and we therefore probe different evolution times and not only $t = 1/(4\nu)$. The second difference is that the effective potential is only harmonic outside the repulsive bath. Thus, only evolution times up to at most $t \approx 1/(2\nu)$ are expected to follow the simple rotation in phase space.

To extract the impurity energy, we compare two different approaches with the first one being the density-weighted potential energy and the second one only focusing on the energy of peak of the impurity distribution. In both cases, the data processing is analogous to the processing discussed in Sec. 5.4. In short, the average impurity distribution is extracted by averaging several runs and from this, the radially integrated density $n_{int}(r) = \int n(r,\phi)d\phi$ is extracted. A typical run taken at a bath-impurity interaction of $\ln(k_n a) = -10$ and $\delta = 4$ kHz is shown in the inset of Fig. 5.7(a), where the x-axis is time, the y-axis is the radial position and the density is color coded. The spatial distribution already shows the oscillation very clearly. The total energy is extracted for the two interstate interaction strengths $\ln(k_n a)$ = -21 and $\ln(k_n a)$ = -10, and several radio-frequency detunings for each interaction strength. The results are shown in Fig. 5.7, where subplot (a) and (b) use the peak position energy and the density weighted energy, respectively.

In the latter case and for each evolution time within the trap, the time-resolved potential energy can be extracted as

$$E_{pot}(t) = \frac{\frac{1}{2}m_0\omega^2 \int n_{int}(r)r^2 dr}{\int n_{int}(r)dr}. \tag{5.2}$$

In a purely harmonic case, one has $E_{pot}(t) = E_{pot}^{max}(t) \cdot \sin^2(\omega t)$, which in our case should be modified due to the repulsive condensate in the center of the trap. Nevertheless, the maximum potential energy reached will correspond to the total energy of the impurity when leaving the condensate. Fig. 5.6(c) shows the expected values to be extracted for realistic experimental parameters and a classical particle's trajectory.

Note that the presence of the repulsive bath should introduce some effects not accounted for in the simple oscillatory fit. As the impurity returns to the condensate, it will enter it and again acquire an effective mass. This changing effective mass leads to an effective dampening of its motion and to a loss of energy. Additionally, the dynamics within the condensate is slower due to the larger effective mass, mathematically equivalent to a spatially dependent rescaling of the temporal variable. In a very coarse approach, the significance of these effects for the comparably short timescales probed here is estimated by fitting a damped oscillation. While describing the data slightly better, this provides very similar results for the extracted energies. The damping timescales are usually around 5 ms, both when working with the total potential energy and when working with the density peak position.

The energy obtained from the simple oscillatory fit (shown in Fig. 5.7(b)) is very close to the energy provided by the RF pulse, which is indicated by the gray line. A statistically significant deviation only appears for rather large detunings, where impurities are created

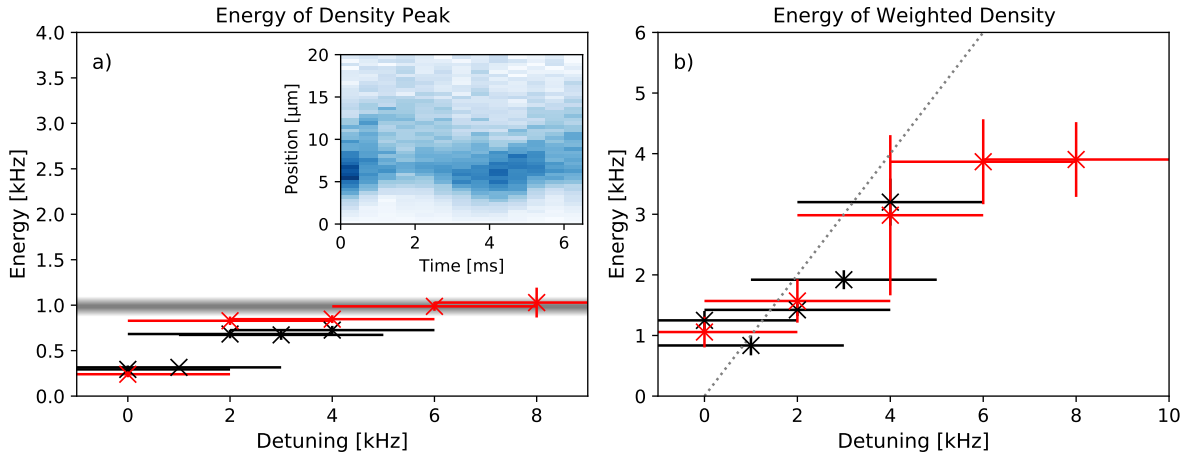

Figure 5.7: Extracted energies from the mapping of the kinetic to potential energy. **a)** Energy extracted from the position of the density peak with an inset showing the radially integrated density for $\ln(k_n a) = -10$ and $\delta = 4$ kHz. The gray line indicates the energy corresponding to an initial speed equal to the peak speed of sound. **b)** Density-weighted integrated potential energy as described in the main text. In both plots, the black data corresponds to $\ln(k_n a) = -21$ and the red data to $\ln(k_n a) = -10$. The x-error bars indicate the frequency width due to the Fourier broadening of the RF pulse and the y-error bars originate from the fit result uncertainty. Only the highest detunings show a significant deviation from the supplied energy by the RF pulse.

near the center of the trap, making the extraction of the difference energy $\Delta E \equiv h\delta - E_{pot}^{max}$ very challenging. Note that even for zero detuning, i.e. when addressing unshifted atoms, a nonzero energy is extracted. We attribute this to the finite pulse width, resulting in a Fourier broadening of the pulse of ∼2 kHz.

The second measure, i.e. the potential energy of the density distribution peak, provides the data shown in Fig. 5.7(a). Within a classical model, atoms positioned at the density peak will stay at the density peak, and the potential energy at the maximum position should correspond to the total energy, which is in stark contrast to the data obtained from the energy extracted by Eq. 5.2. The energy extracted from the density peak shows very little variation and only a rather small difference for the tested interaction strengths. As a reference, the gray bar indicates the energy of a particle leaving the condensate at $R_{TF} \simeq 5$ µm and with a speed between 2.5 µm/ms and 3.2 µm/ms. The extracted values for $\ln(k_n a) = -10$ are close to this classical expectation, while the data from $\ln(k_n a) = -21$ is compatible with initial speeds of ∼1.5 µm/ms. This value is close to the speed of sound in our sample, which will be discussed in more depth in Sec. 5.4.

Results The saturation observed in the integrated potential energy suggests to probe even higher detunings. However, this proved to be challenging: when approaching the peak detuning, the total number of atoms rapidly decreases as the resonant volume

shrinks. The increased density at the center does not compensate for the reduced volume and hence the signal to noise ratio decreases significantly. Furthermore, the higher peak potential energy corresponds to larger radii and hence a larger area the signal is spread out in, further decreasing the signal-to-noise. The combination of these two effects severely limit the applicability of this approach for detunings close to the maximum shift observed in the spectra in Sec. 4.2.

In conclusion, the approach to measure the transferred energy does not seem convincing for extracting parameters like the effective mass. The main reason for this is the low signal-to-noise ratio introduced by the dilute density near the classical turning point, which is amplified by the r^2-factor when extracting the integrated energy, leading to large uncertainties in the final results. While Fig. 5.7(b) shows an onset of the behavior expected from Fig. 5.6(c), this is mostly relying on the last two data points. As already discussed before, probing even higher detuning is very challenging due to the even lower total amount of impurities created and the larger maximal radius they are expected to reach. Probing longer evolution times also does not seem promising: due to the Fourier broadening, the initial positions and energy will have a certain width; and hence, the "delay" introduced by the propagation in the condensate is different for different initial conditions, leading to a dephasing with time.

Instead of following this indirect approach of extracting the total energy further, we decided to instead focus on short evolution times, and directly probe the propagation within the condensate.

5.4 Repulsive Expulsion Dynamics

The following section will focus on the spatially resolved dynamics for short evolution times, where all or a large fraction of the impurity component is still within the Thomas-Fermi radius of the bath. The main observation is that the expected accelerated motion due to the repulsive harmonic potential is not observed; instead an almost constant velocity near the peak speed of sound is extracted. Classical and quantum-mechanical simulations indicate that the observed speeds can be explained when taking into account the two-dimensional friction term derived in [173], while the corresponding three-dimensional expression does not fit the expectations.

We first discuss the experimental procedure used, followed by a detailed discussion of the data processing and parameter extraction. These results are then discussed and compared with results obtained from our simulations. The chapter thereafter is briefly discuss the possibility to extend this scheme to attractive interactions.

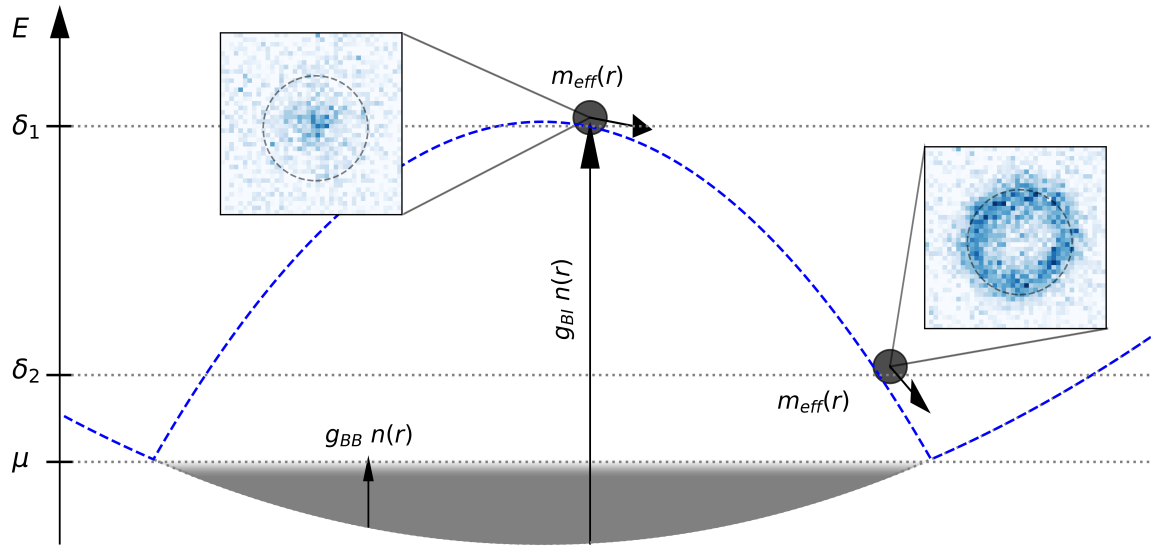

Figure 5.8: Sketch of the experimental setting. Confined by an optical potential the atoms of the bath state form a condensate (shaded gray area). The density distribution is determined by the bath-bath interaction parameter g_{BB}. The potential experienced by a single impurity, in contrast, is determined by the bath-impurity interaction parameter g_{BI}, which in this experiment is usually much larger than g_{BB}. As the interaction shift on mean field level is $\Delta E = g_{BI} \cdot n$, the impurity experiences a strongly repulsive potential hill. When a radio-frequency pulse with a detuning δ_1 close to the maximum shift $g_{BI} n_{peak}/h$ is applied, only impurities near the center of the cloud can be created. A detuning δ_2 closer to the unshifted transition frequency will create impurities closer to the edge of the cloud, where the interaction shift is smaller due to the lower density. After creation, the impurities are expelled from the condensate and will eventually settle between the repulsive bath and the walls provided by the optical potential.

5.4.1 Experimental Procedure

A rough sketch of the experimental procedure described in the following section is depicted in Fig. 5.8. The two-dimensional degenerate cloud, created as described in more detail in Sec. 3.3.2 and confined by an optical trap, forms the bath with interaction parameter g_{BB} between bath atoms; this interaction parameter together with the trapping parameters determines the density profile of the bath cloud. While the effective potential experienced by the bath atoms is, within the Thomas-Fermi approximation, flat, an impurity atom with interaction parameter $g_{BI} \gg g_{BB}$ will experience a strongly repulsive potential formed by the bath cloud. By applying a radio-frequency pulse of suitable frequency, a fraction of the bath atoms can be flipped to another spin state ("impurity state"); and as the interaction shift depends on the density, impurities can be created selectively at different positions by varying the detuning. For near zero detuning, for example, only atoms near the edge of the condensate can be flipped, and the resulting density distribution becomes a ring. For higher detuning near the maximum shift, only atoms near the center of the bath can be transferred to the impurity state.

The shown experiments were performed with $N \simeq 3000$ atoms confined by a radial trapping frequency of $\nu_r \simeq 110$ Hz and a vertical trapping frequency of $\nu_z \simeq 6500$ Hz, leading to peak densities of $n_0^{2D} \simeq 75 - 100$ µm^{-2}. Within the probed region of the bath-impurity Feshbach resonance, the bath-bath interaction parameter $\ln(k_n a_{BB})$ varies between $\sim$-400 and $\sim$-200, corresponding to coupling parameters of $\tilde{g} \simeq 0.02$; the chemical potential μ/k_B in the same region ranges between $\sim 20-30$ nK. The impurity-impurity interaction ranges between $\ln(k_n a) \simeq$-20 and $\ln(k_n a) \simeq +20$, thus entering the regime of $\tilde{g}_{inter} \gtrsim 1$.

The experimental procedure starts with the preparation described in Sec. 3.3.2. After the degenerate cloud has been transferred into the two-dimensional geometry and a short subsequent evaporation to remove any possible heating from the transfer, the field is ramped to the value of interest. After an additional short waiting time to allow eddy currents to decay, a radio-frequency pulse of either 300 µs or 500 µs duration is applied, corresponding to Fourier widths of 3.3 kHz or 2 kHz, respectively. Scattering might of course lead to faster decoherence and further broadening. Both this frequency broadening as well as the finite pulse time lead to an effective spatial broadening in the initial distribution of impurities. A variable evolution time of usually 50 - 550 µs follows the RF pulse, and finally the impurity atoms are imaged on the transition discussed in Sec. 3.3.4. No time-of-flight is used as we are interested in the in-situ distribution.

5.4.2 Data Processing

Typical density images obtained for the explained procedure are shown in Fig. 5.9. These pictures show the impurity density for variable detunings (rows) and different evolution times after the end of the radio-frequency pulse (columns). The dashed circle indicates the rough size of the condensate obtained from other measurements. For low detunings, impurities are created near the edge of the condensate where the local density and hence the interaction shifts are small. With increasing detuning, the resonance region moves further towards the center until the signal vanishes when the detuning becomes too large. The density profile at 6 kHz detuning shows the dynamics especially clearly: the impurities are created within the condensate at about half the Thomas-Fermi radius, and the center shows no impurities as the interaction shift is too large. Within the next few hundred microseconds, the impurities are expelled outwards by the repulsive potential they experience due to the inhomogeneous density, and the initially small "hole" continuously becomes larger. The same data is also presented in the bottom row of Fig 5.9, where the radially integrated density $n_{int}(r)$ is shown. For each of the subplots, the x-axis corresponds to the evolution time and the y-axis corresponds to the radial distance from the center, while the population is color coded. In both the raw images and the radially integrated density profiles, the expulsion is clearly visible.

In the following section, the main observable in the time- and spatially resolved measurements will be the peak position of the impurity density distribution, and it will be used to define an effective speed. The choice to focus on the peak position is motivated by the classical model for the system: when neglecting any back reaction and assuming that the local potential is proportional to the density of the bath, a classical impurity particle initially created at radius r_0 and without initial momentum will experience a harmonic anti-trapping potential. The trajectory of the impurity formally corresponds to a harmonic motion with an imaginary trapping frequency ω, i.e. $r(t) = r_0 \cdot \cosh(\omega \cdot t)$. This solution is of course only valid as long as the impurity is within the condensate. When generalizing this to a distribution of classical, non-interacting particles initially at rest, it is straightforward to verify that the peak of the radially integrated density will also follow the same time evolution as a single particle.[1] Motivated by this classical model, we will focus on the peak position of the radially *integrated* density as our main observable.

One possible way to extract the peak position would be to fit the images directly with a ring-like gaussian distribution of functional form $n(r, \phi) = n_0 \cdot \exp\left[-2 \cdot (r - r_0)^2 / w^2\right]$, where $n(r, \phi)$ is the density in radial coordinates, n_0 is the amplitude, r_0 is the center

[1] Note that this is not the case for the peak of the radially *averaged* density, as the density is spread out over a larger volume when propagating outwards.

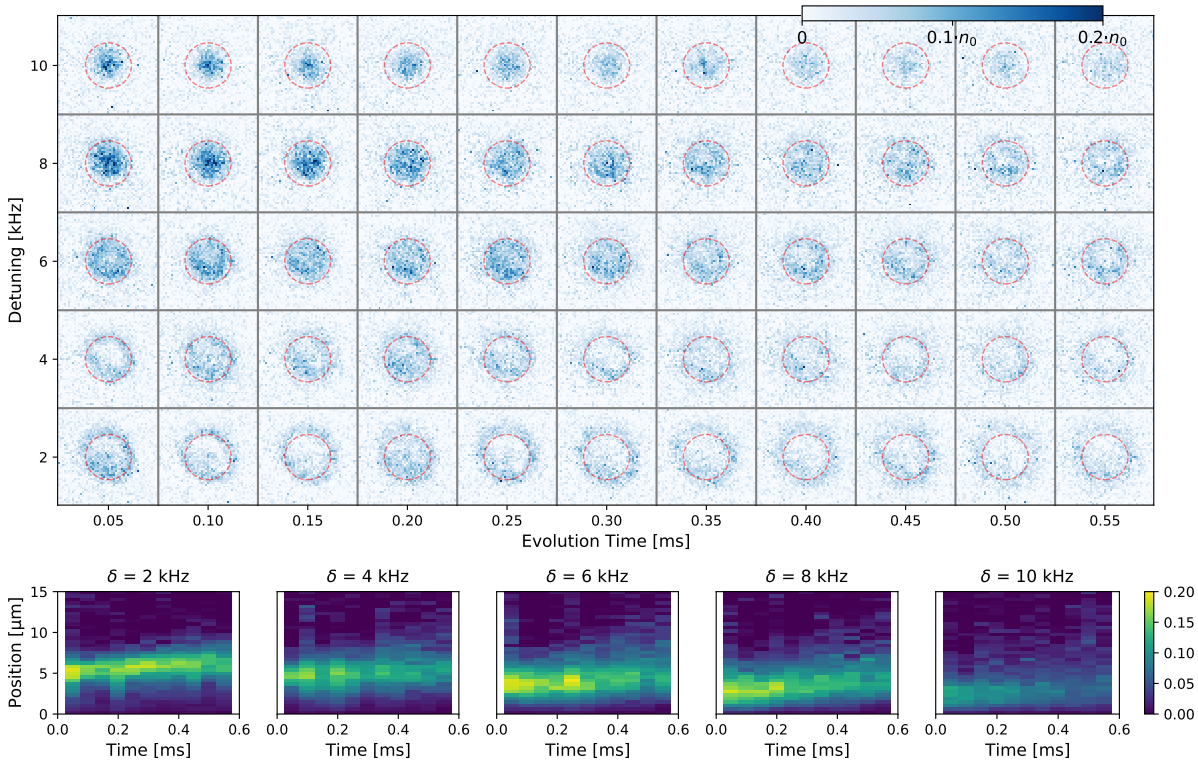

Figure 5.9: Raw impurity density images (top) and radially integrated impurity density profiles (bottom) for repulsive bath-impurity interactions leading to the expulsion of impurities. For this data, the two-dimensional coupling parameters are $\tilde{g}_{BB} \simeq 0.02$ and $\tilde{g}_{BI} \simeq 0.48$ as peak values, i.e. at the center of the trap. **Top part**: Raw density images for different detunings (rows) and evolution times (columns), where the impurity density is color coded. The size of the bath cloud (not visible) is indicated by the red circle. With progressively higher detunings, the impurities are created closer to the center, where the density and therefore the interaction shift is higher. Once created, the impurities start propagating on the repulsive potential and are being expelled from the cloud. This is best visible for a detuning of 6 kHz, where the initially small density depletion in the center is becoming larger as the impurities move further outwards. Similarly, the central hole is only forming after ∼350 µs for a detuning of 8 kHz. After leaving the cloud, the impurity atoms are trapped between the repulsive bath and the attractive optical potential. **Bottom row**: Radial integral of the above data, the outwards propagation is also clearly visible. Within each subplot, the horizontal axis is the evolution time and the vertical axis is the radial position, while the integrated density is color coded, normalized to the peak line integral of the bath density. The radial integral always shows low density at the center due to the vanishing volume.

radius and w is the waist of the ring. While this expression works well for small detunings (e.g. $\delta = 4$ kHz in Fig. 5.9), it fails to extract the radius once the ring becomes small enough to not show a clear depletion in the center anymore. In this case, the extracted parameters r_0 and w become strongly correlated and each individually is not extracted reliably anymore.

Instead, we choose to work with the radially averaged density, as this allows a more reliable extraction of the peak position. In the following paragraph, the extraction pro-

cedure and some relevant details will be discussed in more detail. First, the center of the density profile is extracted by a Gaussian fit. The individual pixel values are then sorted by their distance to the center position. The mean of those values then provides the averaged density $n_{av}(r)$ for each radius[2], and we then estimate the radial integral with the analytical expression $n_{int}(r) = 2\pi \cdot r \cdot n_{av}(r)$.

Fig. 5.10 shows the extracted radial densities $n_{int}(r)$ for the data also presented in Fig. 5.9. To extract the peak position of the impurity density, we fit an analytic profile to the density distribution and use

$$n_{int}(r) = A \cdot r^{\alpha} \cdot \exp(-r\alpha/\lambda) + n_B, \tag{5.3}$$

where A, α, λ and n_B are free parameters to be fitted. Including the exponent α within the exponential function has the advantage that the peak position coincides with the value of λ, as can easily be shown analytically[3]. The individual subplots of Fig. 5.10(a) show the extracted radial densities for different detunings (rows) and evolution times (columns), where the time is always referencing to the start of the RF pulse, which lasted 300 µs in the data shown. The dashed black line in each plot is the fit with the described analytical model, and the vertical dotted line indicates the extracted peak position from this fit.

The extracted peak positions for the different detunings of this data set are shown in black in Fig. 5.10(b). In addition, the peak positions obtained with the same procedure of another experimental run is shown, where the RF power lasted for 500 µs instead of 300 µs. Two main features are visible: the collapse of the 300 µs and the 500 µs data onto a single line when referencing the time variable with respect to the onset of the RF pulse, and the surprisingly linear behavior for each of the time traces.

Curve Collapse Choosing the RF pulse time is a trade-off between the desired energy resolution and the probed evolution times: lower RF pulse times allow us to probe shorter evolution times, but reduce the energy resolution and probe larger regions of the cloud.

[2]It is also possible to obtain the radially integrated signal by summing the values within each position bin, but this turned out to be more prone to systematic errors: due to the discretization of the image, it is not guaranteed that each radial position has the correct number of contributing pixels, and therefore it is also not guaranteed that $n_{int}(r)$ grows linearly with r. This deviation drops out in the average, but will introduce systematic errors when just integrating the values. A possible way to mitigate this effect is to suitably rescale the summed value by the ratio of expected to actually extracted contributions. To avoid this issue, we chose to first obtain the averaged density $n_{av}(r)$ from the data before proceeding in the same way as described in the main text.

[3]Not including it in the exponential in contrast leads to the peak position to depend on both α and λ. Estimating its uncertainty is not straightforward though, as the errors σ_α and σ_λ are strongly correlated and Gaussian error propagation is not applicable. Using the above definition disentangles this and directly provides an error estimate for the peak position.

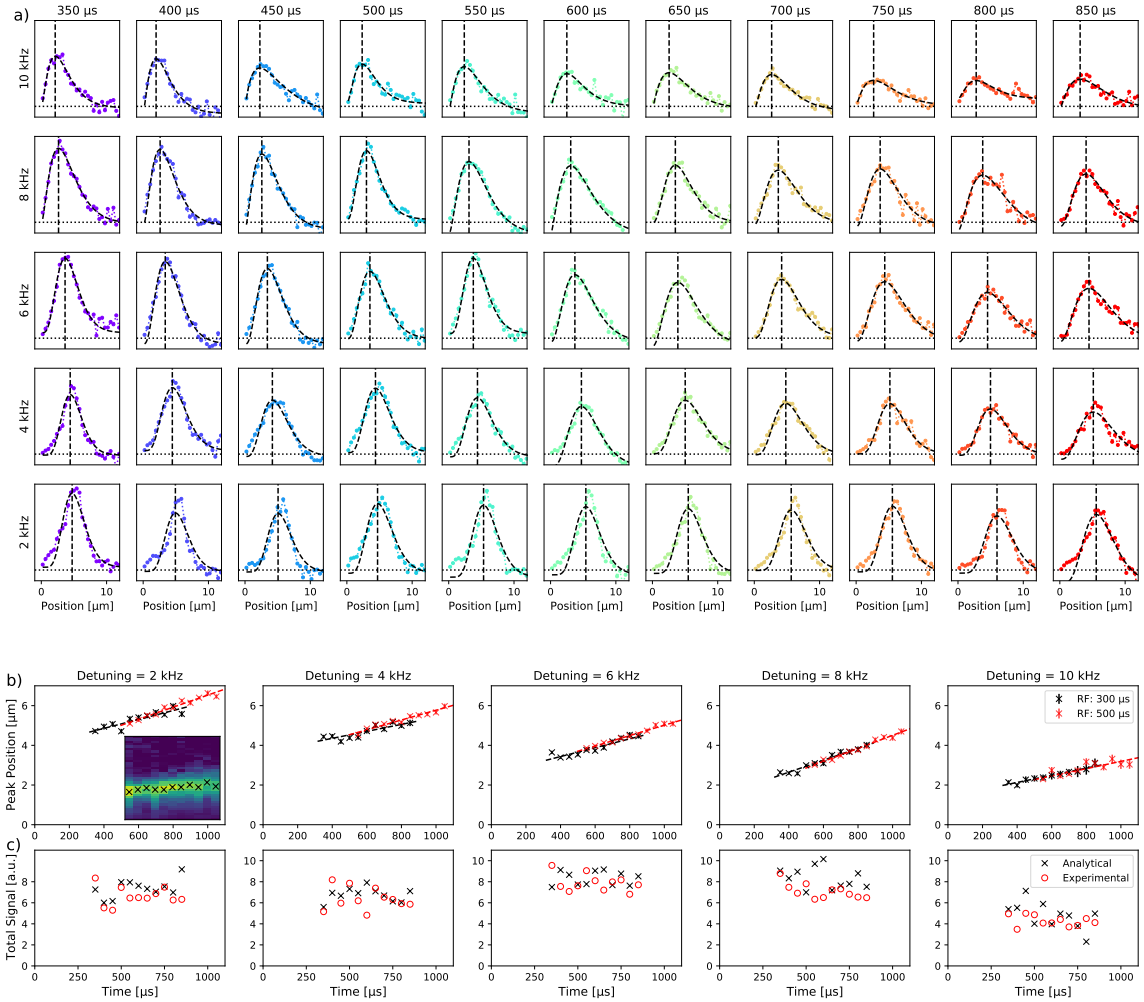

Figure 5.10: Quantitative analysis of repulsive impurity dynamics. **a)** Shown in color are the radially integrated density profiles of the impurity distribution, corresponding to line cuts in the 2D plots of Fig. 5.9, for different detunings (rows) and evolution times (columns). The black dashed line corresponds to the fitting function described in the main text, and the vertical line indicates the maximum position derived from this fit. **b)** Extracted positions of the peak impurity density. For reference, the inset shows the integrated radial density also shown in Fig. 5.9. The peak positions are shown for 300 µs RF pulses (black) and for 500 µs RF pulses (red). Not only show both data sets a perfectly linear behavior, referencing both trajectories to the onset of the RF pulse also lets both curves collapse. This indicates that the onset of motion happens already during the RF pulse. **c)** Both the experimental data and the analytical function do not show any significant reduction in the integrated signal, indicating that three-body losses are negligible.

The perfect collapse onto a single line suggests that the dynamics of the impurities already starts well within the pulse duration. Longer pulse durations mask the initial dynamics and even the relatively short pulses used here do not allow us to unambiguously identify some initial acceleration phase, as will be discussed below. Note that assuming a coherent spin transfer with a Rabi frequency of 1 kHz, one would expect the highest rate of transfer is at 250 µs, suggesting that the propagation dynamics starts to dominate around that

time.

Linear Trajectories Classically, we would expect a $\cosh(\omega t)$-like acceleration, leading to an upwards bending of the peak position curve for longer times. Assuming, for example, a peak repulsive potential of 10 kHz and a Thomas-Fermi radius of 5 µm, we obtain a trapping parameter ω of $\omega \simeq 2\pi \cdot 460$ Hz, and the acceleration should become visible after $\sim 1/\omega \simeq 350$ µs.

Such a linear behavior in the peak position could potentially also be produced not by propagation of the impurities, but spatially dependent loss processes. Three-body losses, for example, scale with the cube of the density, and would lead to higher loss rates in the center of the cloud and therefore shift the peak position to larger radii. This suspicion is discouraged by the integrated signal shown in Fig. 5.10(c), where the black data corresponds to the integrated signal derived from the analytical fit and the red data corresponds to the integral over the raw experimental values. As there is no significant reduction in the total signal within the observed time, we conclude that the atom losses are negligible and are not responsible for the shift in the peak position.

5.4.3 Results and Discussion

In order to explain this linear behavior, we introduce and discuss three different models, with their performance depicted in Fig. 5.11. The first and simplest one just approximates the impurity as a classical particle moving within the effective potential formed by mean field shift of the optical potential. As expected, this leads to an accelerated motion. The second one is a quantum-mechanical simulation within the same potential, which also leads to an accelerated behavior – depending on the width of the initial wave function, the acceleration is even faster than for the classical model. The last one is also a classical simulation, but includes a friction term for velocities above the critical velocity, which we assume to equal the speed of sound. With the theoretically predicted two-dimensional friction term, we can reproduce the observed linear trajectories, while the three-dimensional expression does not agree with our data.

Extracted Trajectories Fig. 5.11 shows the extracted peak positions depending on the evolution time for some different detunings taken at an interstate scattering length of 360 a_0 (black dots). The other lines in these plots refer to different simulations. The gray dotted line is the simplest classical expectation, where the parabolic repulsive potential leads to a cosh-like trajectory while the impurity is within the condensate: $r(t) = r_0 \cdot \cosh(\omega t)$, where ω parametrizes the repulsive potential. The blue and purple solid lines

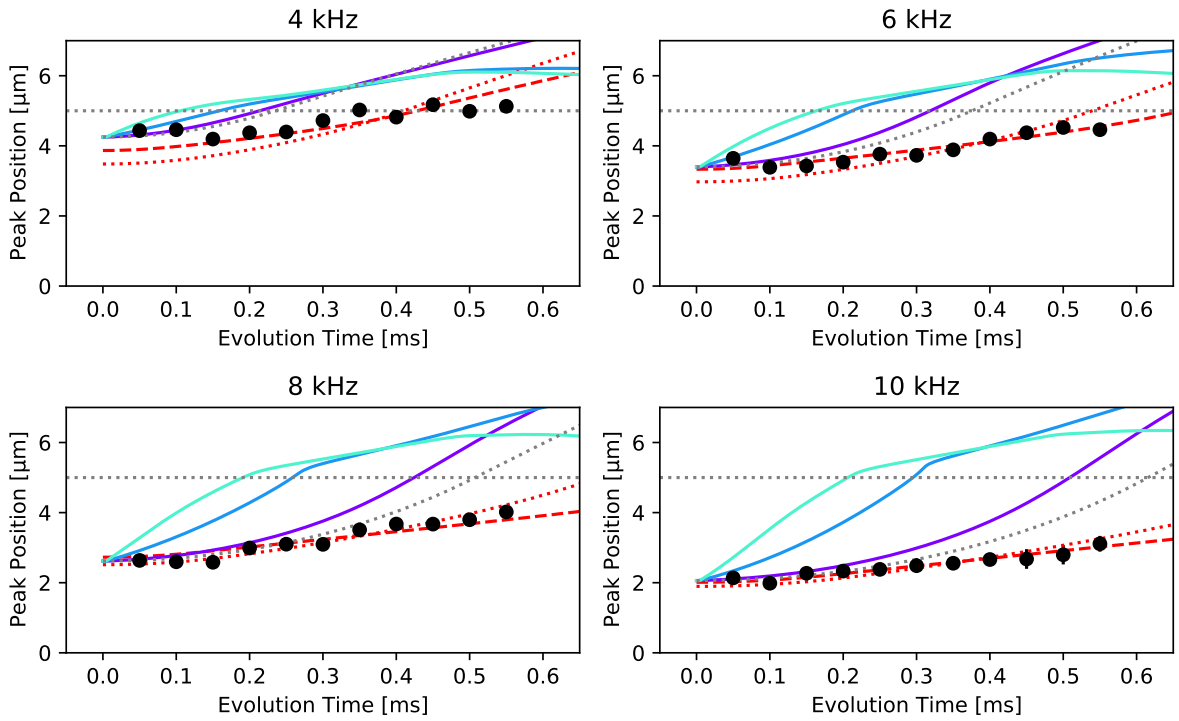

Figure 5.11: Comparing impurity dynamics with theoretical models at $a_{BI} = 360\,a_0$, corresponding to $\tilde{g}_{BI} = 0.48$, for detunings between 4 kHz and 10 kHz. The black dots refer to the experimentally extracted peak positions of the impurity distribution, and the lines correspond to different models: the thin dotted gray line is the non-interacting classical solution of a particle rolling down a harmonic potential hill, while the corresponding quantum mechanical predictions are shown with solid lines. The line indicates the center position of the wave function and the different colors correspond to different waists of the initial wave function (smallest for purple, largest for light blue). The significance of the waist is discussed in the main text. In both the classical and the quantum-mechanical case, the impurity propagates on the effective potential formed by the repulsive bath and the attractive optical potential, and no further effects have been included. Both the classical and the quantum-mechanical model fail to describe the measured data reasonably well. Better agreement with the data is found with a classical model including a friction term as derived in [173]. The dashed red line indicates the propagation when including the friction term derived for two-dimensional systems, while the dotted red line corresponds to the friction term derived for three-dimensional systems. The horizontal line indicates the edge of the condensate.

are quantum-mechanical one-dimensional simulations of a wave function propagating on top of the effective potential formed by the repulsive condensate and the attractive optical potential. The different colors correspond to the peak positions of wave functions starting with the same position, but different initial widths, corresponding to $1 \cdot x_0$ (purple), $3 \cdot x_0$ (dark blue), and $5 \cdot x_0$ (light blue), where x_0 is the harmonic oscillator length. For small widths, the quantum-mechanical trajectory approaches the classical solution, as we would expect. Finally, the red dashed line corresponds to a classical simulation including the friction term derived in[173] for two-dimensional systems, and the red dotted line

corresponds to the same setting with the friction term as derived for a three-dimensional system. In case of the non-interacting calculations (classical and quantum-mechanical), the initial position was defined by the observed peak position for short evolution times; for the classical propagation including the friction term, the initial position was fitted while all other parameters (e.g. radius of the condensate or interaction strength) were fixed.

It is evident that the non-interacting simulations show significant disagreement with the observed data. The non-interacting models predict a substantial acceleration within the observed evolution times, while the data shows no or only very little sign of such an acceleration. Including friction terms to describe the dynamics leads to much better agreement with the observations: as the friction force becomes nonzero above the critical velocity v_c, which is here taken to be the local speed of sound c, motion above this speed will be damped and an equilibrium speed somewhat above the speed of sound is expected.

Simulations In order to better understand the different simulations, we will briefly discuss them in the following paragraphs. As already described above, the solution for a repulsive potential proportional to the local density of the bath is described as $U(r) = U_0 - 1/2m\omega^2 r^2$, which is equivalent to a harmonic oscillator with imaginary trapping frequency. The solution for a particle initially at rest at r_0 is therefore $r(t) = r_0 \cdot \cosh(\omega \cdot t)$. The typical timescale of $2\pi/\omega$ is for our system typically around 1 ms. Outside the condensate, the attractive optical potential leads to harmonic motion with a typical timescale of $1/\nu_{trap} \simeq 10$ ms.

For a more realistic comparison, we perform one-dimensional quantum mechanical simulations. In this simulation, we describe the potential as the sum of the optical potential and the repulsive potential formed by the bath, where we assume that the repulsive interaction is proportional to the density. We start with a gaussian wave packet at a variable position and then time-propagate it. The typical behavior is shown in Fig. 5.12(a): for short times, the wave function shows an accelerated motion as it rolls down from the potential, which is rapidly stopped when reaching the minimum formed between the repulsive bath and the walls of the attractive optical potential. From there on, the wave function still propagates further outwards in the attractive optical potential.

The effects of the free parameters are illustrated in the subplots (b)-(f) in Fig. 5.12. Subplots (d)-(f) show the density as a colormap, while for subplot (b) and (c) we only show the extracted peak position of the time-propagated wave function. The effect of the initial positions is shown in subplot (b) and the effect of the interaction strength (and hence the curvature of the potential hill) is shown in subplot (c). As expected,

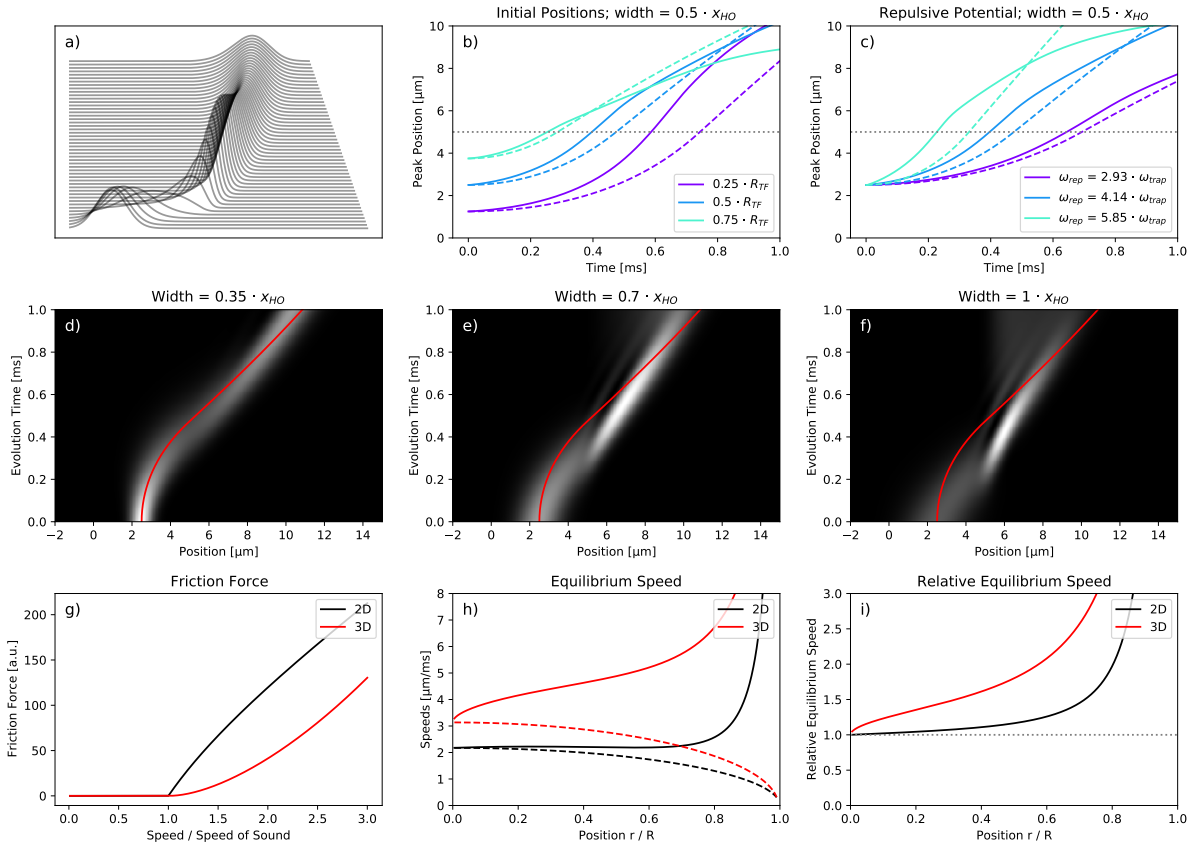

Figure 5.12: Illustration of generic effects for the simulated propagation of impurities in a repulsive condensate. **a)** Quantum-mechanical simulation showing the density of the impurity wave packet for different times. Short times show an accelerated motion caused by the repulsive potential until the edge of the potential is reached and the potential is described purely by the attractive optical trap. The spreading of the wave packet in general leads to experiencing different curvatures and therefore to faster dynamics than classically expected. **b), c)** Extracted time-dependent peak positions for different initial positions and for different potential parameters ω_{rep}, respectively. The classical expectation is indicated by the dashed lines. Stronger repulsion either due to stronger interactions or due to large density gradients near the edge of the condensate lead to stronger deviations from the classical prediction. **d) - f)**: Density plots for different widths of the initial wave function, together with the classical expectation as a red line. Larger wave function spreads lead to two different effects: faster dynamics as the impurities are also sensitive to the higher density slope near the edge of the bath, and stronger interference around the potential minimum formed between the repulsive condensate in the center of the trap and the attractive optical potential. **g)** Friction force as derived in [173] for 2D (black) and 3D (red). **h)** Classically derived equilibrium speed where the friction force equals the repulsive force of the condensate (solid lines) and local speed of sound (dashed lines). **i)** Ratio of the equilibrium speed to the local speed of sound. The 2D friction term grows linearly above the local speed of sound, while the growth is quadratic in $(v - c)$ in three dimensions. Motion above the speed of sound is therefore damped more strongly in two dimensions, where the resulting equilibrium speed shows little variation for values similar to our experimental parameters.

stronger curvature due to larger radii or due to stronger interaction strengths lead to a more rapid acceleration. The dynamics is often more rapid than expected from the classical trajectory, which is shown by the dashed lines. For narrow wave packets (Fig.

5.12(d)), the propagation is close to the classical expectation indicated by the red line. The wider the wave packet is, the more different curvatures of the potential are sampled, which leads to a broadening of the wave function and faster dynamics compared to the classical case, as the average curvature experienced by the impurity will be higher than classically expected. Near the edge of the condensate, a potential minimum is formed between the repulsive condensate and the attractive optical potential. In this region, outward moving parts of the wave function can interfere with those already reflected by the attractive potential, forming an interference patter. This leads to the sudden jumps when only extracting the peak density position, as shown in subplots (b) and (c). The dynamics in the quantum mechanical description therefore also depends on the width of the wave packet, as a broader state will experience a wider range of accelerations, which in general leads to a faster evolution than expected classically.

Friction Fig. 5.12(g)-(i) illustrate the effect of friction. For a two-dimensional condensate the authors of [173] derive the expression

$$F_{2D}(v) = g_{BI}^2 m^2 n_{2D} \frac{v^2 - c^2}{\hbar^3 v}, \tag{5.4}$$

where v is the speed of the impurity, g_{BI} is the coupling parameter between impurity and bath, m is the mass, n_{2D} is the area-density of the system, and c is the speed of sound. The above expression is valid only above c; below c, no phonons can be created and the friction force is zero. For a three-dimensional system, in contrast, the friction force is

$$F_{3D}(v) = 4\pi a_{BI}^2 m n_{3D} v^2 \left(1 - c^2/v^2\right)^2, \tag{5.5}$$

where a_{BI} is the bath-impurity scattering length and n_{3D} is the density of the system. Fig. 5.12(g) illustrates these two friction forces and their dependence on the speed of the impurity. For a 3D-system, the friction force increases quadratically above the speed of sound, while the expression for 2D-systems shows a linear increase of the friction above the speed of sound. The motion of impurities moving above the speed of sound is, in general, stronger damped in a two-dimensional system compared to a three-dimensional system. Considering a harmonic repulsive potential characterized by the trapping parameter ω, it is straightforward to derive a classical equilibrium speed, at which the local acceleration due to the repulsive condensate is balanced by the friction force:

$$v_{eq}^{2D}(r) = \frac{1}{2}\left(\alpha + \sqrt{\alpha^2 + 4c_{peak}^2[1 - (r/R_{TF})^2]}\right), \tag{5.6}$$

where $\alpha(r) = \hbar^3\omega^2 r/g_{BI}^2 m n_{peak}[1-(r/R_{TF})^2]$. The corresponding expression in 3D is

$$v_{eq}^{3D}(r) = \left[\frac{\beta}{2} + \frac{1}{2}\sqrt{\beta^2 - 4c_{peak}^4[1-(r/R_{TF})^2]^2}\right]^{0.5}, \tag{5.7}$$

with $\beta(r) = 2c_{peak}^2[1-(r/R_{TF})^2] + (\omega^2 r)/(4\pi n_{peak}[1-(r/R_{TF})^2]a_{BI}^2)$. The equilibrium speed depends on the radial position as the acceleration increases towards the edge of the condensate, while the friction reduces as the density reduces and scattering events become less likely. The resulting equilibrium speeds are shown in Fig. 5.12(h) as solid lines for typical parameters of our system. The slow onset of friction in the three-dimensional system quickly leads to equilibrium speeds well above the local speed of sound shown as a dashed line, while the two-dimensional system allows for less excess and shows a very flat profile up until $r \simeq 0.7 \cdot R_{TF}$, above which the small density reduces the friction while the slope of the repulsive potential keeps growing, leading to a rapid increase in the equilibrium speed. Note that the expressions Eq. 5.6 and Eq. 5.7 assume a quadratic density profile with a sharp edge and neglect the optical trapping potential. Mathematically, the different behavior for small r/R_{TF} in 2D and 3D originates in the fact that the lowest non-vanishing order in 3D scales as $\sqrt{r/R_{TF0}}$, while the lowest order in 2D is $\propto r/R_{TF}$ and, for our experimental parameters, has a prefactor. Furthermore the quadratic order in 2D has the opposite sign, leading to the very flat profile.

Extracted Speeds The extracted average speeds for all data sets of different interactions are shown in Fig. 5.13. For each detuning, the data of the 300 µs and 500 µs pulse lengths have been combined to extract one average speed of the total data set, and the applied detuning has been normalized to the maximum shift of the respective interaction strength. All interactions show similar behavior in the extracted average speed: starting at low detuning, the average speed starts increasing as the impurities are created further inside the repulsive cloud, and therefore experience longer times of repulsive acceleration before leaving the cloud and propagating in the attractive optical potential. This trend increases up to some about 30%-50% of the peak detuning (corresponding to $r \approx 0.75 R_{TF}$), where the maximum speed is observed. Above this detuning, the speed slowly decreases and approaches the local speed of sound at the center of the trap. This decrease is expected from the classical treatment discussed above, where the equilibrium speed reduces both due to the decrease in acceleration as the condensate's profile becomes flatter and the increase in friction as the density increases. In terms of the local speed of sound as shown in 5.13(b), the speed of sound constantly increases when creating the impurities further towards the cloud's edge. As $c_{local} \propto \sqrt{n}$, the local speed of sound approaches

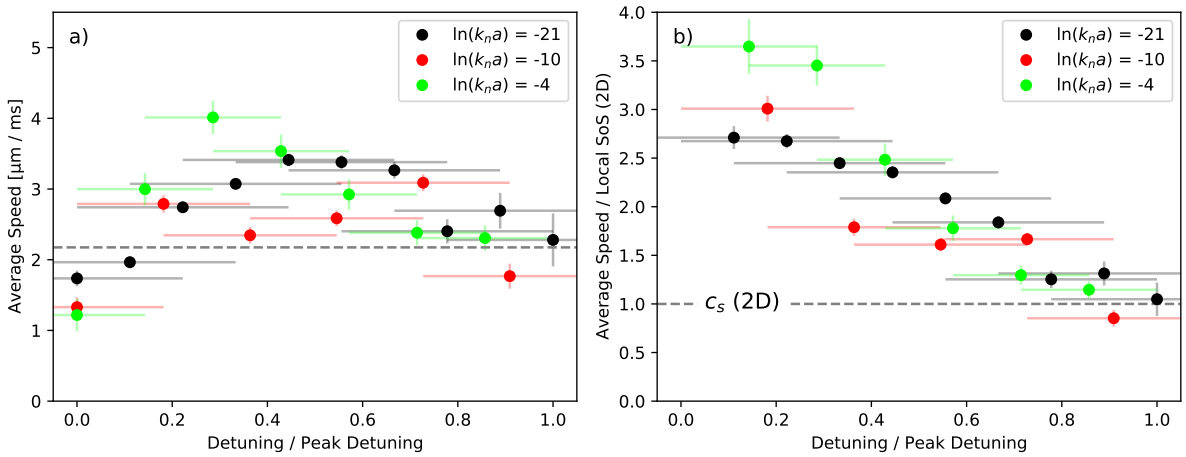

Figure 5.13: Extracted average speeds for different interaction parameters of $\ln(k_n a)$ = -21 ($\tilde{g}_{BI} \simeq 0.28$, black), $\ln(k_n a)$ = -10 ($\tilde{g}_{BI} \simeq 0.56$, red), and $\ln(k_n a)$ = -4 ($\tilde{g}_{BI} \simeq 1.2$, green). **a)** Extracted average speeds depending on the normalized detuning. **b)** Extracted average speeds normalized to the local speed of sound at the position of creation, assuming $\delta \propto n$. In both plots, the detunings have been normalized by the peak observed detuning in order to make the different interactions comparable. The dashed gray line represents the speed of sound at the highest density, i.e. in the center of the cloud. All interaction strengths show similar behavior: impurities created near the center of the cloud propagate with a speed close to the peak speed of sound. As impurities are created farther from the center, their average speed increases due to greater local acceleration, while friction decreases due to reduced density. Moving even closer to the edge of the bath cloud, the average speed decreases again, as the impurity's wave function begins extending beyond the repulsive bath, resulting in a decrease in average acceleration. The ratio v_{av}/c_{local} constantly increases as the local speed of sound decreases $\propto \sqrt{n(r)}$ and approaches zero at the cloud's edge.

zero at $\delta/\delta_{max} = 0$. This decrease is slower than the decrease of the extracted average speed and hence the ratio increases steadily.

5.5 Attractive Dynamics

After investigating the repulsive dynamics, we now discuss the prospects of applying a similar scheme to attractive interactions.

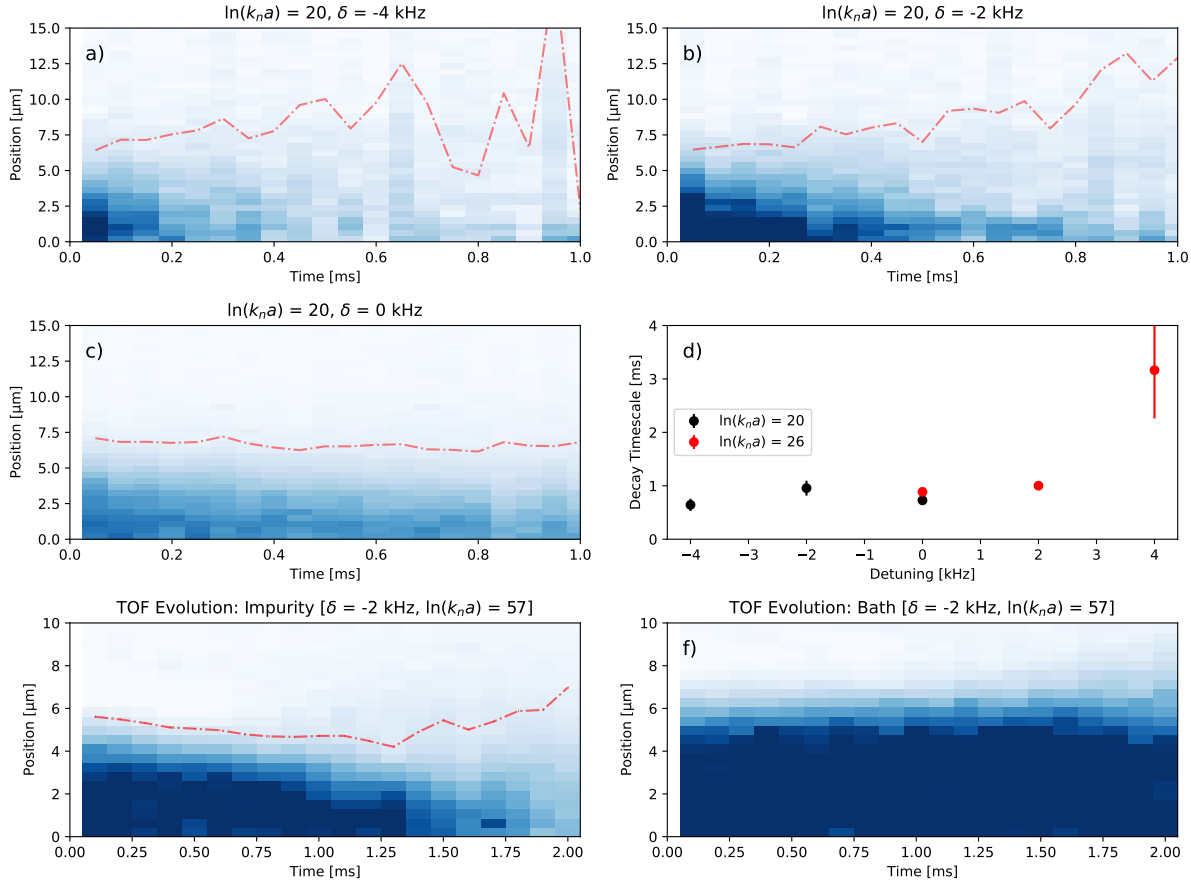

Figure 5.14: Impurity dynamics for attractive interstate interaction. **a) - c)** Radially averaged impurity densities for different RF detunings for $\ln(k_n a) = 20$ ($\tilde{g}_{BI} \simeq -0.33$. **d)** Extracted decay timescales from the loss of integrated impurity weight. **e) - f)** Spatial impurity and bath distribution, respectively, after release from the optical trap. Where present, the thin red lines indicate the extracted gaussian waist of the distribution at the respective time, showing the increase at later time when the thermal population becomes more relevant. Creating impurities at negative detunings leads to rapid losses, where the integrated weight follows an exponential decay with a timescale of ∼1 ms. A similar decay timescale can be observed in TOF data (e, f) taken at weakly attractive interactions of $\ln(k_n a) \simeq 57$ ($\tilde{g}_{BI} \simeq -0.11$), although the density of the surrounding bath drops rapidly within $\sim 1/\nu_z \simeq 150$ µs due to the rapid expansion along the line-of-sight.

The direct equivalent to the repulsive probing scheme consists of ramping to a suitable interstate interaction strength, flipping atoms at negative detunings with respect to the unshifted resonance, and observing the subsequent dynamics in the effective potential formed by the bath. Dynamical properties of interest could be the effect of friction or a signature of an effective mass significantly different from the bare mass. Radially averaged

density profiles of such runs are shown in Fig. 5.14(a)-(c) for an interaction parameter of $\ln(k_n a) = 20$ and detunings between -4 kHz and 0 kHz. As discussed before, attractive interactions do not show the ring-shaped spatial structure observed for low detunings at repulsive interactions, but always produce almost homogeneous impurity distributions, where the outer radius of the distribution decreases with more negative detuning. While the size of the central density peak indeed decreases when applying a negative RF detuning to create impurities, the dominant effect is an exponential loss of signal within ∼1 ms. At the same time, a weaker second component becomes visible with much larger radii, indicating a temperature of $\sim 0.1 \cdot U_{trap}$. On the other hand, creating impurities at zero or positive detuning leads to a cloud of impurity atoms which barely changes its size, but shows a similar loss time. For rather large positive detuning ($\delta = 4$ kHz), the extracted lifetime of the small impurity population shows a longer decay time.

We attribute these effects mostly to losses due to collisions with bath atoms. For negative or zero detuning, the created impurities are confined within the effective potential formed by the condensate and intrinsically have a large scattering probability, leading to the short lifetimes. The hotter component formed for negative detunings originate then from elastic collisions, where one excited impurity is scattered into a lower-lying state within the potential, while a second impurity atom gains energy and is able to leave the confining potential formed by the bath. The signal at positive detunings is interpreted as higher excited states that are not bound within the condensate, and therefore have a significantly smaller overlap, leading to an increase in lifetime for higher detunings. While it is possible to assign a speed to the decrease of the central, high density impurity part – e.g. ~ 1.1 µm/ms for $\delta = -2$ kHz – the rapid, probably spatially inhomogeneous losses prevent a clear interpretation of extraction of a propagation speed of the impurities rolling into the potential. Thus, we did not follow this approach further.

Data obtained from a similar alternative approach is displayed in Fig. 5.14(e, f). Here, we focus on impurity dynamics after releasing the atoms from the optical trap. Due to the high z-confinement, the cloud rapidly expands in the vertical direction, leading to a fast reduction of the density on the timescale of $1/\nu_{trap} \ll 1$ms, and should therefore reduce the impurity losses. Furthermore, the sudden release should map the initial high effective mass to a high momentum state when the interaction is suddenly reduced: the strong localization due to the dressing of the impurity atom with bath atoms, i.e. the origin of the increased effective mass, corresponds to higher momentum contributions for the impurity state. Assuming that the reduction of surrounding density happens rapidly enough, the higher momentum remains and is visible in the time-of-flight measurement.

Fig. 5.14(e) shows that the behavior is not as naively expected: while the bath,

shown in Fig. 5.14(f), behaves as expected and slowly grows radially (the rapid vertical expansion is not visible due to the integration along the line-of-sight), the impurity signal shows a shrinking instead of an increasing size, as expected for a cloud released from the confining potential. The behavior is very similar to the confined case discussed above and indicates that the fast vertical expansion is not sufficient to freeze out the interactions. Scattering and losses still dominate the dynamics, preventing us to extract the dynamical properties mentioned above.

Chapter 6

Conclusion and Outlook

In this thesis, I presented experimental work which enabled the few atom counting in a tweezer-based setup of fermionic ^{40}K, and experiments exploring polaronic physics in degenerate bosonic three-dimensional and two-dimensional systems.

For small systems of the fermionic ^{40}K, we implemented and characterized a novel two-color MOT for precise atom number counting, reaching fidelities of 98% for up to five atoms and exceeding 85% for up to 17 atoms. This atom counting scheme is an essential tool in the preparation and probing of low-entropy tweezer systems. Furthermore, we established a clear road map for the next steps towards the observation of Anderson's orthogonality catastrophe in the limit of low atom numbers within such a tweezer system.

For the bosonic isotope ^{39}K we upgraded the setup to reach degeneracy in bulk systems. Among other things, these upgrades included adaptions and additions in the laser systems, new optical potentials, adaptions to the system preparation, and finally the evaporation to degeneracy, resulting in a Bose-Einstein condensate of ^{39}K. Furthermore, by utilizing suitable optical potentials – most notably a repulsive lattice confining the atomic motion in one spatial direction – we created two-dimensional samples in the regime of BKT superfluidity. For both the three-dimensional and the two-dimensional case, the interactions between all magnetic substates of the relevant hyperfine state can be tuned by Feshbach resonances. This applies to intrastate interactions within one spin state as well as to interstate interactions between two different spin states, for example after preparing a spin mixture via a suitable radio-frequency transfer.

In the three-dimensional Bose-Einstein condensates, we used injection spectroscopy to measure the polaron spectrum: by employing radio-frequency pulses to flip atoms into a different spin state, we created a system consisting of impurities immersed in a bosonic bath. A Feshbach resonance between the impurity state and the bath state allowed us control not only the interaction strength, but also to switch between repulsive and

attractive interactions. The polaron energy shift is then encoded in the RF detuning needed to flip atoms into the interacting impurity state. The spectrum obtained in this manner shows a repulsive branch that is well separated from the unshifted resonance and exhibits decreasing weight close to the Feshbach resonance. For attractive interactions, we do not observe a distinct branch but instead observe the strongest signal near the unshifted detuning and a decreasing amplitude towards further negative detuning, i.e. stronger bound states. We modeled the observed line shapes for both attractive and repulsive interactions with good accuracy with phenomenological models, where the inclusion of excited states was essential. Especially for attractive interactions, our models suggest a significant influence of excited states still bound within the effective potential formed by the bath. The observed energy shifts are in agreement with previous work, but our line shapes are not modeled well with expressions from previous work.

In a similar way we measured the polaron spectrum in a two-dimensional Bose gas for the first time and extracted the peak energy shifts. In the two-dimensional case, repulsive interactions do not exhibit a well separated branch but instead show a behavior similar to attractive interactions, where the strongest signal is observed near the unshifted frequency and is reduced for larger detuning. With models similar to the ones used in the three-dimensional case, we again achieve good agreement with the measured line shapes, again finding support for the relevance of excited states.

Furthermore, we explored the spatially and temporally resolved impurity dynamics in a two-dimensional Bose gas. We observed correlated bath-impurity dynamics for both repulsive and attractive interactions, but in the latter case, the rapid loss of particle only allowed us to follow the dynamics for about 1 ms. In the repulsive regime, in contrast, we observe and track the expulsion of impurities from the condensate and can model the motion to good accuracy when including the two-dimensional friction term relevant for speeds above the local speed of sound. This friction term counteracts the expected acceleration near the edge of the condensate and the combination of the two leads to a motion with almost constant velocity.

Outlook While we measured the energy shifts in the polaron spectrum, our attempt to extract the effective mass has not been successful yet. The quasi-particle residue - another fundamental quantity describing the polaron - is also not accessible yet in our setup, but both might be in reach with a comparably simple further upgrade in the machine. A digital mirror device (DMD) would allow us to generate very flexible potential geometries within the horizontal plane and could be used to replace the current harmonic radial confinement by a ring of steep walls. The potential inside of these walls could for example be flat or

feature a linear potential gradient. The latter would lead to the Thomas-Fermi profile of the bath also showing a linear increase in one spatial dimension. Position selective spin flips and the subsequent dynamics would not suffer from the large errors discussed in Sec. 5.3 as the motion would be effectively one-dimensional, leading to a much better signal-to-noise ratio and hence making the extraction of the effective mass realistic.

In case of the flat potential and therefore uniform density, the extraction of the quasi-particle residue seems feasible. In the harmonic trap, we always average over a range of interaction parameters $\ln(k_n a)$, either globally as in the case of the spectra or locally as in chapter 5, where the range was defined by the Fourier width of the RF pulse. This average is crucial when trying to extract the quasi-particle residue since this is usually done by measuring a reduction in the Rabi frequency of the spin transfer into the impurity state. The average over densities and hence interaction parameters then leads to an average over Rabi oscillations with different frequencies, leading to rapid decoherence. For a constant density within the system, only one interaction parameter contributes, thereby eliminating the dominant contribution to decoherence.

Furthermore, faster RF pulses are more useful in systems of uniform density. As briefly discussed above, faster RF pulses lead to a larger Fourier width and therefore to a larger range of densities being addressed. For the observation of impurity dynamics in a harmonic trap, this reduces the selectivity on the initial position, which is a clear disadvantage when tracking the impurity motion. However, in a homogeneous system the larger Fourier width is of no concern. Faster Rabi oscillations can therefore be used to observe more spin oscillations and enhance any effect of the reduced quasi-particle residue.

But even without taking advantage of the spatial resolution, the homogeneous system promises valuable information: the exact energies of the excited states should be measurable in a homogeneous system, therefore shedding light on their character. In addition, the observation of the vertical momentum distribution of the excited states would be interesting, i.e. the momentum along the tight trapping direction. This is in principle accessible in time-of-flight measurements when imaging along the horizontal plane.

Employing techniques discussed in the context of ^{40}K, one could also add tweezers to provide a small, localized light shift within the homogeneous cloud, preferably on a transition only the impurity state is sensitive to in order to reduce the disturbance of the bath. The shifted transition frequency would then allow us to create impurities selectively only at the position of the tweezers. When using a single tweezer, this could open up the pathway to study the predicted self-trapping regime of impurities, where the usually expected delocalization is suppressed [174]. For two tweezers, probing the polaron-polaron interaction in a collider-like setting is a promising endeavor.

Appendix A

Decay Ratio Table

Excited state decay ratios are relevant for different stages of the experiment, for example optical pumping. For convenience, the calculated branching ratios are collected here, both for 39K and 40K. All calculations follow the procedure outlined in [166] and only take into account dipol transitions at zero field.

Tables A.1 and A.4 state the decay ratios without m_F resolution, i.e. the probabilities for all possible m_F values in the final state are summed. The remaining tables always indicate the m_F-resolved decay ratios.

^{39}K Decay Ratios

^{39}K D1 Line and D2 Line: Not Spin Resolved

	$4p_{3/2}$ (D2 Line)				$4p_{1/2}$ (D1 Line)	
final \ initial	$\|\mathbf{F=3}\rangle$	$\|\mathbf{F=2}\rangle$	$\|\mathbf{F=1}\rangle$	$\|\mathbf{F=0}\rangle$	$\|\mathbf{F=2}\rangle$	$\|\mathbf{F=1}\rangle$
$\|\mathbf{4s_{1/2}, F=2}\rangle$	1.0	1/2	1/6		1/2	5/6
$\|\mathbf{4s_{1/2}, F=1}\rangle$		1/2	5/6	1.0	1/2	1/6

Table A.1: Not spin resolved decay ratios for ^{39}K, i.e. probabilities are summed over all possible m_F values in the final state. The columns corresponds to different initial states in the excited state, and the rows to different final states after decay. Empty boxes indicate forbidden transitions, such that the transition probability is highly suppressed.

^{39}K D1 Line

final \ initial	$\|\mathbf{2},\mathbf{2}\rangle$	$\|\mathbf{2},\mathbf{1}\rangle$	$\|\mathbf{2},\mathbf{0}\rangle$	$\|\mathbf{2},-\mathbf{1}\rangle$	$\|\mathbf{2},-\mathbf{2}\rangle$	$\|\mathbf{1},\mathbf{1}\rangle$	$\|\mathbf{1},\mathbf{0}\rangle$	$\|\mathbf{1},-\mathbf{1}\rangle$
$\|\mathbf{2},\mathbf{2}\rangle$	0.333	0.167				0.5		
$\|\mathbf{2},\mathbf{1}\rangle$	0.167	0.083	0.25			0.25	0.25	
$\|\mathbf{2},\mathbf{0}\rangle$		0.25		0.25		0.083	0.333	0.083
$\|\mathbf{2},-\mathbf{1}\rangle$			0.25	0.083	0.167		0.25	0.25
$\|\mathbf{2},-\mathbf{2}\rangle$				0.167	0.333			0.5
$\|\mathbf{1},\mathbf{1}\rangle$	0.5	0.25	0.083			0.083	0.083	
$\|\mathbf{1},\mathbf{0}\rangle$		0.25	0.333	0.25		0.083		0.083
$\|\mathbf{1},-\mathbf{1}\rangle$			0.083	0.25	0.5		0.083	0.083

Table A.2: ^{39}K decay ratios for decays from the $4p_{1/2}$-state to the electronic ground state $4s_{1/2}$, i.e. on the **D1** line. The columns corresponds to different initial states in the excited state, and the rows to different final states after decay. Labels always indicate the F and m_F quantum numbers: $|F, m_F\rangle$. Empty boxes indicate forbidden transitions, such that the transition probability is highly suppressed.

^{39}K D2 Line: Excited States with F = 3

final \ initial	$\|\mathbf{3},\mathbf{3}\rangle$	$\|\mathbf{3},\mathbf{2}\rangle$	$\|\mathbf{3},\mathbf{1}\rangle$	$\|\mathbf{3},\mathbf{0}\rangle$	$\|\mathbf{3},-\mathbf{1}\rangle$	$\|\mathbf{3},-\mathbf{2}\rangle$	$\|\mathbf{3},-\mathbf{3}\rangle$
$\|\mathbf{2},\mathbf{2}\rangle$	1.0	0.333	0.067				
$\|\mathbf{2},\mathbf{1}\rangle$		0.667	0.533	0.2			
$\|\mathbf{2},\mathbf{0}\rangle$			0.4	0.6	0.4		
$\|\mathbf{2},-\mathbf{1}\rangle$				0.2	0.533	0.667	
$\|\mathbf{2},-\mathbf{2}\rangle$					0.067	0.333	1.0

^{39}K D2 Line: Excited States with F = 2, F = 1, or F = 0

final \ initial	$\|\mathbf{2},\mathbf{2}\rangle$	$\|\mathbf{2},\mathbf{1}\rangle$	$\|\mathbf{2},\mathbf{0}\rangle$	$\|\mathbf{2},-\mathbf{1}\rangle$	$\|\mathbf{2},-\mathbf{2}\rangle$	$\|\mathbf{1},\mathbf{1}\rangle$	$\|\mathbf{1},\mathbf{0}\rangle$	$\|\mathbf{1},-\mathbf{1}\rangle$	$\|\mathbf{0},\mathbf{0}\rangle$
$\|\mathbf{2},\mathbf{2}\rangle$	0.333	0.167				0.1			
$\|\mathbf{2},\mathbf{1}\rangle$	0.167	0.083	0.25			0.05	0.05		
$\|\mathbf{2},\mathbf{0}\rangle$		0.25		0.25		0.017	0.067	0.017	
$\|\mathbf{2},-\mathbf{1}\rangle$			0.25	0.083	0.167		0.05	0.05	
$\|\mathbf{2},-\mathbf{2}\rangle$				0.167	0.333			0.1	
$\|\mathbf{1},\mathbf{1}\rangle$	0.5	0.25	0.083			0.417	0.417		0.333
$\|\mathbf{1},\mathbf{0}\rangle$		0.25	0.333	0.25		0.417		0.417	0.333
$\|\mathbf{1},-\mathbf{1}\rangle$			0.083	0.25	0.5		0.417	0.417	0.333

Table A.3: ^{39}K decay ratios for decays from the $4p_{3/2}$-state to the electronic ground state $4s_{1/2}$, i.e. on the **D2** line. The columns corresponds to different initial states in the excited state, and the rows to different final states after decay. Labels always indicate the F and m_F quantum numbers: $|F, m_F\rangle$. Empty boxes indicate forbidden transitions, such that the transition probability is highly suppressed.

^{40}K Decay Ratios

^{40}K D1 Line and D2 Line: Not Spin Resolved

final \ initial	$4p_{3/2}$ (D2 Line)				$4p_{1/2}$ (D1 Line)	
	$\|\mathbf{F = 11/2}\rangle$	$\|\mathbf{F = 9/2}\rangle$	$\|\mathbf{F = 7/2}\rangle$	$\|\mathbf{F = 5/2}\rangle$	$\|\mathbf{F = 9/2}\rangle$	$\|\mathbf{F = 7/2}\rangle$
$\|\mathbf{4s_{1/2}, F = 9/2}\rangle$	1.0	16/27	7/27		11/27	20/27
$\|\mathbf{4s_{1/2}, F = 7/2}\rangle$		11/27	20/27	1.0	16/27	7/27

Table A.4: Not spin resolved decay ratios for ^{40}K, i.e. probabilities are summed over all possible m_F values in the final state. The columns corresponds to different initial states in the excited state, and the rows to different final states after decay. Empty boxes indicate forbidden transitions, such that the transition probability is highly suppressed.

D2 Line: Excited States with F = 11/2

final \ initial	$\|11/2, 11/2\rangle$	$\|11/2, 9/2\rangle$	$\|11/2, 7/2\rangle$	$\|11/2, 5/2\rangle$	$\|11/2, 3/2\rangle$	$\|11/2, 1/2\rangle$
$\|9/2, 9/2\rangle$	1.0	0.182	0.018			
$\|9/2, 7/2\rangle$		0.818	0.327	0.055		
$\|9/2, 5/2\rangle$			0.655	0.436	0.109	
$\|9/2, 3/2\rangle$				0.509	0.509	0.182
$\|9/2, 1/2\rangle$					0.382	0.545
$\|9/2, -1/2\rangle$						0.273

D2 Line: Excited States with F = 9/2

final \ initial	$\|9/2, 9/2\rangle$	$\|9/2, 7/2\rangle$	$\|9/2, 5/2\rangle$	$\|9/2, 3/2\rangle$	$\|9/2, 1/2\rangle$
$\|9/2, 9/2\rangle$	0.485	0.108			
$\|9/2, 7/2\rangle$	0.108	0.293	0.192		
$\|9/2, 5/2\rangle$		0.192	0.15	0.251	
$\|9/2, 3/2\rangle$			0.251	0.054	0.287
$\|9/2, 1/2\rangle$				0.287	0.006
$\|9/2, -1/2\rangle$					0.299
$\|7/2, 7/2\rangle$	0.407	0.091	0.011		
$\|7/2, 5/2\rangle$		0.317	0.158	0.034	
$\|7/2, 3/2\rangle$			0.238	0.204	0.068
$\|7/2, 1/2\rangle$				0.17	0.226
$\|7/2, -1/2\rangle$					0.113

Table A.5: ^{40}K decay ratios for decays from the $4p_{3/2}$-state to the electronic ground state $4s_{1/2}$, i.e. on the **D2** line. The columns corresponds to different initial states in the excited state, and the rows to different final states after decay. Labels always indicate the F and m_F quantum numbers: $|F, m_F\rangle$. Empty boxes indicate forbidden transitions, such that the transition probability is highly suppressed. This table only shows the initial states for $F = 11/2$ and $F = 9/2$; $F = 7/2$ and $F = 5/2$ are shown in the next table. Only the decay ratios for excited states with positive m_F are shown; decay ratios for the negative m_F values are the same as for the respective positive m_F values, only with the signs of the m_F quantum number of the final states flipped.

D2 Line: Excited States with F = 7/2

final \ initial	$\|\mathbf{7/2}, \mathbf{7/2}\rangle$	$\|\mathbf{7/2}, \mathbf{5/2}\rangle$	$\|\mathbf{7/2}, \mathbf{3/2}\rangle$	$\|\mathbf{7/2}, \mathbf{1/2}\rangle$
$\|\mathbf{9/2}, \mathbf{9/2}\rangle$	0.207			
$\|\mathbf{9/2}, \mathbf{7/2}\rangle$	0.046	0.161		
$\|\mathbf{9/2}, \mathbf{5/2}\rangle$	0.006	0.081	0.121	
$\|\mathbf{9/2}, \mathbf{3/2}\rangle$		0.017	0.104	0.086
$\|\mathbf{9/2}, \mathbf{1/2}\rangle$			0.035	0.115
$\|\mathbf{9/2}, \mathbf{-1/2}\rangle$				0.058
$\|\mathbf{7/2}, \mathbf{7/2}\rangle$	0.576	0.165		
$\|\mathbf{7/2}, \mathbf{5/2}\rangle$	0.165	0.294	0.282	
$\|\mathbf{7/2}, \mathbf{3/2}\rangle$		0.282	0.106	0.353
$\|\mathbf{7/2}, \mathbf{1/2}\rangle$			0.353	0.012
$\|\mathbf{7/2}, \mathbf{-1/2}\rangle$				0.376

D2 Line: Excited States with F = 5/2

final \ initial	$\|\mathbf{5/2}, \mathbf{5/2}\rangle$	$\|\mathbf{5/2}, \mathbf{3/2}\rangle$	$\|\mathbf{5/2}, \mathbf{1/2}\rangle$
$\|\mathbf{7/2}, \mathbf{7/2}\rangle$	0.75		
$\|\mathbf{7/2}, \mathbf{5/2}\rangle$	0.214	0.536	
$\|\mathbf{7/2}, \mathbf{3/2}\rangle$	0.036	0.357	0.357
$\|\mathbf{7/2}, \mathbf{1/2}\rangle$		0.107	0.429
$\|\mathbf{7/2}, \mathbf{-1/2}\rangle$			0.214

Table A.6: ^{40}K decay ratios for decays from the $4p_{3/2}$-state to the electronic ground state $4s_{1/2}$, i.e. on the **D2** line. The columns corresponds to different initial states in the excited state, and the rows to different final states after decay. Labels always indicate the F and m_F quantum numbers: $|F, m_F\rangle$. Empty boxes indicate forbidden transitions, such that the transition probability is highly suppressed. This table only shows the initial states for $F = 7/2$ and $F = 5/2$; $F = 11/2$ and $F = 9/2$ are shown in the previous table. Only the decay ratios for excited states with positive m_F are shown; decay ratios for the negative m_F values are the same as for the respective positive m_F values, only with the signs of the m_F quantum number of the final states flipped.

D1 Line: Excited States with F = 9/2

final \ initial	$\|\mathbf{9/2, 9/2}\rangle$	$\|\mathbf{9/2, 7/2}\rangle$	$\|\mathbf{9/2, 5/2}\rangle$	$\|\mathbf{9/2, 3/2}\rangle$	$\|\mathbf{9/2, 1/2}\rangle$
$\|\mathbf{9/2, 9/2}\rangle$	0.333	0.074			
$\|\mathbf{9/2, 7/2}\rangle$	0.074	0.202	0.132		
$\|\mathbf{9/2, 5/2}\rangle$		0.132	0.103	0.173	
$\|\mathbf{9/2, 3/2}\rangle$			0.173	0.037	0.198
$\|\mathbf{9/2, 1/2}\rangle$				0.198	0.004
$\|\mathbf{9/2, -1/2}\rangle$					0.206
$\|\mathbf{7/2, 7/2}\rangle$	0.593	0.132	0.016		
$\|\mathbf{7/2, 5/2}\rangle$		0.461	0.23	0.049	
$\|\mathbf{7/2, 3/2}\rangle$			0.346	0.296	0.099
$\|\mathbf{7/2, 1/2}\rangle$				0.247	0.329
$\|\mathbf{7/2, -1/2}\rangle$					0.165

D1 Line: Excited States with F = 7/2

final \ initial	$\|\mathbf{7/2, 7/2}\rangle$	$\|\mathbf{7/2, 5/2}\rangle$	$\|\mathbf{7/2, 3/2}\rangle$	$\|\mathbf{7/2, 1/2}\rangle$
$\|\mathbf{9/2, 9/2}\rangle$	0.593			
$\|\mathbf{9/2, 7/2}\rangle$	0.132	0.461		
$\|\mathbf{9/2, 5/2}\rangle$	0.016	0.23	0.346	
$\|\mathbf{9/2, 3/2}\rangle$		0.049	0.296	0.247
$\|\mathbf{9/2, 1/2}\rangle$			0.099	0.329
$\|\mathbf{9/2, -1/2}\rangle$				0.165
$\|\mathbf{7/2, 7/2}\rangle$	0.202	0.058		
$\|\mathbf{7/2, 5/2}\rangle$	0.058	0.103	0.099	
$\|\mathbf{7/2, 3/2}\rangle$		0.099	0.037	0.123
$\|\mathbf{7/2, 1/2}\rangle$			0.123	0.004
$\|\mathbf{7/2, -1/2}\rangle$				0.132

Table A.7: ^{40}K decay ratios for decays from the $4p_{1/2}$-state to the electronic ground state $4s_{1/2}$, i.e. on the **D1** line. The columns corresponds to different initial states in the excited state, and the rows to different final states after decay. Labels always indicate the F and m_F quantum numbers: $|F, m_F\rangle$. Empty boxes indicate forbidden transitions, such that the transition probability is highly suppressed. Only the decay ratios for excited states with positive m_F are shown; decay ratios for the negative m_F values are the same as for the respective positive m_F values, only with the signs of the m_F quantum number of the final states flipped.

Bibliography

[1] L. D. Landau. *Über die Bewegung der Elektronen in Kristallgitter.* Phys. Z. Sowjetunion **3**:644 (1933).

[2] L. D. Landau and S. I. Pekar. *Effektivnaya Massa Polyarona.* Zhurnal Eksperimentalnoi i Teoreticheskoi Fiziki **18(5)**:419 (1948).

[3] H. Fröhlich. *Electrons in lattice fields.* Advances in Physics **3**(11):325 (1954).

[4] T. D. Lee, F. E. Low and D. Pines. *The Motion of Slow Electrons in a Polar Crystal.* Phys. Rev. **90**:297 (1953).

[5] J. T. Devreese. *Polarons.* G. L. Trigg, editor, *Encyclopedia of Applied Physics*, volume 14, pages 383–409. VCH, Weinheim (1996).

[6] J. Kondo. *Resistance Minimum in Dilute Magnetic Alloys.* Progress of Theoretical Physics **32**(1):37 (1964).

[7] A. J. Millis, P. B. Littlewood and B. I. Shraiman. *Double Exchange Alone Does Not Explain the Resistivity of* $La_{1-x}Sr_xMnO_3$. Phys. Rev. Lett. **74**:5144 (1995).

[8] A. S. Alexandrov and A. M. Bratkovsky. *Carrier Density Collapse and Colossal Magnetoresistance in Doped Manganites.* Phys. Rev. Lett. **82**:141 (1999).

[9] Y. Tokura. *Colossal Magnetoresistive Oxides.* CRC Press, London (2000).

[10] D. M. Edwards. *Ferromagnetism and electron-phonon coupling in the manganites.* Advances in Physics **51**(5):1259 (2002).

[11] A. S. Alexandrov. *Bipolaron anisotropic flat bands, Hall mobility edge, and metal-semiconductor duality of overdoped high-T_c oxides.* Phys. Rev. B **53**:2863 (1996).

[12] J. G. Bednorz and K. A. Müller. *Perovskite-type oxides—The new approach to high-T_c superconductivity.* Rev. Mod. Phys. **60**:585 (1988).

[13] K. Müller. *Recent experimental insights into HTSC materials.* Physica C: Superconductivity **341-348**:11 (2000). Materials and Mechanisms of Superconductivity High Temperature Superconductors VI.

[14] J. T. Devreese. *Polarons.* R. G. Lerner and G. L. Trigg, editors, *Encyclopedia of Physics*, volume 3, pages 383–409. Wiley-VCH, Weinheim (2005).

[15] M. E. Gershenson, V. Podzorov and A. F. Morpurgo. *Colloquium: Electronic transport in single-crystal organic transistors.* Rev. Mod. Phys. **78**:973 (2006).

[16] V. V. Klimov. *Spectrum of Elementary Fermi Excitations in Quark Gluon Plasma. (In Russian).* Sov. J. Nucl. Phys. **33**:934 (1981).

[17] H. A. Weldon. *Dynamical holes in the quark-gluon plasma.* Phys. Rev. D **40**:2410 (1989).

[18] E. Nakano, K. Iida and W. Horiuchi. *Quasiparticle properties of a single α particle in cold neutron matter.* Phys. Rev. C **102**:055802 (2020).

[19] P. W. Anderson. *Plasmons, Gauge Invariance, and Mass.* Phys. Rev. **130**:439 (1963).

[20] F. Englert and R. Brout. *Broken Symmetry and the Mass of Gauge Vector Mesons.* Phys. Rev. Lett. **13**:321 (1964).

[21] P. W. Higgs. *Broken Symmetries and the Masses of Gauge Bosons.* Phys. Rev. Lett. **13**:508 (1964).

[22] G. S. Guralnik, C. Hagen and T. W. Kibble. *Global Conservation Laws and Massless Particles.* Physical Review Letters **13**(20):585 (1964).

[23] G. S. Guralnik. *The history of the Guralnik, Hagen and Kibble development of the theory of spontaneous symmetry breaking and gauge particles.* International Journal of Modern Physics A **24**(14):2601–2627 (2009).

[24] A. J. Moerdijk, B. J. Verhaar and A. Axelsson. *Resonances in ultracold collisions of ^{6}Li, ^{7}Li, and ^{23}Na.* Phys. Rev. A **51**:4852 (1995).

[25] P. Wieburg. *A Novel Fermionic Quantum Gas Microscope: Concept, Design and Construction.* Ph.D. thesis, University of Hamburg, Germany (2019).

[26] T. Uehlinger. *A 2D Magneto-Optical Trap as a High-Flux Source of Cold Potassium Atoms* (2008). Diploma Thesis.

[27] D. S. Petrov. *Three-Boson Problem near a Narrow Feshbach Resonance.* Physical Review Letters **93**(14) (2004).

[28] A. Mozdzen. *Creating Degenerate Two-Dimensional Bose Gases with Tuneable Interaction Strength (In preparation).* Ph.D. thesis, University of Hamburg, Germany (2024).

[29] C. D'Errico, M. Zaccanti, M. Fattori, G. Roati, M. Inguscio, G. Modugno and A. Simoni. *Feshbach resonances in ultracold 39K.* New Journal of Physics **9**(7):223 (2007).

[30] M. Lysebo and L. Veseth. *Feshbach resonances and transition rates for cold homonuclear collisions between* ^{39}K *and* ^{41}K *atoms.* Phys. Rev. A **81**:032702 (2010).

[31] J. Etrych, G. Martirosyan, A. Cao, J. A. P. Glidden, L. H. Dogra, J. M. Hutson, Z. Hadzibabic and C. Eigen. *Pinpointing Feshbach resonances and testing Efimov universalities in* ^{39}K. Phys. Rev. Res. **5**:013174 (2023).

[32] T. Loftus, C. A. Regal, C. Ticknor, J. L. Bohn and D. S. Jin. *Resonant Control of Elastic Collisions in an Optically Trapped Fermi Gas of Atoms.* Phys. Rev. Lett. **88**:173201 (2002).

[33] M. Schlederer, A. Mozdzen, T. Lompe and H. Moritz. *Single-atom counting in a two-color magneto-optical trap.* Physical Review A **103**(3) (2021).

[34] P. W. Anderson. *Infrared Catastrophe in Fermi Gases with Local Scattering Potentials.* Physical Review Letters **18**(24):1049 (1967).

[35] Y. Miroshnychenko, W. Alt, I. Dotsenko, L. Förster, M. Khudaverdyan, D. Meschede, D. Schrader and A. Rauschenbeutel. *An atom-sorting machine.* Nature **442**:151 (2006).

[36] K. D. Nelson, X. Li and D. S. Weiss. *Imaging single atoms in a three-dimensional array.* Nature Physics (3):556 (2007).

[37] C. Gross and I. Bloch. *Quantum simulations with ultracold atoms in optical lattices.* Science **357**(6355):995 (2017).

[38] C. Gross and W. S. Bakr. *Quantum gas microscopy for single atom and spin detection.* Nature Physics **17**(12):1316–1323 (2021).

[39] M. T. DePue, C. McCormick, S. L. Winoto, S. Oliver and D. S. Weiss. *Unity Occupation of Sites in a 3D Optical Lattice.* Phys. Rev. Lett. **82**:2262 (1999).

[40] N. Schlosser, G. Reymond, I. Protsenko and P. Grangier. *Sub-poissonian loading of single atoms in a microscopic dipole trap.* Nature **411**:1014 (2001).

[41] N. Schlosser, G. Reymond and P. Grangier. *Collisional Blockade in Microscopic Optical Dipole Traps.* Phys. Rev. Lett. **89**:023005 (2002).

[42] G. Grynberg and J.-Y. Courtois. *Proposal for a Magneto-Optical Lattice for Trapping Atoms in Nearly-Dark States.* Europhysics Letters **27**(1):41 (1994).

[43] D. Boiron, C. Triché, D. R. Meacher, P. Verkerk and G. Grynberg. *Three-dimensional cooling of cesium atoms in four-beam gray optical molasses.* Phys. Rev. A **52**:R3425 (1995).

[44] D. R. Fernandes, F. Sievers, N. Kretzschmar, S. Wu, C. Salomon and F. Chevy. *Sub-Doppler laser cooling of fermionic 40K atoms in three-dimensional gray optical molasses.* Europhysics Letters **100**(6):63001 (2012).

[45] A. T. Grier, I. Ferrier-Barbut, B. S. Rem, M. Delehaye, L. Khaykovich, F. Chevy and C. Salomon. Λ*-enhanced sub-Doppler cooling of lithium atoms in D1 gray molasses.* Phys. Rev. A **87**:063411 (2013).

[46] D. Nath, R. K. Easwaran, G. Rajalakshmi and C. S. Unnikrishnan. *Quantum-interference-enhanced deep sub-Doppler cooling of* ^{39}K *atoms in gray molasses.* Phys. Rev. A **88**:053407 (2013).

[47] J. A. Devlin and M. R. Tarbutt. *Three-dimensional Doppler, polarization-gradient, and magneto-optical forces for atoms and molecules with dark states.* New Journal of Physics **18**(12):123017 (2016).

[48] K. N. Jarvis, J. A. Devlin, T. E. Wall, B. E. Sauer and M. R. Tarbutt. *Blue-Detuned Magneto-Optical Trap.* Physical Review Letters **120**(8) (2018).

[49] B. Arora, M. S. Safronova and C. W. Clark. *Determination of electric-dipole matrix elements in K and Rb from Stark shift measurements.* Phys. Rev. A **76**:052516 (2007).

[50] B. Arora, M. S. Safronova and C. W. Clark. *Determination of electric-dipole matrix elements in K and Rb from Stark shift measurements.* Phys. Rev. A **76**:052516 (2007).

[51] C. A. Regal and D. S. Jin. *Measurement of Positive and Negative Scattering Lengths in a Fermi Gas of Atoms.* Phys. Rev. Lett. **90**:230404 (2003).

[52] J. S. Krauser, J. Heinze, S. Götze, M. Langbecker, N. Fläschner, L. Cook, T. M. Hanna, E. Tiesinga, K. Sengstock and C. Becker. *Investigation of Feshbach resonances in ultracold ^{40}K spin mixtures.* Phys. Rev. A **95**:042701 (2017).

[53] Z. Hu and H. J. Kimble. *Observation of a single atom in a magneto-optical trap.* Optics Letters **19**(22):1888 (1994).

[54] F. Ruschewitz, D. Bettermann, J. Peng and W. Ertmer. *Statistical investigations on single trapped neutral atoms.* EPL **34**(9):651 (1996).

[55] C. Chen, Y. Li, K. Bailey, T. O'Conner, L. Young and Z.-T. Lu. *Ultrasensitive Isotope Trace Analyses with a Magneto-Optical Trap.* Science **286**(5442):1139 (1999).

[56] D. Haubrich, H. Schadwinkel, F. Strauch, B. Ueberholz, R. Wynands and D. Meschede. *Observation of individual neutral atoms in magnetic and magneto-optical traps.* EPL (Europhysics Letters) **34**(9):663 (1996).

[57] N. Schlosser, G. Reymond, I. Protsenko and P. Grangier. *Sub-poissonian loading of single atoms in a microscopic dipole trap.* Nature **411**(6841):1024 (2001).

[58] W. Alt, D. Schrader, S. Kuhr, M. Müller, V. Gomer and D. Meschede. *Single atoms in a standing-wave dipole trap.* Physical Review A **67**(3):033403 (2003).

[59] S. Yoon, Y. Choi, S. Park, J. Kim, J.-H. Lee and K. An. *Characteristics of single-atom trapping in a magneto-optical trap with a high magnetic-field gradient.* Journal of Physics: Conference Series **88**:211104 (2006).

[60] F. Serwane, G. Zürn, T. Lompe, T. Ottenstein, A. Wenz and S. Jochim. *Deterministic preparation of a tunable few-fermion system.* Science **332**(6027):336 (2011).

[61] D. B. Hume, I. Stroescu, M. Joos, W. Muessel, H. Strobel and M. K. Oberthaler. *Accurate atom counting in mesoscopic ensembles.* Physical Review Letters **111**(25):253001 (2013).

[62] A. Wenz, G. Zürn, S. Murmann, I. Brouzos, T. Lompe and S. Jochim. *From few to many: Observing the formation of a Fermi sea one atom at a time.* Science **342**(6157):457 (2013).

[63] I. Stroescu, D. B. Hume and M. K. Oberthaler. *Double-well atom trap for fluorescence detection at the Heisenberg limit.* Physical Review A **91**(1):013412 (2015).

[64] A. Hüper, C. Pür, M. Hetzel, J. Geng, J. Peise, I. Kruse, M. Kristensen, W. Ertmer, J. Arlt and C. Klempt. *Preparation of mesoscopic atomic ensembles with single-particle resolution.* arXiv preprint arXiv:1912.05689 (2019).

[65] L. Bayha, M. Holten, R. Klemt, K. Subramanian, J. Bjerlin, S. M. Reimann, G. M. Bruun, P. M. Preiss and S. Jochim. *Observing the emergence of a quantum phase transition shell by shell.* Nature **587**(7835):583 (2020).

[66] A similar two-color MOT has been used but not described in Ref. [67] to measure small atom numbers .

[67] C. Shkedrov, Y. Florshaim, G. Ness, A. Gandman and Y. Sagi. *High-Sensitivity rf Spectroscopy of a Strongly Interacting Fermi Gas.* Phys. Rev. Lett. **121**:093402 (2018).

[68] C. F. Ockeloen, A. F. Tauschinsky, R. J. C. Spreeuw and S. Whitlock. *Detection of small atom numbers through image processing.* Physical Review A **82**(6):061606(R) (2010).

[69] M. Dendzik, R. P. Xian, E. Perfetto, D. Sangalli, D. Kutnyakhov, S. Dong, S. Beaulieu, T. Pincelli, F. Pressacco, D. Curcio, S. Y. Agustsson, M. Heber, J. Hauer, W. Wurth, G. Brenner, Y. Acremann, P. Hofmann, M. Wolf, A. Marini, G. Stefanucci, L. Rettig and R. Ernstorfer. *Observation of an Excitonic Mott Transition through Ultrafast Core-cum-Conduction Photoemission Spectroscopy.* Phys. Rev. Lett. **125**:096401 (2020).

[70] G. D. Mahan. *Many-Particle Physics: Physics of Solids and Liquids.* Springer Science + Business Media, LLC, New York (1981). Chapter 9.3.3.

[71] J. Goold, T. Fogarty, N. Lo Gullo, M. Paternostro and T. Busch. *Orthogonality catastrophe as a consequence of qubit embedding in an ultracold Fermi gas.* Physical Review A **84**(6) (2011).

[72] M. Knap, A. Shashi, Y. Nishida, A. Imambekov, D. A. Abanin and E. Demler. *Time-Dependent Impurity in Ultracold Fermions: Orthogonality Catastrophe and Beyond.* Physical Review X **2**(4) (2012).

[73] M. Cetina, M. Jag, R. S. Lous, I. Fritsche, J. T. M. Walraven, R. Grimm, J. Levinsen, M. M. Parish, R. Schmidt, M. Knap and E. Demler. *Ultrafast many-body interferometry of impurities coupled to a Fermi sea.* Science **354**(6308):96 (2016).

[74] A. Bergschneider. *Strong correlations in few-fermion systems.* Ph.D. thesis, Ruperto-Carola University of Heidelberg Germany (2017). Chapter 5.3.

[75] C. Weitenberg, M. Endres, J. F. Sherson, M. Cheneau, P. Schauß, T. Fukuhara, I. Bloch and S. Kuhr. *Single-spin addressing in an atomic Mott insulator.* Nature **471**(7338):319 (2011).

[76] R. Wei and E. J. Mueller. *Magnetic-field dependence of Raman coupling in alkali-metal atoms.* Phys. Rev. A **87**:042514 (2013).

[77] L. Schäfer. *Aufbau einer Dipolfalle für evaporatives Kühlen von 40Kalium* (2020). Bachelor Thesis. University of Hamburg, Germany.

[78] C. Lobo, A. Recati, S. Giorgini and S. Stringari. *Normal State of a Polarized Fermi Gas at Unitarity.* Phys. Rev. Lett. **97**:200403 (2006).

[79] N. Prokof'ev and B. Svistunov. *Fermi-polaron problem: Diagrammatic Monte Carlo method for divergent sign-alternating series.* Phys. Rev. B **77**:020408 (2008).

[80] M. Punk, P. T. Dumitrescu and W. Zwerger. *Polaron-to-molecule transition in a strongly imbalanced Fermi gas.* Physical Review A **80**(5) (2009).

[81] F. Chevy and C. Mora. *Ultra-cold polarized Fermi gases.* Reports on Progress in Physics **73**(11):112401 (2010).

[82] S. Pilati, G. Bertaina, S. Giorgini and M. Troyer. *Itinerant Ferromagnetism of a Repulsive Atomic Fermi Gas: A Quantum Monte Carlo Study.* Phys. Rev. Lett. **105**:030405 (2010).

[83] A. Schirotzek, C.-H. Wu, A. Sommer and M. W. Zwierlein. *Observation of Fermi Polarons in a Tunable Fermi Liquid of Ultracold Atoms.* Phys. Rev. Lett. **102**:230402 (2009).

[84] S. Nascimbène, N. Navon, K. J. Jiang, L. Tarruell, M. Teichmann, J. McKeever, F. Chevy and C. Salomon. *Collective Oscillations of an Imbalanced Fermi Gas: Axial Compression Modes and Polaron Effective Mass.* Phys. Rev. Lett. **103**:170402 (2009).

[85] C. Kohstall, M. Zaccanti, M. Jag, A. Trenkwalder, P. Massignan, G. M. Bruun, F. Schreck and R. Grimm. *Metastability and coherence of repulsive polarons in a strongly interacting Fermi mixture.* Nature **485**(7400):615–618 (2012).

[86] M. M. Parish. *Polaron-molecule transitions in a two-dimensional Fermi gas.* Phys. Rev. A **83**:051603 (2011).

[87] M. Klawunn and A. Recati. *Fermi polaron in two dimensions: Importance of the two-body bound state.* Phys. Rev. A **84**:033607 (2011).

[88] S. Zöllner, G. M. Bruun and C. J. Pethick. *Polarons and molecules in a two-dimensional Fermi gas.* Phys. Rev. A **83**:021603 (2011).

[89] J. Levinsen and S. K. Baur. *High-polarization limit of the quasi-two-dimensional Fermi gas.* Physical Review A **86**(4) (2012).

[90] M. Koschorreck, D. Pertot, E. Vogt, B. Fröhlich, M. Feld and M. Köhl. *Attractive and repulsive Fermi polarons in two dimensions.* Nature **485**(7400):619–622 (2012).

[91] N. Spethmann, F. Kindermann, S. John, C. Weber, D. Meschede and A. Widera. *Dynamics of Single Neutral Impurity Atoms Immersed in an Ultracold Gas.* Phys. Rev. Lett. **109**:235301 (2012).

[92] R. Scelle, T. Rentrop, A. Trautmann, T. Schuster and M. K. Oberthaler. *Motional Coherence of Fermions Immersed in a Bose Gas.* Phys. Rev. Lett. **111**:070401 (2013).

[93] G. E. Marti, A. MacRae, R. Olf, S. Lourette, F. Fang and D. M. Stamper-Kurn. *Coherent Magnon Optics in a Ferromagnetic Spinor Bose-Einstein Condensate.* Physical Review Letters **113**(15) (2014).

[94] M.-G. Hu, M. J. Van de Graaff, D. Kedar, J. P. Corson, E. A. Cornell and D. S. Jin. *Bose Polarons in the Strongly Interacting Regime.* Physical Review Letters **117**(5) (2016).

[95] N. B. Jørgensen, L. Wacker, K. T. Skalmstang, M. M. Parish, J. Levinsen, R. S. Christensen, G. M. Bruun and J. J. Arlt. *Observation of Attractive and Repulsive Polarons in a Bose-Einstein Condensate.* Physical Review Letters **117**(5) (2016).

[96] L. A. Peña Ardila, N. B. Jørgensen, T. Pohl, S. Giorgini, G. M. Bruun and J. J. Arlt. *Analyzing a Bose polaron across resonant interactions.* Phys. Rev. A **99**:063607 (2019).

[97] Z. Z. Yan, Y. Ni, C. Robens and M. W. Zwierlein. *Bose polarons near quantum criticality.* Science **368**(6487):190–194 (2020).

[98] M. G. Skou, T. G. Skov, N. B. Jørgensen, K. K. Nielsen, A. Camacho-Guardian, T. Pohl, G. M. Bruun and J. J. Arlt. *Non-equilibrium quantum dynamics and formation of the Bose polaron.* Nature Physics **17**(6):731–735 (2021).

[99] M. G. Skou, K. K. Nielsen, T. G. Skov, A. M. Morgen, N. B. Jørgensen, A. Camacho-Guardian, T. Pohl, G. M. Bruun and J. J. Arlt. *Life and death of the Bose polaron.* Physical Review Research **4**(4) (2022).

[100] A. M. Morgen, S. S. Balling, K. K. Nielsen, T. Pohl, G. M. Bruun and J. J. Arlt. *Quantum beat spectroscopy of repulsive Bose polarons* (2023).

[101] F. M. Cucchietti and E. Timmermans. *Strong-Coupling Polarons in Dilute Gas Bose-Einstein Condensates.* Phys. Rev. Lett. **96**:210401 (2006).

[102] J. Tempere, W. Casteels, M. K. Oberthaler, S. Knoop, E. Timmermans and J. T. Devreese. *Feynman path-integral treatment of the BEC-impurity polaron.* Phys. Rev. B **80**:184504 (2009).

[103] S. P. Rath and R. Schmidt. *Field-theoretical study of the Bose polaron.* Phys. Rev. A **88**:053632 (2013).

[104] W. Li and S. Das Sarma. *Variational study of polarons in Bose-Einstein condensates.* Phys. Rev. A **90**:013618 (2014).

[105] L. A. P. Ardila and S. Giorgini. *Impurity in a Bose-Einstein condensate: Study of the attractive and repulsive branch using quantum Monte Carlo methods.* Physical Review A **92**(3) (2015).

[106] R. S. Christensen, J. Levinsen and G. M. Bruun. *Quasiparticle Properties of a Mobile Impurity in a Bose-Einstein Condensate.* Phys. Rev. Lett. **115**:160401 (2015).

[107] F. Grusdt, Y. E. Shchadilova, A. N. Rubtsov and E. Demler. *Renormalization group approach to the Fröhlich polaron model: application to impurity-BEC problem.* Scientific Reports **5**(1) (2015).

[108] J. Levinsen, M. M. Parish and G. M. Bruun. *Impurity in a Bose-Einstein Condensate and the Efimov Effect.* Phys. Rev. Lett. **115**:125302 (2015).

[109] Y. E. Shchadilova, R. Schmidt, F. Grusdt and E. Demler. *Quantum Dynamics of Ultracold Bose Polarons.* Phys. Rev. Lett. **117**:113002 (2016).

[110] J. Levinsen, M. M. Parish, R. S. Christensen, J. J. Arlt and G. M. Bruun. *Finite-temperature behavior of the Bose polaron.* Phys. Rev. A **96**:063622 (2017).

[111] N.-E. Guenther, P. Massignan, M. Lewenstein and G. M. Bruun. *Bose Polarons at Finite Temperature and Strong Coupling.* Phys. Rev. Lett. **120**:050405 (2018).

[112] S. M. Yoshida, S. Endo, J. Levinsen and M. M. Parish. *Universality of an Impurity in a Bose-Einstein Condensate.* Physical Review X **8**(1) (2018).

[113] M. Drescher, M. Salmhofer and T. Enss. *Theory of a resonantly interacting impurity in a Bose-Einstein condensate.* Phys. Rev. Res. **2**:032011 (2020).

[114] P. Massignan, N. Yegovtsev and V. Gurarie. *Universal Aspects of a Strongly Interacting Impurity in a Dilute Bose Condensate.* Phys. Rev. Lett. **126**:123403 (2021).

[115] J. Levinsen, L. A. P. Ardila, S. M. Yoshida and M. M. Parish. *Quantum Behavior of a Heavy Impurity Strongly Coupled to a Bose Gas.* Physical Review Letters **127**(3) (2021).

[116] R. Schmidt and T. Enss. *Self-stabilized Bose polarons.* SciPost Physics **13**(3) (2022).

[117] A. Christianen, J. I. Cirac and R. Schmidt. *Phase diagram for strong-coupling Bose polarons* (2023).

[118] N. Mostaan, N. Goldman and F. Grusdt. *A unified theory of strong coupling Bose polarons: From repulsive polarons to non-Gaussian many-body bound states* (2023).

[119] W. Casteels, J. Tempere and J. T. Devreese. *Polaronic properties of an impurity in a Bose-Einstein condensate in reduced dimensions.* Phys. Rev. A **86**:043614 (2012).

[120] F. Grusdt and M. Fleischhauer. *Tunable Polarons of Slow-Light Polaritons in a Two-Dimensional Bose-Einstein Condensate.* Phys. Rev. Lett. **116**:053602 (2016).

[121] V. Pastukhov. *Polaron in dilute 2D Bose gas at low temperatures.* Journal of Physics B: Atomic, Molecular and Optical Physics **51**(15):155203 (2018).

[122] E. Akaturk and B. Tanatar. *Two-dimensional Bose polaron using diffusion Monte Carlo method.* International Journal of Modern Physics B **33**(21):1950238 (2019).

[123] L. A. P. Ardila, G. E. Astrakharchik and S. Giorgini. *Strong coupling Bose polarons in a two-dimensional gas.* Physical Review Research **2**(2) (2020).

[124] O. Hryhorchak, G. Panochko and V. Pastukhov. *Mean-field study of repulsive 2D and 3D Bose polarons.* Journal of Physics B: Atomic, Molecular and Optical Physics **53**(20):205302 (2020).

[125] J. Sánchez-Baena, L. A. P. Ardila, G. Astrakharchik and F. Mazzanti. *Universal properties of dipolar Bose polarons in two dimensions* (2023).

[126] R. Jackiw. *Lower dimensional gravity.* Nuclear Physics B **252**:343 (1985).

[127] J. M. Leinaas and J. Myrheim. *On the theory of identical particles.* Niovo Cim B **37**:1 (1977).

[128] F. Wilczek. *Magnetic Flux, Angular Momentum, and Statistics.* Phys. Rev. Lett. **48**:1144 (1982).

[129] L. D. Landau and E. M. Lifshitz. *Quantum Mechanics.* Pergamon Press Ltd., Oxford (1977). Chapter 6.

[130] S. M. Apenko. *Weakly bound states in 2+ϵ dimensions.* Journal of Physics A: Mathematical and General **31**(6):1553–1562 (1998).

[131] L. D. Landau and E. M. Lifshitz. *Statistical Physics.* Pergamon Press Ltd., Oxford (1980).

[132] H. Wagner. *Long-wavelength excitations and the Goldstone theorem in many-particle systems with "broken symmetries".* Zeitschrift für Physik pages 273–299 (1966).

[133] P. C. Hohenberg. *Existence of Long-Range Order in One and Two Dimensions.* Phys. Rev. **158**:383 (1967).

[134] N. D. Mermin and H. Wagner. *Absence of Ferromagnetism or Antiferromagnetism in One- or Two-Dimensional Isotropic Heisenberg Models.* Phys. Rev. Lett. **17**:1133 (1966).

[135] N. D. Mermin. *Crystalline Order in Two Dimensions.* Phys. Rev. **176**:250 (1968).

[136] Z. Hadzibabic and J. Dalibard. *Two-dimensional Bose fluids: An atomic physics perspective.* La Rivista del Nuovo Cimento **34**(6):389–434 (2011).

[137] V. L. Berezinskiĭ. *Destruction of Long-range Order in One-dimensional and Two-dimensional Systems having a Continuous Symmetry Group I. Classical Systems.* Soviet Journal of Experimental and Theoretical Physics **32**:493 (1971).

[138] J. M. Kosterlitz and D. J. Thouless. *Ordering, metastability and phase transitions in two-dimensional systems.* Journal of Physics C: Solid State Physics **6**(7):1181 (1973).

[139] Z. Hadzibabic, P. Krüger, M. Cheneau, B. Battelier and J. Dalibard. *Berezinskii–Kosterlitz–Thouless crossover in a trapped atomic gas.* Nature **441**(7097):1118–1121 (2006).

[140] S. Sunami, V. P. Singh, D. Garrick, A. Beregi, A. J. Barker, K. Luksch, E. Bentine, L. Mathey and C. J. Foot. *Universal scaling of the dynamic BKT transition in quenched 2D Bose gases.* Science **382**(6669):443–447 (2023).

[141] T. R. S. A. of Sciences. *The Nobel Prize in Physics 2016.* Online: https://www.nobelprize.org/prizes/physics/2016/summary/ (accessed on 2024-01-16).

[142] R. H. Kraichnan. *Inertial Ranges in Two-Dimensional Turbulence.* The Physics of Fluids **10**(7):1417 (1967).

[143] L. H. Thomas. *The calculation of atomic fields.* Mathematical Proceedings of the Cambridge Philosophical Society **23**(5):542–548 (1927).

[144] E. Fermi. *Eine statistische Methode zur Bestimmung einiger Eigenschaften des Atoms und ihre Anwendung auf die Theorie des periodischen Systems der Elemente.* Zeitschrift für Physik **48**:73 (1928).

[145] L. P. Pitaevskii. *Vortex Lines in an Imperfect Bose Gas.* JETP **13**(2):451 (1961).

[146] E. P. Gross. *Structure of a quantized vortex in boson systems.* Il Nuovo Cimento (1955-1965) **20**:454 (1961).

[147] T.-L. Ho and Q. Zhou. *Obtaining phase diagram and thermodynamic quantities of bulk systems from the densities of trapped gases.* Nature Physics **6**:131 (2010).

[148] M. G. Lingham, K. Fenech, S. Hoinka and C. J. Vale. *Local Observation of Pair Condensation in a Fermi Gas at Unitarity.* Phys. Rev. Lett. **112**:100404 (2014).

[149] J. D. Griffiths. *Introduction to Quantum Mechanics.* Pearson Prentice Hall (1995).

[150] C. J. Pethick and H. Smith. *Bose-Einstein Condensation in Dilute Gases*. Cambridge University Press, Cambridge (2002).

[151] S. K. Adhikari. *Quantum scattering in two dimensions*. American Journal of Physics **54**(4):362 (1986).

[152] D. S. Petrov, M. Holzmann and G. V. Shlyapnikov. *Bose-Einstein Condensation in Quasi-2D Trapped Gases*. Phys. Rev. Lett. **84**:2551 (2000).

[153] D. S. Petrov and G. V. Shlyapnikov. *Interatomic collisions in a tightly confined Bose gas*. Phys. Rev. A **64**:012706 (2001).

[154] N. Prokof'ev, O. Ruebenacker and B. Svistunov. *Critical Point of a Weakly Interacting Two-Dimensional Bose Gas*. Phys. Rev. Lett. **87**:270402 (2001).

[155] E. Arimondo, M. Inguscio and P. Violino. *Experimental determinations of the hyperfine structure in the alkali atoms*. Rev. Mod. Phys. **49**:31 (1977).

[156] S. Falke, E. Tiemann, C. Lisdat, H. Schnatz and G. Grosche. *Transition frequencies of the D lines of* ^{39}K*,* ^{40}K*, and* ^{41}K *measured with a femtosecond laser frequency comb*. Phys. Rev. A **74**:032503 (2006).

[157] T. G. Tiecke. *Feshbach resonances in ultracold mixtures of the fermionic quantum gases 6Li and 40K*. Ph.D. thesis, University of Amsterdam (2009).

[158] G. Salomon, L. Fouché, P. Wang, A. Aspect, P. Bouyer and T. Bourdel. *Gray-molasses cooling of 39K to a high phase-space density*. Europhysics Letters **104**(6):63002 (2014).

[159] M. Landini, S. Roy, G. Roati, A. Simoni, M. Inguscio, G. Modugno and M. Fattori. *Direct evaporative cooling of* ^{39}K *atoms to Bose-Einstein condensation*. Physical Review A **86**(3) (2012).

[160] Physikalisch-Technische Bundesanstalt, Braunschweig, Germany. *The Earth's magnetic field at PTB*. Online: https://www.ptb.de/cms/nc/en/ptb/fachabteilungen/abt2/fb-25/ag-251/live-data-earths-magnetic-field.html (accessed on 2023-11-27).

[161] N. Semakov, A. Kovalev, A. Pavlov and O. Fedotova. *Moving daily average of the hourly magnetic field values - the example of usage at Novosibirsk Observatory during 2011 (results and prospects). E3S Web of Conferences*, volume 196 of *E3S Web of Conferences*, page 02020 (2020).

[162] B. G. Survey. *The Earth's Magnetic Field: An Overview.* Online: http://www.geomag.bgs.ac.uk/education/earthmag.html (accessed on 2023-11-27).

[163] N. G. M. Team and B. G. Survey. *World Magnetic Model 2020* (2019).

[164] Manufacturer Andor, type Zyla 5.5 sCMOS .

[165] T. Thiele, Y. Lin, M. O. Brown and C. A. Regal. *Self-Calibrating Vector Atomic Magnetometry through Microwave Polarization Reconstruction.* Physical Review Letters **121**(15) (2018).

[166] L. J. LeBlanc. *The Hyperfine Structure of Potassium-40* (2006). Online: https://www.physics.utoronto.ca/ jht/reprints/LeBlanc40K.pdf (Accessed on 2024-01-24).

[167] N. Ramsey. *Molecular Beams.* Oxford University Press (1986).

[168] R. J. Wild, P. Makotyn, J. M. Pino, E. A. Cornell and D. S. Jin. *Measurements of Tan's Contact in an Atomic Bose-Einstein Condensate.* Phys. Rev. Lett. **108**:145305 (2012).

[169] I. Shvarchuck, C. Buggle, D. S. Petrov, K. Dieckmann, M. Zielonkowski, M. Kemmann, T. G. Tiecke, W. von Klitzing, G. V. Shlyapnikov and J. T. M. Walraven. *Bose-Einstein Condensation into Nonequilibrium States Studied by Condensate Focusing.* Phys. Rev. Lett. **89**:270404 (2002).

[170] A. H. van Amerongen, J. J. P. van Es, P. Wicke, K. V. Kheruntsyan and N. J. van Druten. *Yang-Yang Thermodynamics on an Atom Chip.* Phys. Rev. Lett. **100**:090402 (2008).

[171] S. Tung, G. Lamporesi, D. Lobser, L. Xia and E. A. Cornell. *Observation of the Presuperfluid Regime in a Two-Dimensional Bose Gas.* Phys. Rev. Lett. **105**:230408 (2010).

[172] P. A. Murthy, D. Kedar, T. Lompe, M. Neidig, M. G. Ries, A. N. Wenz, G. Zürn and S. Jochim. *Matter-wave Fourier optics with a strongly interacting two-dimensional Fermi gas.* Phys. Rev. A **90**:043611 (2014).

[173] G. E. Astrakharchik and L. P. Pitaevskii. *Motion of a heavy impurity through a Bose-Einstein condensate.* Phys. Rev. A **70**:013608 (2004).

[174] M. Bruderer, W. Bao and D. Jaksch. *Self-trapping of impurities in Bose-Einstein condensates: Strong attractive and repulsive coupling.* EPL (Europhysics Letters) **82**(3):30004 (2008).

Eidesstattliche Versicherung

Hiermit versichere ich an Eides statt, die vorliegende Dissertationsschrift selbst verfasst und keine anderen als die angegebenen Hilfsmittel und Quellen benutzt zu haben.

Hamburg, den 29.01.2024

Unterschrift der Doktorandin / des Doktoranden